THE UNIVERSITY OF ADELAIDE

Department of Mechanical Engineering

TIME-AVERAGED HOLOGRAPHY FOR THE STUDY OF THREE-DIMENSIONAL VIBRATIONS

by

Renzo Tonin, B.Sc. (Hons.)

Thesis for the Degree of Doctor of Philosophy

March 1978

SUMMARY

The theory of time-averaged holography is extended to take into account three-dimensional phasor vibrations of a single frequency. The vibration is considered to be characterised by a spatially varying Fourier expansion of superposed spatial modes and temporally dependent coupled modes in three dimensions leading to the derivation of the general characteristic equation. The method of Generalized Least Squares is introduced to solve the non-linear general characteristic equation including phase without the need to modulate the laser beam.

The new theory and method of analysis is applied to a number of vibrating objects including a clamped circular plate, wine glass, stainless-steel beaker and cylinders of various materials with shear-diaphragm ends. For the first time the radial, tangential and longitudinal vibration components are determined experimentally and compared with theoretical predictions.

The theory of vibration of cylinders of varying wall thicknesses is solved using the Rayleigh-Ritz method and the mode shapes experimentally determined, for the case of a cylinder with non-concentric inner bore and outer surface and a cylinder with a thin longitudinal strip, using the new holographic theory.

A number of coupled modes in a near perfect cylinder are analysed and the phase component determined for the first time without modulating the laser beam. Results are compared with predictions for one-dimensional phasor vibrations.

New experimental techniques such as the translating hologram table, resonance unit and data system are described which aid in the generation and analysis of time-averaged holograms of complex vibrations.

Finally, the sound radiation efficiency of various cylinders is measured in a reverberation room and compared with theory.

TABLE OF CONTENTS

STATEMENT OF ORIGINALITY

This thesis contains no material which has been accepted for the award of any other degree or diploma in any University. To the best of the author's knowledge and belief, this thesis contains no material previously published or written by another person, except where due reference is made in the text.

R. TONIN

March 1978

ACKNOWLEDGEMENTS

To my supervisor Dr. David Bies I express my greatest thanks. His ideas have been my major source of inspiration and it has been a pleasure working under him as he is a fine gentleman and a good friend. His dedication to his work and unselfish giving of his time will have a lasting impression.

Thanks goes to Professor Sam Luxton, Chairman of the Department, for arranging my candidature particularly since my under-graduate work was involved in another discipline. His belief in my ability is highly treasured.

Many thanks to Colin Hansen for his tutoring in hologram production and to Andrew Davis and Phil Walker for help in setting up the data system without which at least another year would have been needed to complete this thesis.

I am also indebted to Dudley Morrison and Ron Parfitt for their engineering excellence which made possible the manufacture of the close-tolerance cylinders.

To all those fine people in the department whose names I did not mention but whose help I could not have done without, a special word of thanks.

Finally I acknowledge the generous financial assistance of the Australian Research Grants Committee, without which much of the experimental work would not have been possible.

FIGURES

TABLES

SYMBOLS

A	Longitudinal vibration amplitude
A^o	Unperturbed complex analytical signal
$\overline{A}$	Average complex analytical signal
$\underline{A}$	Matrix of the normal equations
A_R	Area of reverberation room
$A(H,t)$	Complex analytical signal in the plane of the hologram
$A(S)$	Complex analytical signal in the plane of the object
AA	Distance from aperture to centre of object
B	Tangential vibration amplitude
BB	Distance defined in Fig. 3-7
C	Radial vibration amplitude
CC	Distance defined in Fig. 3-7
D	Aperture diameter
D_p	Distance defined in Fig. 3-1
$\underline{D}$	Generalized stiffness matrix
E	Young's Modulus
F	Matrix defined by equation (2.52)
G	Matrix of differentials defined by equation (2.43)
H	General hologram co-ordinate
H_n	Hankel function of the first kind of order n
I	Number of coupled temporal modes
J_n	Bessel function of the first kind of order n
$\underset{\sim}{K}_1$	Illumination vector
$\underset{\sim}{K}_2$	Observation vector
K_q	Geometrical factor defined by equation (2.25)
K_a	Non-dimensional frequency parameter
L	Principal length of object
L_v	Principal length of object in photograph
L_w	Power level re 10^{-12} watts/m^2

L_p	Sound pressure level re 20 μPa
M	General characteristic function
N	Number of superposed spatial modes
O_D	Origin - direct view
O_I	Origin - imaged view
P	Distance from centre of object to point illumination
P_{mn}	Function defined in equation (A6.6)
Q_q	Geometrical factor defined in equation (2.25)
$\underline{Q}$	Generalized mass matrix
R	General space co-ordinate
$\underline{R}$	Vector of amplitude parameters
$\underline{\hat{R}}$	Optimum vector of amplitude parameters
R_{mn}	Radial harmonic of the pressure field
S	General surface co-ordinate
S_q	Geometrical factor defined in equation (2.25)
S_D	Angle through which cylinder is rotated
St	Strain energy
S_A	Radiation area
T	Kinetic energy
T_{60}	Reverberation time
U	Time-varying longitudinal vibration amplitude
V	Time-varying tangential vibration amplitude
V_R	Reverberation room volume
W	Time-varying radial vibration amplitude
X	Cartesian co-ordinate
Y	Cartesian co-ordinate
Y_n	Neumann's function of order n
Y_D	Length defined in Fig. 2-11
Z	Cartesian co-ordinate

a	Longitudinal vibration component
a_v^R	Right radius of imaged cylinder in photograph
a_v^L	Left radius of imaged cylinder in photograph
a_v	Radius of cylinder in photograph
a_o	Mean radius of cylinder
a_1	Inner radius of cylinder
a_2	Outer radius of cylinder
b	Tangential vibration component
c	Radial vibration component
c_o	Propagation speed
$\underset{\sim}{d}$, $\underline{d}$	Total vibration phasor
d_v	Diameter of imaged cylinder in photograph
e	Eccentricity
e_1, e_2, e_3	Principal co-ordinates
$\underset{\sim}{e}_1$, $\underset{\sim}{e}_2$, $\underset{\sim}{e}_3$	Unit vectors
f_q	Residual function
f	Frequency
g	Number defined in Appendix IV
h	Cylinder wall thickness
h_1, h_2	Principal hologram co-ordinates
h^+	Outer thickness measured from cylinder middle surface
h^-	Inner thickness measured from cylinder middle surface
k	Wave number or propagation constant. $k = \omega/c_o$
k_m	Axial wave number. $k_m = m\pi/L$
ℓ	Length co-ordinate along the surface contour
m	Longitudinal mode order
n	Circumferential mode order
p	Order of distortion component
p_w	Weight of amplitude parameter

p_r	Sound pressure
q	Point on the surface contour
r	Two dimensional space co-ordinate
s	Non-dimensional axial co-ordinate. $s = X/a_o$
s_1, s_2	Principal surface co-ordinates
t	Time
u	Asymmetric longitudinal amplitude component
v	Symmetric longitudinal amplitude component
w	Asymmetric tangential amplitude component
x	Asymmetric radial amplitude component
y	Symmetric radial amplitude component
z	Symmetric tangential amplitude component
Δ	Phasor phase difference
∇	Angle defined in Fig. 3-7
Λ	Non-dimensional eigen frequency
Γ	Matrix defined by equation (2.51)
$\underline{T}$	Matrix differential operator
Π	Acoustic power
$\Pi^{ij\ldots}_{k\ell\ldots}$	Integral function defined in Appendix V
τ	Total number of data points
χ	Distance from aperture to screen
Ω	Argument of the characteristic function
$\underline{\Omega}$	Vector of fringe parameters
$< >_{st}$	Average over space and time
α	Angle subtended by centre line AA and illumination line P.
α^i	Longitudinal component phase
β^i	Tangential component phase
γ	Angle defined by equation (2.59)

γ^i	Radial component phase
$\underline{\delta}$	Correction vector
ϵ	Angle defining orientation of mode around cylinder
κ	Non-dimensional thickness parameter. $\kappa = h^2/12a_o^2$
λ	Non-dimensional axial wavelength. $\lambda = m\pi a_o/L$
μ	Angle defined in Fig. 4-6
ν	Poisson's ratio
ξ	Angular co-ordinate along a surface contour
π	pi
ρ	Density
θ	Angular co-ordinate
θ_I	Angular co-ordinate in imaged view
θ_1	Angle subtended by surface normal and illumination vector
θ_2	Angle subtended by surface normal and observation vector
σ	Radiation efficiency
ζ	Sum of squares of residuals
$\hat{\zeta}$	Least sum of squares of residuals
ϕ	Angular co-ordinate
ψ	Angle between direct and imaged views of cylinder
ω	Angular frequency

CHAPTER 1

LITERATURE SURVEY

1.1 HOLOGRAPHIC INTERFEROMETRY

The discovery of holographic interferometry, notably by Powell and Stetson [1] in 1965, has led to a remarkable development in the field of vibration analysis. Here is a developmental tool with the same impact on dynamics as quantum theory had on mechanics - a contact-less probe into the miniscule vibratory motions of structures. Stetson and Powell [2] in 1966 demonstrated the equivalence concept, which is basic to the theory of holographic interferometry, that exposing the holographic plate with the reference beam and object beam in sequence gives the same result as simultaneous recording. This leads to the concept of real-time holographic interferometry. Representing the electromagnetic field of the laser radiation as an angular spectrum of plane waves [3], Brown et al derive semi-rigorous equations for time-averaged and real-time holographic interferometry of one dimensional simple harmonic vibration [4]. Butusov [5] presents the theory for time-averaged holography in a mathematically more rigorous form and Hildebrand [6] generalizes the theory of holography.

The basic requirements for making a good hologram are coherent, monochromatic light and freedom from extraneous vibrations. Lurie [7] shows in theory, if the reference beam is a plane wave, the reconstruction is sharp even though the light is only partially coherent. The variation in coherence over the object surface is a greater factor in the loss of clarity. If the object is moved linearly during the recording the image intensity is modulated by a sinc-function which is responsible

for the perceived blurring [8]. For sinusoidal disturbance, the degree of blurring is proportional to the vibration amplitude [9].

The theory of time-averaged holography developed by Powell and Stetson was verified for one dimensional simple harmonic vibration by Lurie and Zambuto [10]. The authors recognize that the integral

$$\frac{1}{T}\int_{o}^{T} \exp[ikc(t)(\cos\theta_1 + \cos\theta_2)]dt,$$

is valid for any motion c(t) no matter how complex it may be. In the equation θ_1 and θ_2 are the angles subtended by the surface normal and the illumination and observation vectors respectively and k is the radiation wavenumber. The errors [11] involved in the determination of a displacement are principally

1. inaccuracy in determining θ_1 and θ_2 (1° error results in about 1% error in displacement amplitude) and

2. inaccuracy in determining the fringe order due to fringe width which is inversely proportional to signal to noise ratio (0.5 fringe error results in roughly 5% error in displacement amplitude). Nevertheless the analysis of simple harmonic motion by time-averaged holography can be trivial with the formula derived by Borza [12].

One of the limitations of holographic interferometry of vibrations is that only relatively small amplitudes (less than about 2μm) can be analyzed since fringe intensity is inversely proportional to fringe order which is determined by the argument of the characteristic fringe function. For time-averaged holography the intensity of the fringes varies as J_o^2 where the characteristic fringe function J_o is the zero order Bessel function. In this case the tenth bright fringe is less than 2% the intensity of the zeroth order bright fringe. For real-time holography the contrast is poorer since the intensity varies as $(1+J_o)$ [4]. One method of improving the dynamic range is to artificially

increase the wavelength of the radiating light by a Moiré technique used in the study of stress deformations in transparent objects [13]. Rowe [14] describes a method of projecting interference fringes onto an object surface and recording a time-averaged hologram of a fixed rotation of the object in the usual way. The fringes interfere to form a Moiré pattern analogous to the normal Bessel fringes except that quite large displacements are analysed. Hung et al [15] have extended this method to analyse vibrations of large amplitudes and Joyeux [16] describes an on-line instrument which measures displacements directly using this Moiré technique.

The object under study is usually required to scatter light diffusely. However, phase objects (usual in gas dynamics problems) have been analysed using the principles of holographic interferometry. Ovechkin et al [17] describe a double exposure method with the object in the path of the object beam. Another technique [18] is to project the phase-varying object beam onto a flat diffuse surface which then functions as a normal diffuse object.

Holographic interferometry requires only one reference beam. However, Dändliker et al [19] and Tsuruta et al [20] describe a method of two reference beams as a means of adding flexibility to conventional double exposure interferometry. This procedure enables information of objects to be taken separately or with mutual interference. Tsuruta et al use this principle, in lieu of the double exposure technique, which has alignment problems, to investigate an object which has been modified and replaced in the object beam.

The theory of holographic interferometry of simple vibrations in one dimension has found widespread applications in other disciplines. Bies [21] shows how the normal component of vibration, as determined from holograms, can be used to predict radiation efficiencies of vibrating surfaces - an important problem in acoustics. Frankort [22] predicts

the radiation behaviour of loudspeaker cones in this way. Vasil'yev et al [23] analyse vibration components of blades and discs of compressors in aircraft engines. Zakharov et al [24] describe a potentially portable laser microprobe to analyse vibrations in the field using the principles of holographic interferometry. In the biomedical sciences Greguss [25] and Hogmoen and Gundersen [26] describe the use of interferometry in the analysis of the vibration of the human tympanic membrane, stresses in teeth (holodontometry), deformation of the femur (orthopedics) and respiration contours of the human body. The possibility of colour interferograms has also been considered by Chernov and Gorbatenko [27]. Fryer [28] and Rogent and Brown [29] have written reviews on holographic vibration analysis covering almost every aspect of holographic interferometry.

The extension of one-dimensional holographic interferometry into three dimensions was a natural progression. Haines and Hildebrand (1966) [30], to whom the discovery of holographic interferometry is also attributed, extended the theory to include static rotation and translation of the object in three dimensions. The resulting formulae are difficult to use in practice hence Sollid [31] developed two schemes - the single hologram method utilizing parallax and fringe counting and a multiple hologram method using interference order assignment. The first scheme involves counting the number of fringes that shift past an object point as the point of observation is moved from one position on the hologram to another. Dhir and Sikora [32] improve this technique by expressing the components of displacement as a set of linear equations which are solved by the least squares method and they note that only the sign of one component was necessary *a priori* to determine the others. The second scheme utilized a set of holograms with several directions of observation or illumination and was improved by Sciammarella and Gilbert [33] who determined the displacement components by the method

of least squares. Although the first scheme has been automated for data processing [34] its main disadvantage is that for small displacements the field of the hologram may not be large enough to enable at least a few fringe counts. For this reason in this thesis the author prefers the second scheme which is also easier to adapt to data processing.

Stetson [35] and with Pryputniewicz [36] use the second technique to separate rigid-body motion and homogeneous deformation with the application of the least squares method to an overdetermined set of linear equations. Hu et al [37] describe a Moiré technique which compensates for rigid-body motion using two holographic interferograms, one on each side of the object, and reconstructed together to produce Moiré isopachic fringes of the stress displacement only.

Ennos [38] makes use of the technique of multiple holograms to measure the strain in one direction only in the plane of a surface under tension. Sciammarella and Gilbert [39] extend this method with the aid of a Moiré technique to optically separate two components of displacement of a surface under compression.

Using light scattered by the interior of a three dimensional transparent object from a sheet of coherent light passing through the body Barker and Fourney [40] describe how displacement information may be recorded in sections to describe fully the deformation of the object. This broad concept is used in this thesis to construct a fully three-dimensional vibration map of any object surface in two-dimensional sheets or slices, with the result that the mathematics is less complex and hence more applicable to real analysis.

A rigorous theory of fringe formation and localization has been derived by Stetson as an improvement of more complex and approximate descriptions; for example that of Tsuruta et al [41]. In a series of excellently planned papers Stetson [42-48] derives a rigorous form-

ulation of the generalized fringe function, discusses in depth the factors affecting the argument of the fringe function, predicts fringe loci and localization for a combination of whole body rotations and translations and supports the theory by a large number of experiments. The results most applicable to this thesis are

1. that fringe spacing and localization are unaffected by the curvature of an object surface and

2. the observer-projection theorem (fringes observed localized in any plane may be projected on to the object plane) justifies the use of a camera and photographic enlarger to produce pictures of the holographic interferogram.

Walles [49] extends the concept of homologous rays to compute and visualize fringe localization for arbitrary movements, including strain and shear.

Abramson [50-55] introduces the holo-diagram which is a pictorial representation of the formation of fringes in holographic interferometry. The distance between the point of illumination and the hologram determines the sensitivity. Hence the process makes optimum use of the coherence length of the laser radiation and objects up to 2m in length may be studied. Abramson also introduces the sandwich hologram [56] to eliminate whole body movement in holographic interferograms of deformed objects.

Matsumoto et al [57] analyse the measuring errors of three-dimensional displacements by holographic interferometry. In particular, for the case of the multiple hologram technique, the contributions of optical errors and fringe-reading errors are least for orthogonal systems of illumination or observation directions.

Holographic interferometry has been applied to the measurement of steady velocity [58-59] where it is shown the characteristic function is the sinc function. Gupta and Singh [60-63] analyse the

characteristic functions of time-averaged holography for non-linear vibrations of the form of Jacobian elliptics. Such motion is typical of vibrations in a shaft connected to a crank and piston or in propellers. However, no experimental application of the theory has yet been reported. Janta and Miler [64] calculate the characteristic function of time-averaged holography for sinusoidal damped oscillations and from fringe data devise a scheme to determine the damping coefficient. Zambuto and Lurie [65] derive the characteristic function for various complex motions - constant velocity (ramp) motion, superposition of ramp motion and sinusoidal vibration and step motion - by considering the effect of motion on coherence. On the other hand, Vikram [66-69] and Vikram and Sirohi [70-72] analyse the same motion using the phase variation equation [1] and suggest various schemes including Moiré techniques, amplitude modulation and spatial variation of the object beam to separate the components of vibration.

In addition to the study of hologram interferometry of complex motions, various workers have considered one dimensional vibrations of a number of modes of more than one frequency. Wilson and Strope [73] show that the characteristic function of two rationally related modes with non-zero phase difference is a linear combination of the product of two Bessel functions of the first kind and of various orders. Wilson [74] extends the concept to include irrationally related modes and generates computer images of the fringe patterns of a circular clamped plate vibrating in such modes. A special case of this is discussed by Reddy [75]. Stetson [76] introduces the method of stationary phase to predict fringe patterns of vibrations of modes of different frequencies and phases. The method assumes that the main contribution of the time-varying propagation argument, Ω, to points in the hologram which reconstruct the brightest, occurs at $\partial\Omega/\partial t = 0$.

The theory is shown to agree well with experimental observations of two modes with rationally related frequencies and of various phase and is physically more meaningful than that proposed by Wilson and Strope.

Vikram [77] suggests a stroboscopic technique to separate two modes of different frequencies. The method consists of pulsing the laser light at times when the amplitude of one mode is invariant and vice-versa for the other mode whereby the separation of the two modes is accomplished by analysing the two holograms.

The more general case of an unlimited number of modes of different frequencies and varying phase has been considered by Dallas and Lohmann [78]. The deciphering concept uses a moving grating in the Fourier plane to deconvolve the coefficients of vibration from the optical Fourier coefficients in the hologram. By "synchronizing" the grating velocity with the frequency of vibration, the mode of vibration for that frequency is separated from the rest. Wilson [79] derives the general characteristic function for any number of modes with different frequencies and phase in terms of a linear combination of a product of Bessel functions of the first kind and various orders. Stetson [80-81] introduces the concept of analysis by density functions. The general characteristic function is expressable as a finite sum of Fourier transforms of the vibration modes. Finally, Vikram and Bose [82] analyse damped oscillations with two frequencies by illuminating the object from two different directions resulting in a Moiré pattern by which the amplitudes of vibration and the damping coefficients are determined.

The material contained in this thesis applies to vibrations of one frequency. The analysis of vibrations involves in part determining the geometry and phases of modes both of which contribute to the resulting fringe pattern of a holographic interferogram. Firstly,

the geometry of the vibration may be separated by considering the motion to consist of a number of linearly independent superposed modes, a method which dates back to Rayleigh (1894). The analysis then involves finding the amplitudes of the contributing modes. This concept was introduced to holographic interferometry by Stetson and Taylor [83]. The pure mode shapes of a clamped rectangular plate were analysed by hologram interferometry and these were used to predict the static deflection resulting from the application of point forces to the plate. In another paper, Stetson and Taylor [84] predict vibration patterns that result from mode combinations in an asymmetrically loaded disk by applying the holographically determined pure mode data of an unloaded disk. Evensen [85] determines the amplitudes of the normal modes of a fluttering panel by a strobing technique.

The phases of the contributing modes are usually determined by beam modulation in contrast to the method presented in this thesis which determines both amplitude and phase information from normal time-averaged holograms. The combination of modes of different phase was shown by Molin and Stetson [86] to result in the addition of their corresponding fringe functions as if they were phasors. Shajenko and Johnson [87] introduced stroboscopic holographic interferometry to "freeze" the phasor motion at any portion of the cycle. Miler [88] improves the theory by assuming the object moves linearly during the exposure period rather than remaining stationary. Takai et al [89] show that by sinusoidally modulating the amplitude of the reference beam the characteristic fringe function is $J_1 \cos\Delta$ where Δ is the phase difference between the phasor vibration and sinusoidal modulation and J_1 is the first-order Bessel function. Hence phase information is observable as a brightness variation of the fringes.

Aleksoff [90] introduces phase modulation of the reference

beam in lieu of amplitude modulation and the theory and technique are analysed in detail by Neumann et al [91] and Aleksoff [92]. The characteristic fringe function is essentially $J_o(k\Delta)$ where Δ includes the phase difference between the phasor vibration and the beam modulation and k is the propagation constant for the laser light. Mottier [93] shows that by phase modulating the reference beam with a triangular function rather than a sinusoidal function, fringes near points vibrating with the same phase reconstruct brighter than others.

Gupta and Aggarwal [94] report on a scheme for determining the direction of motion of static deflections by a triple exposure technique with a change of phase of π radians for one exposure. Stetson [95] studies the effects of beam modulation on fringe loci and localization in time-average hologram interferometry of phasor vibrations. Lokberg and Hogmoen [96] extend the theory of vibration phase mapping to electronic speckle pattern interferometry. Belogorodskii et al [97], Butusov [98] and Yoneyama et al [99] use a small mirror on a point of the vibrating surface to phase modulate the reference beam thereby separating rigid-body motion from other vibration. Finally, Levitt and Stetson [100] describe a phase-mapping procedure to generate vibration-phase contour maps.

The theory of time-averaged holographic interferometry was first applied to three-dimensional vibrations by Liem et al [101]. They reported a strange shift in the calculated geometrical vibration over the surface of a cylinder when illuminated from various positions. Tonin and Bies [102] explained the anomaly by pointing out that the cylinder vibrated with components in three orthogonal directions and hence the application of the normal one dimensional theory of Powell and Stetson was erroneous. They subsequently extend the theory of static holographic interferometry of surface strains in two dimensions

[103] to simple harmonic motion in three dimensions and successfully apply it to a vibrating beaker and wine glass with no strange geometrical shift. Tuschak and Allaire [104] determine the radial and longitudinal components of an ultrasonic resonator using a simple extension of three dimensional static holographic theory. Tonin and Bies [105] improve the method of analysis by assuming the vibration to consist of a series of orthogonal superposed modes and determine the amplitudes by the method of least squares.

Tonin and Bies [106] extend this to include phasor vibrations in three dimensions and show how the amplitudes and phases of superposed and coupled modes (phasor vibrations) are determined without modulating the laser beam. The theory also obviates the need to arbitrarily assign signs to fringes, a method reported by Vlasov and Shtan'ko [107]. Finally, Archbold and Ennos [108] consider two-dimensional vibrations of two frequencies.

The theory of holographic interferometry applied to general three-dimensional surfaces requires that the angles subtended by the illumination and observation vectors to the surface normal be known. The author believes the best way to achieve this is by application of contour holography. If the surface contour and the geometry of the optics are known then the required angles may be determined. Hence a complete vibration analysis would require a set of hologram pairs - a contour hologram and a vibration hologram - which may be taken sequentially. The list of references includes methods of hologram contouring using single frequency lasers [109-120], dual frequency lasers [121-123] and incoherent light [124].

1.2 VIBRATIONS OF CYLINDERS

Most of the three dimensional holographic theory in this thesis will be applied to vibrations of cylinders as they provide simple curved

surfaces and three dimensional motion which is analytically predictable. The flexural vibrations of perfectly cylindrical shells is well documented by Leissa [125] who summarizes ten theories which generally give results too similar to be experimentally distinguished. The Arnold Warburton theory in the author's mind is perhaps the best reported in the literature [126-130].

The theory of vibrations of distorted cylinders is reported using exact methods, semi-empirical methods (e.g. Rayleigh-Ritz, Least squares) or finite element methods. The methods consistent with the holographic theory developed in this thesis are those which assume solutions which are eigen function expansions. Such methods applied to one-dimensional beam problems are listed in the references [131-135]. In particular, the Rayleigh-Ritz method is excellently described by Hurty and Rubinstein [136, Chapt. 4].

Firth [137] predicts the generation of extra-ordinary modes (or superposed modes) by describing irregularities in a shell as a Fourier series in the radius and hence solving the Helmholtz equation by assuming solutions to be a combination of the modes for an undistorted cylinder. In a similar way, Rosen and Singer [138,139] solve the Kármán-Donnell non-linear shell equations to study the effect on the resonant frequency of the superposed modes. Yousri and Fahy [140] generalize the distortion to include anisotropies in the radius of the cylinder, wall thickness and Young's Modulus. Combining all three distortions into one term and solving the Reissner-Naghdi-Berry equations they obtain an expression for the radial displacement. The Rayleigh-Ritz method is used by Toda and Komatsu [141] and the finite difference method by Brogan et al [142] to determine the resonance frequencies and mode shapes of a cylinder with cut-outs. Tonin and Bies [143] determine the resonance frequencies and mode shapes for a cylinder of

variable wall thickness using the Rayleigh-Ritz method and verify the theory using holographic interferometry.

1.3 SOUND RADIATION FROM VIBRATING CYLINDERS

Holographic interferometry has been applied to the study of sound radiation from plates by Hansen and Bies [144] and pipes by Kuhn and Morfey [145]. Measurement of acoustic power by holographic methods is possible if the radial component of vibrating modes is known [146 Chapt. 6, 147]. The theory of sound radiation from a cylinder of finite length is presented by Junger and Feit [148] but no experimental evidence is available in the literature [149-152] to support this theory. However, experiments have been conducted by the author and results are presented in Appendix VI.

CHAPTER 2

TIME-AVERAGED HOLOGRAPHY

The theory of time-averaged holography for static displacements is extended to include three-dimensional vibrations of the most general kind at a single frequency. Additionally the Theory of Generalized Least Squares is introduced to solve the characteristic equation. The determination of component amplitudes and phase is shown to be possible using this method. Also the experimental equipment used in this research and method of analysis are described.

2.1 THEORY OF TIME-AVERAGED HOLOGRAPHY

2.1.1 The Argument of the Characteristic Function in Spherical Co-ordinates

A spherical co-ordinate system is used through the discussion to follow as it is well suited to describe the optical arrangement and is amenable for use in describing the curved cylindrical surfaces of principal concern in this work. Additionally the spherical co-ordinate system, being curvilinear, is most convenient for describing the small scale vibratory motion of concern here as it reduces locally to a Cartesian system. Finally the optical process to be described requires that a number of holograms of different orientations be taken and interpreted. This enables the Least Squares procedure to converge with confidence and hence use is made of a double turntable arrangement - one turntable rotates the object about a horizontal axis and simultaneously rotates on another turntable with vertical axis, not unsimilar to a turret. This arrangement is best described by a spherical co-ordinate system.

Consider any point on a surface at rest as the origin [see Fig 2-1 (a)]. The co-ordinate system for the vibration is defined such that the principal co-ordinate e_1 is the surface normal, a choice dictated by the fact that in acoustics (an area in which the author is concerned), the vibration component normal to the surface is responsible for the generation of sound. If a time-varying force of constant frequency is applied to the object, the point under consideration executes three-dimensional harmonic motion with a locus most generally described as an ellipse. In addition, the vibration is assumed to be statistically stationary. The locus of vibration is then a spatially oriented plane ellipse. The time-varying vector which describes the motion of the point is

$$\underset{\sim}{d}(t) = c(t)\underset{\sim}{e}_1 + b(t)\underset{\sim}{e}_2 + a(t)\underset{\sim}{e}_3 \qquad (2.1)$$

where the orthogonal components of vibration c(t), b(t) and a(t) are time dependent. The choice of letters c,b,a and their order is borrowed from shell theory for cylinders where they correspond to the radial, tangential and longitudinal components of vibration respectively.

Fig. 2-1 (b) shows the co-ordinate system for the optical arrangement. $\underset{\sim}{K}_1$ is the illumination vector, $\underset{\sim}{K}_2$ the observation vector and as is usually the case in time-averaged holographic theory θ_1 and θ_2, the angles subtended by $\underset{\sim}{K}_1$ and $\underset{\sim}{K}_2$ in the plane e_1e_2 are measured from the surface normal e_1 and positive in the directions indicated. The optical path difference is [33]

$$\text{o.p.d.} = \frac{(\underset{\sim}{K}_2 - \underset{\sim}{K}_1) \cdot \underset{\sim}{d}}{k} = \frac{\Omega}{k} \qquad (2.2)$$

where k is the wavenumber $(2\pi/\lambda)$ of the laser radiation and Ω is the argument of the characteristic function $M(\Omega)$ [33,86]. From the geometry

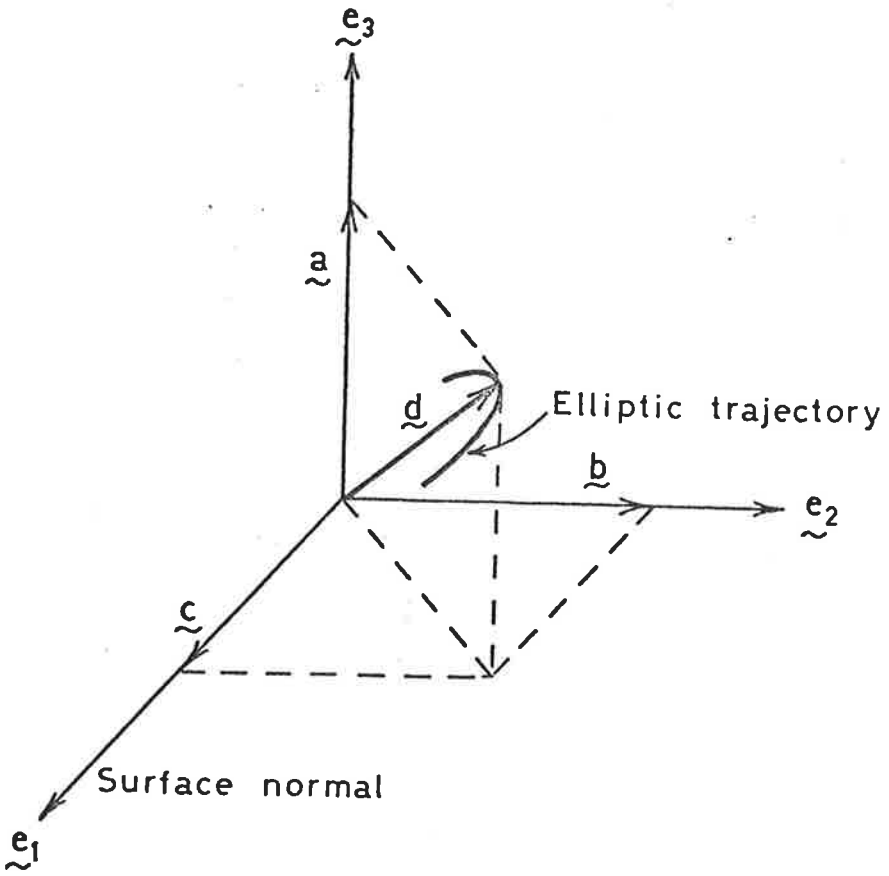

FIG. 2-1 (a) CO-ORDINATE SYSTEM FOR THE VIBRATION COMPONENTS OF A POINT ON THE SURFACE OF THE OBJECT

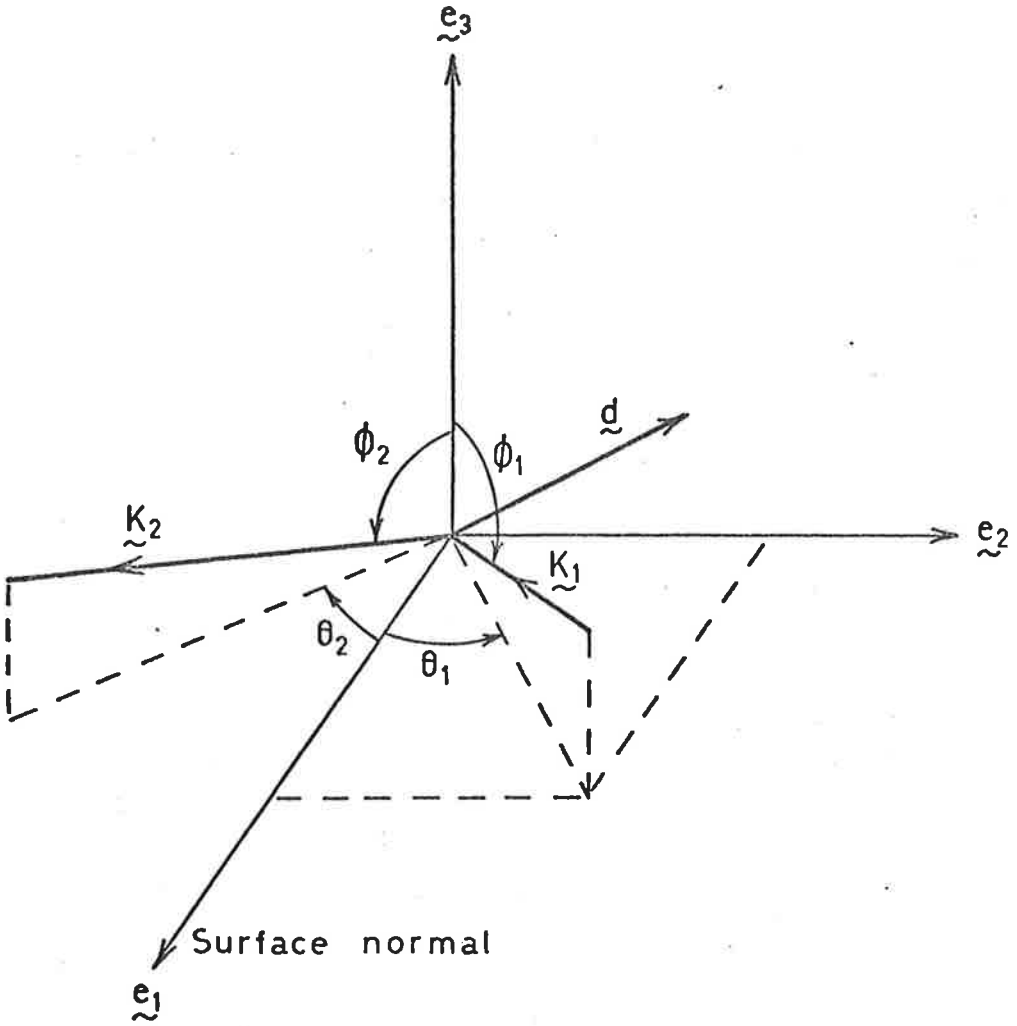

FIG. 2-1 (b) CO-ORDINATE SYSTEM OF THE OPTICS FOR A POINT ON THE SURFACE OF THE OBJECT

Arrows show positive increasing direction.

of Fig. 2-1 (b),

$$\underset{\sim}{K}_1 = -k\cos\theta_1 \sin\phi_1 \underset{\sim}{e}_1 - k\sin\theta_1 \sin\phi_1 \underset{\sim}{e}_2 - k\cos\phi_1 \underset{\sim}{e}_3 \tag{2.3}$$

$$\underset{\sim}{K}_2 = k\cos\theta_2 \sin\phi_2 \underset{\sim}{e}_1 - k\sin\theta_2 \sin\phi_2 \underset{\sim}{e}_2 + k\cos\phi_2 \underset{\sim}{e}_3 \tag{2.4}$$

Substituting equations (2.1), (2.3) and (2.4) into equation (2.2) gives the general result

$$\begin{aligned}\frac{\Omega}{k} = {} & c(t)(\cos\theta_1 \sin\phi_1 + \cos\theta_2 \sin\phi_2) \\ & + b(t)(\sin\theta_1 \sin\phi_1 - \sin\theta_2 \sin\phi_2) \\ & + a(t)(\cos\phi_2 + \cos\phi_1)\end{aligned} \tag{2.5}$$

2.1.2 Coupled and Superposed Modes of Vibration

In general, vibration is a function of spatial variables as well as time dependent. In order to make the analysis practical, the vibration is analysed on a series of surface contours which are defined as the intersection of the object surface and the hyperplane $\phi = \phi_o$ (see Fig. 2-2). In the case of a cylinder, for example, the surface contour is a principal circumference. Hence the location of any point on the surface contour is virtually defined by a singular angular co-ordinate ξ and the total vibration determined "slice-wise" over the entire surface of the object. The vector $\underset{\sim}{d}$ describing the vibration of points on a surface contour is

$$\underset{\sim}{d}(\xi,t) = c(\xi,t)\underset{\sim}{e}_1 + b(\xi,t)\underset{\sim}{e}_2 + a(\xi,t)\underset{\sim}{e}_3 \tag{2.6}$$

and the components of vibration may be expressed as eigen functions [84,85] of the form

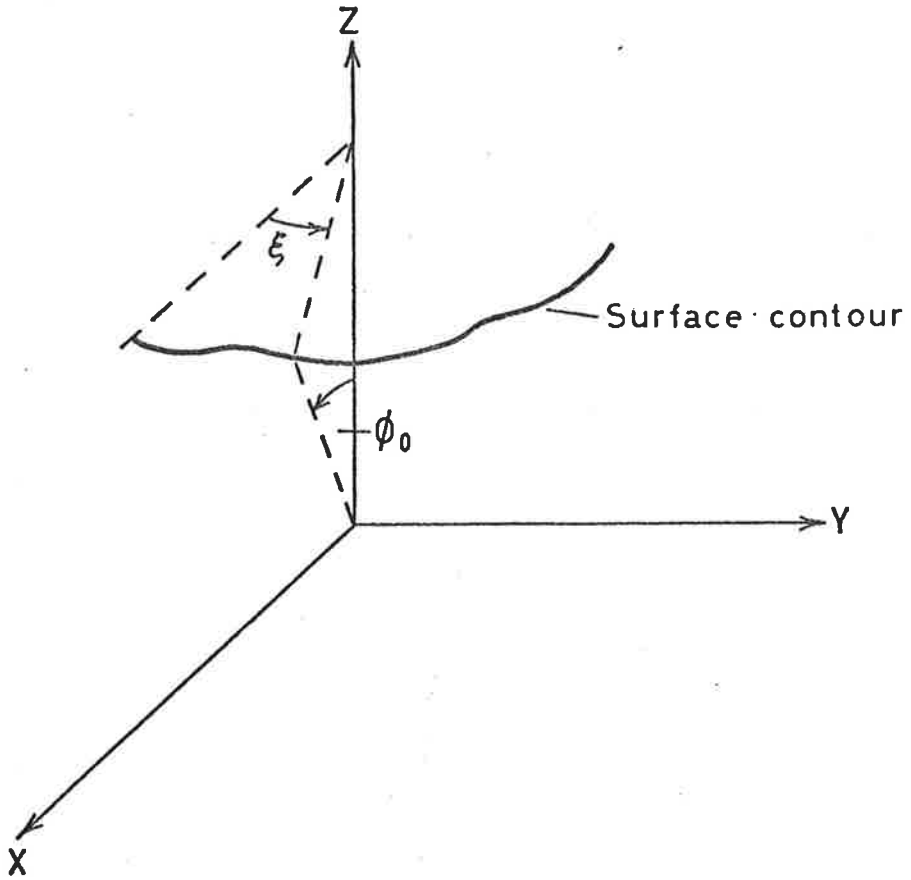

FIG. 2-2 CO-ORDINATE SYSTEM FOR THE OBJECT SURFACE

The surface contour is the intersection of the object surface and the surface $\phi = \phi_o$.

$$c(\xi,t) = \sum_{i=1}^{I} c^i(\xi)\cos(\omega t + \gamma^i) \tag{2.7}$$

$$b(\xi,t) = \sum_{i=1}^{I} b^i(\xi)\cos(\omega t + \beta^i) \tag{2.8}$$

$$a(\xi,t) = \sum_{i=1}^{I} a^i(\xi)\cos(\omega t + \alpha^i) \tag{2.9}$$

Taking the c component as an example the i-th term in equation (2.7) is a mode and the I terms are referred to as COUPLED TEMPORAL MODES since they are generated by the driving force of constant frequency and couple together with a time-invariant phase relationship, γ^i. The amplitudes of the coupled temporal modes - $c^i(\xi)$, $b^i(\xi)$ and $a^i(\xi)$ - vary over the surface contour and may be expanded into a trigonometric series [102] of order (N+1) thus

$$c^i(\xi) = \sum_{n=o}^{N} [x_n^i \sin(n^i\xi) + y_n^i \cos(n^i\xi)] \tag{2.10}$$

$$b^i(\xi) = \sum_{n=o}^{N} [w_n^i \sin(n^i\xi) + z_n^i \cos(n^i\xi)] \tag{2.11}$$

$$a^i(\xi) = \sum_{n=o}^{N} [u_n^i \sin(n^i\xi) + v_n^i \cos(n^i\xi)] \tag{2.12}$$

The form of this expansion is particularly relevant since the vibration of any structure may be considered as a combination of normal modes [83,84]. The (N+1) terms in each expansion are called SUPERPOSED SPATIAL MODES since they do not exist independently in the physical sense but describe mathematically a complex spatial function of period 2π.

2.1.3 Theory of Time-Averaged Holography for One-Dimensional Vibration

The following rigorous derivation of the theory of time-averaged holography for one-dimensional simple harmonic motion of a constant frequency is due to Butusov [5]. The complex analytical signal in the plane of the hologram H is [3]

$$A(H,t) = \frac{-i}{kZ} \int\int_S A(S)\, e^{ikR(H,S,t)}\, dS \tag{2.13}$$

where A(S) is the amplitude of the laser light in the plane of the object surface S, Z is the separation between object and hologram and

$$R = [Z^2 + (h_1 - s_1)^2 + (h_2 - s_2)^2]^{\frac{1}{2}} \tag{2.14}$$

(refer to Fig. 2-3). If the vibration $\underset{\sim}{d}(S)$ is normal to the surface and executes simple harmonic motion of frequency ω then

$$\underset{\sim}{R} = \underset{\sim}{R}_o(H,S) + \underset{\sim}{d}(H,S)\sin\omega t \tag{2.15}$$

Hence equation (2.13) becomes

$$A(H,t) = \frac{-i}{kZ} \int\int_S A(S)\, e^{ikR_o(H,S)}\, e^{ikd(H,S)\sin\omega t}\, dS \tag{2.16}$$

where [4]

$$d(H,S) = d(S)[\cos\theta_1(H,S) + \cos\theta_2(H,S)] \tag{2.17}$$

with θ_1 and θ_2 defined in section 2.1.1.

Substituting

$$e^{iZ\sin\S} = \sum_{j=-\infty}^{\infty} J_q(Z)\, e^{ij\S} \tag{2.18}$$

equation (2.16) becomes

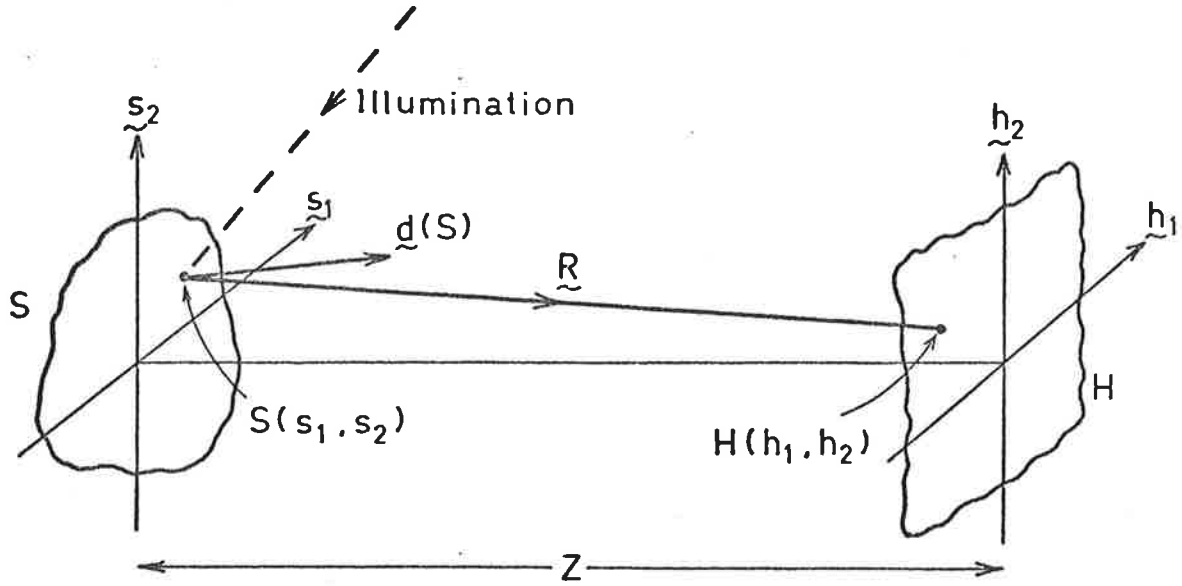

FIG. 2-3 SCHEMATIC OF HOLOGRAPHIC PROCESS

$$A(H,t) = \frac{-i}{kZ} \int\int_S A(S) e^{ikR_o(H,S)} \left(\sum_{j=-\infty}^{\infty} J_j(kd) e^{ij\omega t} \right) dS$$

$$= \sum_{j=-\infty}^{\infty} J_j(kd) e^{ij\omega t} \left[\frac{-i}{kZ} \int\int_S A(S) e^{ikR_o(H,S)} dS \right] \qquad (2.19)$$

where the term in the square brackets is simply the original complex wave amplitude denoted $A^o(H)$. Hence,

$$A(H,t) = J_o(kd)A^o(H) + \sum_{\substack{j=-\infty \\ j\neq o}}^{\infty} J_j(kd) e^{ij\omega t} A^o(H) \qquad (2.20)$$

where J_n is the n-th order Bessel function of the first kind. For time-averaged holography, this field is averaged over time t thus

$$\bar{A}(H) = \frac{1}{t} \int_o^t A(H,t)\, dt \qquad (2.21)$$

Assuming $t >> 2\pi/\omega$ then the second term of equation (2.20) is zero and the average field $\bar{A}(H)$ becomes

$$\bar{A}(H) = J_o(kd)A^o(H) \qquad (2.22)$$

That is, the surface of the reconstructed object is modulated by the Bessel function of zero order which is also called the characteristic function for this vibration. In general the characteristic function is defined as [86]

$$M(\Omega) = \frac{1}{t} \int_o^t e^{i\Omega} dt \qquad (2.23)$$

whereupon equation (2.22) is

$$\bar{A}(H) = M(\Omega)\, A^o(H) \qquad (2.24)$$

The argument of the characteristic function denoted Ω is equal to kd,

with d given by equation (2.17), for the vibration considered here.

2.1.4 Theory of Time-Averaged Holography for Three-Dimensional Vibration and Application

In section 2.1.1 the argument of the fringe function Ω was derived for three-dimensional vibration. On substituting equations (2.7), (2.8) and (2.9) into equations (2.5) and (2.23) and denoting the geometrical factors in equation (2.5) as

$$\left.\begin{aligned} K_q &= \cos\theta_1\sin\phi_1 + \cos\theta_2\sin\phi_2 \\ S_q &= \sin\theta_1\sin\phi_1 - \sin\theta_2\sin\phi_2 \\ Q_q &= \cos\phi_2 + \cos\phi_1 \end{aligned}\right\} \qquad (2.25)$$

then,

$$M = \frac{1}{t}\int_o^t e^{ik[\Omega_1\cos\omega t - \Omega_2\sin\omega t]}\,dt \qquad (2.26)$$

where,

$$\left.\begin{aligned} \Omega_1 &= \sum_{i=1}^{I}[c^i\cos(\gamma^i)K_q + b^i\cos(\beta^i)S_q + a^i\cos(\alpha^i)Q_q] \\ \Omega_2 &= \sum_{i=1}^{I}[c^i\sin(\gamma^i)K_q + b^i\sin(\beta^i)S_q + a^i\sin(\alpha^i)Q_q] \end{aligned}\right\} \qquad (2.27)$$

which is of the same form as derived by Molin and Stetson [86] for two one-dimensional vibrations in phase quadrature. The solution of equation (2.26) as derived in the latter paper is

$$M(\Omega) = J_o\{k(\Omega_1^2 + \Omega_2^2)^{\frac{1}{2}}\} \qquad (2.28)$$

Hence for every point q on the surface contour,

$$\frac{\Omega_q^2}{k^2} = \left[\sum_{i=1}^{I} (c^i\cos(\gamma^i)K_q + b^i\cos(\beta^i)S_q + a^i\cos(\alpha^i)Q_q\right]^2$$

$$+ \left[\sum_{i=1}^{I} (c^i\sin(\gamma^i)K_q + b^i\sin(\beta^i)S_q + a^i\sin(\alpha^i)Q_q\right]^2 \qquad (2.29)$$

which is the general solution for time-averaged holography of three-dimensional vibrations of a single frequency where the spatially varying amplitudes c^i,b^i and a^i are given by equations (2.10) to (2.12). The variables which are determined from time-averaged holograms are Ω_q, K_q, S_q, Q_q and ξ_q. The other variables are the unknowns.

Equation (2.29) will now be applied to some cases of particular interest. For simplicity, the surface contour is assumed to lie on the XY plane (see Figs. 2-1 and 2-2) and hence $\phi_o = \phi_1 = \phi_2 = \pi/2$. Equations (2.25) become

$$\left.\begin{aligned} K_q &= \cos\theta_1 + \cos\theta_2 \\ S_q &= \sin\theta_1 - \sin\theta_2 \\ Q_q &= 0 \end{aligned}\right\} \qquad (2.30)$$

SPECIAL CASE 1

The simplest kind of simple harmonic motion in one dimension is single mode rectilinear vibration. An example of this is the vibration of a cantilever or simply-supported beam. With $I = 1$ and $b^1 = a^1 = 0$, equation (2.29) reduces to

$$\frac{\Omega}{k} = c(\cos\theta_1 + \cos\theta_2) \qquad (2.31)$$

which is the classical result [4] (the subscript q is assumed).

SPECIAL CASE 2

Consider a number of one-dimensional modes with non-zero phase differences. For this case, $b^i = a^i = 0$. Equation (2.29) becomes

$$\frac{\Omega^2}{k^2} = [(c^1\cos\gamma^1 + c^2\cos\gamma^2 + \ldots)^2 + (c^1\sin\gamma^1 + c^2\sin\gamma^2 + \ldots)^2](\cos\theta_1 + \cos\theta_2)^2 \qquad (2.32)$$

the term in the square brackets is also the square of the phasor sum of the individual vibration components. Here is proof of the implication of the statement made by Stetson and Taylor [84] that "the magnitude of the phasor sum of the argument functions corresponding to each of the component motions (is) the argument function for the combined motion".

SPECIAL CASE 3

The simplest kind of simple harmonic motion in three dimensions is single mode rectilinear vibration. An example of this is the vibration of a perfect cylinder. With $I = 1$ and $\gamma^1 = \beta^1$, equation (2.29) becomes

$$\frac{\Omega}{k} = c^1(\cos\theta_1 + \cos\theta_2) + b^1(\sin\theta_1 - \sin\theta_2) \qquad (2.33)$$

which is exactly the expression derived by Tonin and Bies [102] and applied to a beaker vibrating in a Love mode of order $n = 2$. Fig. 2-4 (a) is a pictorial representation of the way in which the variables of equation (2.33) contribute to Ω/k which determines the order of the fringes on the hologram.

SPECIAL CASE 4

The motion having the next highest degree of complexity is simple elliptic motion which may also be described as a single coupled mode ($I = 1$) with the c and b components out of phase ($\gamma^1 \neq \beta^1$). Hence equation (2.29) becomes

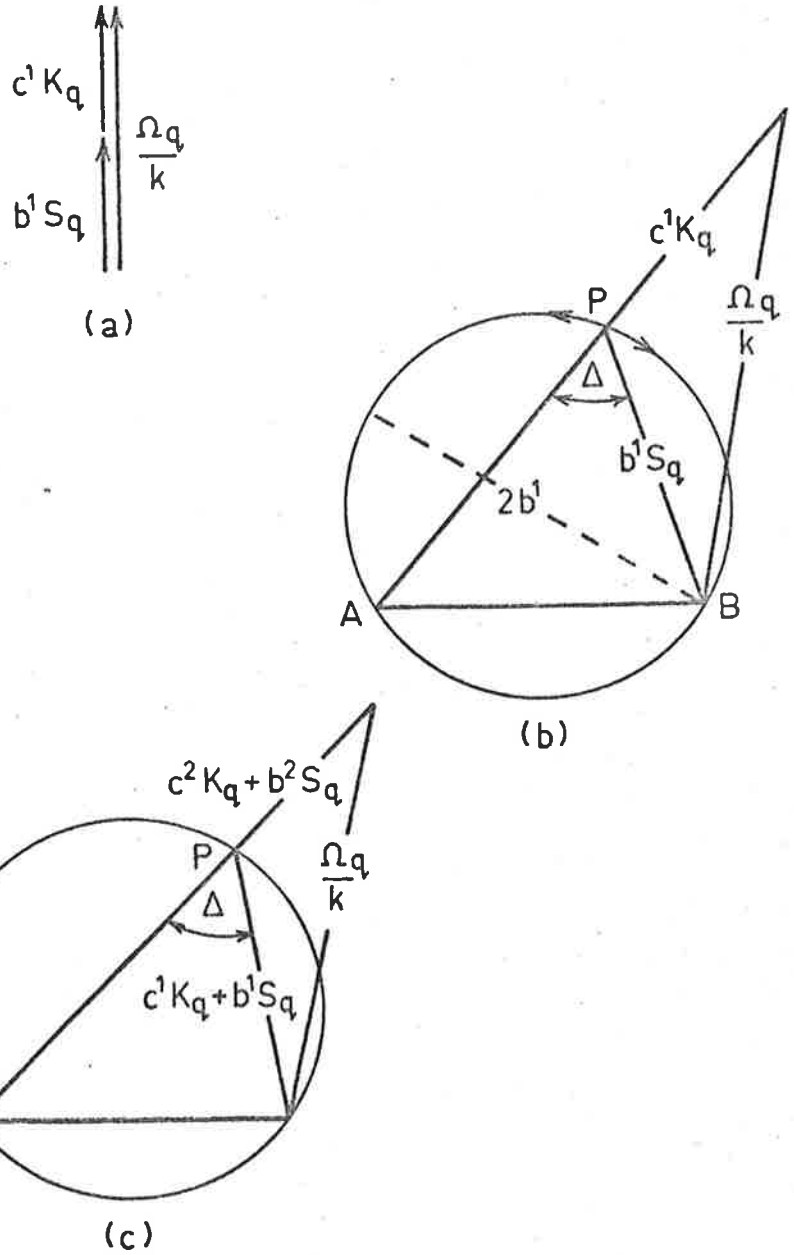

FIG. 2-4 (a) Single coupled mode.

(b) Single coupled mode with out-of-phase components. Simplest kind of elliptic motion.

(c) Two coupled modes.

$$\frac{\Omega_q^2}{k^2} = (c^1K_q)^2 + (b^1S_q)^2 + 2\cos\Delta(c^1K_q)(b^1S_q) \qquad (2.34)$$

$$\text{with} \quad \Delta = \gamma^1 - \beta^1 \qquad (2.35)$$

Fig. 2-4 (b) shows how c^1, b^1 and Δ in particular influence the fringe order, determined by Ω_q/k. It is assumed that the phase difference Δ in equation (2.35) remains invariant over the vibrating surface. This is represented by an angle subtended from a chord AB in a circle of diameter $2b^1$ (or equivalently $2c^1$) which is the maximum value of $b^1(\sin\theta_1 - \sin\theta_2)$. The order of the fringes on the object surface is represented by the position of point P on the circumference of the circle. This simple phasor-like picture clearly shows the role played by Δ. If Δ is zero or a multiple of π then Fig. 2-4 (b) reduces to Fig. 2-4 (a) and the variation of Ω_q/k with Δ is small and hence errors in the determination of Δ from Ω_q/k will be largest for these cases.

It is interesting to note that the characteristic equation (2.34) for a single coupled mode with the c and b components out of phase is similar to that for two one-dimensional vibrations of the kind considered in Special Case 2. Equation (2.32) becomes

$$\frac{\Omega_q^2}{k^2} = (c^1K_q)^2 + (c^2K_q)^2 + 2\cos\Delta(c^1K_q)(c^2K_q) \qquad (2.36)$$

$$\text{with} \quad \Delta = \gamma^1 - \gamma^2 \qquad (2.37)$$

The vibrations corresponding to equations (2.34) and (2.36) are distinguished by varying θ_1 and θ_2, the illumination and observation angles and hence the determination of the motion is unambiguous.

SPECIAL CASE 5

The next order of complexity of three-dimensional vibration is two coupled modes (I = 2) for which the phases of components within

a mode are identical but there exists a phase difference between the modes i.e. $\gamma^1 = \beta^1$, $\gamma^2 = \beta^2$, $\gamma^1 \neq \gamma^2$. The path trajectory is elliptic as in Special Case 4 but the total motion is the phasor addition of four components. An example of such motion is the simultaneous excitation of two modes in a cylinder. Equation (2.29) becomes

$$\frac{\Omega_q^2}{k^2} = (c^1K_q + b^1S_q)^2 + (c^2K_q + b^2S_q)^2$$

$$+ 2\cos\Delta(c^1K_q + b^1S_q)(c^2K_q + b^2S_q) \qquad (2.38)$$

$$\text{with} \quad \Delta = \gamma^1 - \gamma^2 \qquad (2.39)$$

Again, the method of formation of the fringe orders is represented by the phasor-like diagram in Fig. 2-4 (c) which is a combination of Fig. 2-4 (a) and 2-4 (b). As in Special Case 4, a one-dimensional phasor vibration considered in Special Case 2 exists which is described in a similar way to equations (2.38) and (2.39) but the two vibrations are distinguished by the geometrical factors of equation (2.30).

For three-dimensional phasor vibration the statement of Stetson and Taylor quoted previously may be generalized to:
The magnitude of the phasor sum of the argument functions corresponding to each of the component motions of three-dimensional vibration is the argument function for the combined motion.
Hence providing a number of holographic interferograms are taken of the vibrating surface there is no ambiguity in resolving the motion.

2.1.5 The Theory of Generalized Least Squares

The theory of Generalized Least Squares presented here is due to Spendley [153] and Powell [154]. Given a function $\phi(R,\xi)$ involving parameter values $R = R(x_1, \ldots, x_n)$ and independent variables $\xi = \xi(\xi_1, \ldots, \xi_k)$ the deviation of an observed value y_q from a

predicted value $\phi(R,\xi_q)$ is of the form

$$f_q(R) = [y_q - \phi(R,\xi_q)] \tag{2.40}$$

where f is called the Residue Function. It is required to find the set of parameters $\underline{R}$ that will minimize

$$\zeta = \sum_{q=1}^{\tau} [f_q(R)]^2 \tag{2.41}$$

where τ is the number of data points.

Now
$$\frac{\partial \zeta}{\partial R_j} = 2 \sum_{q=1}^{\tau} f_q(R) \frac{\partial f_q}{\partial R_j} \quad , \; j = 1, \; \ldots \; , \; n \tag{2.42}$$

It is assumed that ζ is a quadratic function in the R_j and hence $f_q(R)$ must be linear in R_j. Essentially the derivation assumes that the function ϕ has been linearized about approximate values of the R_j. However as the derivation shows this is not essential. It is worth noting that monotonic convergence is by no means assured.

Thus
$$\frac{\partial f_q}{\partial R_j} = \text{const} = G_j^{(q)} \tag{2.43}$$

say, and if $\underline{\delta}$ is a correction vector which is the difference between vector $\underline{R}$ and $\underline{\hat{R}}$ for which ζ is minimum

$$\text{i.e.} \qquad \underline{\delta} = \underline{\hat{R}} - \underline{R} \tag{2.44}$$

then
$$f_q(\hat{R}) = f_q(R) + \sum_{i=1}^{n} \delta_i \, G_i^{(q)} \tag{2.45}$$

and substituting in equation (2.42),

$$\left(\frac{\partial \zeta}{\partial R_j}\right)_{R=\hat{R}} = 2 \sum_{q=1}^{\tau} \left[f_q(R) + \sum_{i=1}^{n} \delta_i G_i^{(q)}\right] G_j^{(q)} \tag{2.46}$$

$$= 0 \qquad \text{(for all j)} \tag{2.47}$$

since $\zeta(R = \hat{R}) = \hat{\zeta}$ is a minimum.

Rearranging, we have

$$\sum_{i=1}^{n} \delta_i \sum_{q=1}^{\tau} G_i^{(q)} . G_j^{(q)} = - \sum_{q=1}^{\tau} f_q(R) . G_j^{(q)} \tag{2.48}$$

or in matrix notation

$$\underline{\Gamma}\,\underline{\delta} = \underline{F} \tag{2.49}$$

$$\underline{\delta} = \Gamma^{-1}\underline{F} \tag{2.50}$$

where $$\Gamma(i,j) = \sum_{q=1}^{\tau} G_i^{(q)} . G_j^{(q)} \tag{2.51}$$

and the jth element of the column vector F is

$$F(j) = - \sum_{q=1}^{\tau} f_q(R) . G_j^{(q)} \tag{2.52}$$

Thus, given $\underline{F}$ and $\underline{\Gamma}$, the correction vector $\underline{\delta}$ is determined and the optimum solution $\hat{\underline{R}}$ attained in a series of iterations.

2.1.6 Solution of the Characteristic Equation by Method of Least Squares

As equation (2.29) is non-linear in the parameters, the conventional theory of least squares is not directly applicable. Linearization of the characteristic equation results in an extremely large number of unknown coefficients which require an even greater number of data points for a solution. By using the method of Generalized Least

Squares, however, linearization is not required and the available data is used to its fullest advantage.

The residue function, from equations (2.10), (2.11), (2.12), (2.29) and (2.40) is

$$f_q = [\sum_{i=1}^{I}\{\sum_{n=o}^{N} x_n^i \sin(n^i\xi_q) + y_n^i\cos(n^i\xi_q)\}\cos(\gamma^i)K_q + \ldots + \ldots]^2$$

$$+ [\sum_{i=1}^{I}\{\sum_{n=o}^{N} x_n^i \sin(n^i\xi_q) + y_n^i\cos(n^i\xi_q)\}\sin(\gamma^i)K_q + \ldots + \ldots]^2$$

$$- \frac{\Omega_q^2}{k^2} \qquad (2.53)$$

Note there is no need to allocate a sign to Ω_q as in references [102] and [107] since it appears as a square in equation (2.53). The columns of matrix G are the derivatives of equation (2.53) with respect to each unknown and the rows correspond to each datum, q. Firstly, for the x components,

$$G_j^{(q)} = \frac{\partial f_q}{\partial x_\eta^\ell} = 2[\sum_{i=1}^{I} c^i\cos(\gamma^i)K_q + \ldots + \ldots]\sin(\eta^\ell\xi_q)\cos(\gamma^\ell)K_q$$

$$+ 2[\sum_{i=1}^{I} c^i\sin(\gamma^i)K_q + \ldots + \ldots]\sin(\eta^\ell\xi_q)\sin(\gamma^\ell)K_q \qquad (2.54)$$

$$\text{for } j = 1, \ldots, I(N+1)$$

Next, the y components,

$$G^{(q)}_{j+I(N+1)} = \frac{\partial f_q}{\partial y^{\ell}_{\eta}} = 2[\sum_{i=1}^{I} c^i \cos(\gamma^i)K_q + \ldots + \ldots]\cos(\eta^{\ell}\xi_q)\cos(\gamma^{\ell})K_q$$

$$+ 2[\sum_{i=1}^{I} c^i \sin(\gamma^i)K_q + \ldots + \ldots]\cos(\eta^{\ell}\xi_q)\sin(\gamma^{\ell})K_q \qquad (2.55)$$

$$\text{for } j = 1, \ \ldots \ , I(N+1)$$

And, for γ the phase,

$$G^{(q)}_{j+2I(N+1)} = \frac{\partial f_q}{\partial \gamma^{\ell}} = -2[\sum_{i=1}^{I} c^i \cos(\gamma^i)K_q + \ldots + \ldots]c^{\ell}K_q \sin(\gamma^{\ell})$$

$$+ 2[\sum_{i=1}^{I} c^i \sin(\gamma^i)K_q + \ldots + \ldots]c^{\ell}K_q \cos(\gamma^{\ell}) \qquad (2.56)$$

$$\text{for } j = 1, \ \ldots \ , I$$

Similar equations for w,z,β and u,v,α complete matrix $\underline{G}$.

If the number of data points in τ, the number of superposed modes $(N+1)$ and the number of coupled modes I then, $\underline{G}$ is of order τ by $3I(2N+3)$, $\underline{\Gamma}$ is a $3I(2N+3)$ square matrix and $\underline{F}$ a column vector of order $3I(2N+3)$. The vector $\underline{R}$ describing the parameters is

$$\underline{R} = (x^1_1, x^1_2, \ldots, y^1_1, y^1_2, \ldots, \gamma^1, \gamma^2, \ldots, w^1_1, w^1_2, \ldots, \alpha^I) \qquad (2.57)$$

2.2 EXPERIMENTAL EQUIPMENT AND DATA ANALYSIS

2.2.1 HOLOGRAPHY

A schematic of the optical system used to generate holograms is shown in Fig. 2-5, this system being common to almost all experiments reported in this thesis. Depending upon availability at the time of the experiment any of the following Helium-Neon (6328Å) lasers were

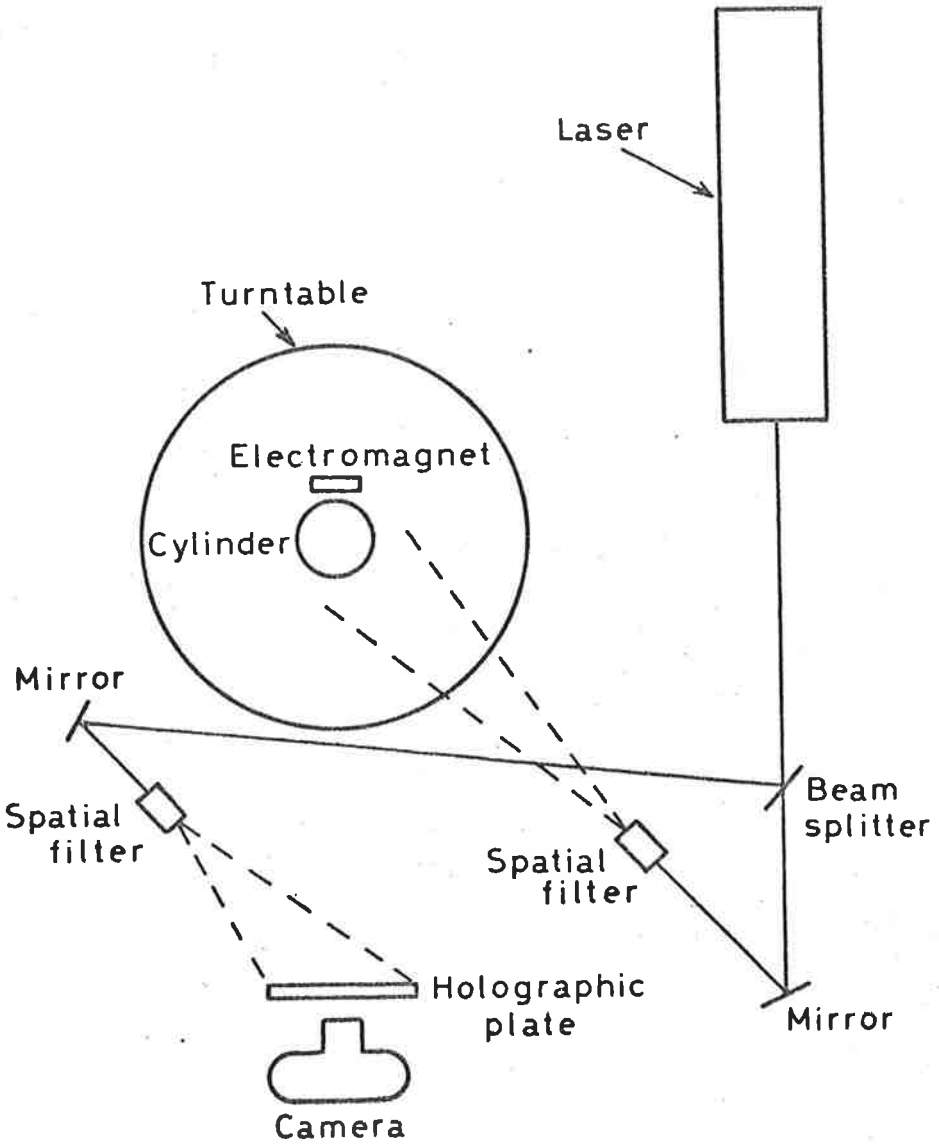

FIG. 2-5 OPTICAL SYSTEM

used - Lasertron LE105 (15mW), LE205 (5mW) or Metrologic MV910A (1mW). The optical powers were monitored with a Tektronix J16 digital photometer. Each spatial filter is fitted with a 10μ pin hole which was measured by ray-tracing to be 35 ±1mm behind the lens. Holograms are recorded on Ilford He-Ne/1 (50erg/cm^2), Agfa 10E75 (50erg/cm^2) or Kodak 131-02 (5erg/cm^2) plates nominally 1mm thick and 120mm by 90mm in size. Exposed plates are developed for 7 minutes in Ilford Microphen, Agfa G5c or Kodak Microdol-X developer. Exposure times varied from 20 sec to 120 sec depending on laser power, plate and developer. The best combination is Kodak plate with Agfa G5c developer. After developing, the plates are immersed in a 1% solution of Acetic Acid stop bath for 5 seconds and fixed in a 1/1 solution of Ilfofix Acid Hardening Fixer for 10 minutes. The plates are washed in running water for 15 minutes, immersed in an 80% solution of industrial alcohol for 5 minutes to remove the anti-halo coating and then dried.

During exposure, the beam splitter is set for a 4/1 ratio of reference to object beam intensity. On reconstruction, all the laser light is directed to the reference beam and the image photographed with a Minolta SRT303 35mm camera loaded with Ilford HP4 (400ASA) or FP4 (125ASA) film. The aperture setting on the camera is important - too low a setting will result in broad fringes due to variation of the observation angle and conversely a high setting results in very long exposure times. The f5.6 stop results in less than .02rad observation variation and maximum exposure time of 60 sec and was used throughout the experiments.

The object under investigation is lightly spray-painted with matt white primer which ensures an optically diffuse surface. In some experiments retro-reflective paint was used but with a different optical system. The object is placed on a low-profile turntable graduated in degree increments. A translation table and hologram mask were

constructed to enable six holograms to be recorded on one plate which avoids the problem of cutting the plates. The translation table and "windows" of the mask are so arranged that each hologram is taken from the same position in space which enables the same geometry to be used in the analysis. Fig. 2-6 is a photograph of the optics and Fig. 2-7 of the translation table and mask with a typical hologram in the foreground. Unless otherwise stated, seven holograms are taken of each mode of the vibrating object at 15° angular increments of the turntable, a procedure which uses two plates.

2.2.2 Modal Driving System

To prevent distortion of the modes electromagnets were used to excite the object without contact. These are bar magnets wound with a coil of wire and positioned close to the surface of the object hence providing a steady force which is then modulated. For the ferromagnetic objects no problem was encountered, however, for the non-ferromagnetic objects the steady biasing force could only be induced by fastening a small piece of ferromagnetic material to the object at the point to be driven. Thus although a metallic surface may be driven with an electromagnet making use of the field of induced eddy currents [155] the resulting forcing function will always be unidirectional, one of attraction or repulsion depending upon whether the surface is paramagnetic or diamagnetic and in consequence the wave form of the forcing function will always be rich in harmonics which is not desired.

The spatial distribution of the excitation force is often an important factor in determining the mode shape. Shirakawa and Mizoguchi [156] determine the mode shapes of a cylinder excited by a periodic point force. For a slightly imperfect cylinder for example the mode will usually orient itself with the asymmetries no matter where the force is applied. It is not necessary to excite the modes at the antinodes. By

FIG. 2-6

Optics for the generation of holograms.

FIG. 2-7

The translation table (T), hologram stage (S), typical hologram (H) and mask (M).

contrast, for a near-perfect cylinder a large degree of modal coupling is evident for antinodal excitation and is only reduced by positioning the drivers close to the shear-diaphragm ends thereby decreasing the magnitude of the cross-correlation between the mode to be driven and the spatial fourier components of the forcing function.

As the holographic exposure time could be as long as 60 sec the mode under study must be stable for that period of time. For modes of high Q use of a driving oscillator is impossible due to problems of drift. Hence use is made of a technique employing a method of positive feedback to create an electro-mechanical oscillator which is self-excited and very stable [157]. A schematic of the system is shown in Fig. 2-8. The heart of the feedback system is the resonance unit designed by the author. This is essentially a voltage controlled amplifier whose gain is determined by the level of the input signal. If this increases then the gain of the unit decreases and vice-versa. Hence the resonance unit provides the required level of output signal which will maintain a constant input level. Additionally a 0-360 degree phase shift circuit is incorporated into the unit to enable correct phase matching.

A Bruel & Kjaer (B & K) miniature accelerometer type 8307 monitors the vibration level with a minimum of loading (the weight of the accelerometer is only 0.4 grams). The signal is amplified by a B & K spectrometer type 2112, fed to the resonance unit and then to a power amplifier and the electromagnet. The gain of the power amplifier is set such that the system gain is greater than unity hence ensuring sustained oscillation. However, if the system gain is too high the vibration will hunt. To select any mode, the spectrometer third-octave band filter is set to include the frequency of that mode. The phase and gain of the resonance unit and power amplifier are then adjusted for optimum oscillatory stability. Finally, the level of vibration is set

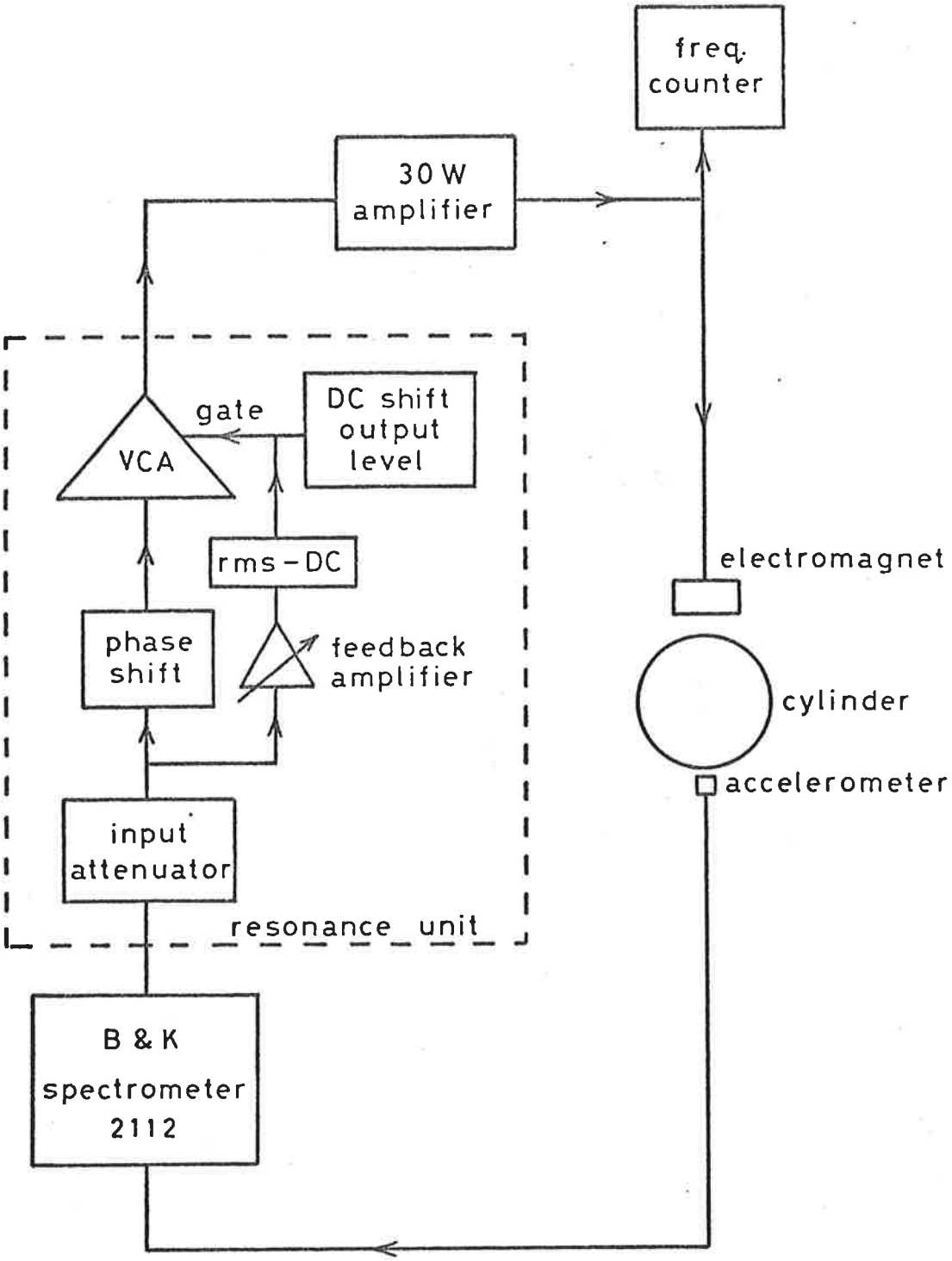

FIG. 2-8 MODAL DRIVING SYSTEM

by adjusting the DC conditions at the gate of the voltage controlled amplifier in the resonance unit. The system is so successful that a mode may be kept stable for hours with no frequency or amplitude variation (as limited by the accuracy of the instruments). A photograph of the equipment is shown in Fig. 2-9.

2.2.3 Geometry for the Analysis of Cylinders

As the analysis of the reconstructed holograms is common to all experiments excepting those in sections 3.1 and 3.2 it will be described here. The basic geometry is due to Liem et al [101]. A cross-section through the optical plane for a vertically standing cylinder of outer radius a_2 is shown in Fig. 2-10 where the angles θ_1 and θ_2 are to be calculated for dark fringes on a photograph of the hologram reconstruction. The perspective of the object is taken into account by making use of the pin-hole camera concept. The process of photographing the reconstruction and printing the photograph with an enlarger is considered equivalent to photographing the reconstruction with a pin-hole camera consisting of an aperture of diameter D and a screen. If D is made small compared to the distance AA by suitable choice of the camera f-stop and the size of the image formed on the imaginary screen is made exactly equal to the size of the image in the photograph by suitable choice of the distance χ then firstly considering a plane photograph of the cylinder

$$\tan\gamma^* = \frac{a_v}{\chi} = \frac{a_2}{AA} \tag{2.58}$$

where a_v is the radius of the cylinder in the photograph and the asterisk indicates the maximum value of the angle γ. Now, for any other point on the surface of the cylinder

FIG. 2-9

The electronic equipment used to drive and monitor vibration modes.

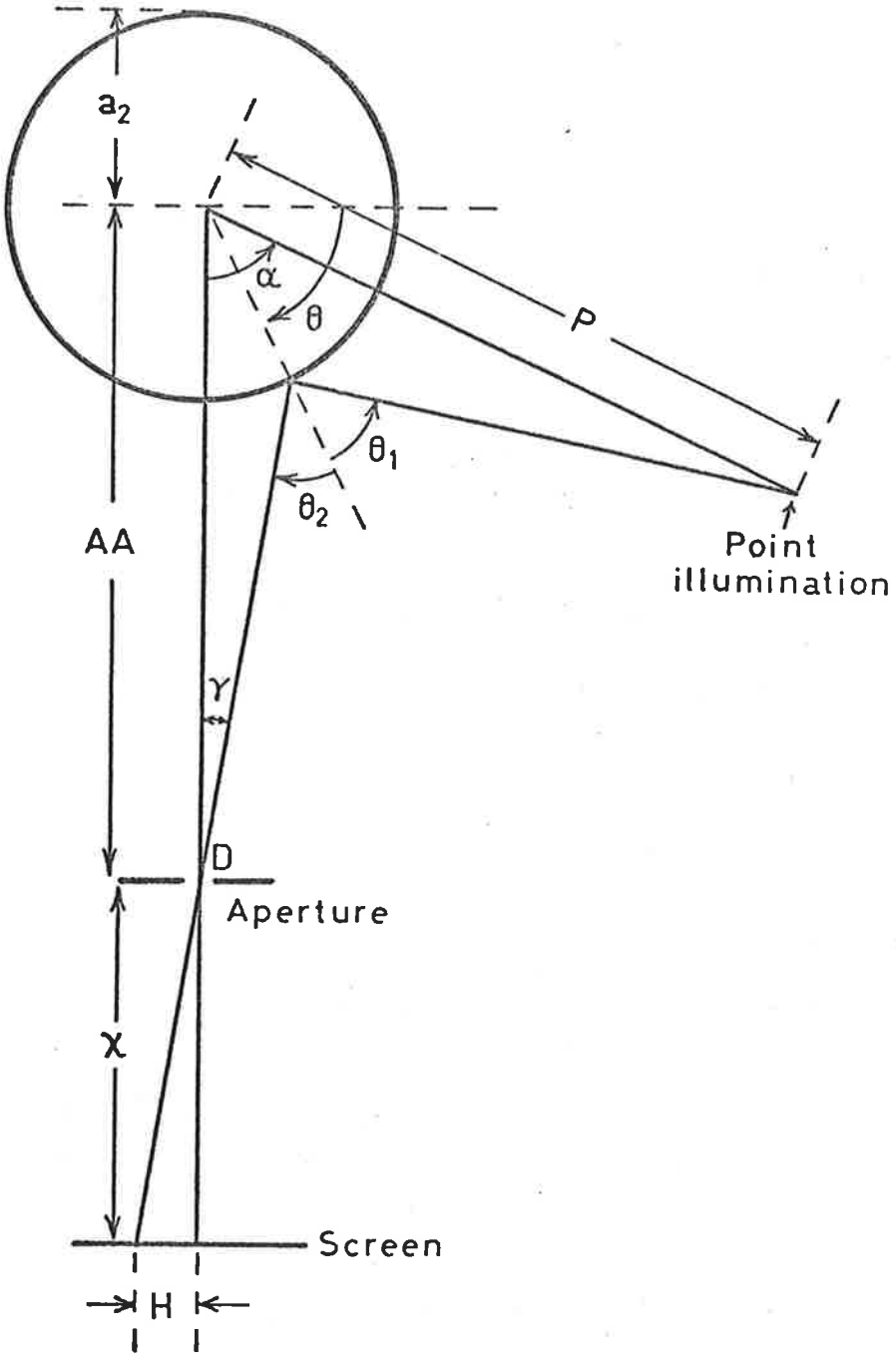

FIG. 2-10 GEOMETRY FOR INTERPRETATION OF HOLOGRAM PHOTOGRAPHS

Cylinder Vertical

$$\tan\gamma = \frac{H}{X} = \frac{H.a_2}{AA.a_v} \qquad (2.59)$$

by equation (2.58). The angle θ is calculated by application of the sine rule for triangles hence,

$$\frac{AA}{\sin[\pi - (\pi/2 - \theta) - \gamma]} = \frac{a_2}{\sin\gamma} \qquad (2.60)$$

or,
$$\theta = \cos^{-1}(AA\sin\gamma/a_2) + \gamma \qquad (2.61)$$

If P is the distance from the cylinder axis to the point of illumination and α is the angle subtended by this line and AA then again by the sine rule,

$$\frac{P}{\sin\theta_1} = \frac{a_2}{\sin(\theta_1 - [\alpha - (\pi/2 - \theta)])} \qquad (2.62)$$

or,
$$\theta_1 = \tan^{-1}\{P\cos(\alpha+\theta)/[a_2 - P\sin(\alpha+\theta)]\} \qquad (2.63)$$

and θ_2 is given by

$$\theta_2 = \pi/2 - \theta + \gamma \qquad (2.64)$$

Hence using equations (2.59), (2.61), (2.63) and (2.64) the angles θ [which is equivalent to ξ in equation (2.29)], θ_1 and θ_2 are determined for each fringe along the surface contour which is the intersection of the cylinder and the optical plane. If the cylinder is rotated an amount S_D radians (S_D is positive anticlockwise in Fig. 2-10) then the values of θ_1 and θ_2 determined from equations (2.63) and (2.64) pertain to the point $(\theta + S_D)$ radians from the origin.

For this arrangement the geometric term Q_q is zero for all points along the surface contour and reference to equation (2.29) shows the

components a^i cannot be determined. This is overcome by positioning the cylinder on its side with its axis in the optical plane. The surface contour is now a straight line parallel to the generator. Reference to Fig. 2-11 shows

$$\tan\gamma^* = \frac{L/2}{AA - a_2} = \frac{L_v/2}{\chi} \tag{2.65}$$

where L_v is the length of the cylinder in the photograph without rotation ($S_D = 0$) and the asterisk again indicates the maximum value of the angle γ. Now, for any other point on the surface contour,

$$\tan\gamma = \frac{H}{\chi} = \frac{H.L}{L_v.(AA - a_2)} \tag{2.66}$$

which is true even if the geometric centre of the cylinder does not intersect the axis of the turntable. From the sine rule,

$$\frac{Y_D}{\sin\gamma} = \frac{AA}{\sin[(\pi/2 + S_D - \alpha - \phi) + (\pi/2 - \gamma - S_D)]} \tag{2.67}$$

and considering the right angled triange of which Y_D is the hypotenuse

$$Y_D = a_2/\cos(S_D - \alpha - \phi) \tag{2.68}$$

Combining equations (2.67) and (2.68) and solving for ϕ gives

$$\phi = \tan^{-1}\left[\frac{a_2\sin(\alpha+\gamma) - AA\sin\gamma\cos(S_D-\alpha)}{AA\sin\gamma\sin(S_D-\alpha) - a_2\cos(\alpha+\gamma)}\right] \tag{2.69}$$

Also,
$$\ell = a_2/[\tan(\pi/2 + S_D - \alpha + \phi)] \tag{2.70}$$

and
$$\theta_2 = \gamma + S_D \tag{2.71}$$

where ℓ is a length co-ordinate along the surface contour related to the

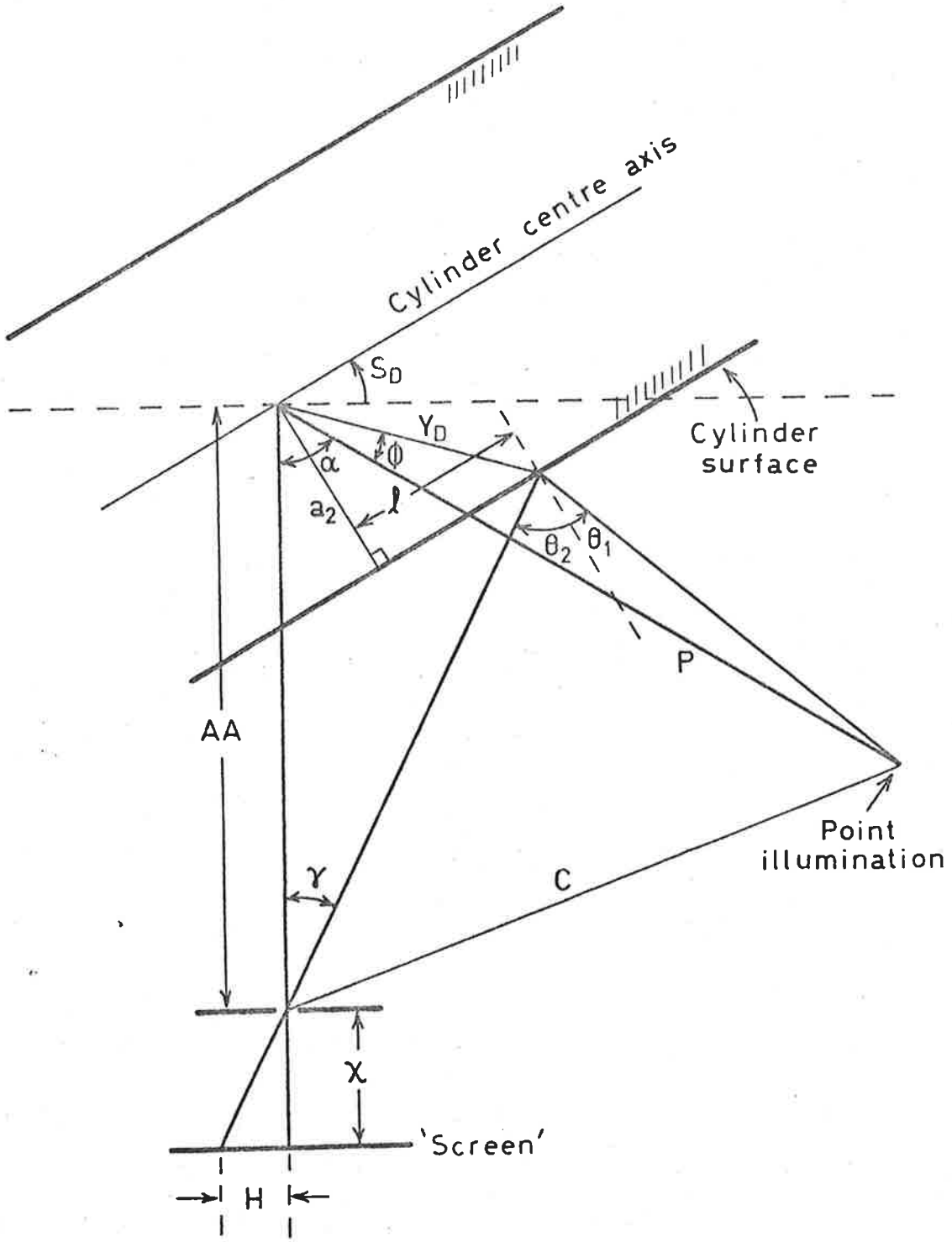

FIG. 2-11 GEOMETRY FOR INTERPRETATION OF HOLOGRAM PHOTOGRAPHS

Cylinder Horizontal

angular co-ordinate ξ of equation (2.29) by the transformation

$$\xi = \pi \ell / L \tag{2.72}$$

and the circular mode number n is replaced by the longitudinal mode number m in equations (2.10) to (2.12). Also from the sine rule,

$$\frac{Y_D}{\sin[\pi - (\pi/2 + \theta_1 + \pi/2 + S_D - \alpha - \phi + \phi)]} = \frac{P}{\sin(\pi/2 + S_D - \alpha - \phi + \pi/2 + \theta_1)} \tag{2.73}$$

which is solved for θ_1 to give

$$\theta_1 = \tan^{-1}\left[\frac{a_2 \tan(\alpha + \phi - S_D) - P \sin(\alpha - S_D)}{a_2 - P\cos(\alpha - S_D)}\right] \tag{2.74}$$

Hence using equations (2.66), (2.69), (2.70), (2.71), (2.72) and (2.74) the angles θ_1, θ_2 and co-ordinate ξ are determined for each fringe along the surface contour.

For the cylinder horizontal, a vertical pointing rod at the centre of the turntable indicated the position of the origin in the hologram reconstructions. In this case, P is the distance from the origin to the point of illumination and α is the angle subtended by this line and AA.

2.2.4 Data Analysis

The measurement of fringe positions on photographs is a laborious process with only the aid of a straight-edge. Hence a data system was assembled by the author to digitise fringe co-ordinates, store and edit the information on cassette tape and transmit the data to a central computer. Fig. 2-12 is a photograph of the data system, Fig. 2-13 a schematic of the system. In Appendix I a flow diagram of

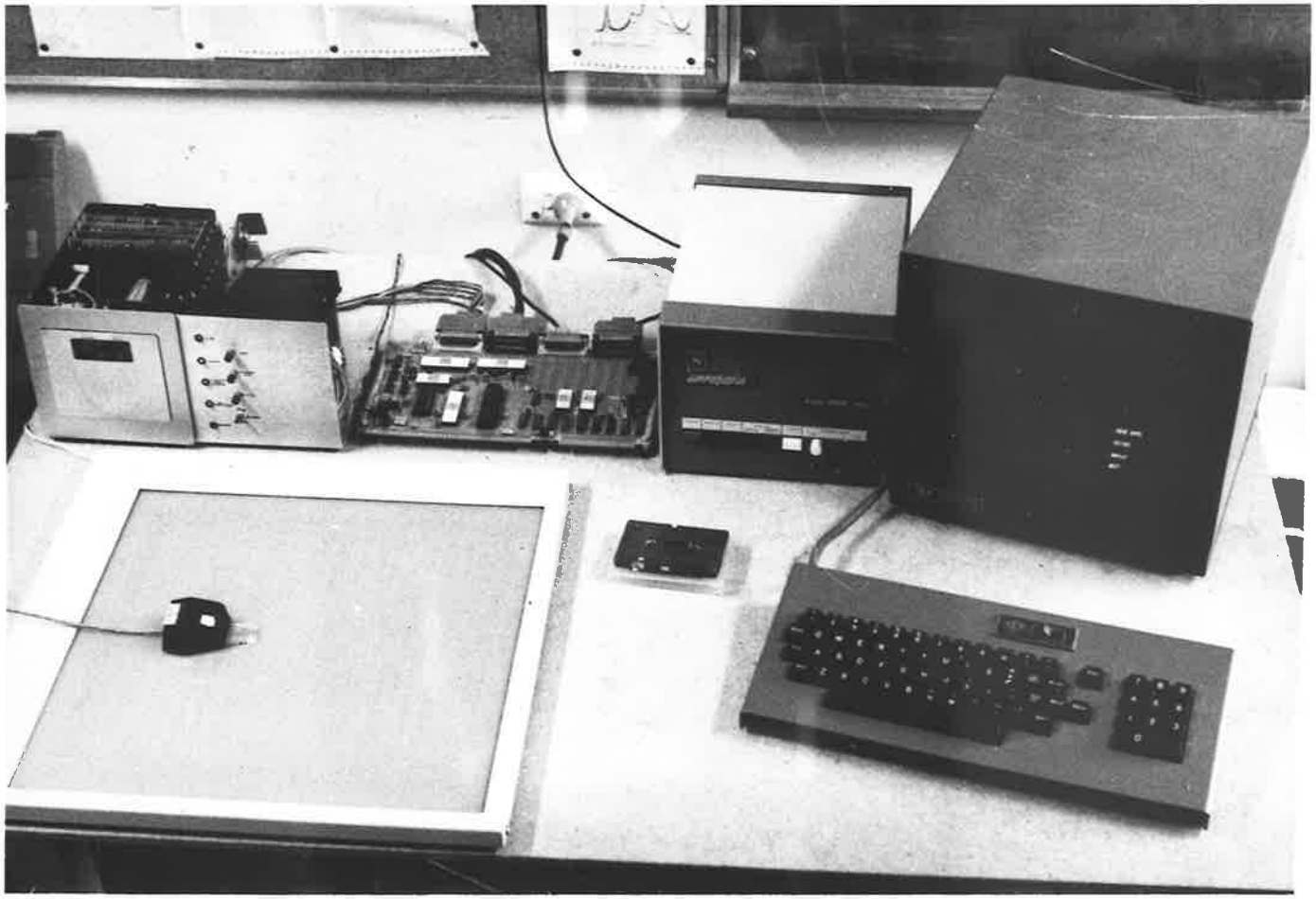

FIG. 2-12

The Data System.

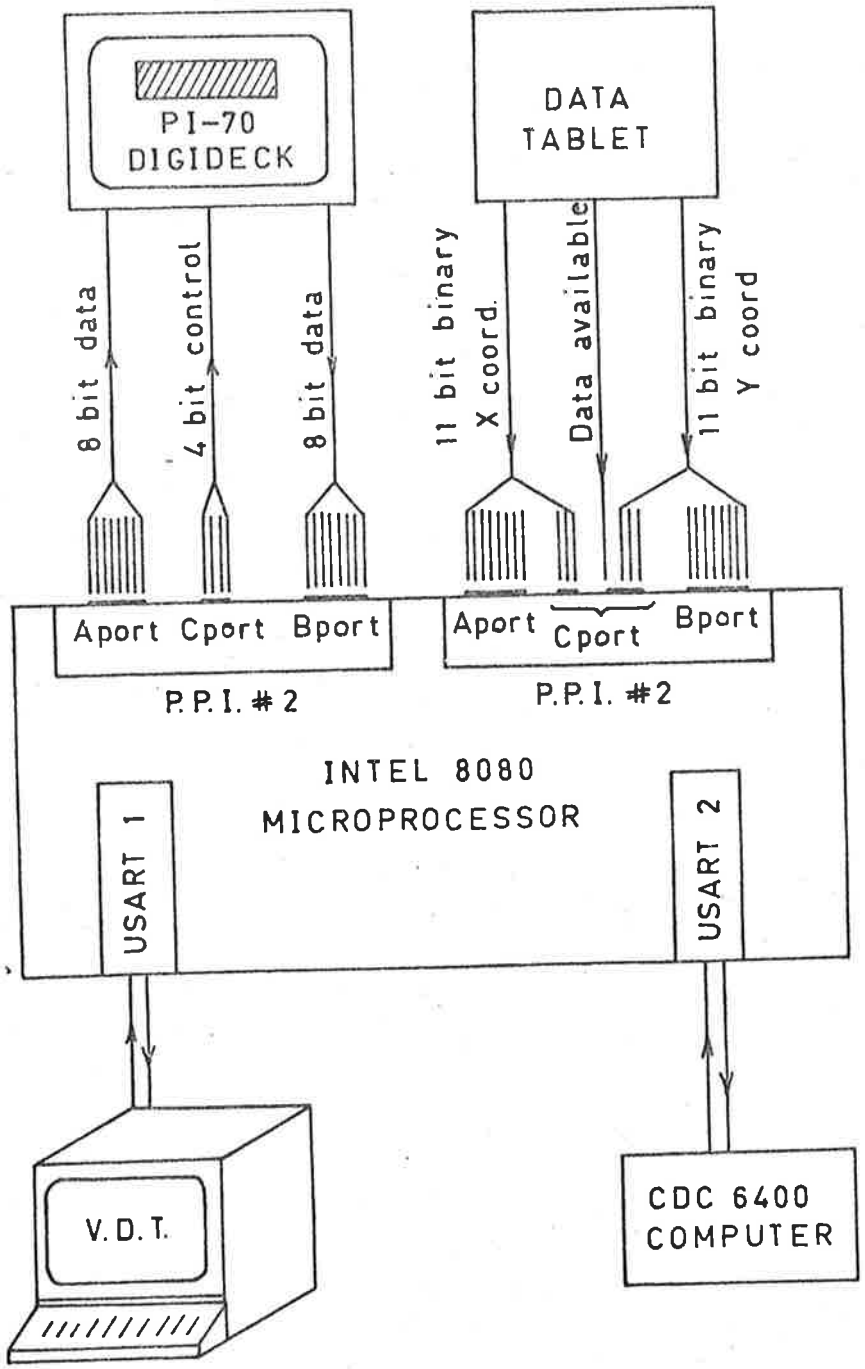

FIG. 2-13 SCHEMATIC OF THE DATA SYSTEM

the microprogram is given.

Data is taken from the photographs using a Summagraphics HW-L-14-TT Data Tablet having two 11 bit binary outputs corresponding to the X and Y co-ordinates of a cursor which is moved over the tablet surface, the resolution being .01 inch. The outputs are connected to the second Programmable Peripheral Interface (P.P.I #2) of an Intel 8080 Microprocessor fitted with 4K of E.P.R.O.M. (Erasable Programmable Read Only Memory) and 1K of R.A.M. (Random Access Memory). Data is recorded with a Digideck PI-70 cassette unit which is interfaced to P.P.I. #1. A Video Display Terminal (V.D.T.) enables commands to be fed to the system via U.S.A.R.T. #1 (Universal Synchronous / Asynchronous Receiver / Transmitter) at 2400 Baud (bits/second). Additionally U.S.A.R.T. #2 is connected to a CDC6400 computer via a 300 Baud Intercom line.

The system has five modes of operation which are selected sequentially with the ESCAPE key and the system responds by printing the mode title on the right hand side of the VDT screen. These are as follows:

1) ..INTERCOM.. A two-way link with the CDC6400 computer. Files are created and programs run using keyboard commands.

2) ..SEND DATA.. Information recorded previously on cassette is transmitted to the computer at a rate of 300 Baud.

3) ..RECORD.. Keyboard characters or co-ordinates from the data tablet are recorded on tape and displayed on the screen at the rate of 50 characters per second with seven co-ordinate pairs (corresponding to X and Y) per line.

4) ..REPLAY.. Recorded information is reviewed on the screen only.

5) ..EDIT.. Enables one character at a time to be reviewed with the SPACE key or one line at a time with the CARRIAGE RETURN (C/R)

key. To enter the EDIT mode from the REPLAY mode key E is depressed. To alter a character the ESCAPE key is depressed which transfers the system to the RECORD mode.

With this data system, the digitising of holographic information is simplified enormously. In addition the data tablet has a STREAM MODE selector by which the co-ordinates of the cursor are transmitted at the system rate of 50 char./sec. Hence a fringe may be digitised in a matter of seconds simply by tracing it with the cursor on the data tablet.

CHAPTER 3

PURE AND SUPERPOSED SPATIAL MODES

The theory of time-averaged holography for three-dimensional vibrations outlined in Chapter 2 is applied to a vibrating clamped circular plate, wine glass, stainless-steel beaker and four cylinders with shear-diaphragm end conditions. In addition the analysis is applied to a vibrating cylinder with a seam. The application of the method of least squares will be shown to make optimal use of the data. This chapter also will show step by step the ideology leading to the formulation of the general analysis described in Chapter 2.

3.1 CLAMPED CIRCULAR PLATE

3.1.1 Holographic and Geometric Theory

The study of vibration of clamped circular plates by holography is reported by Hansen and Bies [144]. The modes are characterized by a single component of vibration normal to the plate with a complex Bessel distribution over the surface. For this case equation (2.29) becomes

$$\frac{\Omega}{k} = c(\xi).[\cos\theta_1 + \cos\theta_2] \qquad (3.1)$$

The mode shape $c(\xi)$ as determined by time-averaged holography has been shown [144] to agree well with the theory for $\theta_1 = \theta_2 = 0$ (retro-reflective illumination). An experiment to be described will demonstrate the validity of equation (3.1) for various illumination and observation angles.

Considering first a change of illumination direction, Fig. 3-1 shows the geometry in the optical plane. For fixed angles of illumination and observation, θ_1 and θ_2, the resulting surface contour is a

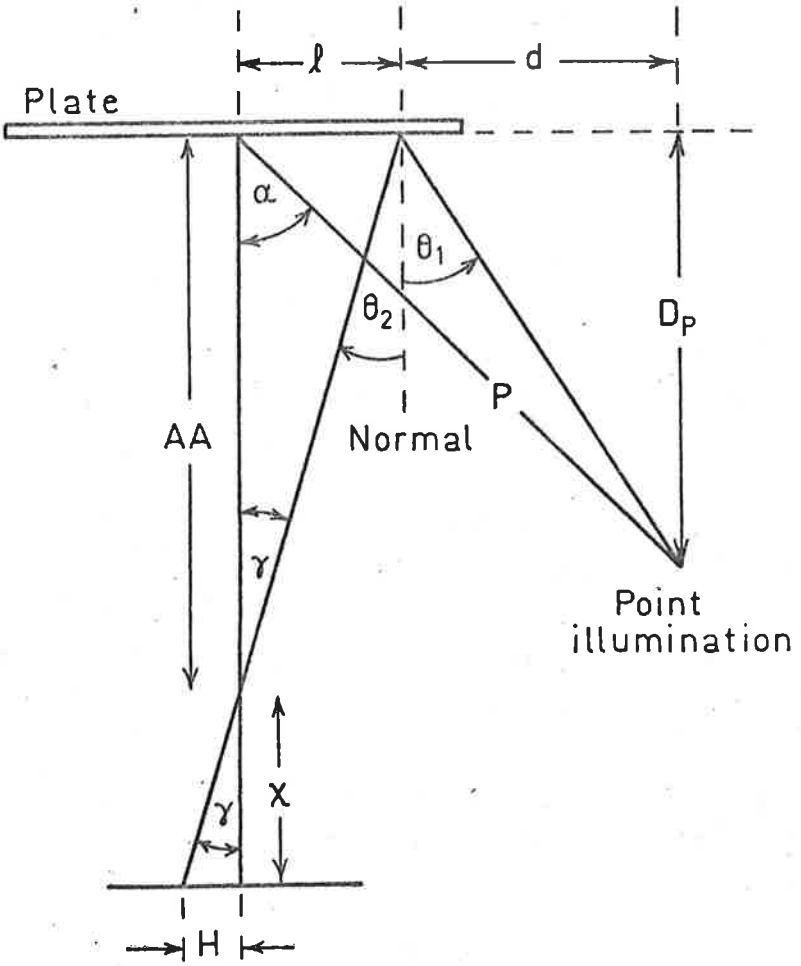

FIG. 3-1 CIRCULAR PLATE WITH VARYING DIRECTION OF ILLUMINATION

a straight line and using again the concept of the pin-hole camera,

$$\tan\gamma = \frac{H}{\chi} = \frac{\ell}{AA} \tag{3.2}$$

If L is the plate diameter then

$$\tan\gamma^* = \frac{L_v/2}{\chi} = \frac{L/2}{AA} \tag{3.3}$$

where the asterisk denotes the maximum value of γ and L_v is the plate diameter in the photograph. Using simple geometry and combining equations (3.2) and (3.3),

$$\ell = H.L/L_v \tag{3.4}$$

$$\theta_2 = \tan^{-1}(\ell/AA) \tag{3.5}$$

and

$$\theta_1 = \tan^{-1}(\tan\alpha - h/D_p) \tag{3.6}$$

Consider now a change of observation direction accomplished by rotating the plate about a vertical axis through its centre. Reference to Fig. 3-2 shows

$$\tan\gamma = \frac{H}{\chi} \tag{3.7}$$

and from the sine rule for triangles,

$$\frac{L/2}{\sin\gamma^*} = \frac{AA}{\sin(\pi/2 - [S_D + \gamma^*])} = \frac{AA}{\cos(S_D + \gamma^*)} \tag{3.8}$$

Hence the angle of rotation of the plate as determined from the photographs is

$$S_D = \cos^{-1}(2AA \sin\gamma^*/L) - \gamma^* \tag{3.9}$$

where if $S_D = 0$ and L_v is the plate diameter in the photograph then χ

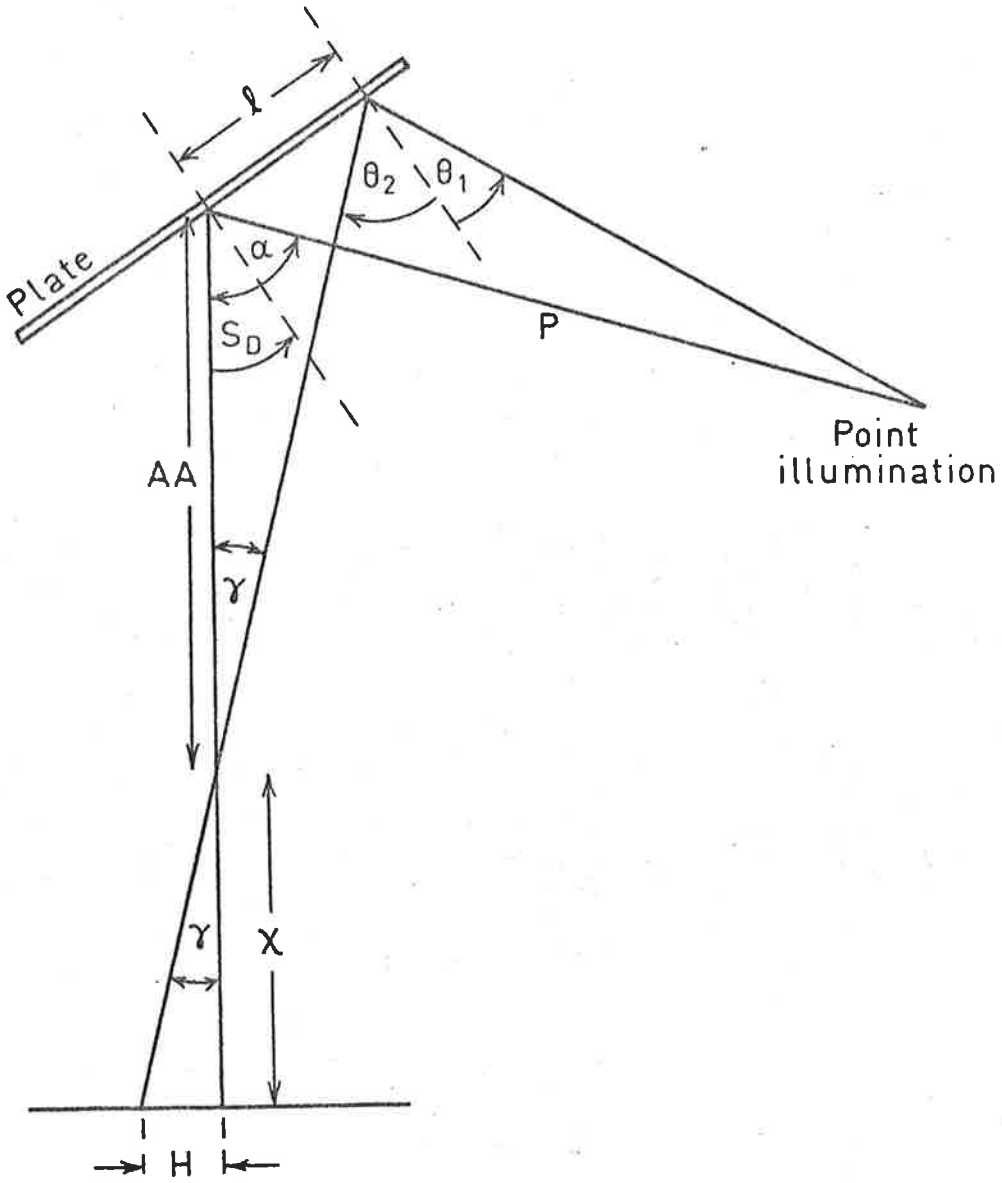

FIG. 3-2 CIRCULAR PLATE WITH VARYING DIRECTION OF OBSERVATION

is determined from

$$\frac{L/2}{AA} = \frac{L_v/2}{\chi} \tag{3.10}$$

and hence

$$\gamma^* = \tan^{-1}\left(\frac{H.L}{AA.L_v}\right) \tag{3.11}$$

The other constants are determined as follows using the sine rule,

$$\frac{\ell}{\sin\gamma} = \frac{AA}{\sin(\pi/2 - [S_D + \gamma])} \tag{3.12}$$

or
$$\ell = AA \sin\gamma / \cos(S_D + \gamma) \tag{3.13}$$

and
$$\frac{\ell}{\sin([\alpha - S_D] - \theta_1)} = \frac{P}{\sin(\pi/2 + \theta_1)} \tag{3.14}$$

hence
$$\theta_1 = \tan^{-1}\left[\frac{P \sin(\alpha - S_D) - \ell}{P \cos(\alpha - S_D)}\right] \tag{3.15}$$

and
$$\theta_2 = S_D + \gamma \tag{3.16}$$

where γ is determined from equation (3.7)

3.1.2 Clamped Plate Experiment and Results

A steel plate of thickness 1.96mm and radius 175.5mm was bolted to a steel structure using a circular ring clamp. Since the edges of the plate were sometimes obscured by this ring, measurement of the plate radius in the photograph, which is required in the analysis, was replaced by measurement of a 200mm long Letraset arrow horizontally orientated and mounted on the plate while another vertical arrow marked the centre of the plate. The plate was driven at its lowest resonant

(0,1) mode of frequency 150 Hz by an electromagnet and oscillator (the resonance unit had not been developed at this stage) and the vibration monitored with an accelerometer and B & K spectrometer 2112.

Six time-averaged holograms were taken with different illumination positions (three positions on the right of the holographic plate and three on the left) with the angle α varying from +50.5° to -52.8°. Reconstructions of holograms for these extreme cases are shown in Fig. 3-3. The results of the analysis outlined in section 3.1.1 are shown in Fig. 3-4 where the consistency of the experimental points clearly demonstrates the validity of the holographic theory.

Seven time-averaged holograms were taken of the plate of varying orientation but vibrating in the same mode. One hologram was recorded with the angle $S_D = 0$, three with S_D positive and maximum angle near $+\pi/4$ and three with S_D negative and maximum angle near $-\pi/4$. Two reconstructions of the holograms are shown in Fig. 3-5. The results of the analysis outlined in section 3.1.1 are shown in Fig. 3-6 where again there is favourable consistency except for one photograph for which it is suspected the oscillator drifted slightly in frequency resulting in a drop in vibration amplitude.

Hence the theory of one-dimensional vibration, being a special case of the general theory, is supported by analysis of a clamped circular plate. Equation (3.1) is demonstrated to be completely sufficient to describe this vibration.

3.2 WINE GLASS AND BEAKER

3.2.1 Holographic and Geometric Theory

Time-averaged holography was first applied to vibrating curved surfaces by Liem et al [101] who analysed the vibrations of a circular cylinder using the formula of equation (3.1) and reported a shift in the amplitude plots when the illumination and observation vectors are

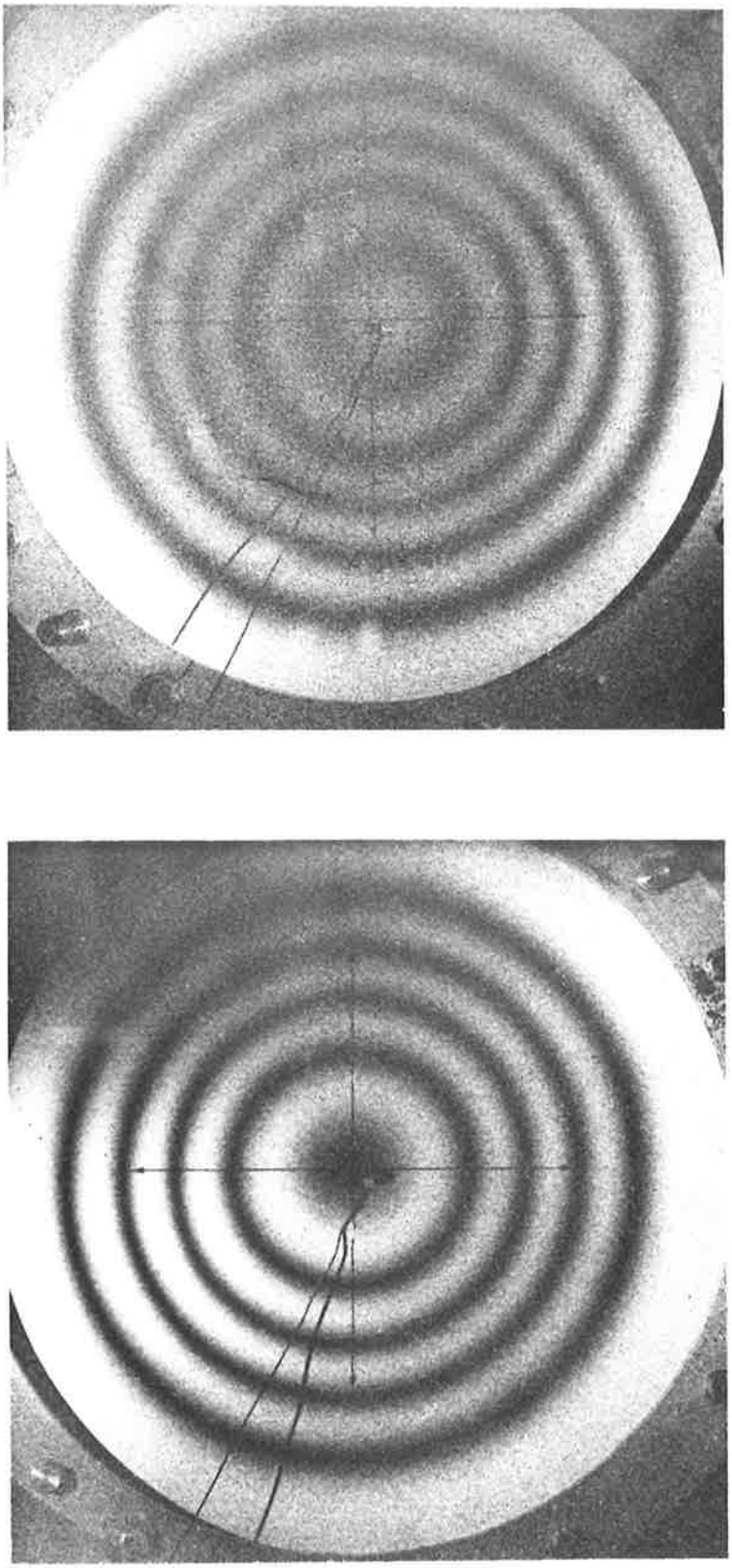

FIG. 3-3

Reconstructions of holograms of a clamped circular plate vibrating in the (0,1) mode and illumination angle $\alpha = +50.5°$ (top) and $\alpha = -52.8°$ (bottom).

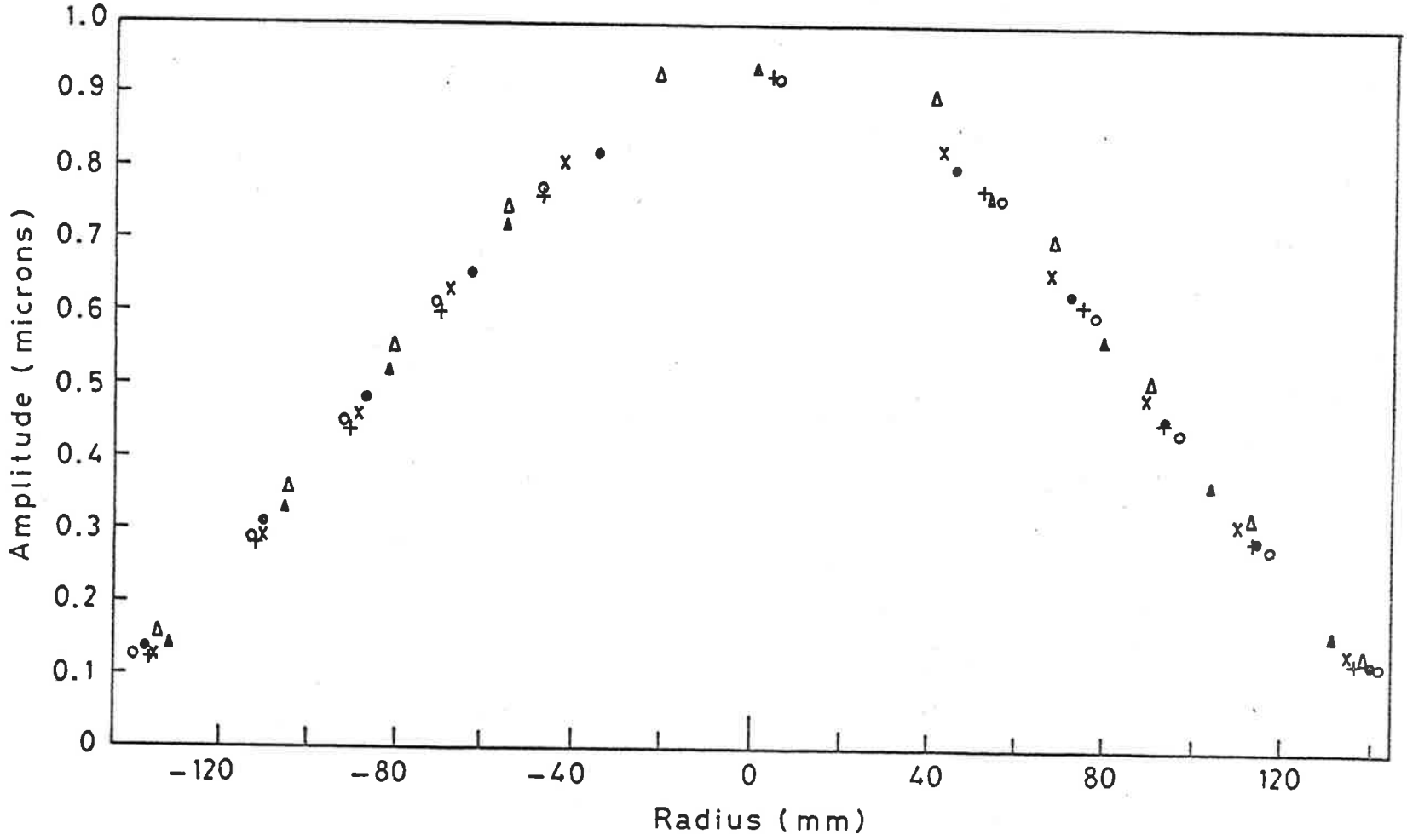

FIG. 3-4 HOLOGRAPHICALLY DETERMINED AMPLITUDES OF CLAMPED CIRCULAR PLATE VIBRATING IN THE (0,1) MODE FOR VARIOUS ILLUMINATION ANGLES.

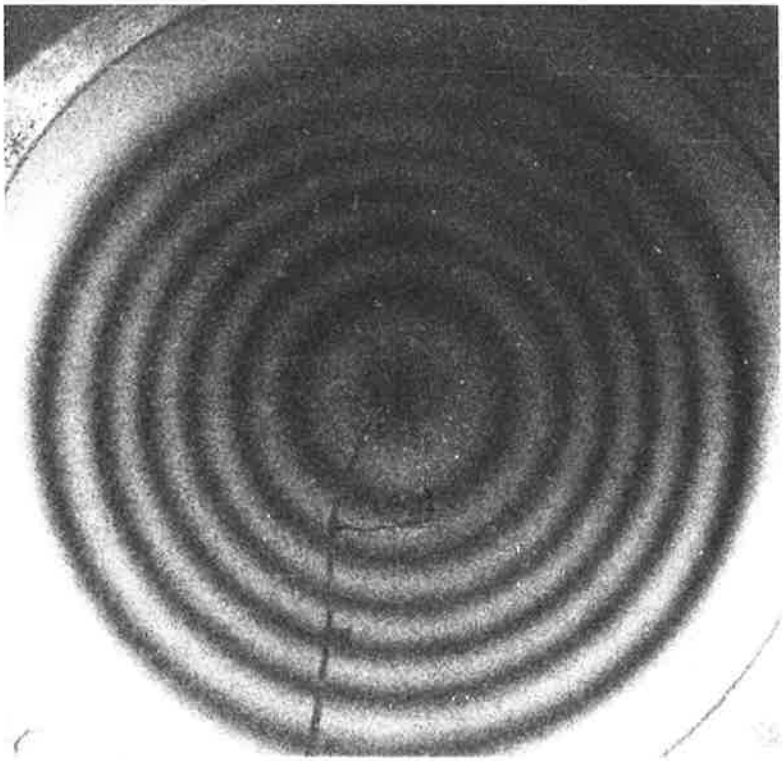

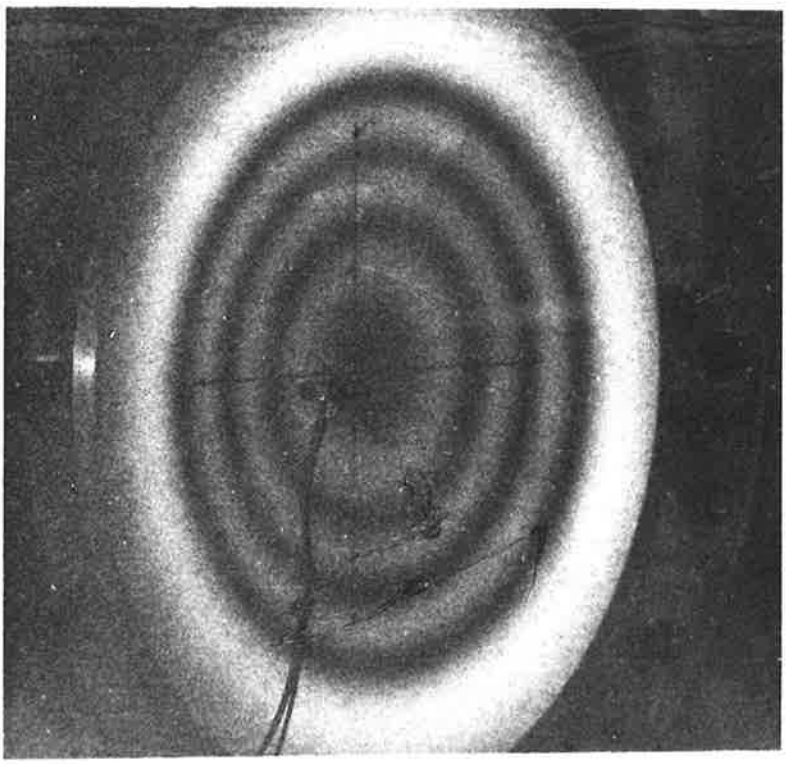

FIG. 3-5

Reconstructions of holograms of a clamped circular plate vibrating in the (0,1) mode and different orientation angles.

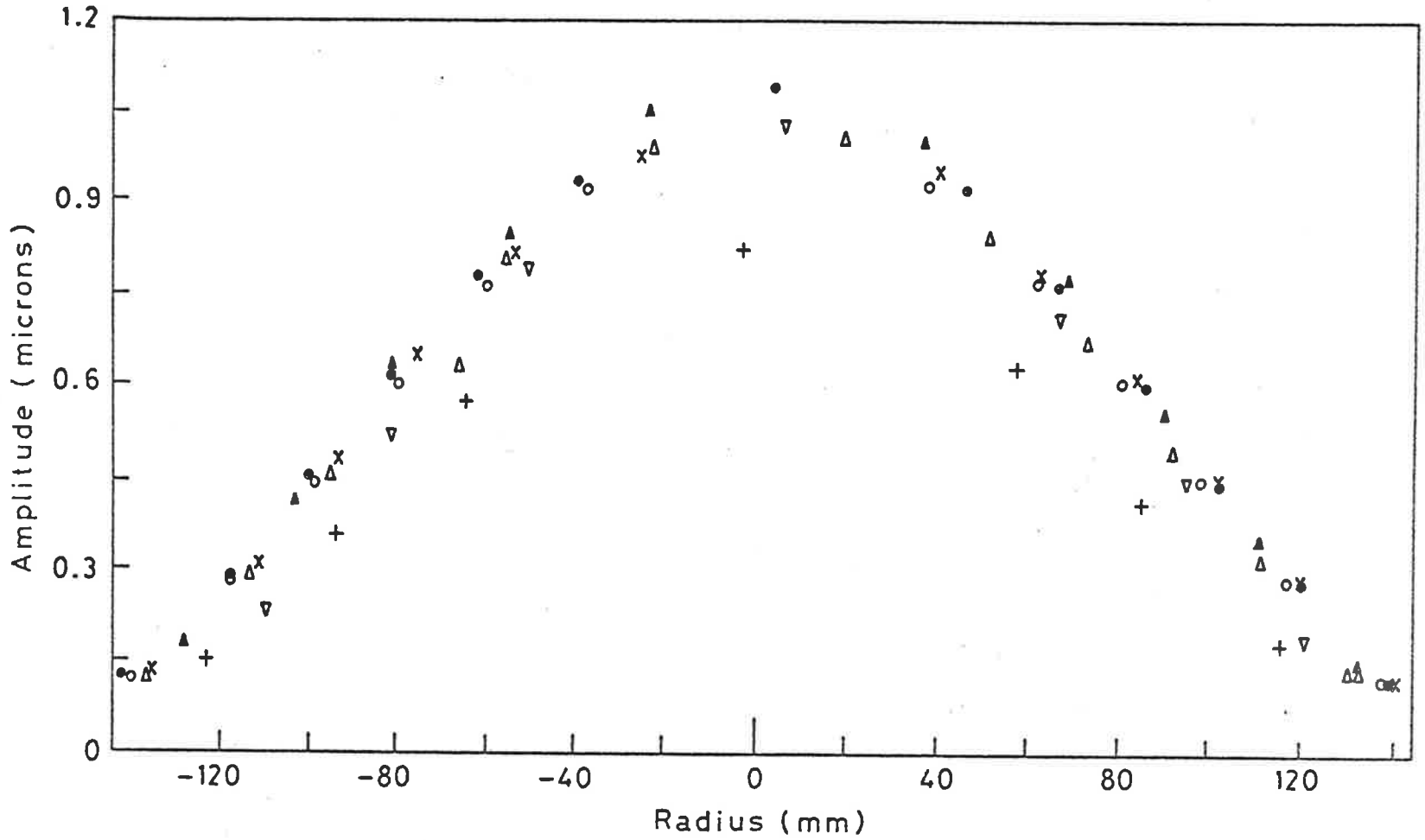

FIG. 3-6 HOLOGRAPHICALLY DETERMINED AMPLITUDES OF CLAMPED CIRCULAR PLATE VIBRATING IN THE (0,1) MODE FOR VARIOUS ORIENTATION ANGLES.

varied and attempted to explain this in terms of localization of fringes and parallax. It was subsequently shown by Tonin and Bies [102] that the shift was in fact due to a misinterpretation of the motion of the cylinder which is three-dimensional rather than one-dimensional.

The surface contour of a vertically mounted cylinder in the optical plane is a circle and the co-ordinate ξ is equivalent to the angular co-ordinate θ. Considering only this surface contour in the analysis then the geometrical factors are given by equations (2.25). Additionally if the radial and tangential components of vibration are respectively of the form

$$\left.\begin{aligned} c(\xi,t) &= C\cos n(\theta+\varepsilon)\cos\omega t \\ b(\xi,t) &= B\sin n(\theta+\varepsilon)\cos\omega t \end{aligned}\right\} \qquad (3.17)$$

then the characteristic equation [equation (2.29)] is

$$\frac{\Omega}{k} = c(\theta)(\cos\theta_1 + \cos\theta_2) + b(\theta)(\sin\theta_1 - \sin\theta_2) \qquad (3.18)$$

where $c(\theta) = C\cos n(\theta+\varepsilon)$

and $b(\theta) = B\sin n(\theta+\varepsilon)$ (3.19)

The experiments of Liem et al were repeated for the case of a wine glass and stainless-steel beaker, which are manufactured easily with high accuracy.

In the case of the wine glass, freedom from distortion is readily demonstrated by rubbing a moist finger around the lip which excites the glass in its lowest energy $n = 2$ flexural mode. Additionally

the mode rotates around the circumference if the finger is removed which clearly shows the degeneracy of the mode. A scheme was devised whereby the two holographic views could be recorded on the same hologram using a plane mirror which was positioned such that the image of the object was fully visible but the illuminating beam did not reflect onto the object from the mirror.

Referring to Fig. 3-7, which shows the geometry in the optical plane, the centre of the imaged cylinder in the photograph (or on the imaginary screen defined in Chapter 2, see figure) is at an angle ψ with respect to the centre of the cylinder in the direct view. The corresponding point T_m on the mirror is in practice marked with a small piece of masking tape such that it coincides with the centre of the imaged cylinder when viewed through the camera eyepiece. Also shown in the figure is the relative illumination direction $\underset{\sim}{K}_1$ and the relative centre line $\mathbb{L}$ for the image and the origins O_D and O_I which are defined for the direct and imaged views respectively. Fig. 3-8 shows the geometry for the imaged view drawn inverted for comparison with Fig. 2-10.

In the case of the direct view the geometrical analysis is that given in section 2.2.3, notably equations (2.59), (2.61), (2.63) and (2.64). For the imaged view it is clear that the photograph is distorted due to perspective. From the sine rule for triangles (see Figs. 3-7 and 3-8),

$$\frac{H}{\sin\gamma} = \frac{\chi/\cos\nabla}{\sin[\pi/2 + (\nabla - \gamma)]} \tag{3.20}$$

Solving for γ,

$$\gamma = \tan^{-1}\left[\frac{H\cos^2\nabla}{\chi - H\cos\nabla\sin\nabla}\right] \tag{3.21}$$

where ∇ is computed from the lengths AA,BB and CC and χ is to be determined. Denote a_v^R as the radius from the image centre to the right edge

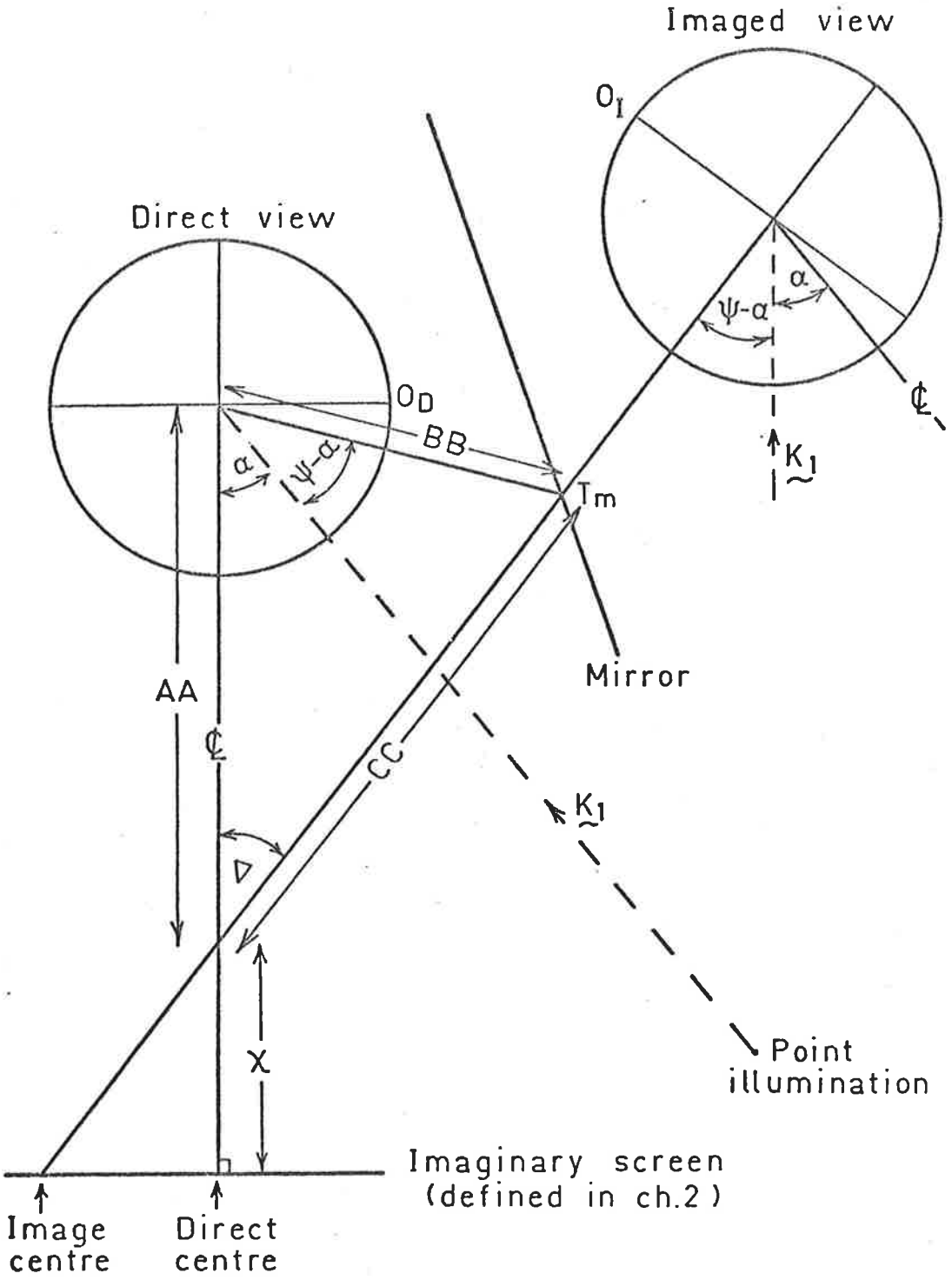

FIG. 3-7 SCHEMATIC OF TWO-VIEW EXPERIMENT USING A PLANE MIRROR

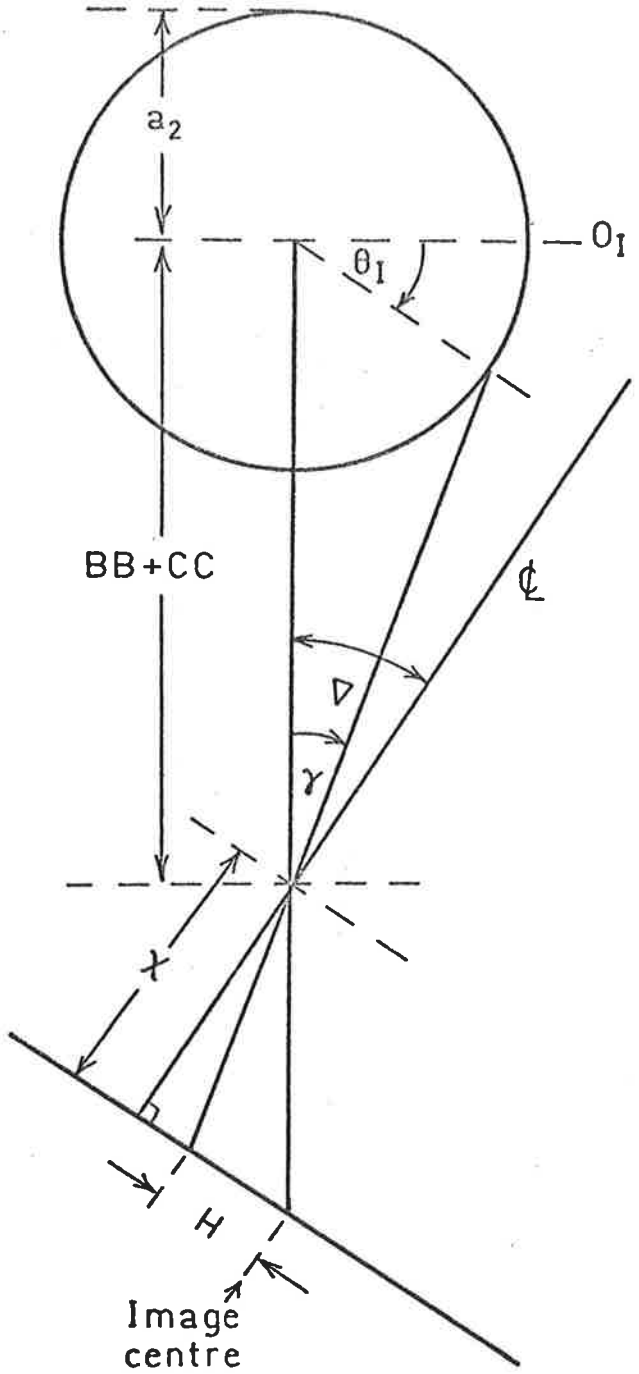

FIG. 3-8 GEOMETRY FOR THE IMAGED VIEW

of the cylinder in the photograph, a_v^L as the radius to the left edge and d_v as the diameter of the cylinder in the photograph. Hence,

$$d_v = a_v^R + a_v^L \tag{3.22}$$

and from equation (3.20),

$$a_v^R = \frac{\chi \sin\gamma^*}{\cos\nabla \cos(\nabla - \gamma^*)} \tag{3.23}$$

and

$$a_v^L = \frac{\chi \sin\gamma^*}{\cos\nabla \cos(\nabla + \gamma^*)} \tag{3.24}$$

where

$$\gamma^* = \tan^{-1}(a_2/AA) \tag{3.25}$$

and the asterisk denotes the maximum value of γ. Combining equations (3.22) to (3.24) gives

$$\chi = \frac{d_v \cos\nabla}{\sin\gamma^*} \left[\frac{1}{\cos(\nabla - \gamma^*)} + \frac{1}{\cos(\nabla + \gamma^*)} \right]^{-1} \tag{3.26}$$

The angle θ_I is determined in a similar way to equation (2.61) with the result that

$$\theta_I = \cos^{-1}([BB + CC]\sin\gamma/a_2) + \gamma \tag{3.27}$$

where, with respect to O_D the origin of the direct view,

$$\theta = \theta_I - \psi \tag{3.28}$$

Hence using equations (3.21) and (3.25) to (3.28) the angle θ is computed for fringes in the imaged view with respect to the origin of the direct view. The observation angle θ_2 is given by equation (2.64) and the illumination angle θ_1 by equation (2.63) but with the angle α

replaced by $(\alpha - \psi)$ thus

$$\theta_1 = \tan^{-1}\{P\cos(\alpha - \psi + \theta)/[a_2 - P\sin(\alpha - \psi + \theta)]\} \tag{3.29}$$

For $n = 2$ the radial component of vibration is determined from equation (3.18) as

$$c(\theta) = \frac{\Omega}{k}\left[\cos\theta_1 + \cos\theta_2 - \frac{B}{C}\tan[n(\theta + \varepsilon)](\sin\theta_1 - \sin\theta_2)\right]^{-1} \tag{3.30}$$

for the direct view; for the imaged view $(\varepsilon - \psi)$ is substituted for ε. The coefficients B/C and ε, the latter which determines the orientation of the mode around the circumference, must be estimated in order to use equation (3.30). This technique is obviously not practical in general and hence a refinement is added in the following analysis of a beaker. For the case

$$\theta_1 = \theta_2 \neq \pi/2 \tag{3.31}$$

equation (3.30) reduces to

$$c(\theta) = \Omega/(2k\cos\theta_1) \tag{3.32}$$

Thus, if the beaker is set on a turntable with its central axis corresponding to the turntable axis which is also normal to the optical plane then a number of points on the cylinder may be analysed for which equation (3.31) is true and the radial component determined separately using equation (3.30).

Reference to Fig. 2-10 and application of the sine rule to the two triangles with sides AA and P gives

$$\frac{AA}{\sin(\pi - \theta_1)} = \frac{a_2}{\sin[\theta_1 - (\pi/2 - \theta)]} \tag{3.33}$$

and
$$\frac{P}{\sin(\pi - \theta_1)} = \frac{a_2}{\sin[\theta_1 - (\alpha - [\pi/2 - \theta])]} \tag{3.34}$$

whereupon eliminating θ by combining equations (3.33) and (3.34) the result is

$$\frac{1}{P}\cos\theta + \frac{1}{AA}\cos(\alpha+\theta) - \frac{1}{a_2}\sin(\alpha+2\theta) = 0 \tag{3.35}$$

which is easily solved for θ by Newton's method [158, page 26]. The corresponding point on the photograph is, from equation (2.59) and (2.60),

$$H = \frac{AA.a_v.\cos\theta}{(AA - a_D\sin\theta)} \tag{3.36}$$

and the illumination angle

$$\theta_1 = \tan^{-1}\left[\frac{AA\cos\theta}{AA\sin\theta - a_2}\right] \tag{3.37}$$

Hence a number of experimental points are obtained for the radial component through which a sinusoidal curve of best fit is drawn and hence the coefficients C and ε determined. The tangential points are thus calculated from

$$b(\theta) = \{\Omega/k - C\cos n(\theta+\varepsilon)[\cos\theta_1 + \cos\theta_2]\}/(\sin\theta_1 - \sin\theta_2) \tag{3.38}$$

which follows from equations (3.18) and (3.19).

3.2.2 Wine Glass and Beaker Experiments and Results

A wine glass of outer radius 27.5mm at the lip sprayed matt white, was fixed to a steel base and positioned with the rim in the optical plane. A cluster of four bar electromagnets arranged in quadrature was suspended from above and lowered a short way into the glass

without touching the sides. The electromagnets were connected such that opposites were in phase but adjacents in antiphase which corresponds to the circumferential mode n = 2. Four tiny pieces of iron were then placed around the circumference of the glass and held in place by the attraction of the electromagnets. In this way the electromagnets and pieces of iron (which we will call the drivers) are positioned for optimum coupling with the mode being driven.

Fig. 3-9 is a picture of the wine glass and electromagnets. The mode was excited at a frequency of 1.34kHz using an audio oscillator and 30W amplifier. The level of vibration was monitored with a Bruel and Kjaer (B & K) spectrometer type 2112 and a B & K half inch microphone type 4133 placed near the glass at a radial antinode. A photograph of a time-averaged hologram is shown in Fig. 3-10.

For the purpose of the analysis a plane back-silvered mirror was placed in the field of view of the camera with a fair degree of overlap of points on the circumference of the glass in the direct and imaged views. A typical photograph of a hologram reconstruction is shown in Fig. 3-11. With AA = 502.5mm, P = 432.5mm, $\alpha = 0.474$rad, $\psi = 0.876$rad, $\nabla = 0.224$rad and BB + CC = 558.5mm the radial component is firstly determined from equation (3.1) and is shown in Fig. 3-12 (a) as circles for the direct view and triangles for the imaged view where the amplitude shift first reported by Liem et al [101] is quite apparent. Next the analysis of orthogonal vibrations is used to calculate the radial component using equation (3.30). The ratio B/C is estimated as 1/n or 0.5 which is borrowed from the theory for cylinders with shear-diaphragm ends [125, page 31] for which it is a good approximation and the angle determining the orientation of the mode around the circumference, ε, is estimated as 0.36rad. The result is shown in Fig. 3-12 (b) which, despite the crude approximations, is extremely

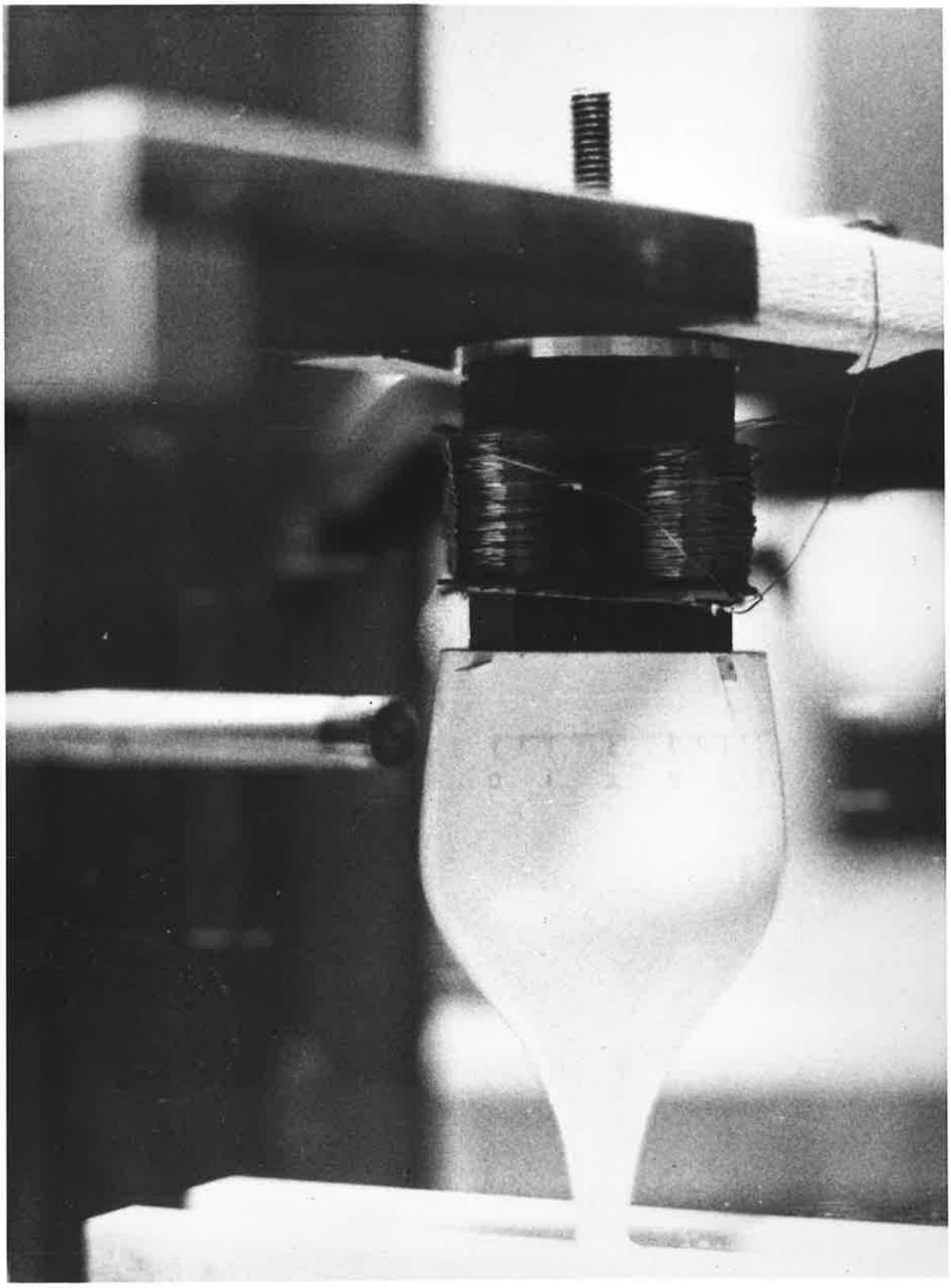

FIG. 3-9

Wine glass and modal driving system.

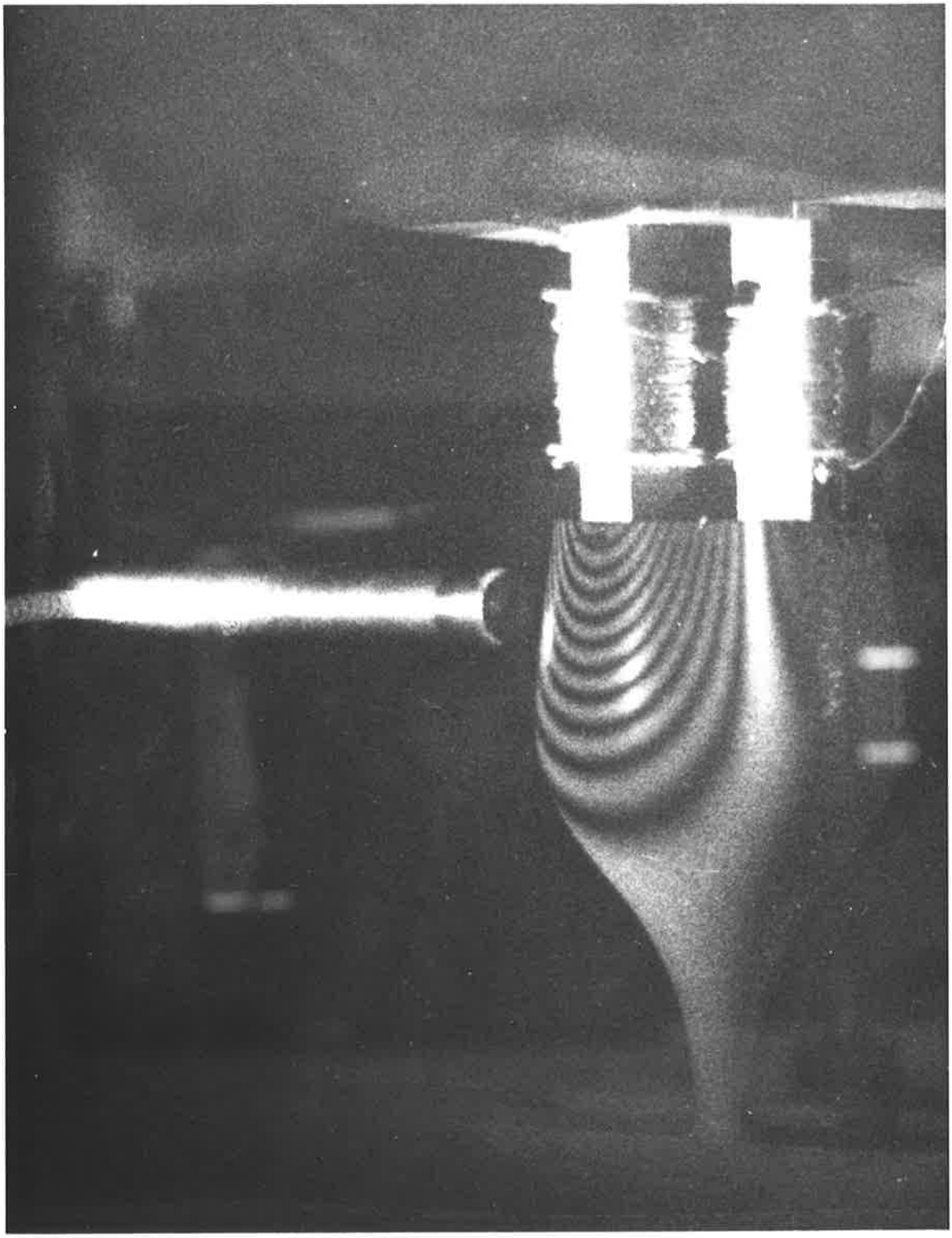

FIG. 3-10

Time-averaged hologram reconstruction of the n = 2 mode for the wine glass.

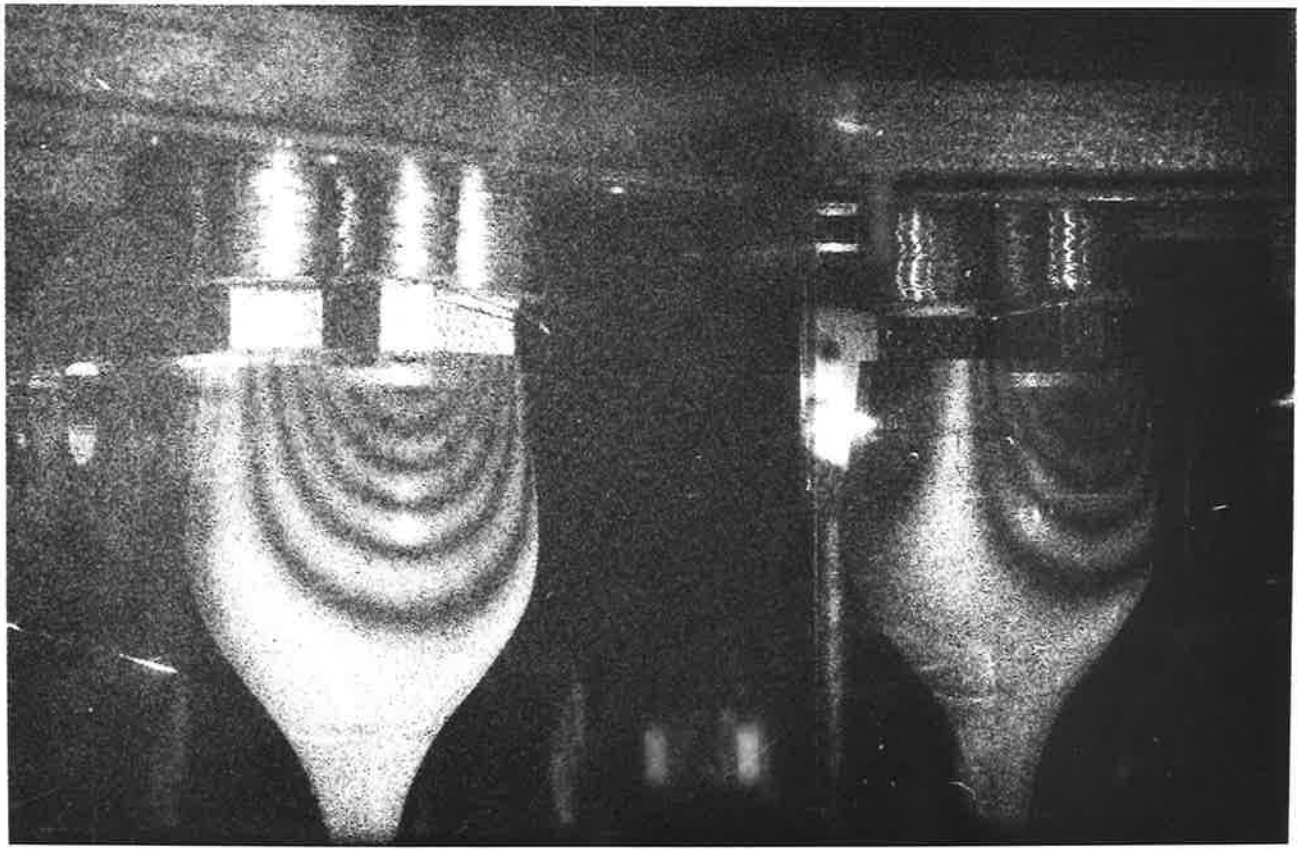

FIG. 3-11

Time-averaged hologram of wineglass vibrating in the n=2 mode and the mirror image.

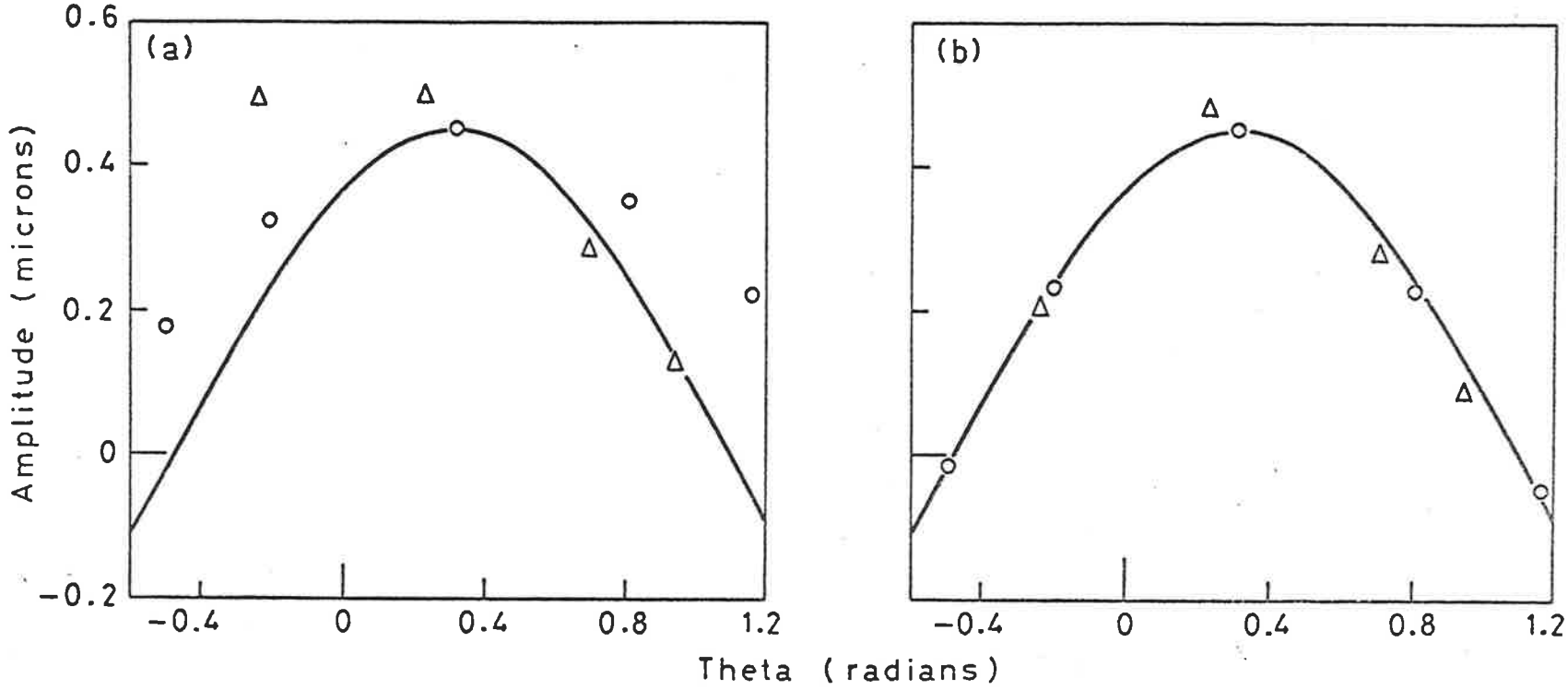

FIG. 3-12 RADIAL COMPONENTS OF A VIBRATING WINE GLASS. (a) Calculated from theory used by Liem et al; (b) Theory extended to include orthogonal components of vibration; o, experimental points, direct view of the cylinder; Δ, experimental points, imaged view of cylinder; ——, sinusoidal curve fitted to data points in (b).

favourable.

Next a stainless-steel beaker of radius $a_2 = 44.2$mm, wall thickness $h = 1.23$mm and length $L = 101.3$mm was sprayed matt white and fastened to a base plate by means of a bolt through its bottom. The modal driving system was similar to that used in the wine glass experiment except that three electromagnets were used arranged symmetrically and wired in-phase and the drivers were slightly heavier tiny steel bolts. The driving frequency was measured as 1011Hz for the $n = 3$ mode.

The beaker and driving mechanism were placed on a turntable with the beaker centreline coincident with the turntable axis. In all, seven holograms were taken of the vibrating beaker at 15° rotation intervals two views of which are shown in Fig. 3-13. With $P = 486.2$mm, $AA = 749.2$mm, $a_2 = 44.2$mm and $\alpha = 0.5492$rad the solution of equation (3.35) is $\theta = 1.2915$rad at which point the sensitivity vector is normal to the surface of the beaker. However, if the beaker is sprayed only lightly with white paint, specular reflection of the illuminating beam occurs at this value for θ and this shows on the photographs of Fig. 3-13 as a thin white line along the length of the beaker.

Solving for the radial component using equation (3.32) requires that a dark fringe coincide with the point where the sensitivity vector is normal to the surface. This is not usually the case, however, and rather than interpolate a value for Ω, a method employed by Tushak and Allaire [104], the two adjacent fringes are analysed. This procedure is justified in view of the excellent agreement of the data points so obtained onto a sine curve of best fit as shown in Fig. 3-14. From the figure the radial vibration component is

$$c(\theta) = .74 \cos[3(\theta - 1.53)] \qquad (3.39)$$

From equations (3.38) and (3.39) the tangential component of vibration

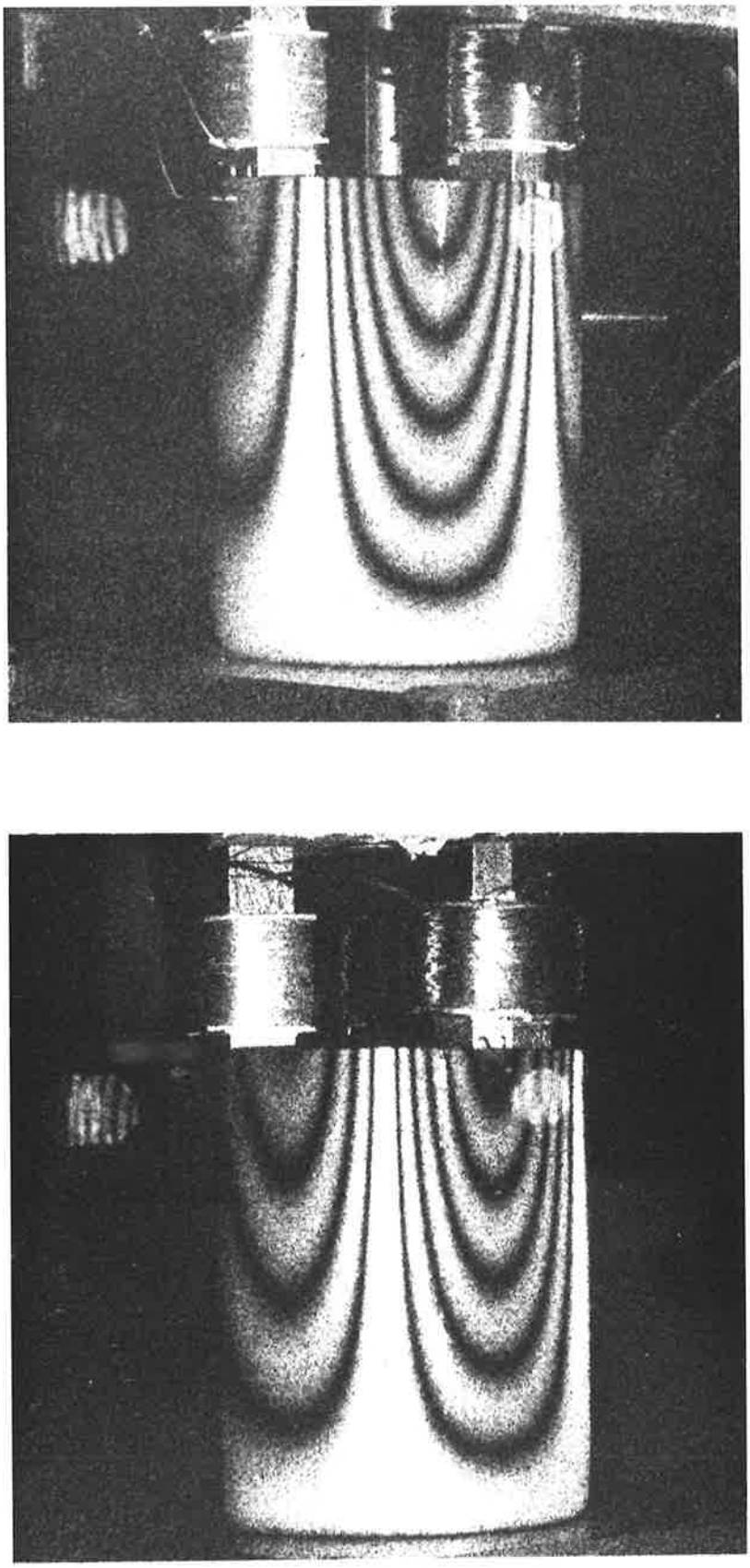

FIG. 3-13

Hologram reconstructions of two views of a beaker vibrating in a love mode of order n = 3.

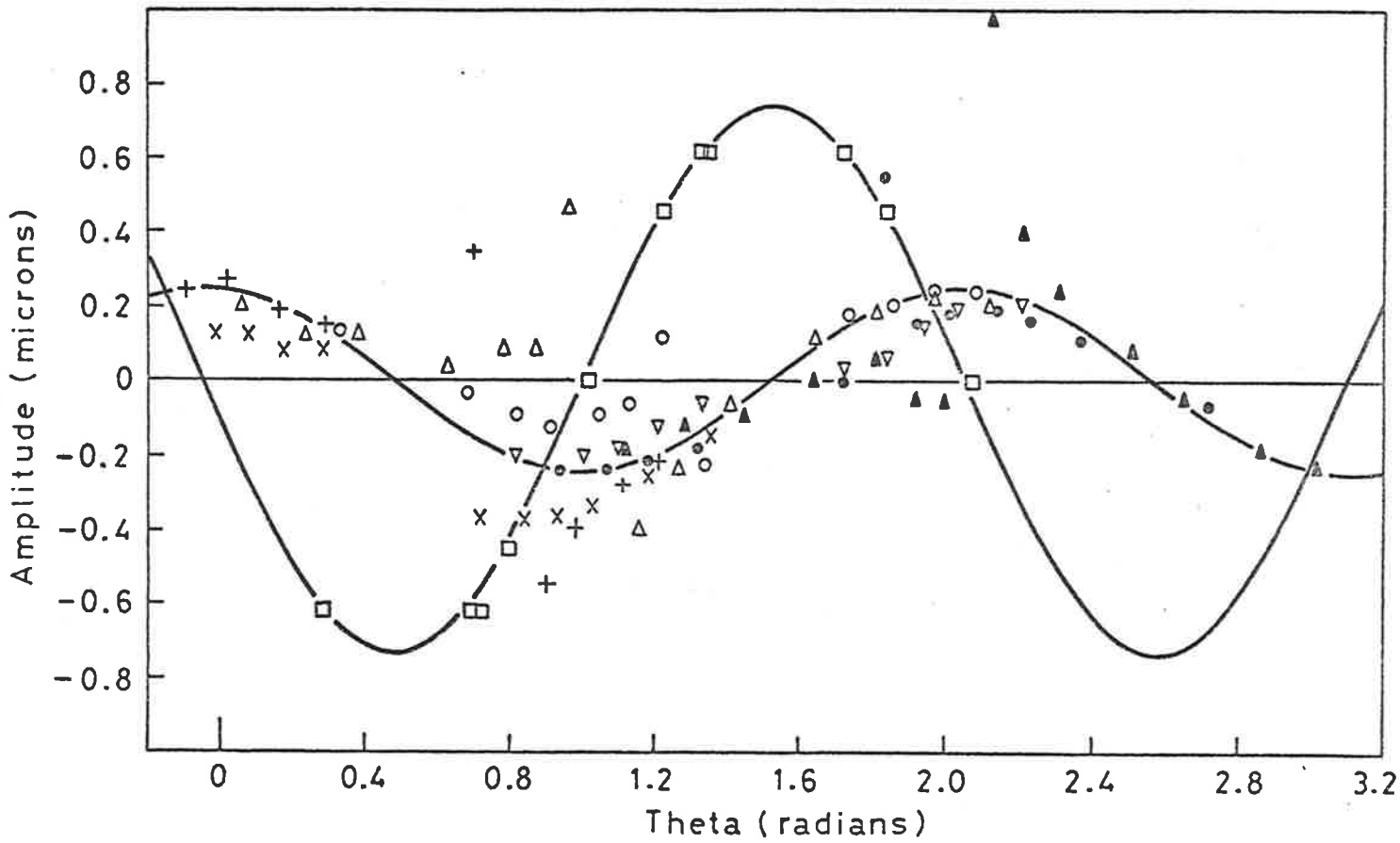

FIG. 3-14 THEORETICAL AND EXPERIMENTAL DETERMINATION OF RADIAL AND TANGENTIAL VIBRATION COMPONENTS OF STAINLESS STEEL BEAKER

—— Theoretical curves; □ , experimentally determined radial components; +,x,o,Δ,●,∇,▲, experimentally determined tangential components from different views of beaker.

$b(\theta)$, is calculated for all dark fringes and the results are shown in Fig. 3-14 as well. The sign of the fringe order, Ω, is chosen as is usually the case in time-averaged holography such that adjacent groups have alternating signs and correspond to the sign of $c(\theta)$ which is the larger component in terms of absolute magnitude.

The theoretical curve for the tangential motion is determined on the assumption that the cylinder vibrates in a Love mode (see reference [125], page 125) which arises from inextensional theory. This is confirmed by the equal spacing between fringes (see Fig. 3-13) along the length of the reconstructed beaker indicating that the sides remain straight. The bottom of the beaker acts effectively as a shear diaphragm satisfying the boundary conditions at the constrained end of the beaker. The frequency of vibration ([125], page 125) of the mode considered is

$$\omega^2 = \frac{E}{\rho} \frac{h^2}{12(1-\nu^2)a_o^4} \left[\frac{n^2(n^2-1)^2}{n^2+1} \right] \left\{ \frac{1+6(1-\nu)a_o^2/n^2L^2}{1+3a_o^2/n^2(n^2+1)L^2} \right\} \qquad (3.40)$$

In this case, assuming $E/\rho = 2.445 \times 10^7\ m^2s^{-2}$, Poisson's ratio $\nu = 0.3$ and $n = 3$ the result is $f = 1183\,Hz$ which is to be compared with the experimental value of 1216 Hz.

In particular, the radial, tangential and longitudinal vibration components are respectively of the forms

$$\left.\begin{aligned} c(\theta,X,t) &= nXC \cos n\theta \cos \omega t \\ b(\theta,X,t) &= XC \sin n\theta \cos \omega t \\ a(\theta,X,t) &= (a/n)C \cos n\theta \cos \omega t \end{aligned}\right\} \qquad (3.41)$$

where X is the length co-ordinate from the shear diaphragm, θ is the

angular co-ordinate and C is an amplitude constant. Note that the radial and tangential components vary linearly with X. Comparing equations (3.17) and (3.41) gives

$$B/C = 1/n = 1/3 \qquad (3.42)$$

The theoretical curve for $b(\theta)$ is thus determined and shown in Fig. 3-14.

The scatter of points requires comment. The denominator in equation (3.38) becomes very small when the sensitivity vector approaches the surface normal. Hence slight errors in the numerator are magnified enormously. Thus extraordinary deviations from the theoretical curve occur at points where the sensitivity vector is near normal to the surface (and hence normal to the tangential component of vibration). Reference to Fig. 3-14 shows that for the points marked o, for example, agreement is poor at about $\theta = 1.8$ radian. In the lower photograph of Fig. 3-13 this corresponds to the region just right of the centre of the photograph and this is where the sensitivity vector is normal to the surface.

Hence a conclusion is that if an accurate determination of the tangential component is required, the range of θ and the positioning of the illumination and observation vectors should be such that the sensitivity vector is never normal to the surface. When it is near normal the curve of best fit would probably be the best one could do.

3.3 CYLINDERS

3.3.1 Holographic and Least Squares Theory

It would be useful to apply the method of the last section to calculate the vibration components of the superposed modes of a distorted surface. Two examples would be the vibration of a cylinder with a seam and a cylinder with an attached lump mass for which typical hologram reconstructions are shown in Fig. 3-15. In the figure the cylinder in (a) is rolled from a thin sheet of brass, soldered at the seam and

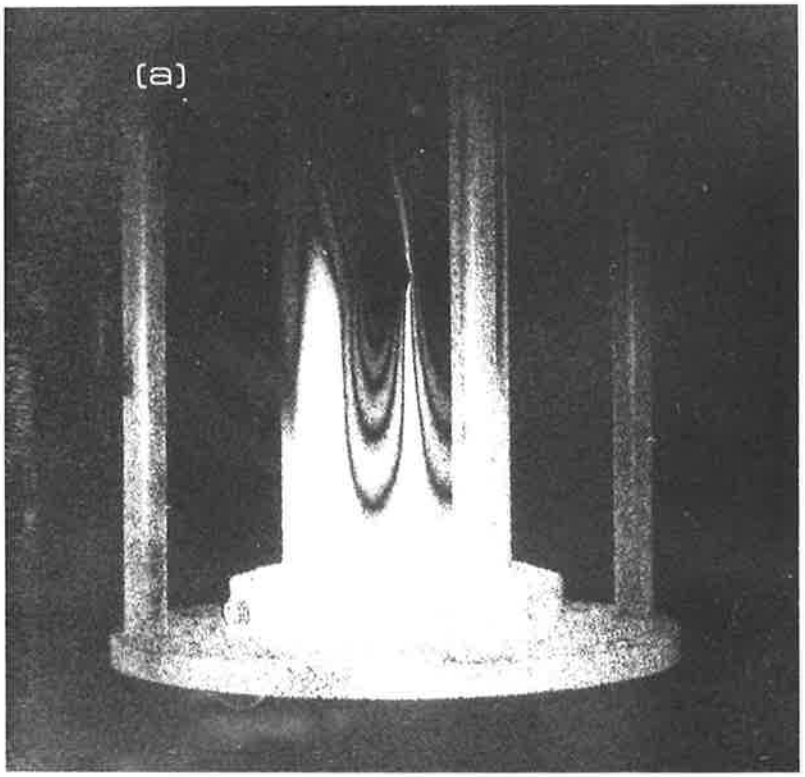

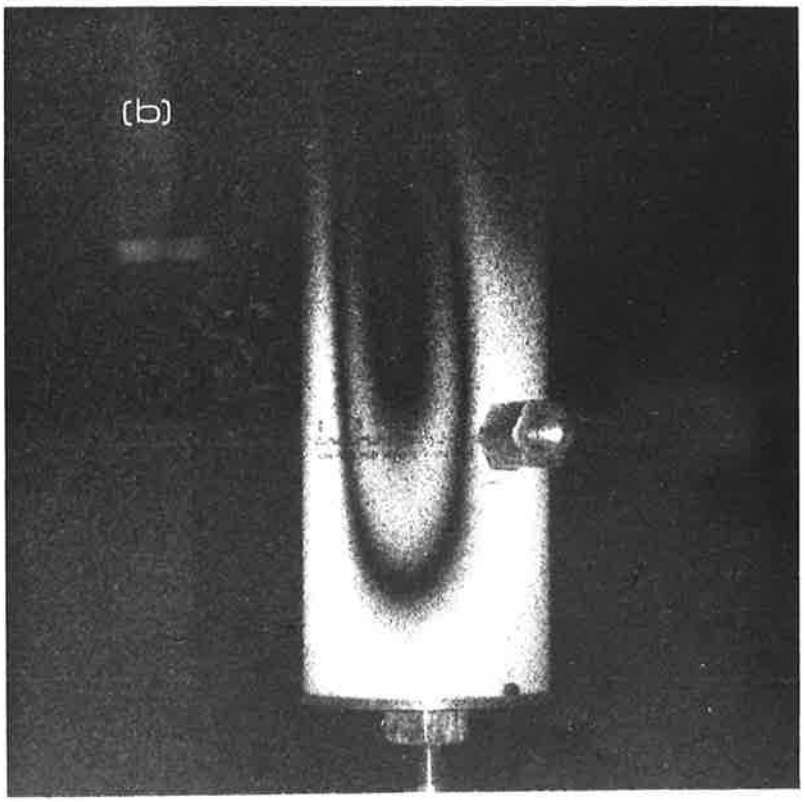

FIG. 3-15

(a) Cylinder with a seam

(b) Cylinder with a lumped mass

supported in a steel structure which is visible in the figure and (b) is a steel cylinder with a brass mass glued on to the surface.

The characteristic equation is equation (3.18) with the radial and tangential vibration components given by equations (2.10) and (2.11). Using these equations the following system of equations for τ points results

$$\left.\begin{aligned} c^1K_1 + b^1S_1 &= \Omega_1/k \\ c^2K_2 + b^2S_2 &= \Omega_2/k \\ &\vdots \\ c^\tau K_\tau + b^\tau S_\tau &= \Omega_\tau/k \end{aligned}\right\} \qquad (3.43)$$

where the geometrical coefficients K_q and S_q are defined by equation (2.30) for a surface contour in the optical plane. It must be emphasised that the bounds of the summation in equations (2.10) and (2.11) are quite arbitrary. In fact these are generalized by replacing the bounds 0 and N by N^1 and N^2 which are respectively the least and greatest orders considered. For example if the fourth order of vibration is being investigated but because of asymmetry in the forcing field the lower second and third orders were present then N^1 would be set at 2 and N^2 would be set at 4. On the other hand if only one term is necessary for an adequate description, N^1 and N^2 would be identical. The series would contain only the single terms as for the analysis in the last section.

Hence, substituting equations (2.10) and (2.11) into equation (3.43) gives for each point q corresponding to a dark fringe

$$\sum_{n=N^1}^{N^2} x_n \sin(n\xi_q) K_q + \sum_{n=N^1}^{N^2} y_n \cos(n\xi_q) K_q$$

$$+ \sum_{n=N^1}^{N^2} w_n \sin(n\xi_q) S_q + \sum_{n=N^1}^{N^2} z_n \cos(n\xi_q) S_q = \Omega_q/k \qquad (3.44)$$

where the ξ_q, K_q, S_q and Ω_q are determined from the time-averaged holograms. These form a set of τ linear equations in $4(N^2 - N^1 + 1)$ parameters or unknowns x_n, y_n, w_n and z_n which are determined by the normal method of least squares as follows. Assume that the left hand side of equation (3.44) is exactly equal to Ω'_q/k but slightly different to Ω_q/k, the value determined by the data. The square of the residual is

$$\left[\sum_{n=N^1}^{N^2} x_n \sin(n\xi_q) K_q + \sum_{n=N^1}^{N^2} y_n \cos(n\xi_q) K_q + \sum_{n=N^1}^{N^2} w_n \sin(n\xi_q) S_q\right.$$

$$\left. + \sum_{n=N^1}^{N^2} z_n \cos(n\xi_q) S_q - \Omega_q/k\right]^2 = [\Omega'_q/k - \Omega_q/k]^2 \qquad (3.45)$$

Denoting

$$f(x_{N^1},\ldots,x_{N^2},y_{N^1},\ldots,y_{N^2},w_{N^1},\ldots,w_{N^2},z_{N^1},\ldots,z_{N^2})$$

$$= \sum_{q=1}^{\tau} (\Omega'_q/k - \Omega_q/k)^2 \qquad (3.46)$$

then by the usual method $f' = 0$ is required where the prime indicates differentiation with respect to each variable in turn.

The NORMAL EQUATIONS are now derived using the matrix method of Buckingham [159]. Firstly set up the matrix $\underline{A}$ of order τ by $4(N^2 - N^1 + 1)$ (see Appendix II for partial expansion)

$$\left.\begin{aligned} A(q,4(n-N^1+1)-3) &= K_q \sin(n\xi_q) \\ A(q,4(n-N^1+1)-2) &= K_q \cos(n\xi_q) \\ A(q,4(n-N^1+1)-1) &= S_q \sin(n\xi_q) \\ A(q,4(n-N^1+1)) &= S_q \cos(n\xi_q) \end{aligned}\right\} \qquad (3.47)$$

for $q = 1$ to τ and $n = N^1$ to N^2

and let $\underline{R}$ and $\underline{\Omega}$ be the column vectors

$$\underline{R} = \begin{bmatrix} x_{N^1} \\ y_{N^1} \\ w_{N^1} \\ z_{N^1} \\ \cdot \\ \cdot \\ \cdot \\ x_{N^2} \\ y_{N^2} \\ w_{N^2} \\ z_{N^2} \end{bmatrix} \qquad \underline{\Omega} = \begin{bmatrix} \Omega_1 \\ \Omega_2 \\ \cdot \\ \cdot \\ \cdot \\ \Omega_\tau \end{bmatrix}$$

Then equation (3.44) is simply expressed as

$$\underline{A}\,\underline{R} = \frac{1}{k}\,\underline{\Omega} \qquad (3.48)$$

The NORMAL EQUATIONS are [159]

$$\underline{A}^T \underline{A} \underline{R} = \frac{1}{k} \underline{A}^T \underline{\Omega} \tag{3.49}$$

where $\underline{A}^T \underline{A}$ is a $4(N^2 - N^1 + 1)$ square matrix. The solution of $\underline{R}$ in equation (3.49) is found by the Gauss elimination method [158, page 398]. As is usually the case in time-averaged holography the signs of the Ω_q arguments are arbitrarily chosen for each group of fringes and for the modes of vibration considered here, adjacent groups take alternating signs. In this way, the magnitudes and signs of the parameters x, y, w, z are automatically computed to give the best fit.

The standard deviation of each parameter of vector $\underline{R}$ is

$$\text{s.d.} = \left[\frac{\sum (\Omega'/k - \Omega/k)^2}{p_w[\tau - 4(N^2 - N^1 + 1)]} \right]^{\frac{1}{2}}$$

where p_w is the weight of the coefficient and is calculated in the following way by the method of Bartlett [160]. In the normal equations define $\underline{A}^T\underline{\Omega}(1) = 1$ and $\underline{A}^T\underline{\Omega}(2) = \ldots = \underline{A}^T\underline{\Omega}[4(N^2 - N^1 + 1)] = 0$ and solve for parameter x_{N^1} in the usual way. The weight of this coefficient is $p_w = 1/x_{N^1}$. Similarly for the weight of x_{N^1+1} define $\underline{A}^T\underline{\Omega}(2) = 0$ and $\underline{A}^T\underline{\Omega}(1) = \underline{A}^T\Omega(3) = \ldots = \underline{A}^T\underline{\Omega}[4(N^2 - N^1 + 1) = 0$ and solve for x_{N^1+1} giving the weight $p_w = 1/x_{N^1+1}$ and so on for the other parameters. The total standard deviation s.d._c for the vibration component $c(\xi)$ is then

$$[\text{s.d.}_c(\xi)]^2 = \sum_{n=N^1}^{N^2} (\sin(n\xi)\text{s.d.}_{x_n})^2 + (\cos(n\xi)\text{s.d.}_{y_n})^2 \tag{3.50}$$

where s.d._{x_n} and s.d._{y_n} are the standard deviations of parameters x_n and y_n with similar equations for the other components.

3.3.2 Theory of Thin Circular Cylindrical Shells

Consider a thin circular cylindrical shell of length L, mean radius a_o and wall thickness h (see Fig. 3-16).

The cylinder is supported by thin circular end caps or shear-diaphragms at which the boundary conditions are

$$b = c = M_x = N_x = 0 \quad \text{at } X = 0, L \tag{3.51}$$

where M_x is the bending moment and N_x the longitudinal membrane force in the shell. If $\underset{\sim}{d} = (a,b,c)$ is the displacement vector for the vibration with longitudinal, tangential and radial components respectively of the form

$$\left.\begin{aligned} a(X,\theta) &= A\cos(\lambda s)\cos(n\theta)\cos(\omega t) \\ b(X,\theta) &= B\sin(\lambda s)\sin(n\theta)\cos(\omega t) \\ c(X,\theta) &= C\sin(\lambda s)\cos(n\theta)\cos(\omega t) \end{aligned}\right\} \tag{3.52}$$

where $\lambda = \dfrac{m\pi a_o}{L}$ and $s = \dfrac{X}{a_o}$ then the equations of motion may be written in matrix form as

$$\underline{T}_{DM}\,\underline{d} = 0 \tag{3.53}$$

where $\underline{T}_{DM}$ is the matrix differential operator derived from the Donnell-Mushtari theory which takes the form [125, Chapt. 2]

$$\underline{T}_{DM} = \begin{bmatrix} \left[\frac{\partial^2}{\partial s^2} + \frac{(1-\nu)}{2}\frac{\partial^2}{\partial \theta^2} - \rho\frac{(1-\nu^2)a_o^2}{E}\frac{\partial^2}{\partial t^2}\right] & \frac{1+\nu}{2}\frac{\partial^2}{\partial s \partial \theta} & \nu\frac{\partial}{\partial s} \\ \frac{(1+\nu)}{2}\frac{\partial^2}{\partial s \partial \theta} & \left[\frac{(1-\nu)}{2}\frac{\partial^2}{\partial s^2} + \frac{\partial^2}{\partial \theta^2} - \rho\frac{(1-\nu^2)}{E}a_o^2\frac{\partial^2}{\partial t^2}\right] & \frac{\partial}{\partial \theta} \\ \nu\frac{\partial}{\partial s} & \frac{\partial}{\partial \theta} & 1+\kappa\nabla^4+\rho\frac{(1-\nu^2)a_o^2}{E}\frac{\partial^2}{\partial t^2} \end{bmatrix} \qquad (3.54)$$

In the equation the non-dimensional thickness parameter $\kappa = h^2/12\,a_o^2$ and

$$\nabla^4 = \left(\frac{\partial^2}{\partial s^2} + \frac{\partial^2}{\partial \theta^2}\right)^2 .$$

The theories of Love - Timoshenko, Goldenveizer - Novozhilov (also Arnold - Warburton), Houghton - Johns, Flügge - Byrne - Lur'ye (also Biezeno - Grammel), Reissner - Naghdi - Berry, Sanders, Vlasov, Epstein - Kennard and a simplified theory due to Kennard are all modelled on the Donnel - Mushtari theory and in fact may be represented by the addition of a modifying matrix $\underline{T}_{MOD}$ as follows

$$\underline{T} = \underline{T}_{DM} + \kappa\underline{T}_{MOD} \qquad (3.55)$$

all of which are listed by Leissa [125, page 33]. Hence the eighth order system of equations represented by equation (3.53) becomes

$$\underline{T}\,\underline{d} = 0 \qquad (3.56)$$

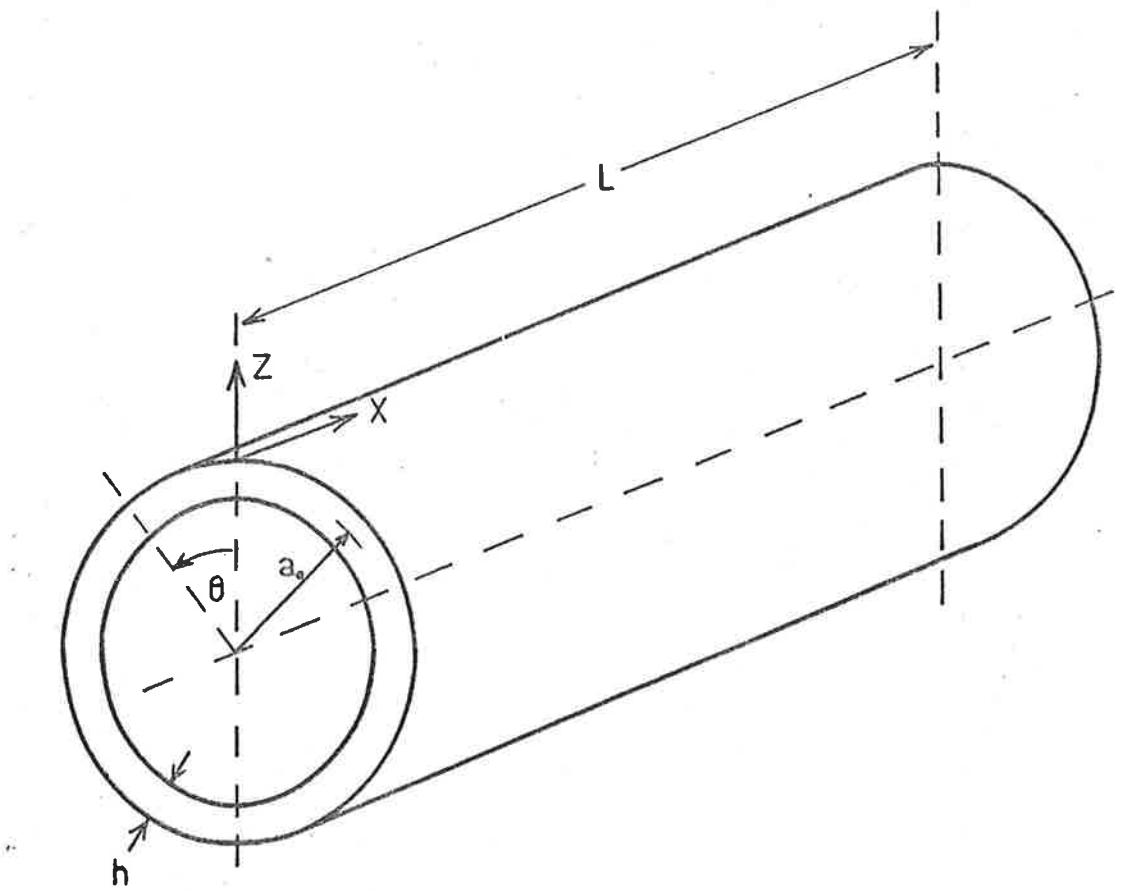

FIG. 3-16 CO-ORDINATE SYSTEM FOR A THIN CYLINDRICAL CLOSED CIRCULAR SHELL

which has a non-trivial solution if and only if

$$\det \underline{T} = 0 \tag{3.57}$$

This results in a third order polynomial of the form

$$\Lambda^6 - (\kappa_2 + \kappa\,\Delta\kappa_2)\,\Lambda^4 + (\kappa_1 + \kappa\,\Delta\kappa_1)\,\Lambda^2 - (\kappa_o + \kappa\,\Delta\kappa_o) = 0 \tag{3.58}$$

where the κ_o, κ_1 and κ_2 are Donnell Mushtari constants and $\Delta\kappa_o$, $\Delta\kappa_1$ and $\Delta\kappa_2$ are the modifying constants for the other theories and are tabulated by Leissa [125, page 45]. The roots of equation (3.58) are the eigen-values Λ^2 where

$$\Lambda^2 = \rho(1-\nu^2)a_o^2\,\omega^2/E \tag{3.59}$$

which determine the resonant frequency ω.

Equation (3.56) cannot be solved for the component amplitudes A, B and C by Cramer's method [158, page 382] due to the constraint imposed by equation (3.57). However, inspection of matrix $\underline{T}$ reveals it has rank order 2 and hence one row is superfluous [158, § 7.6]. Equation (3.56) becomes

$$\begin{bmatrix} T_{11} & T_{12} & T_{13} \\ T_{21} & T_{22} & T_{23} \end{bmatrix} \begin{bmatrix} A \\ B \\ C \end{bmatrix} = 0 \tag{3.60}$$

or, dividing by C,

$$\begin{bmatrix} T_{11} & T_{12} \\ T_{21} & T_{22} \end{bmatrix} \begin{bmatrix} A/C \\ B/C \end{bmatrix} = \begin{bmatrix} -T_{13} \\ -T_{23} \end{bmatrix} \tag{3.61}$$

which is solved for component ratios A/C and B/C by Cramer's method.

For example, the form of equation (3.61) for the Donnell-Mushtari theory is

$$\begin{bmatrix} -\lambda^2 - \frac{(1-\nu)}{2} n^2 + \Lambda^2 & \frac{(1+\nu)}{2} \lambda n \\ \frac{(1+\nu)}{2} \lambda n & -\frac{(1-\nu)}{2} \lambda^2 - n^2 + \Lambda^2 \end{bmatrix} \begin{bmatrix} A/C \\ B/C \end{bmatrix} = \begin{bmatrix} -\nu\lambda \\ n \end{bmatrix} \quad (3.62)$$

For each mode there corresponds three eigen-values Λ^2 which are solutions of equation (3.58) of which the two largest eigen-values result in ratios A/C or B/C greater than unity and frequencies in the untrasonic range for ordinary cylinders. In the case of the smallest eigen-values the ratios A/C and B/C are less than unity (the radial component is greatest in magnitude hence the modes are termed flexural) and frequencies fall in the audio range for at least the lower order modes which are of primary interest.

Differences between theories amount to less than 2% in resonant frequencies and ratios B/C and A/C, determined for a number of cylinders of typical dimensions used in the experiments to be described. As the accuracy of the experiments is at best of this order, it is not possible to distinguish between theories at present. However, the ratios B/C and A/C of flexural modes of a vibrating cylinder are experimentally measured for the first time and reported by Tonin and Bies [105].

3.3.3 Cylinder Experiments and Results

The least squares analysis described in section 3.3.1 is applied to the data of the stainless-steel beaker of section 3.2.2. Fig. 3-17 (a) shows the radial and tangential components of vibration using a single mode in the expansion i.e. $N^1 = N^2 = 3$. The solid lines are the radial and tangential curves of best fit. For each point corresponding to a dark fringe the circles o are values of b computed from

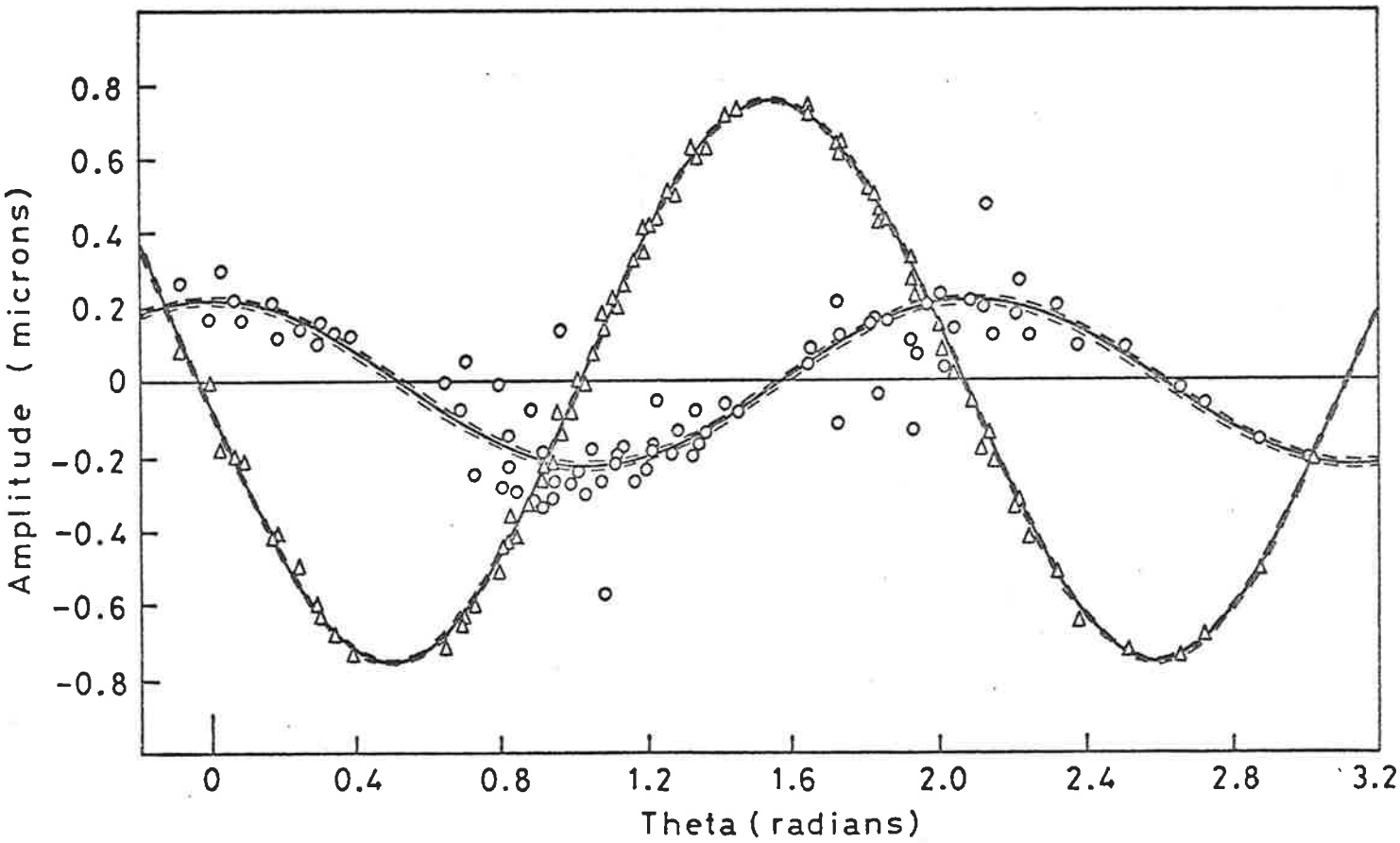

FIG. 3-17 (a) LEAST SQUARES PROCEDURE APPLIED TO DATA OF STAINLESS STEEL BEAKER, $N^1 = N^2 = 3$

—— Least squares curves; - - - standard deviation; Δ experimentally determined radial component; o experimentally determined tangential component.

equation (3.38) using the least squares fit curve for c and the experimental values of θ, θ_1 and θ_2. Similarly the triangles Δ are values of c computed from the least squares fit curve for b using equation (3.38). These component points are termed "experimentally determined" since they cannot be measured singularly without further experimental effort and are in fact a best estimate of what one would measure by ensuring the sensitivity vector to be in turn radial and tangential at those points.

Comparing Fig. 3-17 (a) to Fig. 3-14 shows the improvement of the least squares procedure over the previous method. The improved consistency of the data points is due to a more accurate determination of the radial component. In Fig. 3-17 (b) it is assumed that a small contribution of the $n = 2$ mode is present and the consistency of the experimentally determined points is further improved. However, the standard deviation for both components, shown by the broken curve, is greater since the number of unknown parameters has doubled. Fig. 3-18 shows the results of the least squares procedure applied to the brass cylinder with a seam shown in Fig. 3-15 (a) for which the analysis includes four modes ($N^1 = 2$, $N^2 = 5$).

Having thus proven the superiority of the least squares procedure, it is applied to four cylinders of various diameters, wall thicknesses and materials. The ends of each cylinder were machined flat with a lip on the inside edge to hold an end piece of thickness similar to that of the cylinder. The end pieces were cut so that only one edge touched the cylinder lip around the circumference. An electromagnet was used to excite the cylinder and both electromagnet and cylinder were supported by a steel structure which held the latter by two probes each neatly fitting into a small hole at the centre of each end plate as shown in Fig. 3-19.

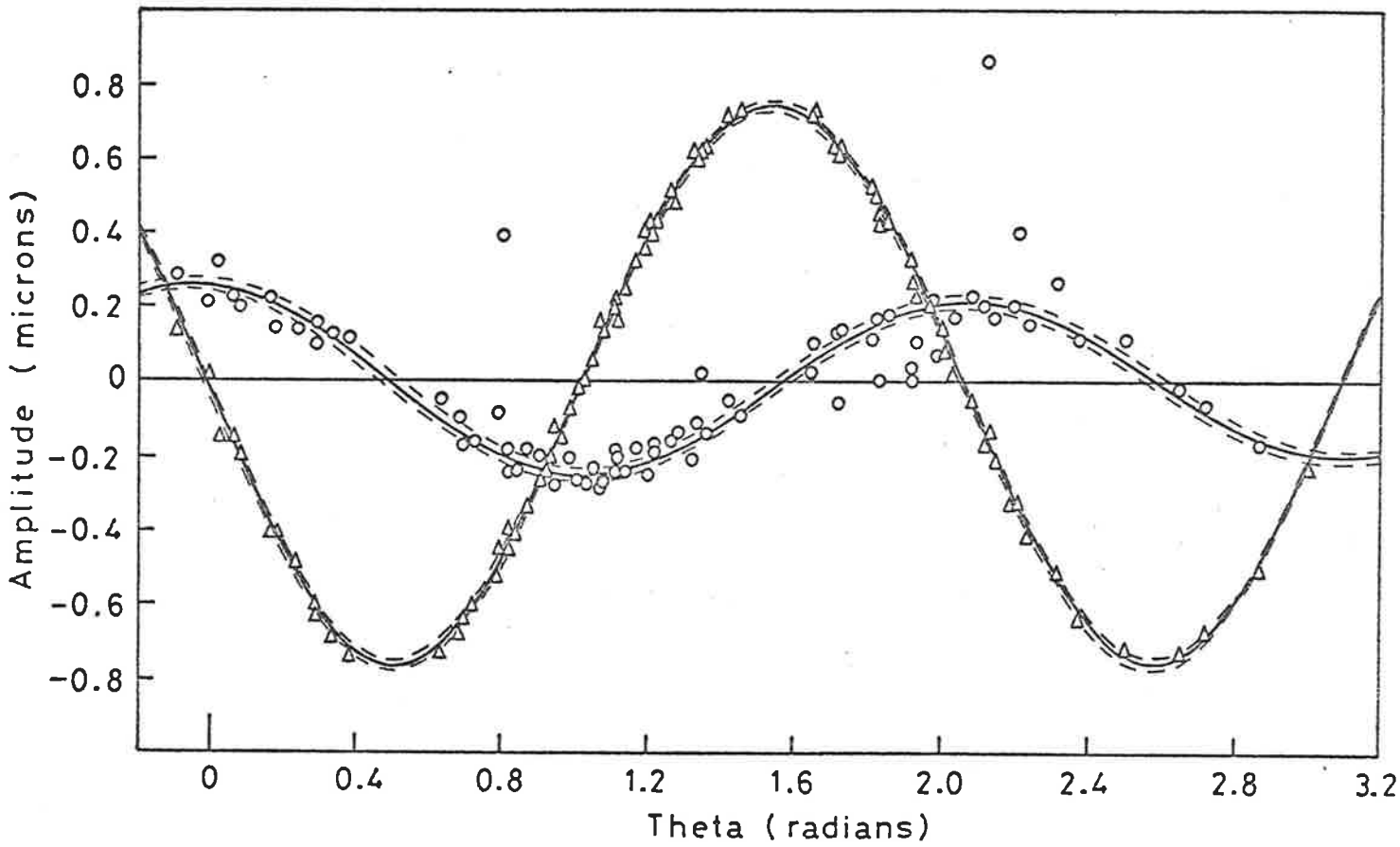

FIG. 3-17 (b) LEAST SQUARES PROCEDURE APPLIED TO DATA OF STAINLESS STEEL BEAKER, $N^1 = 2$, $N^2 = 3$

—— Least squares curves; --- standard deviation; Δ experimentally determined radial component;

o experimentally determined tangential component.

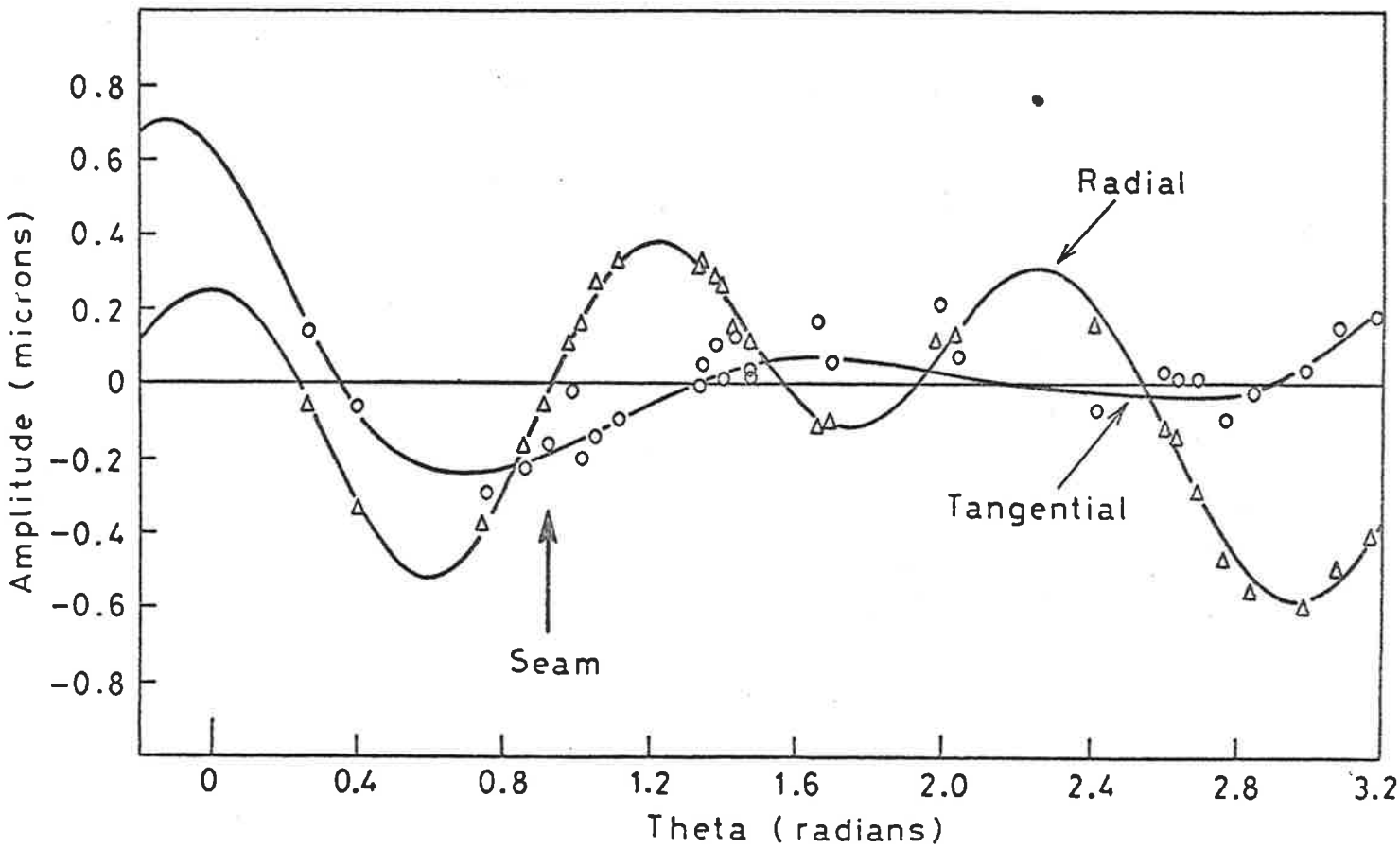

FIG. 3-18 LEAST SQUARES PROCEDURE APPLIED TO DATA OF BRASS CYLINDER WITH A SEAM, $N^1=2$, $N^2=5$

—— Least squares curves; Δ experimentally determined radial component; o experimentally determined tangential component.

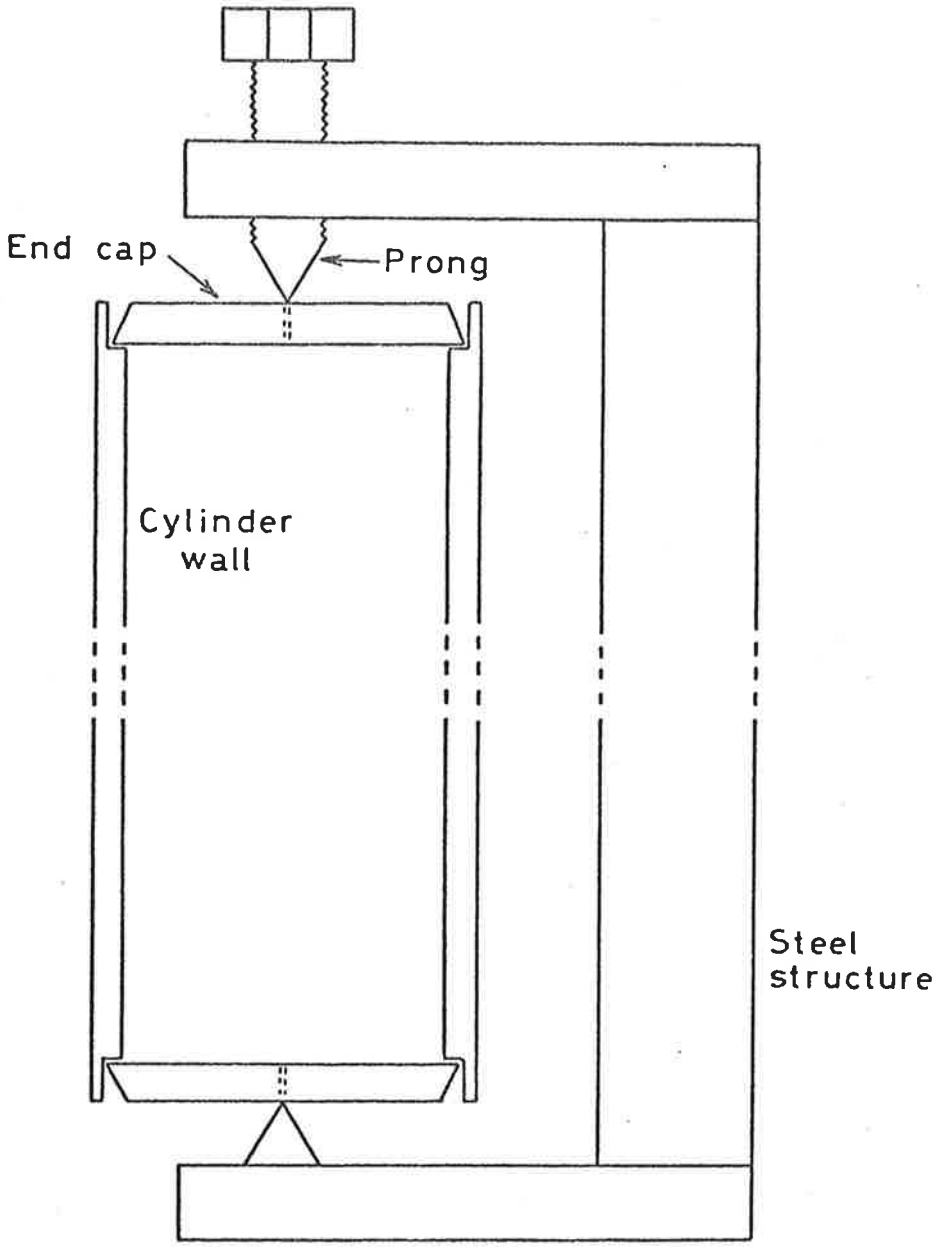

FIG. 3-19 DETAILS OF END MOUNT AND SUPPORT

Table 3-1 lists the physical properties of the cylinders and Tables 3-2 (a) to 3-2 (d) list the theoretical resonant frequencies and the ratios B/C and A/C based on these properties and calculated by the method described in section 3.3.2 using the Reissner - Naghdi - Berry theory. The experimental equipment and experimental method is described in section 2.2 along with the method of analysis.

Figs. 3-20 (a), (b) and (c) show the tangential and radial components of three modes in graphical form for the case where the cylinder is vertical. Figure 3-21 shows two views of time-averaged hologram reconstructions of a small steel cylinder vibrating in the $m = 4$, $n = 3$ mode. Figs. 3-22 (a), (b) and (c) show the longitudinal and radial components of three modes in graphical form for the case where the cylinder is horizontal. Figure 3-23 shows two views of time-averaged hologram reconstructions of a small steel cylinder vibrating in the $m = 2$, $n = 2$ mode. In Fig. 3-22 note that the abcissa labelled "Normalized Length" refers to the distance from the centre of the turntable to any point along the centre axis of the cylinder normalized with respect to the length of the cylinder. There is no need to align the midpoint of the cylinder with the axis of the turntable. The least squares procedure automatically fits the data no matter where the midpoint of the cylinder is.

The solution vector, $\underline{R}$, is calculated for a number of modes of each pipe with $N^1 = N^2$ (i.e. only a single order least squares approximation) and hence the ratios B/C and A/C are determined. Results are shown in parenthesis in Tables 3-2 (a) to 3-2 (d) which are to be compared with the theoretical predictions. The more important sources of error are probably anisotropies in the cylinder, variations in thickness in the cylinder walls, variations in Young's modulus and inaccuracies in the end plates which all contribute to distort the

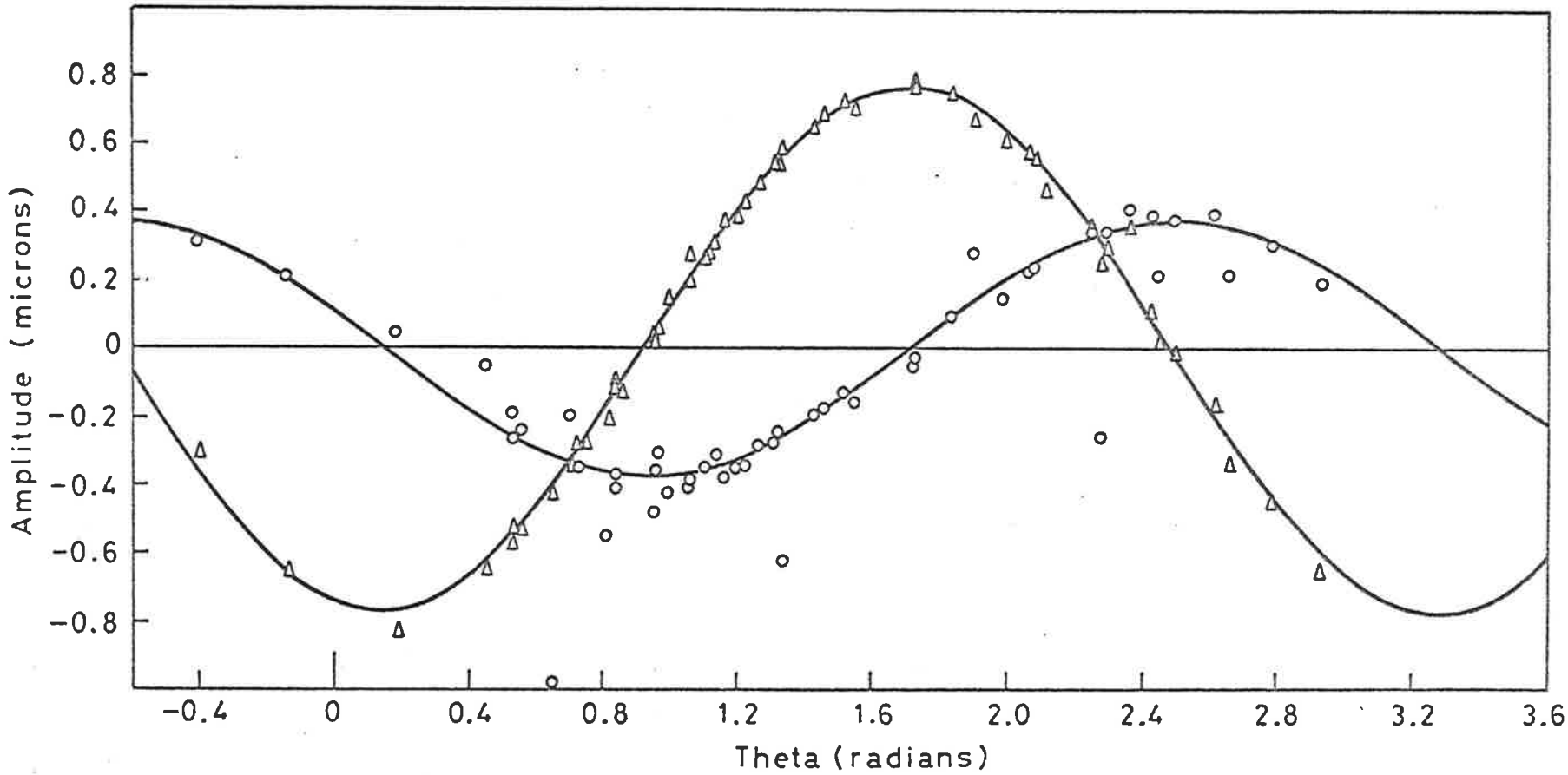

FIG. 3-20 (a) CIRCUMFERENTIAL ORDER N = 2 (SMALL STEEL CYLINDER).

Least Squares Procedure Determination of Radial and Tangential Components of a Circular Cylinder.

Δ Experimentally Determined Radial Component. o Experimentally Determined Tangential Component. ——— Least Squares Curves.

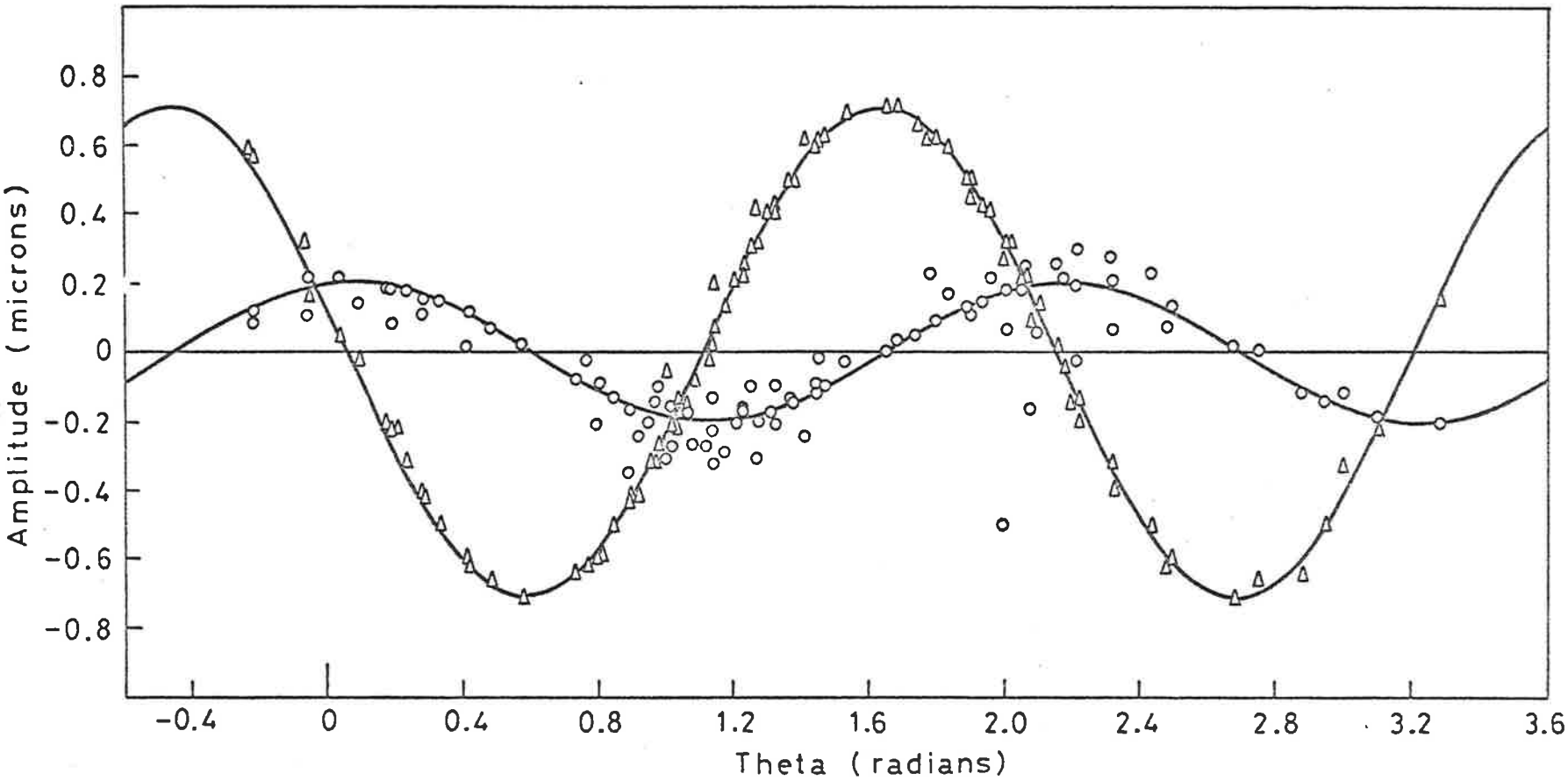

FIG. 3-20 (b) CIRCUMFERENTIAL ORDER N = 3 (SMALL STEEL CYLINDER).

Least Squares Procedure Determination of Radial and Tangential Components of a Circular Cylinder.

Δ Experimentally Determined Radial Component. o Experimentally Determined Tangential Component. ——— Least Squares Curves.

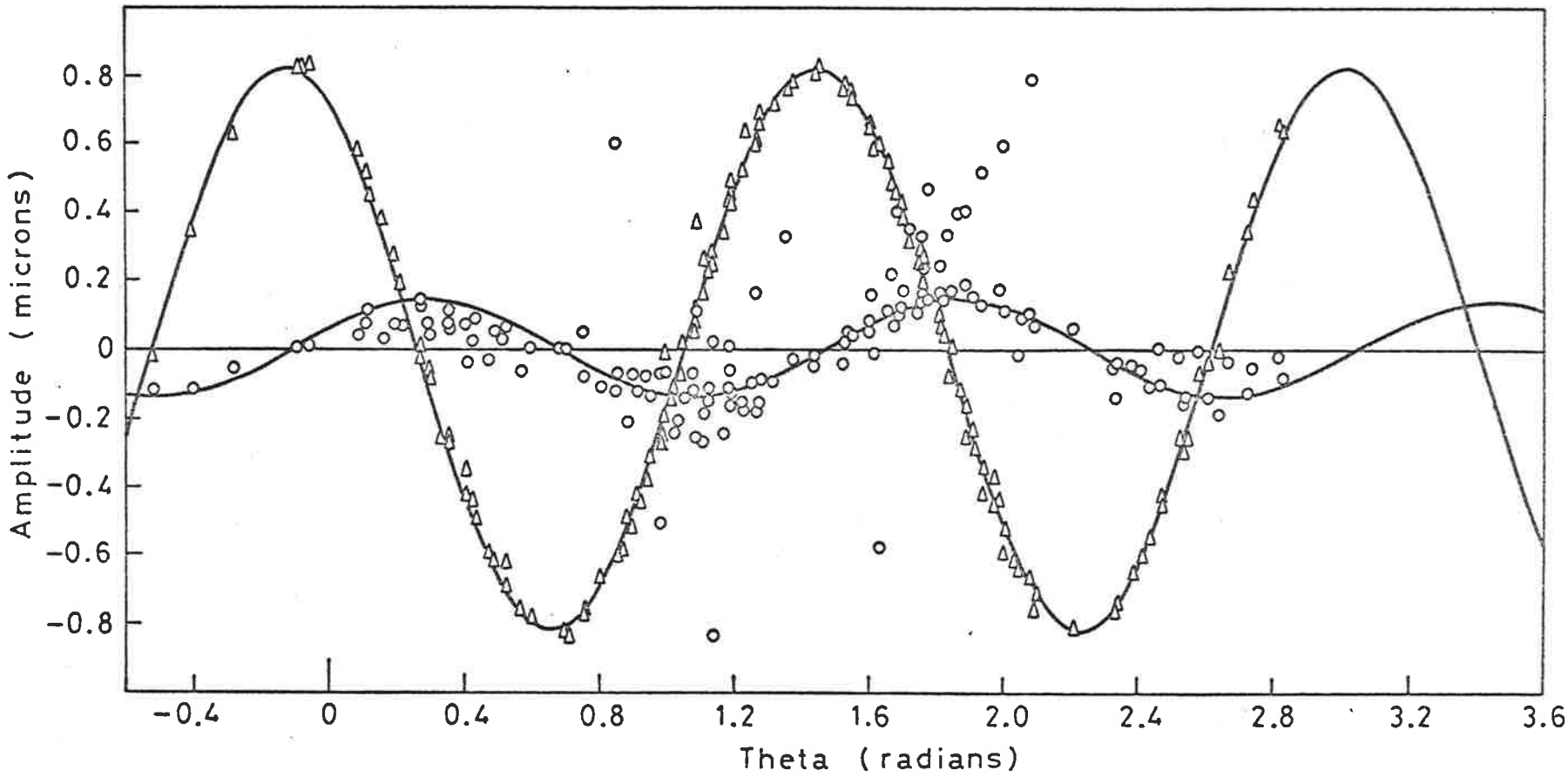

FIG. 3-20 (c) CIRCUMFERENTIAL ORDER N = 4 (SMALL STEEL CYLINDER).

Least Squares Procedure Determination of Radial and Tangential Components of a Circular Cylinder.

Δ Experimentally Determined Radial Component. o Experimentally Determined Tangential Component.

——— Least Squares Curves.

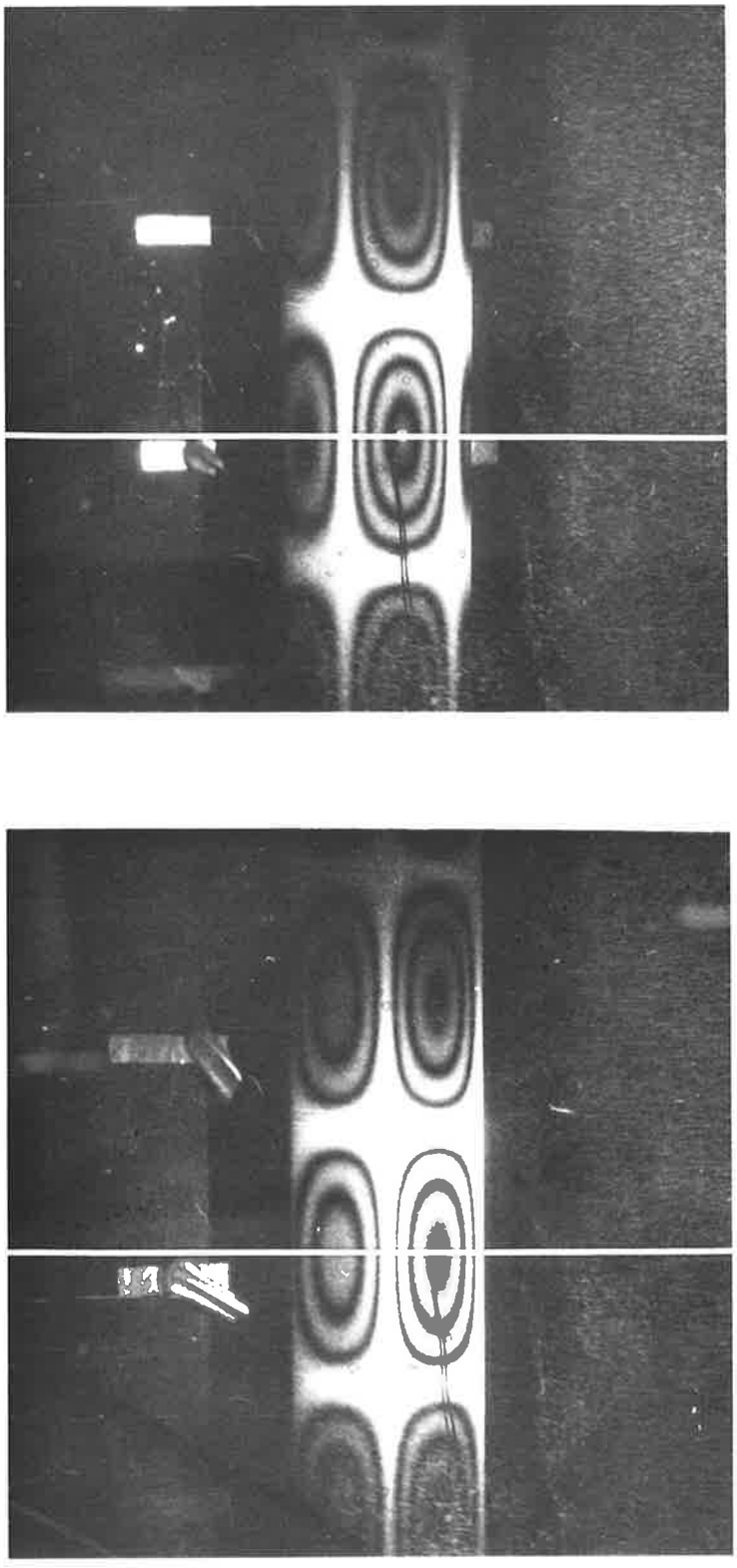

FIG. 3-21

Time-averaged hologram reconstructions of a small steel cylinder vibrating in the $m = 4$, $n = 3$ mode.

The cylinder was rotated 15° between holograms. The white line shows the surface contour along which data points are taken (line of varying ξ).

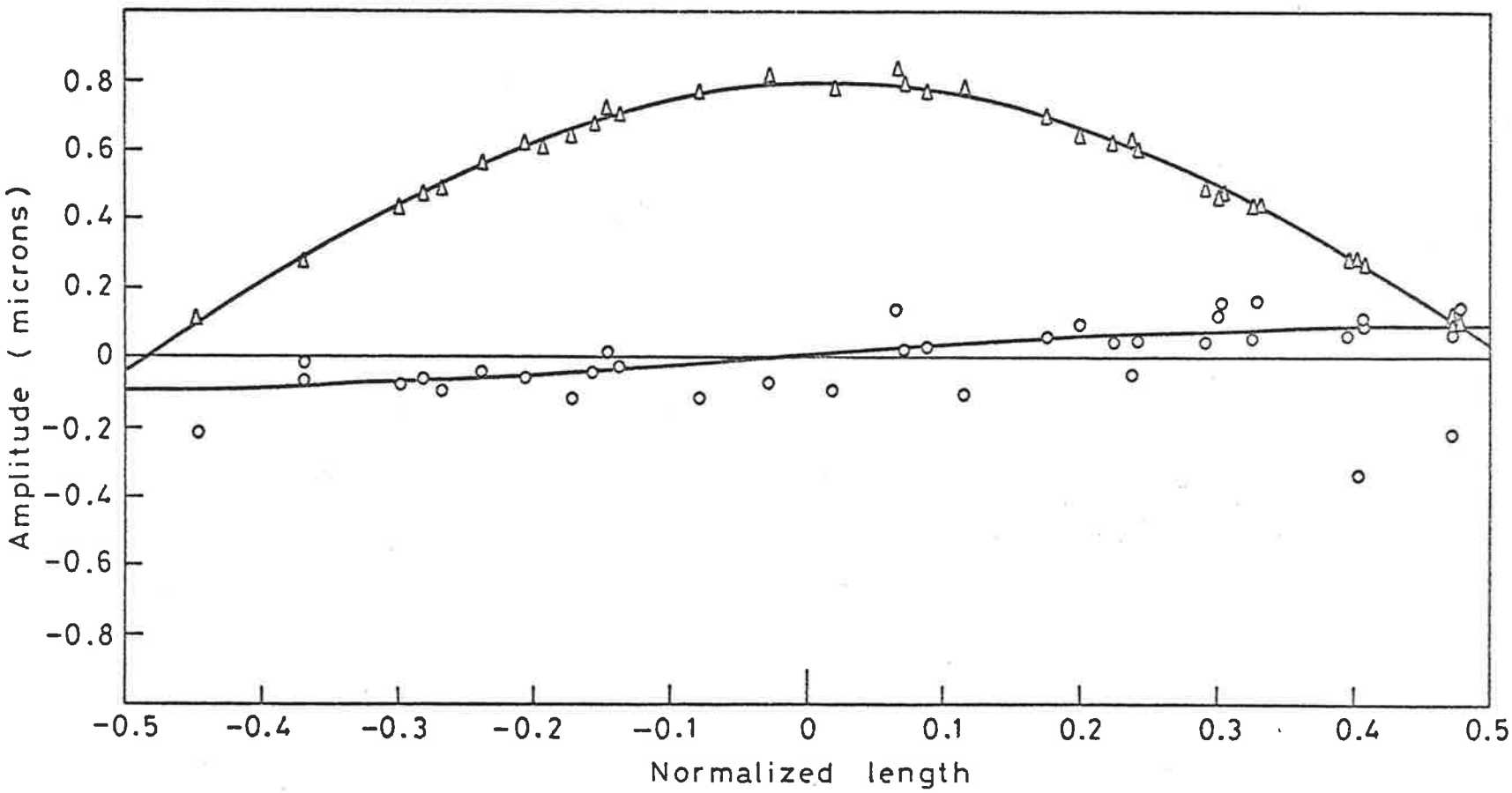

FIG. 3-22 (a) LONGITUDINAL ORDER M = 1 (ALUMINIUM CYLINDER).

Least Squares Procedure Determination of Radial and Longitudinal Components of Circular Cylinder.

Δ Experimentally Determined Radial Component.

o Experimentally Determined Longitudinal Component.

—— Least Squares Curves.

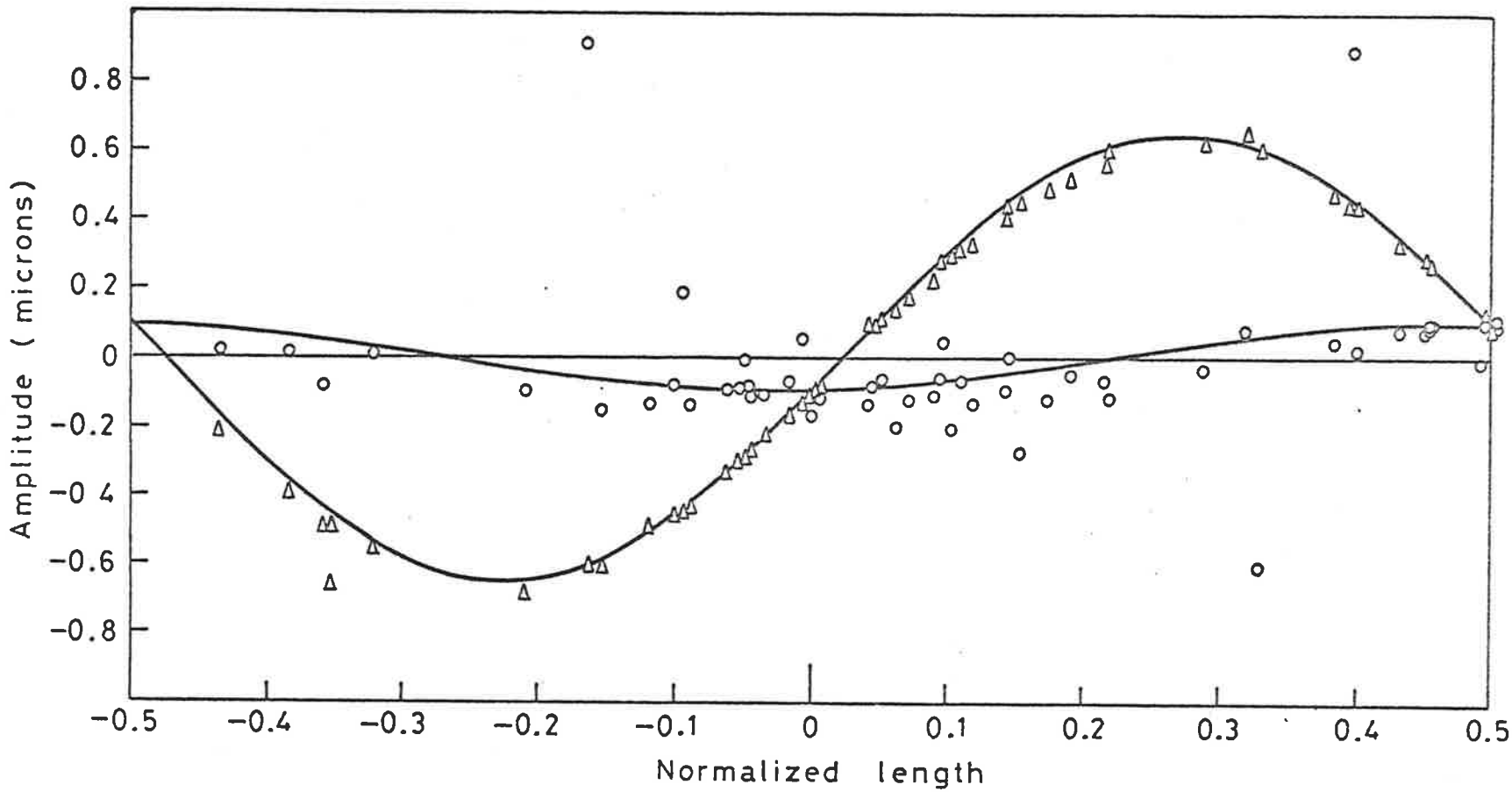

FIG. 3-22 (b) LONGITUDINAL ORDER M = 2 (ALUMINIUM CYLINDER).

Least Squares Procedure Determination of Radial and Longitudinal Components of a Circular Cylinder.

Δ Experimentally Determined Radial Component.

o Experimentally Determined Longitudinal Component.

—— Least Squares Curves.

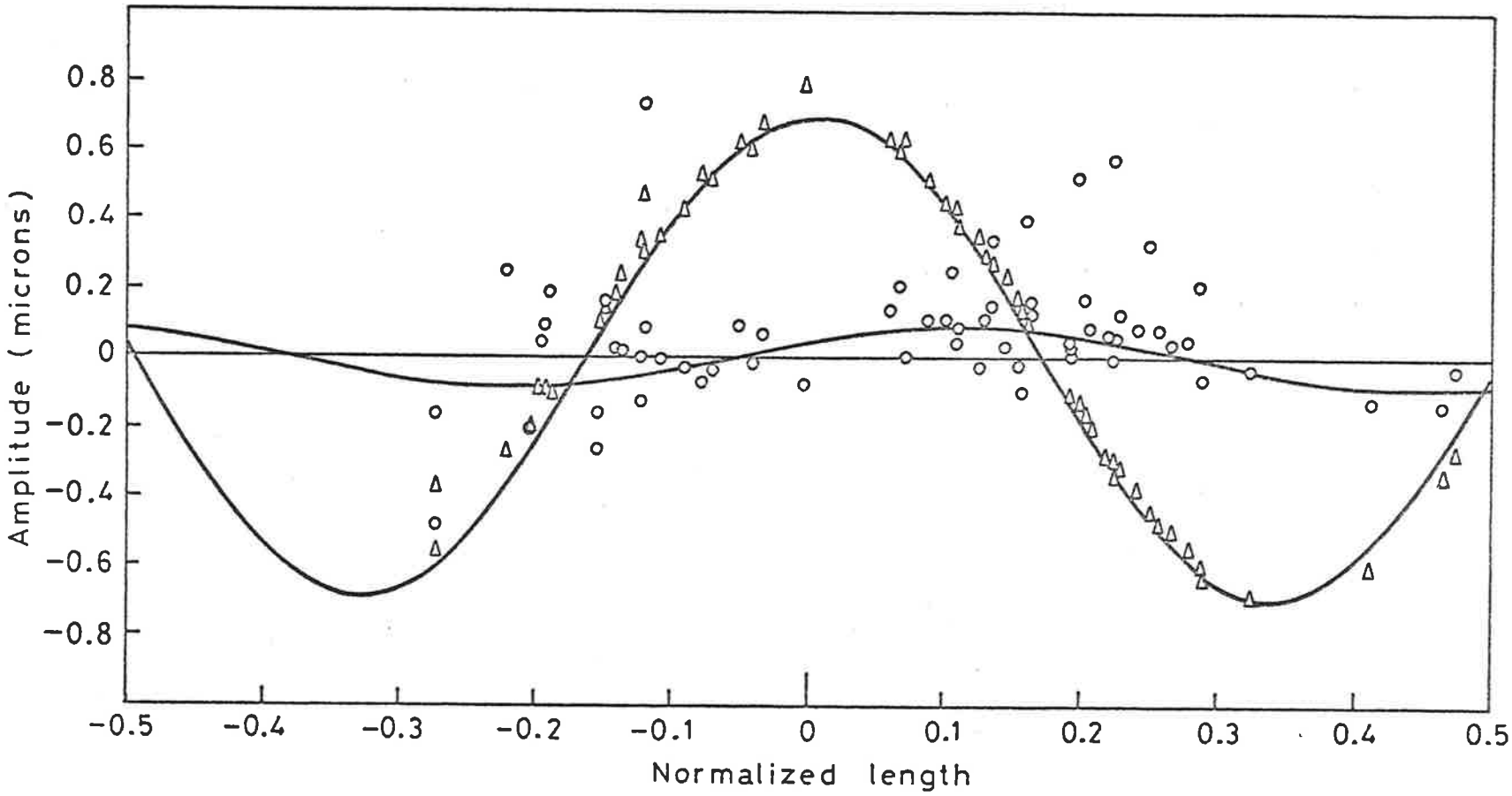

FIG. 3-22 (c) LONGITUDINAL ORDER M = 3 (COPPER CYLINDER).

Least Squares Procedure Determination of Radial and Longitudinal Components of a Circular Cylinder.

Δ Experimentally Determined Radial Component.

o Experimentally Determined Longitudinal Component.

—— Least Squares Curves.

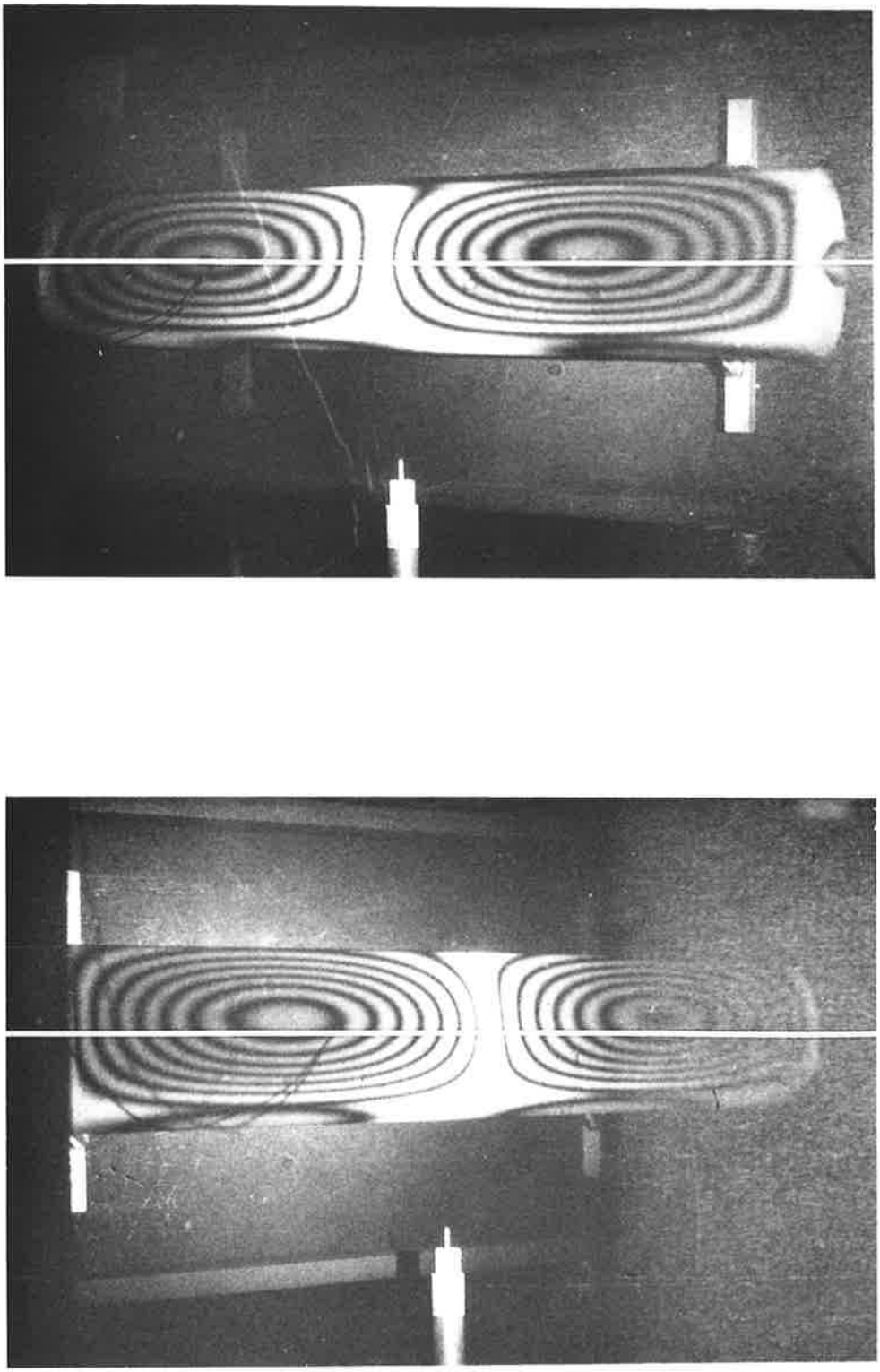

FIG. 3-23

Time-averaged hologram reconstructions of a small steel cylinder vibrating in the $m = 2$, $n = 2$ mode.

The cylinder was rotated 30° between holograms. The white line shows the surface contour along which data points are taken (line of varying ξ).

mode shape. Other factors include the point source excitation which generates coupled spatial modes and spurious effects from the cylinder support. All these factors contribute to modal coupling at a single resonant frequency. Reference to Fig. 3-24 shows how these are accounted for by expanding the least squares procedure into other orders. Fig. 3-24 (a) shows the initial analysis with $N^1 = N^2 = 4$ and Fig. 3-24 (b) shows the improved result with $N^1 = 2$ and $N^2 = 4$ i.e. orders 2, 3 and 4 are present in the second analysis.

Another source of error could be due to internal damping which it is thought causes elliptic motion and needs to be analysed by the more complex procedure described in section 2.1.

Lastly some errors are attributed to the fact that not all surface contours are on the optical plane, especially for the cases where the cylinders are upright. For longitudinal mode numbers $m = 2$ and 4, for example, the surface contours are analysed slightly above or below the optical plane to coincide with the radial antinodes. Hence the geometrical factor Q of equation (2.30) is non-zero.

Reference to Tables 3-2 (a) to 3-2 (d) show that frequencies have been predicted with an accuracy better than 10%. Values of component ratios are not as precise, however, probably due to the reasons outlined above. Nevertheless, the least squares procedure is an invaluable tool for time-averaged holographic analysis of coupled spatial modes and pure modes.

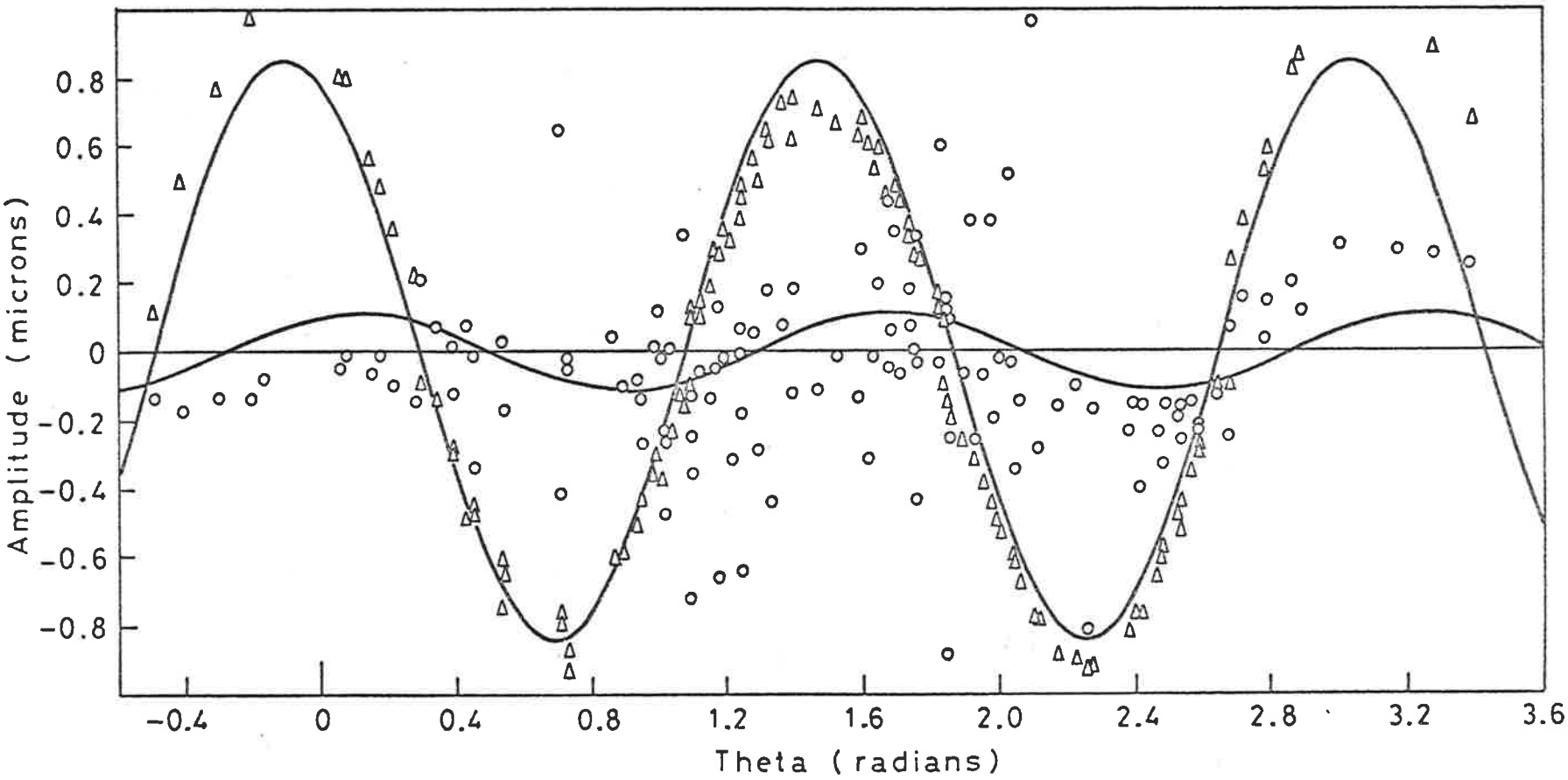

FIG. 3-24 (a) CIRCUMFERENTIAL ORDER N = 4 SINGLE MODE ANALYSIS. (COPPER CYLINDER).

Least Squares Procedure Determination of Radial and Tangential Components of a Circular Cylinder Vibrating in Coupled Modes.

Δ Experimentally Determined Radial Component. o Experimentally Determined Tangential Component.

___ Least Squares Curves.

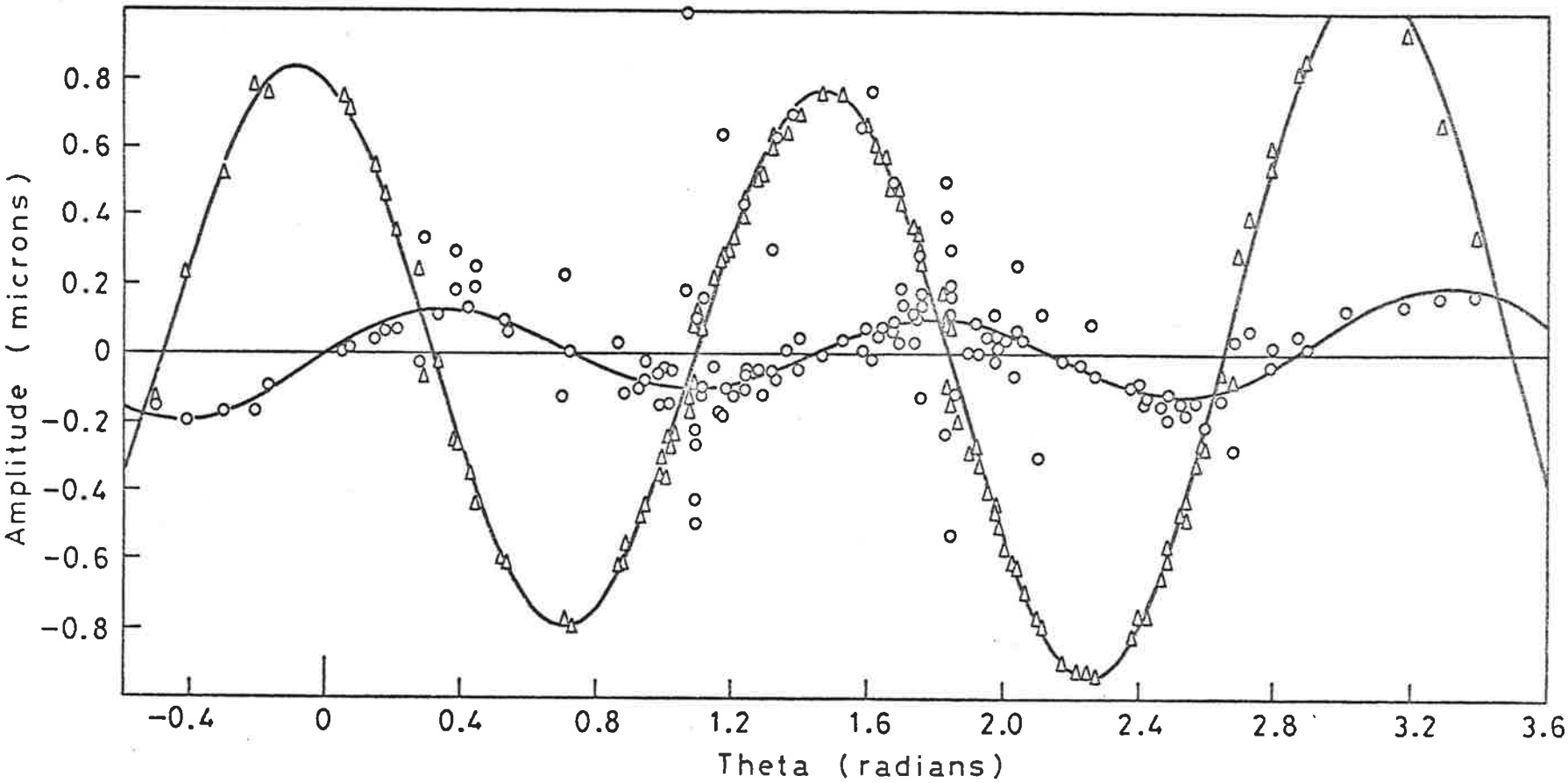

FIG. 3-24 (b) MULTI MODAL ANALYSIS TECHNIQUE $N^1 = 2$ AND $N^2 = 4$. (COPPER CYLINDER).

Least Squares Procedure Determination of Radial and Tangential Components of a Circular Cylinder Vibrating in Coupled Modes.

Δ Experimentally Determined Radial Component. o Experimentally Determined Tangential Component.

—— Least Squares Curves.

TABLE 3-1

PHYSICAL PROPERTIES OF TEST CYLINDERS

Property	Small Steel	Large Steel	Aluminium	Copper
Length (mm)	400	398.5	403.5	402.5
External diameter (mm)	75.1	115.1	91.3	101.6
Wall thickness (mm)	1.2	4.4	1.8	1.7
Poisson Const. ν	0.27	0.27	0.33	0.33
$\frac{E}{\rho} \times 10^{-13}$ (mm^2/sec^2)	2.633	2.633	2.702	1.222

NOTE: Values of ν, E and ρ are due to Faires [161].

TABLE 3-2 (a)

THEORETICAL AND EXPERIMENTAL RESULTS

(EXPERIMENTAL RESULTS IN PARENTHESIS)

SMALL STEEL CYLINDER

		m = 1	m = 2	m = 3
n=2	A/C	.0693 (.1250)	.1213 (.1931)	.1489
	B/C	.5028 (.4851)	.5076 (.4549)	.5086
	FREQ(Hz)	717.4 (714.4)	1649.4 (1587.3)	3194.4
n=3	A/C	.0317 (.0919)	.0596 (.0953)	.0809
	B/C	.3346	.3365 (.2695)	.3385 (.2877)
	FREQ(Hz)	1660.0 (1677.3)	1856.5 (1857.5)	2406.1 (2378.4)
n=4	A/C	.0181 (.0539)	.0349 (.1521)	.0494 (.1581)
	B/C	.2510 (.1707)	.2519 (.1861)	.2531 (.1933)
	FREQ(Hz)	3149.7 (3157.9)	3228.0 (3234.7)	3421.6 (3425.9)

m = axial order, n = circumferential order,

A = longitudinal component, B = tangential component,

C = radial component.

TABLE 3-2 (b)

THEORETICAL AND EXPERIMENTAL RESULTS

(EXPERIMENTAL RESULTS IN PARENTHESIS)

LARGE STEEL CYLINDER

		m = 1	
n = 2	A/C	.0990	(.5161)
	B/C	.5065	(.4765)
	FREQ(Hz)	1159.5	(1073.5)

m = axial order, n = circumferential order, A = longitudinal component, B = tangential component, C = radial component.

TABLE 3-2 (c)

THEORETICAL AND EXPERIMENTAL RESULTS

(EXPERIMENTAL RESULTS IN PARENTHESIS)

ALUMINIUM CYLINDER

	m = 1	m = 2
A/C	.0815 (.1158)	.1346 (.1469)
n = 2 B/C	.5047 (.4717)	.5118 (.4385)
FREQ(Hz)	795.4 (758.9)	1902.1 (1811.2)
A/C	.0378 (.0364)	.0690 (.0952)
n = 3 B/C	.3354 (.2585)	.3387 (.2777)
FREQ(Hz)	1764.4 (1682.3)	2029.0 (1932.0)
A/C	.0217 (.0285)	.0412 (.1406)
n = 4 B/C	.2516 (.1573)	.2532 (.1799)
FREQ(Hz)	3336.2 (3173.1)	3449.8 (3286.7)

m = axial order, n = circumferential order,

A = longitudinal component B = tangential component

C = radial component.

TABLE 3-2 (d)

THEORETICAL AND EXPERIMENTAL RESULTS (EXPERIMENTAL RESULTS IN PARENTHESIS) COPPER CYLINDER

	m = 1	m = 2	m = 3	m = 4	m = 5
	A/C	.0896 (.1422)	.1417	.1513	.1331	.1032
n = 2	B/C	.5055 (.4889)	.5125 (.3173)	.5069	.4835	.4455
	FREQ(Hz)	486.5 (508.3)	1349.4 (1365.0)	2553.9	3821.8	5013.1
	A/C	.0419 (.0512)	.0748 (.0696)	.0942 (.1260)	.1001	.0958
n = 3	B/C	.3355 (.3191)	.3392 (.3116)	.3415 (.2653)	.3393 (.2715)	.3313
	FREQ(Hz)	911.7 (933.9)	1152.8 (1190.2)	1721.6 (1772.9)	2508.7 (2563.7)	3386.3
	A/C	.0241 (.1343)	.0451 (.0390)	.0610 (.0935)	.0708	.0749
n = 4	B/C	.2515 (.2226)	.2534 (.2577)	.2554 (.2457)	.2564 (.1353)	.2554 (.1835)
	FREQ(Hz)	1705.7 (1749.8)	1795.1 (1842.2)	2020.3 (2075.4)	2413.2 (2467.8)	2949.5 (3013.3)
	A/C	.0156 (.2890)	.0300 (.0916)	.0420	.0511	.0570
n = 5	B/C	.2013 (.3225)	.2024 (.1793)	.2038	.2050	.2056
	FREQ(Hz)	2745.0 (2803.4)	2806.0 (2864.8)	2932.8	3147.9	3462.3

m = axial order, n = circumferential order, A = longitudinal component, B = tangential component, C = radial component.

CHAPTER 4

CIRCULAR CYLINDERS WITH VARYING WALL THICKNESS

The least squares procedure has been shown to be a powerful tool for the analysis of vibrations and, in particular, the amplitudes of the superposed spatial modes of any vibrating surface may now be determined. The result that vibration may be expressed as a combination of normal modes has exciting possibilities for the study of vibrating objects with perturbations in some quantity, for example, in the geometry, force or elasticity properties. The Fourier components of the perturbation may be thought of loosely as exciting the corresponding vibration components in the structure although there is no direct relationship between their relative magnitudes. In this chapter the problem posed is the theory for the flexural vibrations of a finite length circular cylinder with shear-diaphragm ends, symmetric thickness variations about the central plane and constant axial thickness. The solution is arrived at using the Rayleigh - Ritz method and the mode shapes so obtained are compared with experiment using the least squares procedure.

4.1 THEORY OF VIBRATION OF CYLINDERS WITH VARYING WALL THICKNESS

The theory to be described considers only thickness variations in the wall of a circular cylinder as in practice these would be the principal sources of anisotropy. The procedure is a three-dimensional extension of the analysis outlined by Hurty and Rubinstein ([136], section 4.5) and uses the Rayleigh-Ritz method to solve the elasticity equations of Arnold and Warburton [126].

Consider a cylindrical shell of length L supported at the

ends by shear-diaphragms (see Fig. 4-1). Assume there exists an unstrained circular middle surface of radius a_o and that the thickness of the shell is symmetrical about the angular co-ordinate $\theta = 0$ and constant along the generator X but whose outer and inner surfaces are independently variable. The outer surface is described by the function $a_2(\theta)$ and the inner surface by $a_1(\theta)$ with the unstrained middle surface as the origin and hence the "outer" thickness and "inner" thickness are respectively

$$\left.\begin{aligned} a_o h^+(\theta) &= a_2(\theta) - a_o \\ a_o h^-(\theta) &= a_1(\theta) - a_o \end{aligned}\right\} \qquad (4.1)$$

These conditions imposed upon the thickness variable serve only to simplify the mathematics as in principle one could solve the elasticity equations for the most general form of thickness variable.

Expressing the thickness variation in terms of a one-dimensional Fourier series gives

$$\left.\begin{aligned} h^+(\theta) &= \sum_p h_p^+ \cos(p\theta) \\ h^-(\theta) &= \sum_p h_p^- \cos(p\theta) \end{aligned}\right\} \qquad (4.2)$$

Clearly, if the unstrained middle surface is to remain circular then $h^+(\theta) = h^-(\theta)$ i.e. the distortion is symmetric about the middle surface. Hence for non-symmetric distortions this analysis will only be valid if the distortion is small whereas for symmetric distortions the only limitations on the theory are those of the Arnold-Warburton theory for the perfect cylinder (i.e. thin walls).

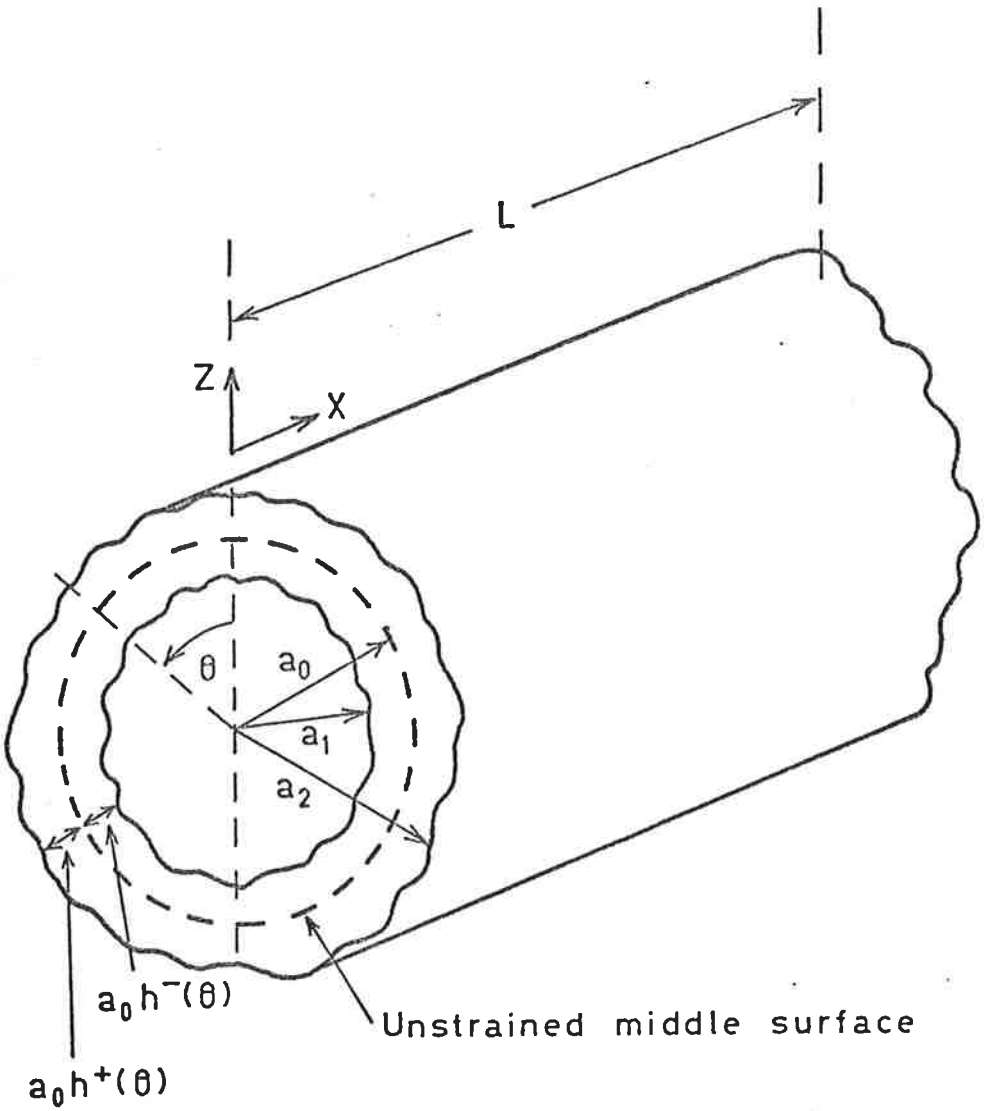

FIG. 4-1: CIRCULAR CYLINDER WITH VARYING ANGULAR WALL THICKNESS.

The symmetric solutions of the longitudinal, tangential and radial components of vibration are assumed to be the sum of the normal modes of a perfect cylinder with no perturbations and are respectively

$$\left.\begin{aligned} a(X,\theta,t) &= \frac{1}{a_o}\sum_{m,n} A_{mn}\cos\frac{\lambda X}{a_o}\cos n\theta\cos\omega t \\ b(X,\theta,t) &= \frac{1}{a_o}\sum_{m,n} B_{mn}\sin\frac{\lambda X}{a_o}\sin n\theta\cos\omega t \\ c(X,\theta,t) &= \frac{1}{a_o}\sum_{m,n} C_{mn}\sin\frac{\lambda X}{a_o}\cos n\theta\cos\omega t \end{aligned}\right\} \qquad (4.3)$$

where, $\lambda = m\pi a_o/L$ is the non-dimensional axial wavelength and (m,n) is the mode of vibration. The asymmetric solutions are obtained by substituting $\sin n\theta$ for $\cos n\theta$ and vice-versa in equations (4.3). The total kinetic energy is [126]

$$T = \frac{\rho a_o^5}{2}\int_o^{2\pi}\int_o^{\frac{L}{a_o}}\int_{h^-}^{h^+}\left[\left(\frac{\partial a}{\partial t}\right)^2 + \left(\frac{\partial b}{\partial t}\right)^2 + \left(\frac{\partial c}{\partial t}\right)^2\right] d\theta\, dX\, dZ \qquad (4.4)$$

where ρ is the density of the cylinder material. It will be useful to note the following

$$\int_{h^-(\theta)}^{h^+(\theta)} dZ = \sum_p (h_p^+ - h_p^-)\cos p\theta \qquad (4.5)$$

and to introduce the following notation

$$\Pi_{k\ell\ldots}^{ij\ldots} = \int_o^{2\pi} \cos iX\cos jX \ldots \sin kX \sin \ell X\, dX, \qquad (4.6)$$

and $U_{ij} = \frac{1}{a_o} A_{ij}\cos\omega t$, $V_{ij} = \frac{1}{a_o} B_{ij}\cos\omega t$, $W_{ij} = \frac{1}{a_o} C_{ij}\cos\omega t$ (4.7)

Substituting equations (4.3) into equation (4.4), making use of equations (4.5), (4.6) and (4.7) then considering the first kinetic energy term of equation (4.4)

$$T_1^s = \frac{\rho a_o^5}{2} \int_o^{2\pi} \int_o^{\frac{L}{a_o}} \int_{h^-(\theta)}^{h^+(\theta)} \left(\frac{\partial a}{\partial t} \right)^2 \, d\theta \, dX \, dZ \tag{4.8}$$

where

$$a = \sum_{mn} U_{mn} \cos \frac{\lambda X}{a_o} \cos n\theta \tag{4.9}$$

and the superscript s indicates symmetric solutions. Hence,

$$T_1^s = \frac{\rho a_o^5}{2} \int_o^{2\pi} \int_o^{\frac{L}{a_o}} \int_{h^-(\theta)}^{h^+(\theta)} \left[\sum_{mn} \dot{U}_{mn} \cos \frac{\lambda X}{a_o} \cos n\theta \right]^2 d\theta \, dX \, dZ \tag{4.10}$$

and the general term in T_1^s is

$$\frac{\rho a_o^5}{2} \int_o^{2\pi} \dot{U}_{ij} \dot{U}_{k\ell} \cos n_j \theta \cos n_\ell \theta \cos p\theta (h_p^+ - h_p^-) \, d\theta$$

$$x \int_o^{\frac{L}{a_o}} \cos \frac{\lambda_i X}{a_o} \cos \frac{\lambda_k X}{a_o} \cdot dX \tag{4.11}$$

Noting that

$$\int_o^{\frac{L}{a_o}} \cos \frac{\lambda_i X}{a_o} \cos \frac{\lambda_k X}{a_o} \, dX = \begin{cases} 0 & i \neq k \\ L/2a_o & i = k \end{cases} \tag{4.12}$$

due to the orthogonality of the cosine functions, then the general term in T_1^s becomes

$$\frac{\rho a_o^5}{2} \cdot \frac{L}{2a_o} \cdot \dot{U}_{ij} \dot{U}_{i\ell} (h_p^+ - h_p^-) \int_o^{2\pi} \cos n_j \theta \cos n_\ell \theta \cos p\theta \, d\theta \tag{4.13}$$

Using the notation of equation (4.6)

$$T_1^s = \frac{\rho a_o^4 L}{4} \sum_{ij\ell p} \dot{U}_{ij} \dot{U}_{i\ell} (h_p^+ - h_p^-) \Pi^{j\ell p} \tag{4.14}$$

where the following notation has been used.

$$\sum_{ij\ell p} = \sum_i \sum_j \sum_\ell \sum_p \tag{4.15}$$

The second kinetic energy term of equation (4.4) is

$$T_2^s = \frac{\rho a_o^5}{2} \int_o^{2\pi} \int_o^{\frac{L}{a_o}} \int_{h^-(\theta)}^{h^+(\theta)} \left(\frac{\partial b}{\partial t}\right)^2 \, d\theta \, dX \, dZ \tag{4.16}$$

where
$$b = \sum_{mn} V_{mn} \sin \frac{\lambda X}{a_o} \sin n\theta \tag{4.17}$$

Hence
$$T_2^s = \frac{\rho a_o^5}{2} \int_o^{2\pi} \int_o^{\frac{L}{a_o}} \int_{h^-(\theta)}^{h^+(\theta)} \left[\sum_{mn} \dot{V}_{mn} \sin \frac{\lambda X}{a_o} \sin n\theta \right]^2 d\theta \, dX \, dZ \tag{4.18}$$

The general term in T_2^s is

$$\frac{\rho a_o^5}{2} \int_o^{2\pi} \dot{V}_{ij} V_{k\ell} \sin n_j\theta \sin n_\ell\theta \cos p\theta \, (h_p^+ - h_p^-) \, d\theta$$

$$\times \int_o^{\frac{L}{a_o}} \sin \frac{\lambda_i X}{a_o} \sin \frac{\lambda_k X}{a_o} \cdot dX \tag{4.19}$$

and using the identity

$$\int_o^{\frac{L}{a_o}} \sin \frac{\lambda_i X}{a_o} \sin \frac{\lambda_k X}{a_o} \, dX = \begin{cases} 0 & i \neq k \\ L/2a_o & i = k \end{cases} \tag{4.20}$$

due to the orthogonality of the sine functions, then

$$T_2^s = \frac{\rho a_o^4 L}{4} \sum_{ij\ell p} \dot{V}_{ij} \dot{V}_{i\ell} (h_p^+ - h_p^-) \Pi^p_{j\ell} \tag{4.21}$$

The equation in W is solved in a similar way. Hence the total expression for the kinetic energy for the symmetric solutions is

$$T^s = \frac{\rho a_o^4 L}{4} \sum_{ij\ell p} (\dot{U}_{ij} \dot{U}_{i\ell} \Pi^{j\ell p} + \dot{V}_{ij} \dot{V}_{i\ell} \Pi^p_{j\ell} + \dot{W}_{ij} \dot{W}_{i\ell} \Pi^{j\ell p})(h_p^+ - h_p^-) \tag{4.22}$$

and for the asymmetric solutions,

$$T^a = \frac{\rho a_o^4 L}{4} \sum_{ij\ell p} (\dot{U}_{ij} \dot{U}_{i\ell} \Pi^p_{j\ell} + \dot{V}_{ij} \dot{V}_{i\ell} \Pi^{j\ell p} + \dot{W}_{ij} \dot{W}_{i\ell} \Pi^p_{j\ell})(h_p^+ - h_p^-) \tag{4.23}$$

The total strain energy with the cylinder in vibration is [126]

$$St = \frac{E a_o^3}{2(1-\nu^2)} \int_o^{2\pi} \int_o^{\frac{L}{a_o}} \int_{h^-}^{h^+} \left\{ \left(\frac{\partial a}{\partial X}\right)^2 - 2Z \frac{\partial a}{\partial X} \frac{\partial^2 c}{\partial X^2} + Z^2 \left(\frac{\partial^2 c}{\partial X^2}\right)^2 + \right.$$

$$+ \left(\frac{\partial b}{\partial \theta}\right)^2 - 2c\frac{\partial b}{\partial \theta} + c^2 - 2Z\left(\frac{\partial b}{\partial \theta} - c\right)\left(\frac{\partial^2 c}{\partial \theta^2} + \frac{\partial b}{\partial \theta}\right) + Z^2 \left(\frac{\partial^2 c}{\partial \theta^2}\right)^2 +$$

$$+ 2Z^2 \frac{\partial^2 c}{\partial \theta^2} \frac{\partial b}{\partial \theta} + Z^2 \left(\frac{\partial b}{\partial \theta}\right)^2 + 2\nu \left[\left(\frac{\partial a}{\partial X} - Z\frac{\partial^2 c}{\partial X^2}\right)\left(\frac{\partial b}{\partial \theta} - c - Z\frac{\partial^2 c}{\partial \theta^2} - Z\frac{\partial b}{\partial \theta}\right)\right] +$$

$$+ \frac{(1-\nu)}{2} \left[\left(\frac{\partial b}{\partial X}\right)^2 + 2\frac{\partial b}{\partial X}\frac{\partial a}{\partial \theta} + \left(\frac{\partial a}{\partial \theta}\right)^2 - 4Z\left(\frac{\partial b}{\partial X} + \frac{\partial a}{\partial \theta}\right)\left(\frac{\partial^2 c}{\partial X \partial \theta} + \frac{\partial b}{\partial X}\right) + \right.$$

$$\left. \left. + 4Z^2 \left(\left(\frac{\partial^2 c}{\partial X \partial \theta}\right)^2 + 2\frac{\partial^2 c}{\partial X \partial \theta}\frac{\partial b}{\partial X} + \left(\frac{\partial b}{\partial X}\right)^2\right)\right] \right\} d\theta\, dX\, dZ \tag{4.24}$$

where E is Young's Modulus and ν is Poisson's ratio. Again making use of equations (4.3), (4.5), (4.6), (4.7) and (4.15) the integral is evaluated and equation (4.24) reduces to

$$St = \frac{E a_o^2 L}{(1-\nu^2)} \sum_{j=1}^{31} St_j \tag{4.25}$$

The thirty one terms in the summation are given in Appendix III for the symmetric St^s and asymmetric St^a modes of vibration.

Application of Lagranges equation to the independent variables U, V and W gives

$$\frac{d}{dt}\left(\frac{\partial T}{\partial \dot{U}_{mn}}\right) - \frac{\partial T}{\partial U_{mn}} = -\frac{\partial St}{\partial U_{mn}} \tag{4.26}$$

and two similar equations in V_{mn} and W_{mn}. Using equation (4.22)

$$\frac{\partial T^s}{\partial \dot{U}_{mn}} = \frac{\rho a_o^4 L}{2} \sum_{jp} \dot{U}_{mj}(h_p^+ - h_p^-)\Pi^{njp} \tag{4.27}$$

and

$$\frac{d}{dt}\left(\frac{\partial T^s}{\partial \dot{U}_{mn}}\right) = \frac{\rho a_o^4 L}{2} \sum_{jp} \ddot{U}_{mj}(h_p^+ - h_p^-)\Pi^{njp} \tag{4.28}$$

From equation (4.7)

$$\ddot{U}_{mj} = -\omega^2 U_{mj} \tag{4.29}$$

hence

$$\frac{d}{dt}\left(\frac{\partial T^s}{\partial \dot{U}_{mn}}\right) = \frac{-\rho a_o^4 L\omega^2}{2} \sum_{jp} U_{mj}(h_p^+ - h_p^-)\Pi^{njp} \tag{4.30}$$

Similarly

$$\frac{d}{dt}\left(\frac{\partial T^s}{\partial \dot{V}_{mn}}\right) = \frac{-\rho a_o^4 L\omega^2}{2} \sum_{jp} V_{mj}(h_p^+ - h_p^-)\Pi^{p}_{nj} \tag{4.31}$$

and

$$\frac{d}{dt}\left(\frac{\partial T^s}{\partial \dot{W}_{mn}}\right) = \frac{-\rho a_o^4 L\omega^2}{2} \sum_{jp} W_{mj}(h_p^+ - h_p^-)\, \Pi^{njp} \tag{4.32}$$

Corresponding equations for the asymmetric solutions are easily written. Noting that

$$\frac{\partial T}{\partial U_{mn}} = \frac{\partial T}{\partial V_{mn}} = \frac{\partial T}{\partial W_{mn}} = 0 \tag{4.33}$$

completes the left hand side of equation (4.26). The right hand side is evaluated in a similar way where for the first strain energy term shown in Appendix III

$$\left.\begin{aligned} \frac{\partial St_1^s}{\partial U_{mn}} &= \tfrac{1}{2} \sum_{jp} \lambda_m^2 U_{mj}(h_p^+ - h_p^-)\, \Pi^{njp} \\ \frac{\partial St_1^s}{\partial V_{mn}} &= \frac{\partial S_1^s}{\partial W_{mn}} = 0 \end{aligned}\right\} \tag{4.34}$$

and for the second

$$\left.\begin{aligned} \frac{\partial S_2^s}{\partial U_{mn}} &= -\tfrac{1}{4} \sum_{jpq} \lambda_m^3 W_{mj}(h_p^+ h_q^+ - h_p^- h_q^-)\Pi^{njpq} \\ \frac{\partial S_2^s}{\partial V_{mn}} &= 0 \\ \frac{\partial S_2^s}{\partial W_{mn}} &= -\tfrac{1}{4} \sum_{jpq} \lambda_m^3 U_{mj}(h_p^+ h_q^+ - h_p^- h_q^-)\, \Pi^{njpq} \end{aligned}\right\} \tag{4.35}$$

and so on for the other terms.

Defining the frequency parameter Λ by

$$\Lambda^2 = \rho a_o^2 \omega^2 (1 - \nu^2)/E \tag{4.36}$$

then the three Lagrange equations of the form of equation (4.26) become

$$\underline{D}\,\underline{R} = \Lambda^2\,\underline{Q}\,\underline{R} \tag{4.37}$$

where $\underline{D}$ and $\underline{Q}$ are the generalized stiffness and mass matrices respectively and $\underline{R}$ is the vector of coefficients of order $3M(N+1)$, where M and N are the limiting orders to which the analysis is taken, and is defined as

$$\left.\begin{aligned} R[3(k-1)(N+1) + i + 1] &= A_{ki} \\ R[3(k-1)(N+1) + i + N + 2] &= B_{ki} \\ R[3(k-1)(N+1) + i + 2N + 3] &= C_{ki} \end{aligned}\right\} \tag{4.38}$$

where $k = 1, \ldots, M$ and $i = 0, \ldots, N$.

The matrices $\underline{D}$ and $\underline{Q}$ are $3M(N+1)$ square matrices with non-zero coefficients about the leading diagonal and zero coefficients elsewhere. Listed in Appendix IV are the coefficients of these matrices for both the symmetric and asymmetric solutions and Appendix V lists the solutions of the Π functions of the form shown in equation (4.6).

Equation (4.37) is simply an eigen-value problem and may be solved by expressing $\underline{D}$ in upper Hessenberg form and $\underline{Q}$ in upper triangular form [162]. To each of the $3M(N+1)$ eigen-values there corresponds an eigen-vector which defines the component amplitudes of the contributing modes. The corresponding resonant frequency is calculated from the eigen-value using equation (4.36).

As in the classical solution for the vibration of a non-distorted cylinder there corresponds three solutions or eigen-vectors for each mode. In two cases the longitudinal components and tangential components contribute mostly to the vibration and the frequencies are

usually very high (well out of the audio range). In the third case the radial component is the largest and the frequencies for the lowest modes are well within the audio range. Although the present analysis solves for all the modes, the only ones of interest to this study are the M(N + 1) modes with the lowest frequency parameters. Also, since a number of modes contribute to the vibration, reference to a single mode hereafter is taken to mean the principal mode unless otherwise qualified.

However equation (4.37) cannot be solved in its existing form. For the symmetric case N = 0 the cylinder is vibrating in a breathing mode and hence the tangential component b is zero. Hence there are M columns in matrices D and Q which are zero corresponding to the zero coefficients V_{10}, V_{20},..., V_{MO} which must be removed else the solution to equation (4.37) is trivial. The corresponding rows created by differentiation with respect to these coefficients ($\partial/\partial V_{10}$, $\partial/\partial V_{20}$,..., $\partial/\partial V_{MO}$) must also be removed. Hence matrices $\underline{D}$ and $\underline{Q}$ and vector $\underline{R}$ are reduced to order M(3N + 2). For the asymmetric case N = 0 the cylinder vibrates in a purely twisting mode and the longitudinal and radial components a and c are zero. The 2M columns in matrices $\underline{D}$ and $\underline{Q}$ corresponding to U_{10}, U_{20},...,U_{MO} and W_{10}, W_{20}, ..., W_{MO} and the corresponding rows which are created by differentiation with respect to these coefficients are removed resulting in the matrices and vector $\underline{R}$ having order M(3N + 1).

4.2 CYLINDER WITH NON-CONCENTRIC BORE

A circular cylinder with a non-concentric bore is one of the simplest symmetric distortions and can be readily manufactured. The Fourier coefficients of the distortion are calculated as follows. Reference to Fig. 4-2 shows that if the radius of the inner bore is a_1, the radius of the outer surface a_2, the radius of the unstrained

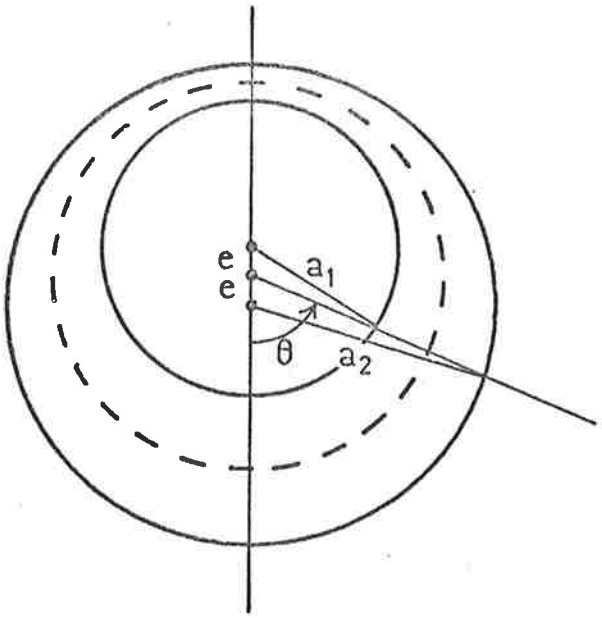

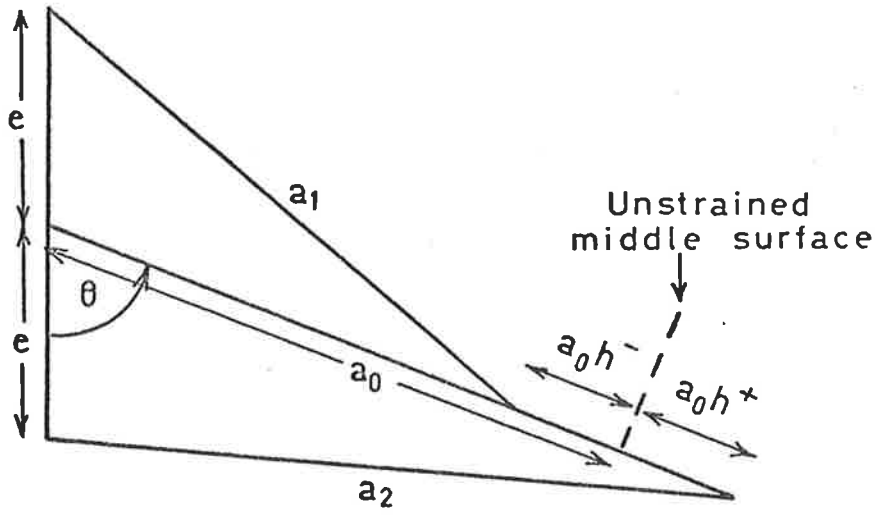

FIG. 4-2: GEOMETRY FOR CALCULATING THE FOURIER COEFFICIENTS OF THE DISTORTION.

middle surface a_o and the displacement of the centres e then

$$\left.\begin{aligned} a_1^2 &= e^2 + a_o^2(1+h^-)^2 + 2\,e\,a_o\,(1+h^-)\cos\theta \\ a_2^2 &= e^2 + a_o^2(1+h^+)^2 - 2\,e\,a_o(1+h^+)\cos\theta \end{aligned}\right\} \qquad (4.39)$$

Hence,

$$\left.\begin{aligned} a_o h^-(\theta) &= -e\cos\theta + (e^2\cos^2\theta - e^2 + a_1^2)^{\frac{1}{2}} - a_o \\ a_o h^+(\theta) &= e\cos\theta + (e^2\cos^2\theta - e^2 + a_2^2)^{\frac{1}{2}} - a_o \end{aligned}\right\} \qquad (4.40)$$

The Fourier coefficients are thus

$$\left.\begin{aligned} h_o^- &= \frac{1}{2\pi}\int_{-\pi}^{\pi} h^-(\theta)\,d\theta \\ h_o^+ &= \frac{1}{2\pi}\int_{-\pi}^{\pi} h^+(\theta)\,d\theta \qquad \text{for } p = 0 \end{aligned}\right\} \qquad (4.41)$$

and

$$\left.\begin{aligned} h_p^- &= \frac{1}{\pi}\int_{-\pi}^{\pi} h^-(\theta)\cos p\theta\,d\theta \\ h_p^+ &= \frac{1}{\pi}\int_{-\pi}^{\pi} h^+(\theta)\cos p\theta\,d\theta \qquad \text{for } p > 0 \end{aligned}\right\} \qquad (4.42)$$

which are evaluated numerically as the integrals are difficult to solve explicitly.

A steel cylinder was fabricated with dimensions a_o = 39.29mm, a_1 = 37.83mm, a_2 = 40.75mm, e = 0.5mm and L = 398.8mm. The ends of the

cylinder were machined flat with a lip on the inside edge which coincides with the unstrained middle surface. Two 1.6mm sheet steel end caps, with the circumference machined to a thin edge, fit into the lip one on each end of the cylinder (see Fig. 3-19) which satisfies the requirements of shear-diaphragm end conditions. Two electromagnets were positioned at $\theta = \pi$ or the thinnest part of the cylinder and near the ends of the cylinder and the techniques of section 2.2 applied to excite and analyse the modes of vibration.

The frequencies of the symmetric modes were experimentally measured using a frequency counter and these are shown in Table 4-1 together with the theoretically calculated frequencies for the symmetric modes. Also shown for comparison are the theoretical resonant frequencies for the same modes but with no distortion. This data is shown in graphical form in Fig. 4-3 from which it is clear that increasing distortion lowers the frequencies of the modes but only for this type of distortion. In general the distortion may lower or raise the resonant frequencies of the modes [139].

The modes were identified with the aid of a flexible plastic tube functioning as a stethoscope. The antinodes and nodes could be easily detected from the loudness of the tone as the tube is moved over the surface of the cylinder. Table 4-1 shows the experimental error in the frequencies to be less than 2% due principally to inaccuracies in machining. Other modes could not be excited due to limitations of the electromagnetic drivers.

The frequencies of the asymmetric solutions are shown in graphical form in Fig. 4-4. These are little different to, except for large distortions, the frequencies of the symmetric modes and the difference is greatest for the lowest axial and circumferential orders.

Table 4-2 shows the theoretical superposed symmetric modes

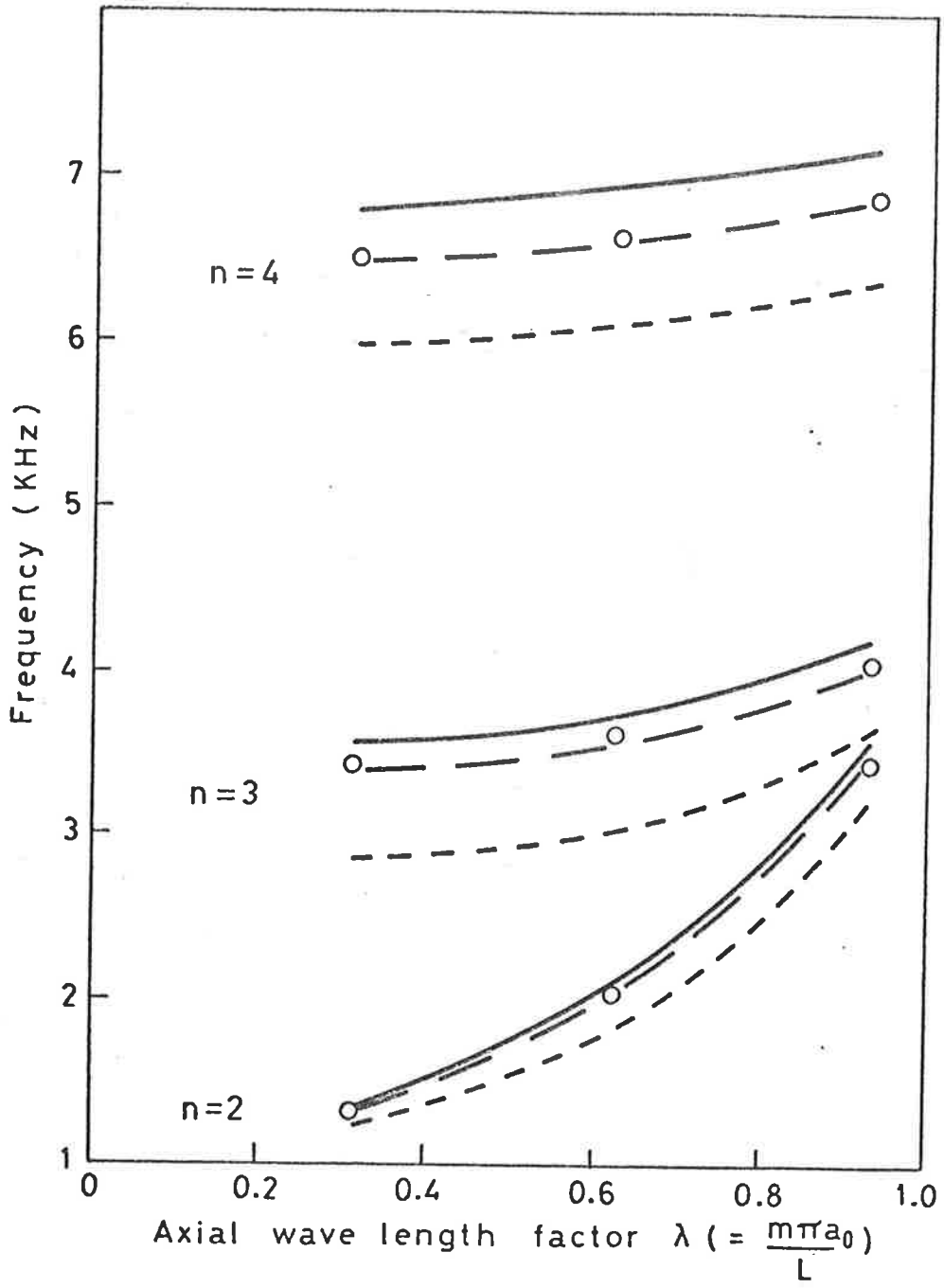

FIG. 4-3 THEORETICAL FREQUENCY CURVES FOR DISTORTED CYLINDER. Symmetric solutions. —— e = 0, ——— e = 0.5, --- e = 1.0, o experimental points for case e = 0.5.

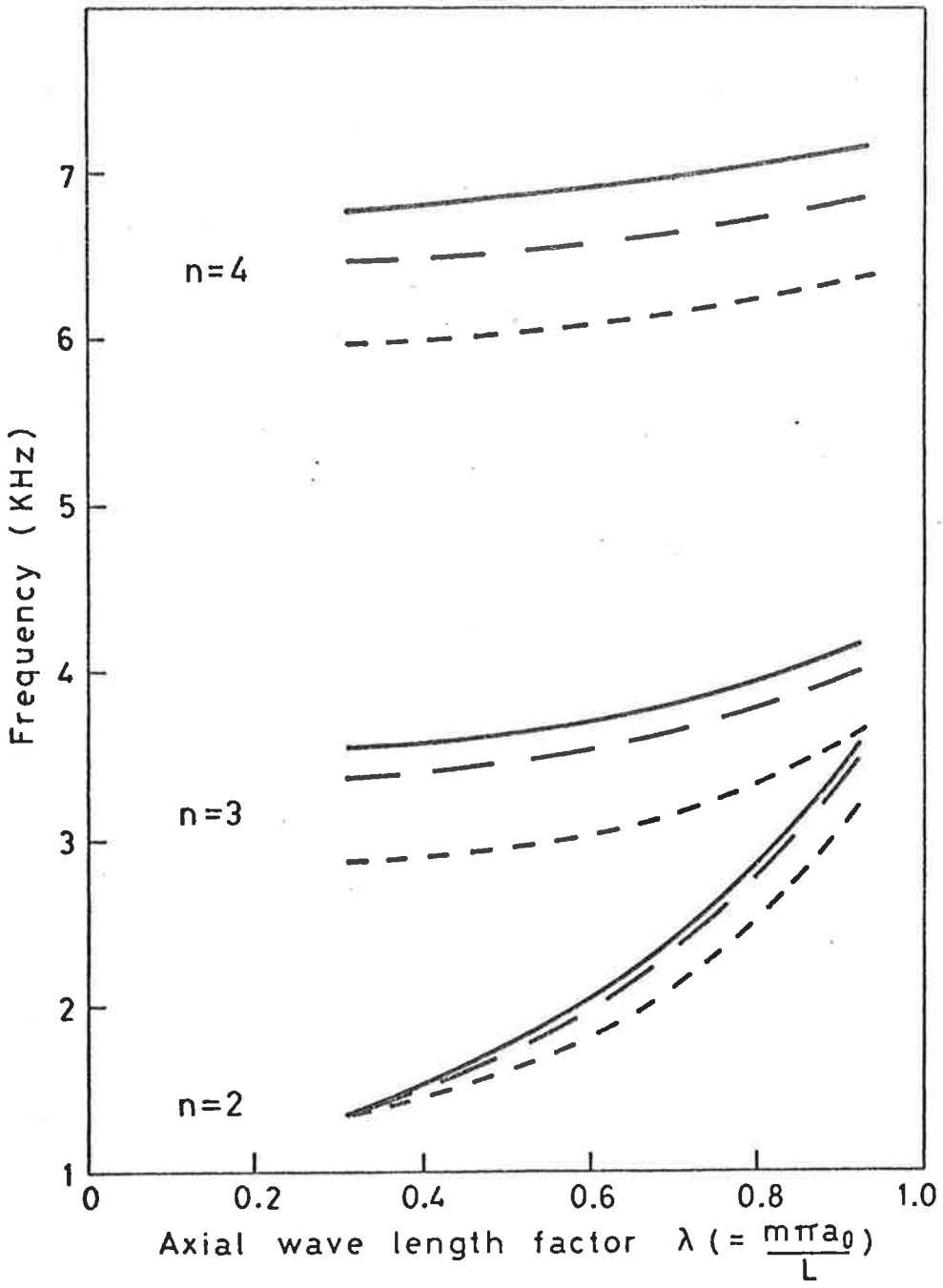

FIG. 4-4 THEORETICAL FREQUENCY CURVES FOR DISTORTED CYLINDER. Asymmetric solutions. —— e = 0, — — — e = 0.5, ---- e = 1.0.

of vibration for four modes of the distorted cylinder. The asymmetric solutions are nearly identical in magnitude and so are not tabulated. Clearly the greater the number of circumferential modes included in the analysis (i.e. the larger the value of N) the more exact will be the theoretical solution. It is found that N = 6 is sufficient to ensure excellent agreement with experiment and favourable in computing time. The solution of the eigen equations is well behaved. If the distortion is set to zero, for example, then the modes decouple completely leaving only the principal mode.

To determine the tangential and radial symmetric components the cylinder was set upright on the turntable and for the longitudinal components it was positioned on its side and holograms taken using the techniques described in section 2.2. Table 4-3 shows the theoretically calculated and experimentally determined vibration components for the distorted cylinder. Due to the mechanical arrangement it is not possible to analyse the circumferentially varying longitudinal modes. The double turntable scheme described in section 2.1 is required. Hence only the ratio of longitudinal to radial vibration is considered which is

$$A_m/C_m = [\,(\sum_n A_{mn}^2)\,/\,(\sum_n C_{mn}^2)\,]^{\frac{1}{2}} \qquad (4.43)$$

and varies sinusoidally along the length of the cylinder as given by equation (4.3). The theoretical and experimental amplitudes for the B and C components are scaled by the factor which makes the C component of the principal mode unity. In addition since the modes are not excited exactly symmetrically due to influence of the magnets then some asymmetric components are present in the experimental analysis. Hence only the magnitudes of the components are shown in Table 4-3.

Figs. 4-5(a) to 4-5(f) show the mode shapes calculated from

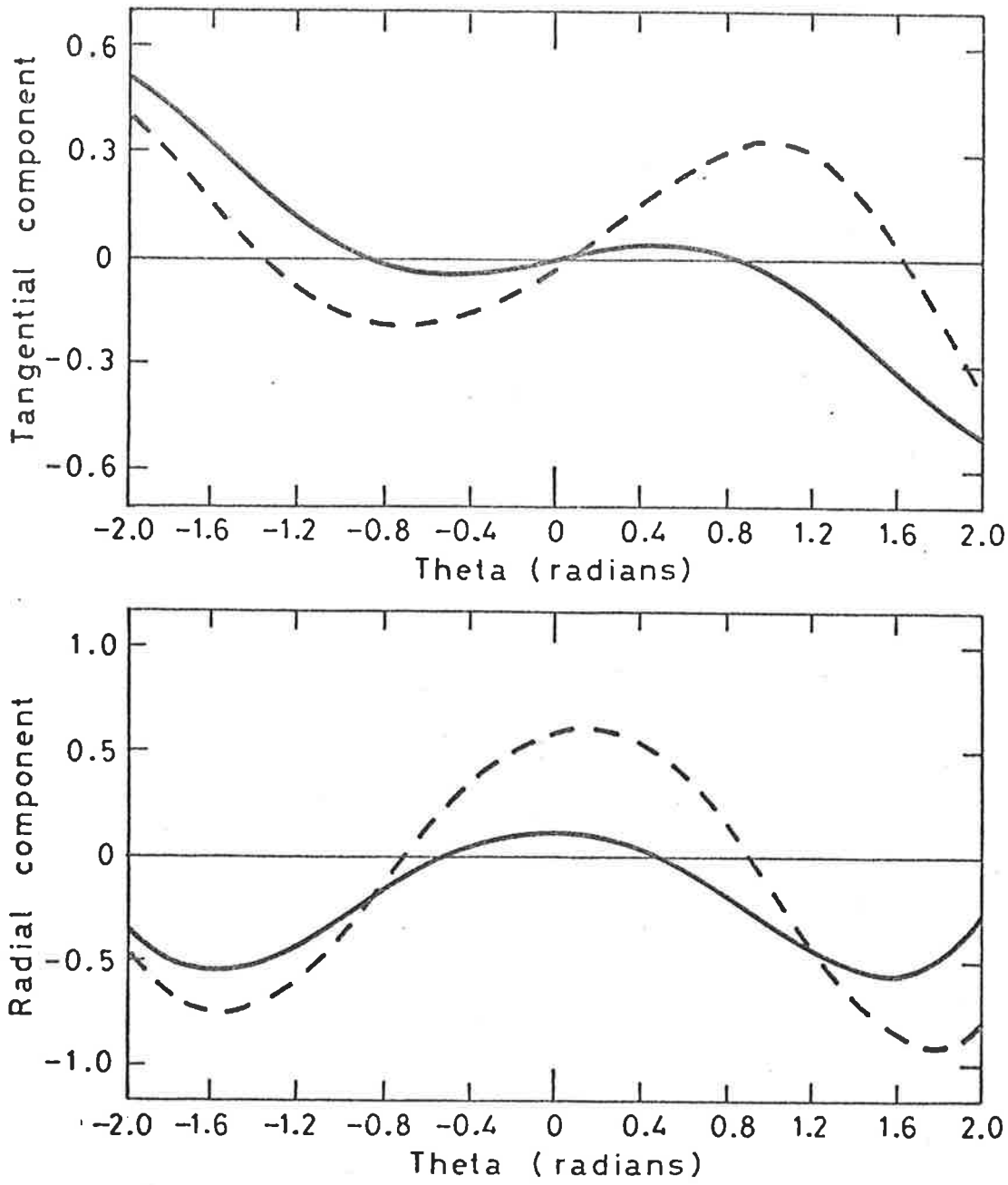

FIG. 4-5 (a) RADIAL AND TANGENTIAL VIBRATION COMPONENTS FOR THE PRINCIPAL SYMMETRIC MODE (1,2) OF A DISTORTED CYLINDER. ——— theory. --- experiment.

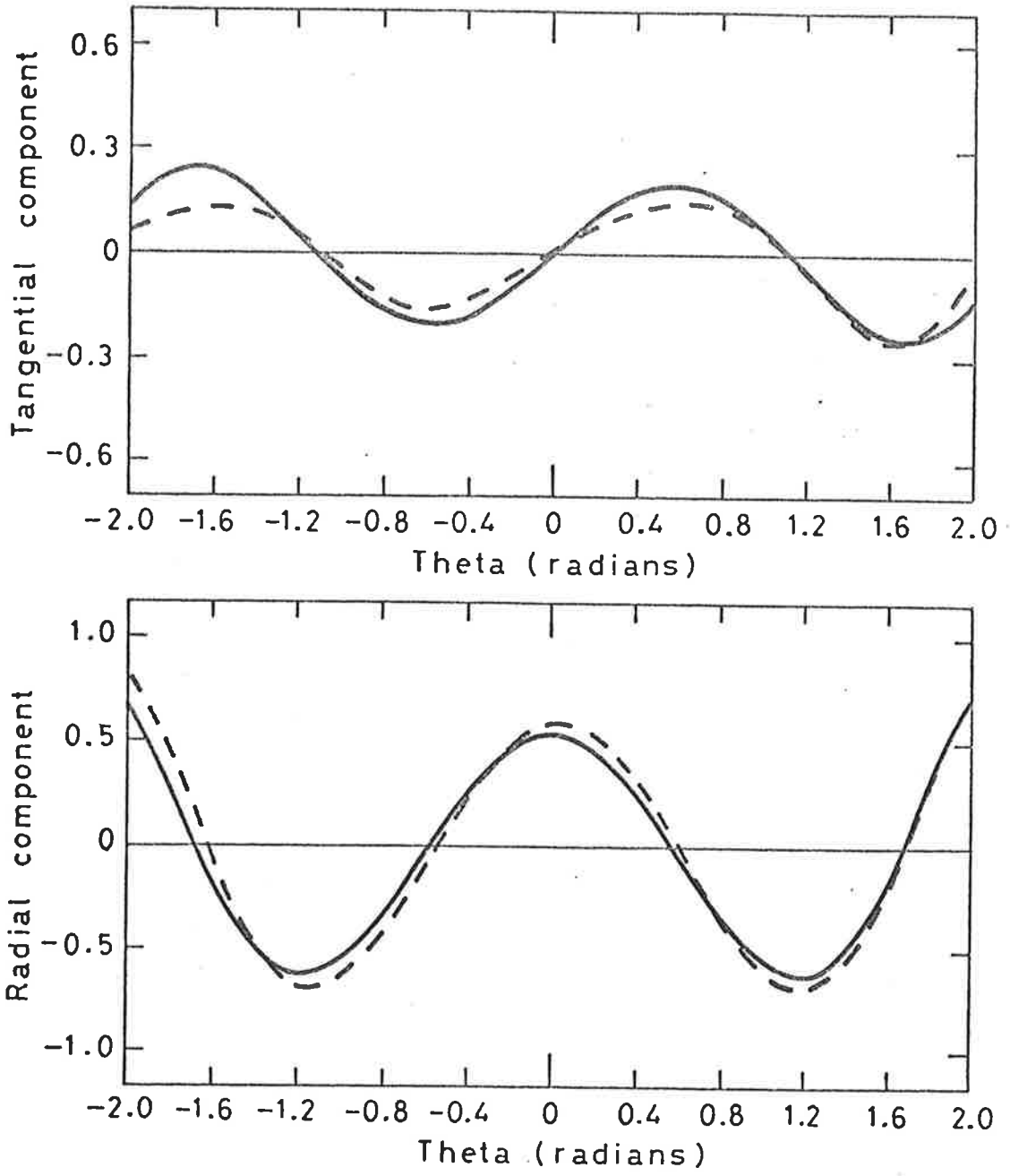

FIG. 4-5 (b) RADIAL AND TANGENTIAL VIBRATION COMPONENTS FOR THE PRINCIPAL SYMMETRIC MODE (1,3) OF A DISTORTED CYLINDER. —— theory. ---- experiment.

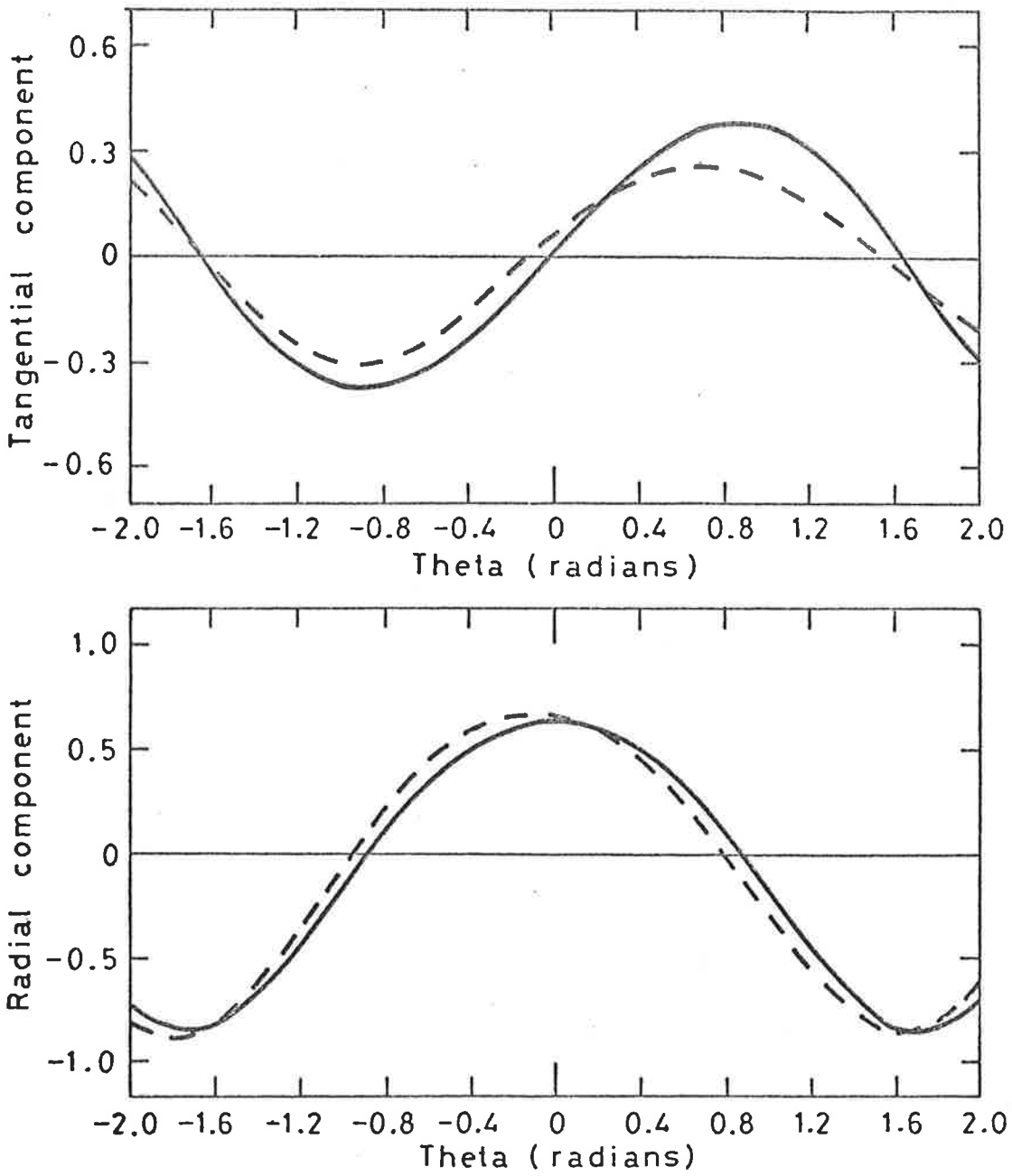

FIG. 4-5 (c) RADIAL AND TANGENTIAL VIBRATION COMPONENTS FOR THE PRINCIPAL SYMMETRIC MODE (2,2) OF A DISTORTED CYLINDER. —— theory. --- experiment.

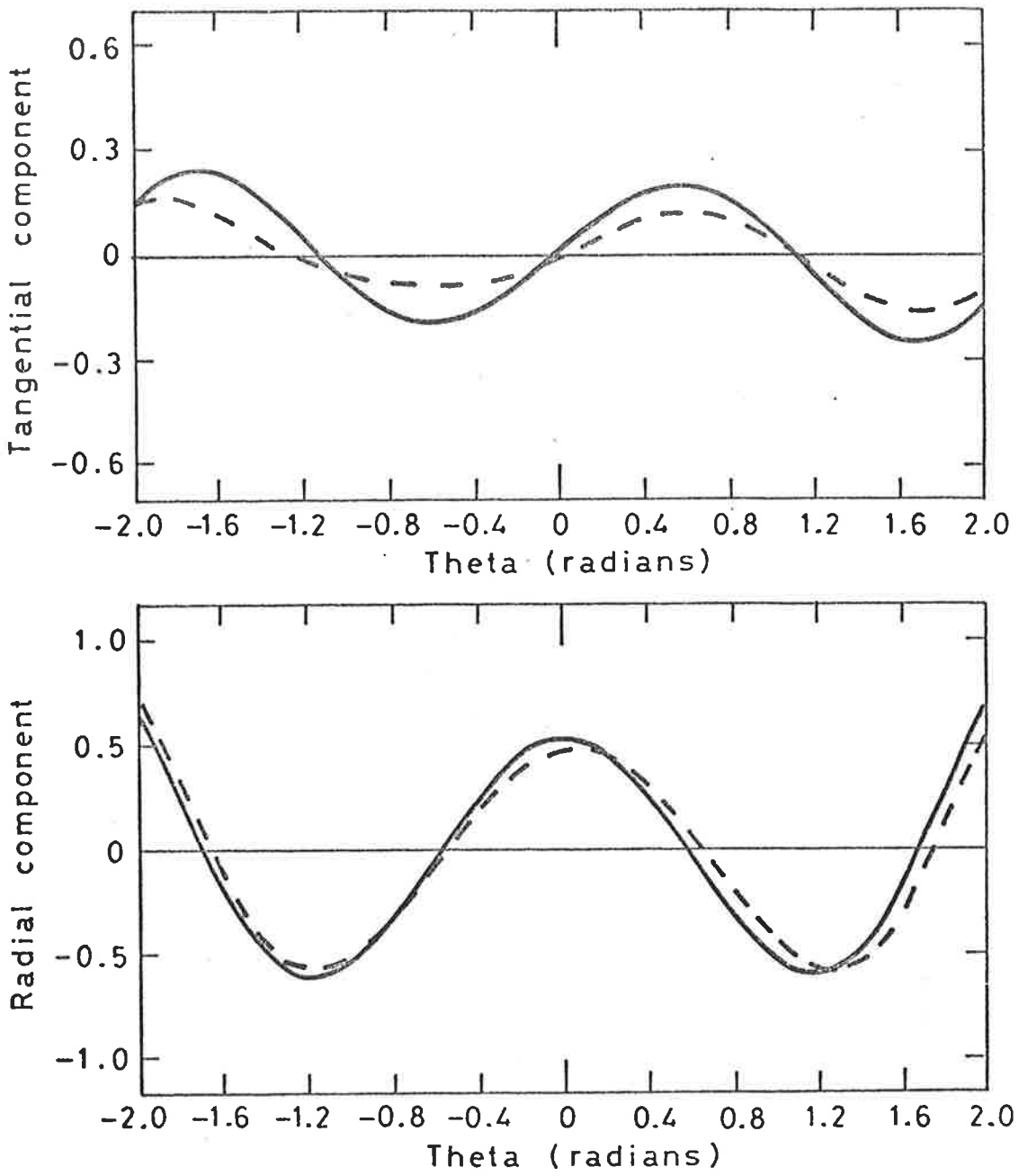

FIG. 4-5 (d) RADIAL AND TANGENTIAL VIBRATION COMPONENTS FOR THE PRINCIPAL SYMMETRIC MODE (2,3) OF A DISTORTED CYLINDER. —— theory. --- experiment.

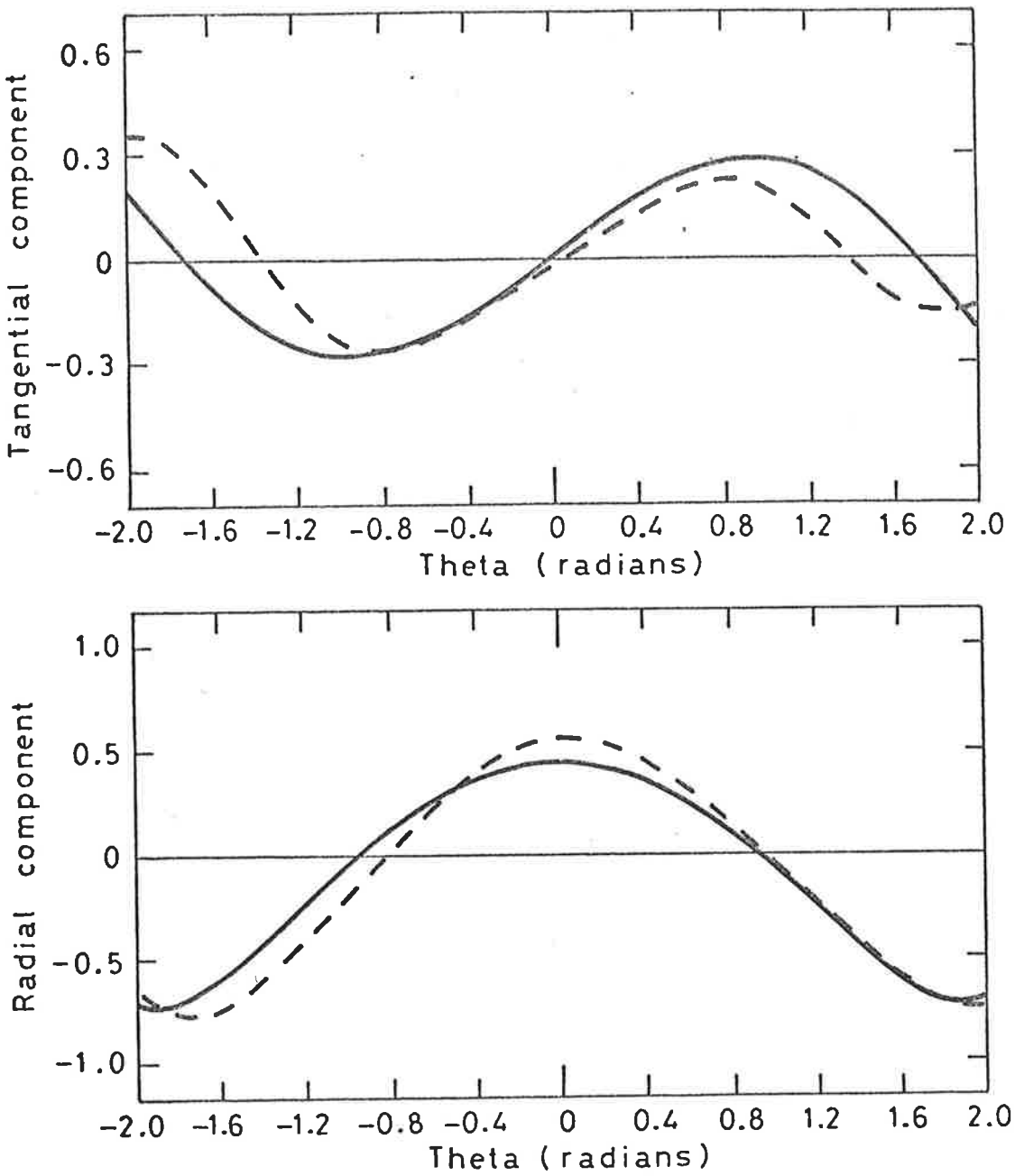

FIG. 4-5 (e) RADIAL AND TANGENTIAL VIBRATION COMPONENTS FOR THE PRINCIPAL SYMMETRIC MODE (3,2) OF A DISTORTED CYLINDER. —— theory. --- experiment.

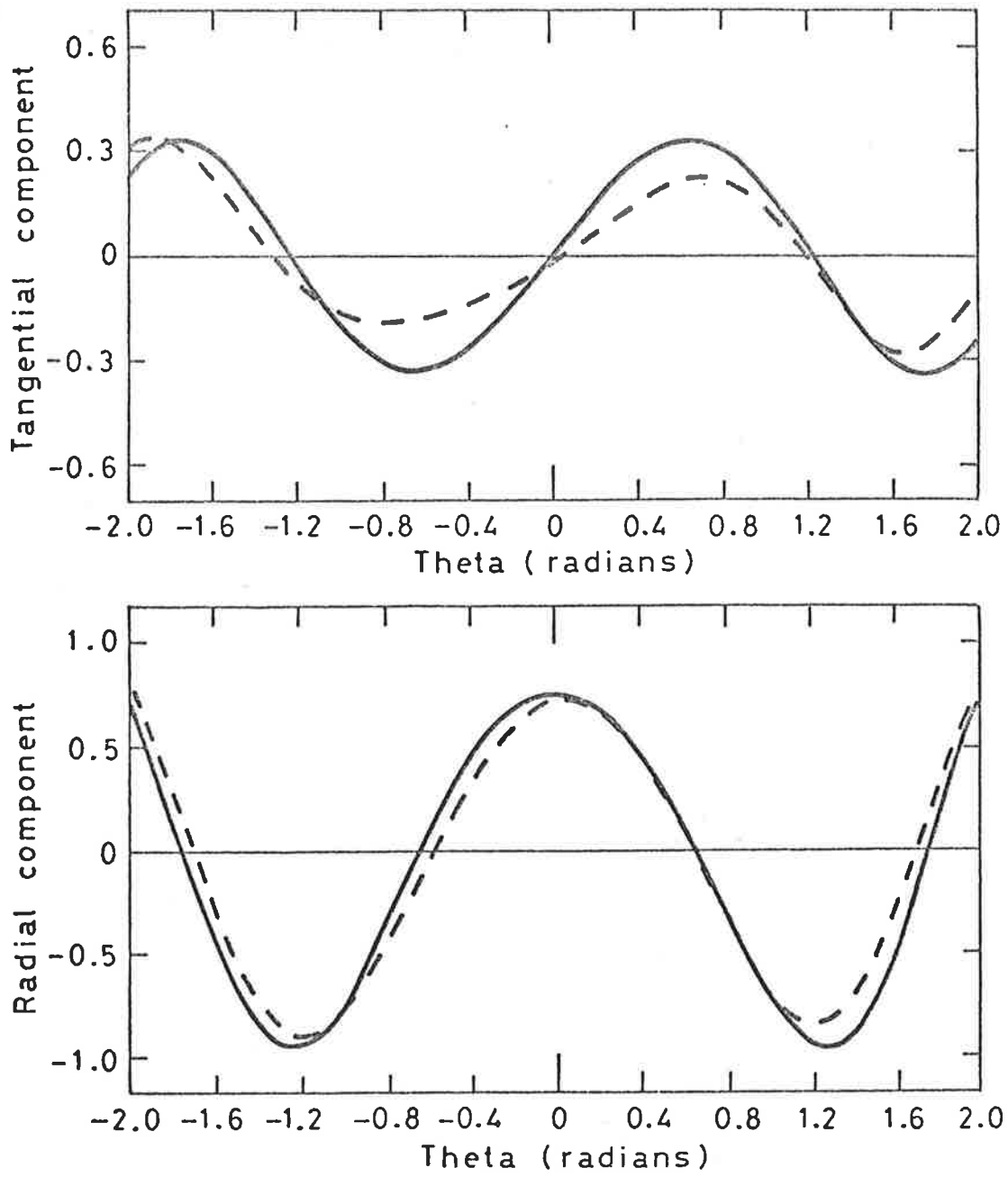

FIG. 4-5 (f) RADIAL AND TANGENTIAL VIBRATION COMPONENTS FOR THE PRINCIPAL SYMMETRIC MODE (3,3) OF A DISTORTED CYLINDER. —— theory. --- experiment.

the theory and those derived experimentally. Evident from the experimental curves is the small contribution of the asymmetric modes discussed above. Nevertheless the agreement is excellent for all modes except the lowest (1,2) mode due to the absence of a significant contribution of the n = 1 mode (see Table 4-3). Note that the origin of the holographic analysis, being different to that of the theory of section 4.1, is transposed for direct comparison.

4.3 CYLINDER WITH A THIN LONGITUDINAL STRIP

A steel cylinder was manufactured with length L = 398.8mm, mean radius a_o = 39.29mm and wall thickness h = 2.05mm. A nominal $\frac{1}{8}$" square-section length of steel rod was attached to the cylinder along a generator with an extremely thin layer of LS-12 adhesive. Assuming that the distorting strip is sufficiently small to neglect errors of curvature, the Fourier components of the distortion are calculated with the aid of Fig. 4-6. Using equations (4.41),

$$\left.\begin{aligned} h_o^- &= -h/2a_o \\ h_o^+ &= h/2a_o + D\mu/\pi a_o \end{aligned}\right\} \qquad (4.44)$$

and from equations (4.42),

$$\left.\begin{aligned} h_p^- &= 0 \\ h_p^+ &= \frac{2D}{\pi p a_o} \sin p\mu \qquad \text{for } p > 0 \end{aligned}\right\} \qquad (4.45)$$

where D = 3.21mm and μ = 0.03876 rad.

Fig. 4-7 shows reconstructions of time-averaged holograms

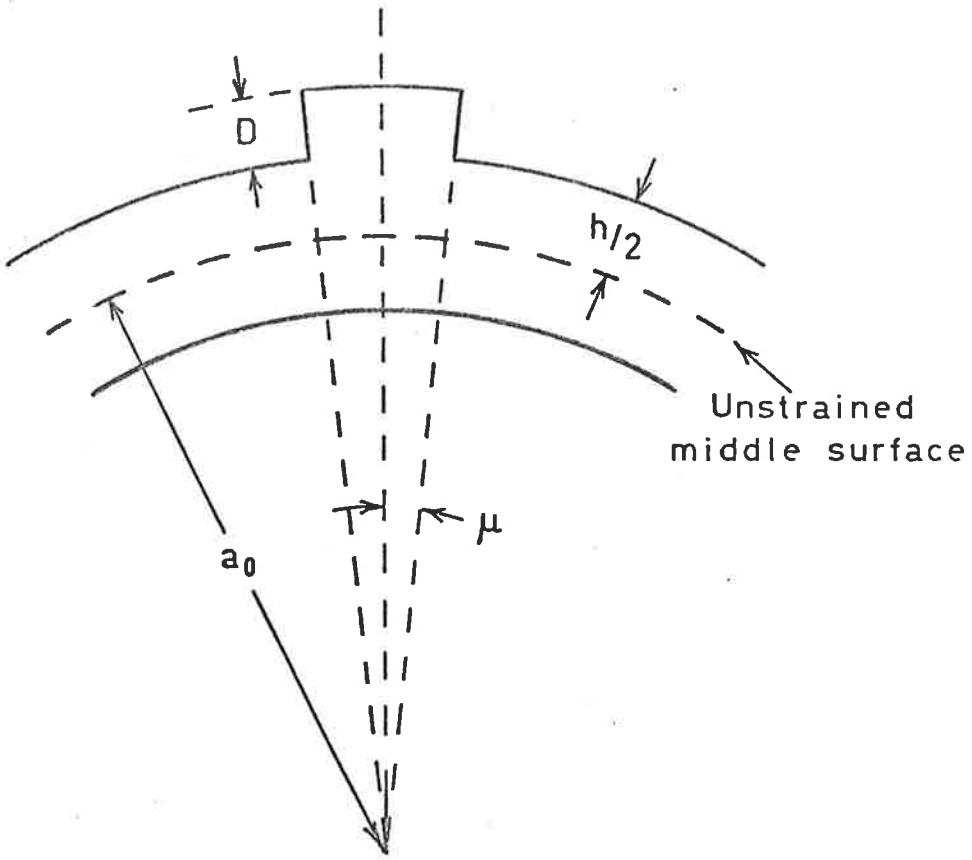

FIG. 4-6 GEOMETRY FOR CALCULATING THE FOURIER COEFFICIENTS OF THE DISTORTION.

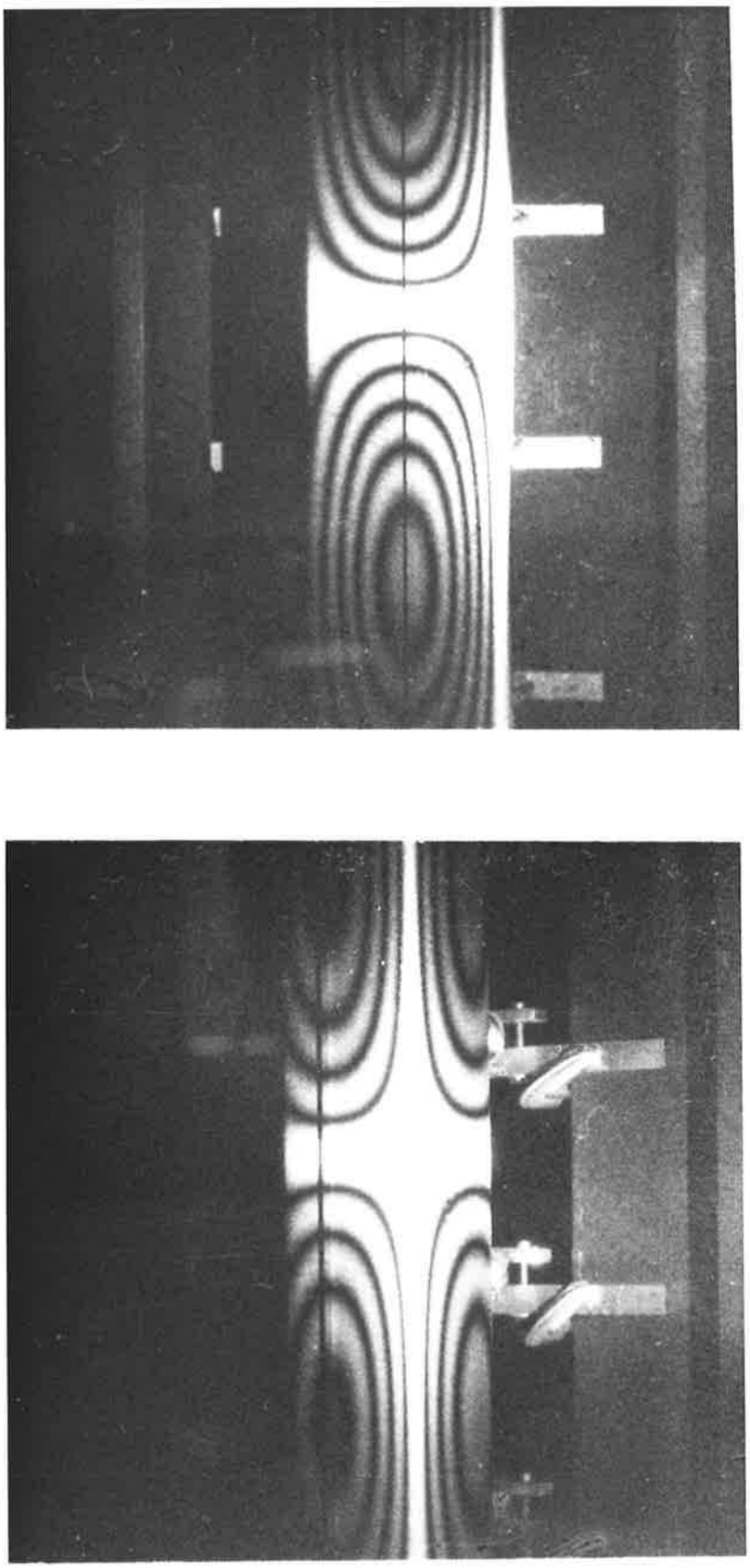

FIG. 4-7

Two views of a cylinder with attached strip vibrating in (2,2) mode.

of the cylinder vibrating in the $m = 2$, $n = 2$ mode. Table 4-4 shows the results of measured and theoretical frequencies with the distortion and without it. For the undistorted cylinder agreement is excellent but with the distortion the predictions are totally inaccurate. The strip was re-attached using a number of fine bolts but with the same results, indicating the adhesive is not an influencing factor. Rather it is thought that the sudden discontinuity of the attached strip dictates the use of functions which satisfy the strict boundary conditions at the strip which the comparitively slowly-varying sinusoidal functions do not. Put another way, the Rayleigh-Ritz method "spreads" the discontinuity over the surface of the cylinder and does not necessarily account for sharp discontinuities.

TABLE 4-1

RESONANT FREQUENCIES FOR SOME MODES OF

DISTORTED CYLINDER

(non-concentric bore)

Principal Mode (m,n)	Theoretical Freq.		Exp. Freq. Distorted	% Error in Exp. Freq.
	Undistorted	Distorted		
1,2	1340	1316	1330	1.1
1,3	3553	3375	3442	2.0
1,4	6774	6465	6495	0.5
2,2	2105	2042	2063	1.0
2,3	3740	3562	3627	1.8
2,4	6905	6594	6617	0.3
3,2	3598	3524	3463	1.7
3,3	4204	4045	4085	1.0
3,4	7159	6847	6861	0.2

TABLE 4-2

THEORETICAL SUPERPOSED SYMMETRIC MODES FOR A CYLINDER WITH NON-CONCENTRIC INNER BORE

FREQ. Hz	PRINC-IPAL MODE (m,n)	COEFF.	MODE AMPLITUDES n =						
			0	1	2	3	4	5	6
1315.6	(1,2)	A_{1n}	-.027	.154	-0.72	.006	.0	.0	.0
		B_{1n}	.0*	.606	-.504	.064	-.007	.001	.0
		C_{1n}	.002	.596	-1.000	.190	-.028	.004	.0
3375.4	(1,3)	A_{1n}	.0	.0	-.002	-.034	.006	-.001	.0
		B_{1n}	.0*	.001	-.010	-.336	.081	-.014	.002
		C_{1n}	.0	.001	-.019	-1.000	.321	-.072	.012
2041.5	(2,2)	A_{2n}	.003	-.015	.127	-.013	.001	.0	.0
		B_{2n}	.0*	-.028	.509	-.076	.009	-.001	.0
		C_{2n}	.0	-.026	1.000	-.225	.038	-.006	.001
		A_{2n}	.0	.001	.005	.064	-.012	.002	.0
		B_{2n}	.0*	.003	.022	.339	-.084	.015	-.002
		C_{2n}	.0	.003	.042	1.000	-.331	.075	-.013

* These coefficients are preset to zero before the eigen equations are solved.

TABLE 4-3

THEORETICAL AND EXPERIMENTAL SYMMETRIC MODE AMPLITUDES OF DISTORTED CYLINDER (NORMALISED MAGNITUDES)

PRINCIPAL MODE(m,n)	n	RADIAL COMPONENT C_{mn}		TANGENTIAL COMPONENT B_{mn}		LONGITUDINAL RATIO A_m/C_m	
		Theory	Expt.	Theory	Expt.	Theory	Expt.
1,2	1	.596	.108	.606	.178	.146	.091
	2	1.000	1.000	.504	.496		
	3	.190	.163	.064	.110		
1,3	3	1.000	1.000	.336	.228	.033	.040
	4	.321	.268	.081	.079		
	5	.072	.034	.014	.054		
2,2	2	1.000	1.000	.509	.346	.126	.186
	3	.225	.191	.076	.044		
2,3	3	1.000	1.000	.339	.216	.062	.105
	4	.331	.386	.084	.100		
	5	.075	.083	.015	.034		
3,2	2	1.000	1.000	.509	.217	.144	.186
	3	.415	.318	.140	.217		
	4	.101	.090	.025	.128		
3,3	2	.238	.139	.122	.064	.087	.169
	3	1.000	1.000	.341	.291		
	4	.362	.282	.092	.147		

TABLE 4-4

RESONANT FREQUENCIES FOR SOME MODES OF DISTORTED CYLINDER.

(Longitudinal Strip)

PRINCIPAL MODE (m,n)	UNDISTORTED CYLINDER			DISTORTED CYLINDER	
	THEORY	EXPERIMENT	% ERROR	THEORY	EXPERIMENT
1,2	990	1007	1.7	1128	999
1,3	2500	2552	2.1	3647	2517
2,2	1871	1852	1.0	1939	1859
2,3	2689	2735	1.7	3717	2705
3,2	3431	3328	3.0	3336	3343
3,3	3195	3225	1.0	4193	3213
4,3	4058	4056	0.0	4636	4067

CHAPTER 5

COUPLED TEMPORAL MODES

It was shown in Chapter 4 that the effect of any distortions in the wall thickness (which may be generalized to include anisotropies in radius or Young's modulus for example) is to couple modes but at the same frequency; such modes are called superposed spatial modes. Alternatively, for a non-distorted cylinder, the applied time-varying point force induces modal coupling with phase-shift between the modes which was demonstrated for the two-dimensional case by Stetson and Taylor [84]. Such modes are termed Coupled Temporal Modes. In this light it is thought that the analysis of Shirakawa and Mizoguchi [156] could be extended to predict coupled temporal mode response for cylinders excited by point forces.

In this chapter the theory of Generalized Least Squares is applied to solve the characteristic equations for the case of cylinders vibrating in two coupled modes, one essentially pure mode and two superposed modes at a single frequency. The temporal phase difference is determined without the need for modulating the laser beam.

5.1 HOLOGRAPHIC THEORY FOR TWO COUPLED MODES

The characteristic equation for two coupled modes with phase difference Δ was determined in section 2.1.4 (special case 5). The argument function for the combined motion was shown to be the phasor sum of the argument functions of each component. Assuming that each coupled mode is a singular superposed mode (i.e. pure mode) then all terms in equations (2.10) to (2.12) are zero except for one - order

N^1 for one mode and N^2 for the other. Hence equation (2.53) becomes

$$f_q = [(x_N^1 \sin N^1\xi_q + y_N^1 \cos N^1\xi_q)K_q + (w_N^1 \sin N^1\xi_q + z_N^1 \cos N^1\xi_q)S_q]^2$$

$$+ [(x_N^2 \sin N^2\xi_q + y_N^2 \cos N^2\xi_q)K_q + (w_N^2 \sin N^2\xi_q + z_N^2 \cos N^2\xi_q)S_q]^2$$

$$+ 2\cos\Delta[(x_N^1 \sin N^1\xi_q + y_N^1 \cos N^1\xi_q)K_q + (w_N^1 \sin N^1\xi_q + z_N^1 \cos N^1\xi_q)S_q]$$

$$.[(x_N^2 \sin N^2\xi_q + y_N^2 \cos N^2\xi_q)K_q + (w_N^2 \sin N^2\xi_q + z_N^2 \cos N^2\xi_q)S_q]$$

$$- \Omega_q^2 / k^2 \qquad (5.1)$$

The equations of the form of equations (2.54) to (2.56) are

$$\left.\begin{aligned}
G_1^{(q)} &= \frac{\partial f_q}{\partial x_N^1} = 2(c^1K_q + b^1S_q)\sin(N^1\xi_q)K_q + 2\cos\Delta(c^2K_q + b^2S_q)\sin(N^1\xi_q)K_q \\
G_2^{(q)} &= \frac{\partial f_q}{\partial x_N^2} = 2(c^2K_q + b^2S_q)\sin(N^2\xi_q)K_q + 2\cos\Delta(c^1K_q + b^1S_q)\sin(N^2\xi_q)K_q \\
G_3^{(q)} &= \frac{\partial f_q}{\partial y_N^1} = 2(c^1K_q + b^1S_q)\cos(N^1\xi_q)K_q + 2\cos\Delta(c^2K_q + b^2S_q)\cos(N^1\xi_q)K_q \\
&\;\;\vdots \qquad\qquad\qquad\qquad \vdots \\
G_8^{(q)} &= \frac{\partial f_q}{\partial z_N^2} = 2(c^2K_q + b^2S_q)\cos(N^2\xi_q)K_q + 2\cos\Delta(c^1K_q + b^1S_q)\cos(N^1\xi_q)K_q \\
G_9^{(q)} &= \frac{\partial f_q}{\partial \Delta} = -2(c^1K_q + b^1S_q)(c^2K_q + b^2S_q)\sin\Delta
\end{aligned}\right\} \qquad (5.2)$$

where

$$\left.\begin{aligned} c^1 &= x_N^1 \sin N^1\xi + y_N^1 \cos N^1\xi \\ c^2 &= x_N^2 \sin N^2\xi + y_N^2 \cos N^2\xi \\ b^1 &= w_N^1 \sin N^1\xi + z_N^1 \cos N^1\xi \\ b^2 &= w_N^2 \sin N^2\xi + z_N^2 \cos N^2\xi \end{aligned}\right\} \qquad (5.3)$$

Hence matrices $\underline{\Gamma}$ and $\underline{F}$ are calculated using equations (2.51) and (2.52) and the correction vector $\underline{\delta}$ from equation (2.50). The inverse matrix $\underline{\Gamma}^{-1}$ is calculated by the Gauss-Jordan method with elimination by partial pivoting [163]. The vector describing the parameters

$$\underline{R} = (x_N^1,\ x_N^2,\ y_N^1,\ y_N^2,\ w_N^1,\ w_N^2,\ z_N^1,\ z_N^2,\ \Delta) \qquad (5.4)$$

is arbitrarily set for the initial iteration but as shown in the next section, local high-order minima could terminate the procedure prematurely. In practice a number of starting points are selected to guard against this possibility.

5.2 EXPERIMENTAL PROCEDURE AND RESULTS

To test the convergence of the method of Generalized Least Squares, five modes of two cylinders were considered. The first cylinder of length 398.8mm, mean radius 39.29mm and thickness 2.050 ± .005mm was carefully machined to make it as near perfect as possible. The second cylinder is the one considered in Chapter 4 with the centre of the inner bore displaced from the centre of the outer circular surface by 1mm for which the theory of vibration predicts a number of superposed modes.

To generate coupled modes in the perfect cylinder two electromagnetic drivers were positioned at the radial antinodes of vibration. Each point force is a disturbance with spatial Fourier components which excite other modes in the cylinder and these couple in some phase relationship resulting in phasor vibration. The degree of coupling of the spatial Fourier components of the force to the cylinder modes depends on the position of the force relative to the modes. Hence moving the point excitation towards the radial nodes (at the cylinder ends) reduces the degree of coupling with the result that only a single mode is induced in the cylinder. This behaviour was confirmed in the experiment.

Fig. 5-1 shows two views of the perfect cylinder vibrating in two coupled modes (3,2) and (3,3). The predominant mode is (3,2). The contribution of the (3,3) mode is seen as a coupling of the fringe groups. This is to be compared with Fig. 3-21 which shows two views of the cylinder vibrating in an essentially pure (4,3) mode. The decoupling of the fringe groups is clear in this instance.

In the analysis of Fig. 3-21 it is normal to allocate a sign to fringe groups, adjacent groups taking alternating signs. This procedure is clearly irrelevant in the analysis of Fig. 5-1 for since the fringe order appears squared in equation (2.29) then only the order of the fringe is recorded.

Fig. 5-2 shows the components of two coupled modes for the perfect cylinder. Stetson and Taylor [84] predict that if the resonances are reasonably sharp then the response of a mode at its resonant frequency is close to $\pi/2$ in phase to any other mode that may be excited in combination. The temporal phase difference Δ was determined as 1.96 rad at the resonant frequency 1852 Hz for the coupled modes (2,2) and (2,3) shown in Fig. 5-2. Fig. 5-3 is the result of reposit-

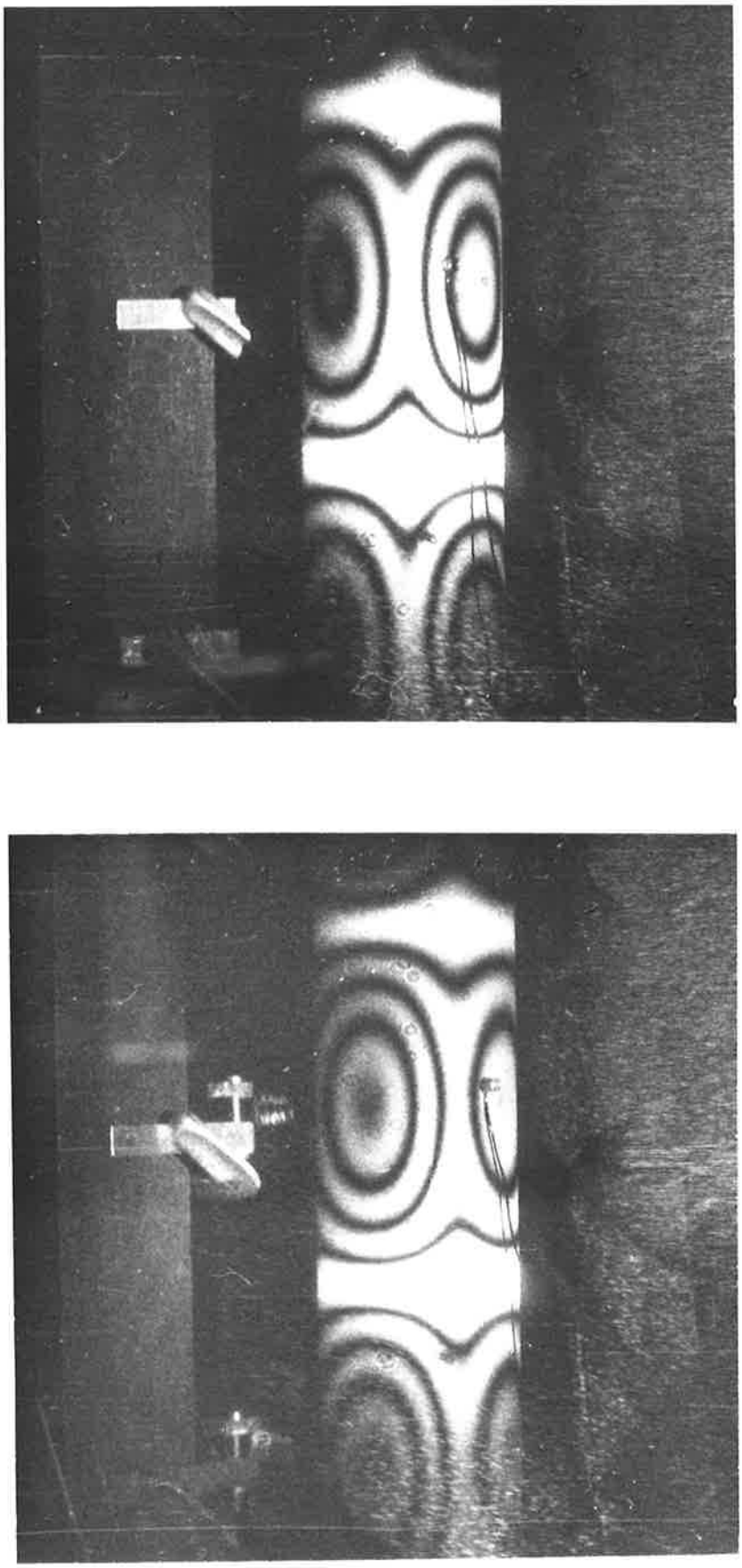

FIG. 5-1

Two views of a cylinder vibrating in two coupled modes.

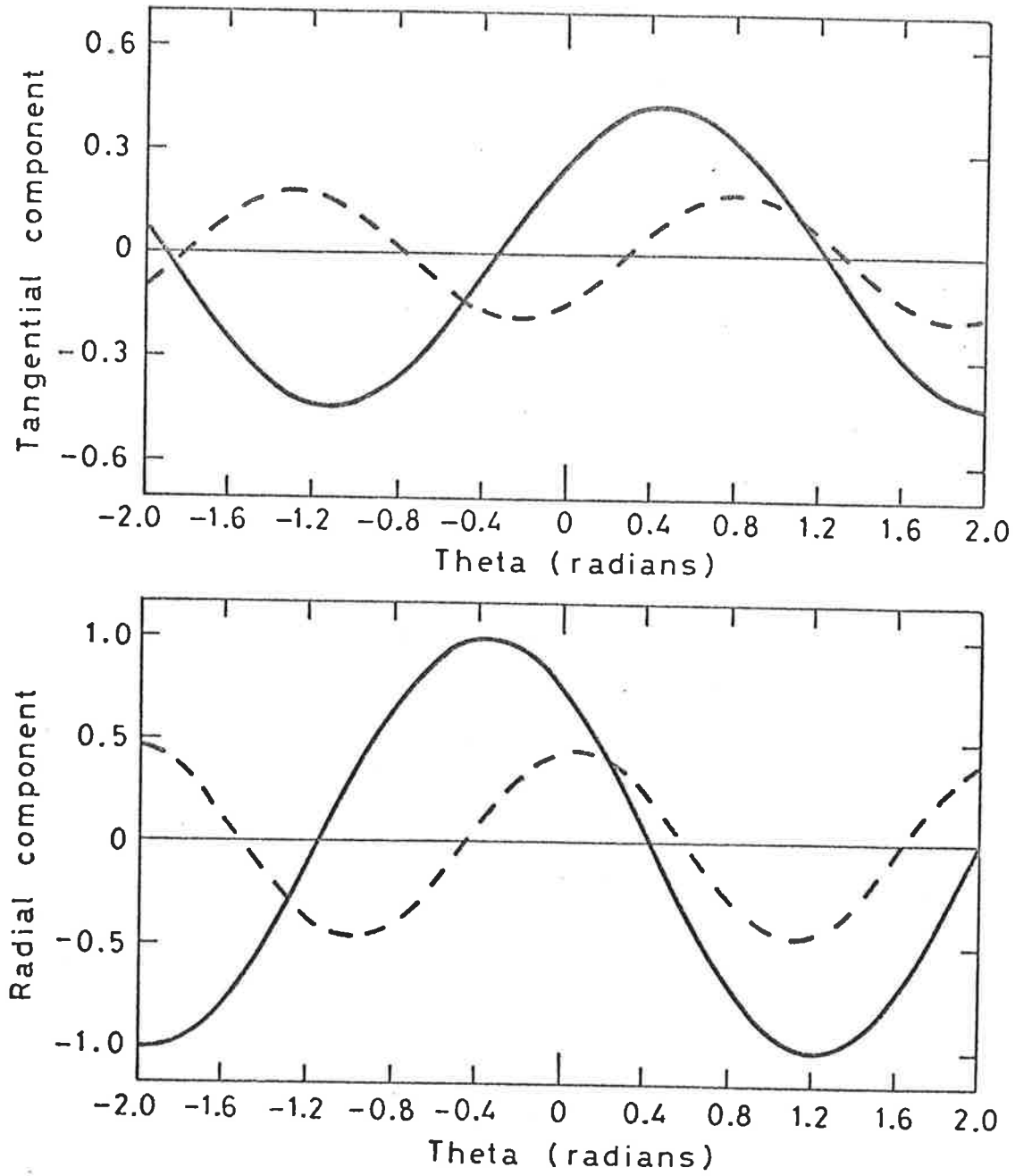

FIG. 5-2 EXPERIMENTALLY DETERMINED COMPONENTS OF TWO COUPLED MODES - PERFECT CYLINDER

—— Mode (2,2)

--- Mode (2,3)

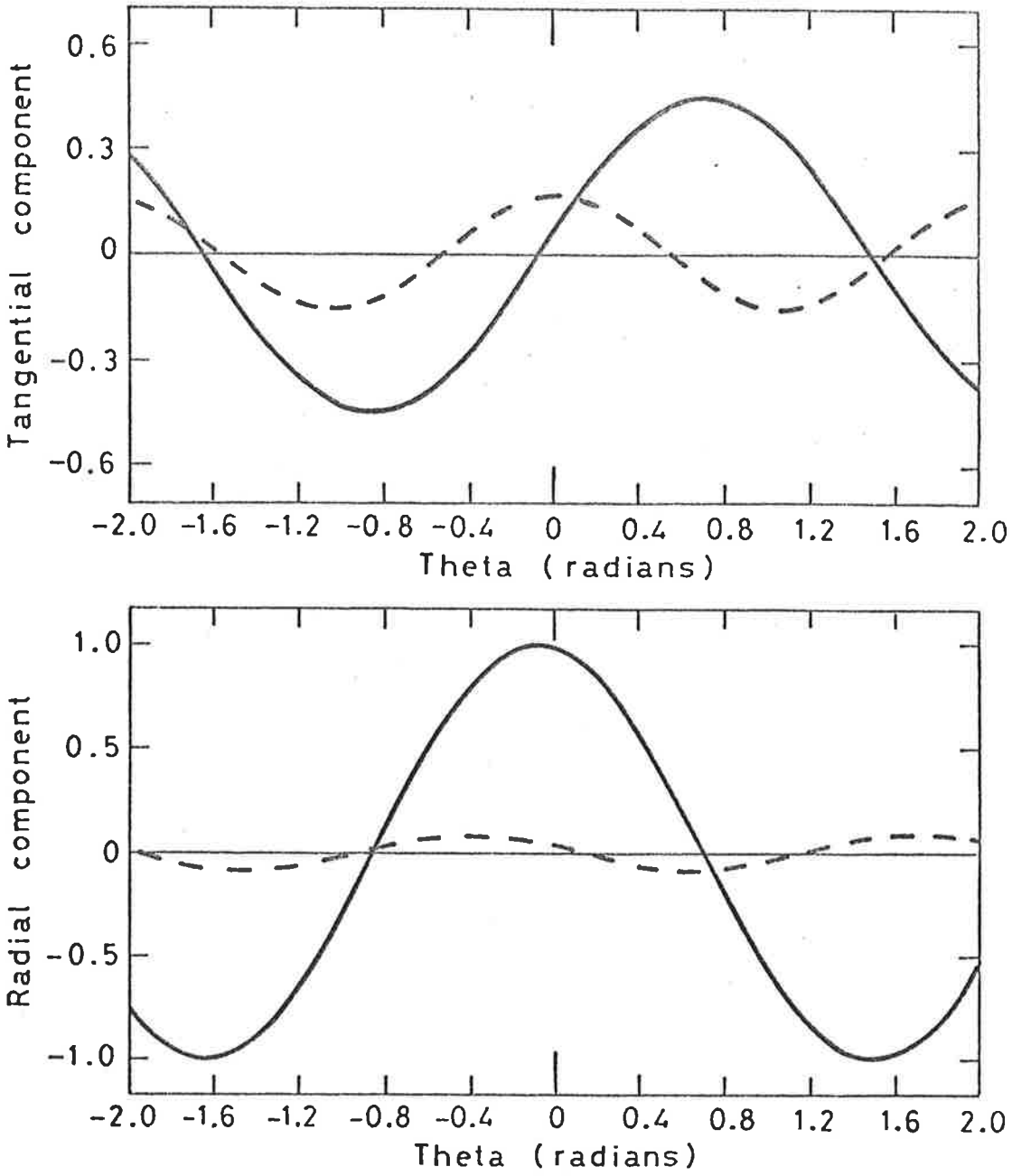

FIG. 5-3 REPOSITIONING THE DRIVERS ALMOST ELIMINATES THE OTHER COUPLED MODE SHOWN IN FIG. 5-2.

—— Mode (2,2)

--- Mode (2,3)

ioning the electromagnets near the ends of the cylinder, the frequency remaining unchanged. The relative level of the coupled mode (2,3) is substantially lower in the case of the radial component but uncertain in the tangential component. The principal mode (2,2) however is well behaved. The ratio of the tangential to radial amplitude (B/C) is 0.436 which is to be compared with 0.503 predicted by the Arnold-Warburton theory for cylinders [126] for a pure mode. To be noted also is the radial component which is in phase quadrature spatially with respect to the tangential component, also predicted from the pure mode theory.

Fig. 5-4 shows the components of two other coupled modes for the perfect cylinder at a frequency of 3332 Hz. For this case, Δ was determined as 1.53 rad compared with the predicted value $\pi/2$ [84]. Again the principal mode is well behaved with B/C = 0.397 compared with the theoretical value of 0.509 and again the radial and tangential components are in spatial phase quadrature. The amplitudes of the components of the coupled mode seem to be uncertain due to their low magnitudes, a situation which again could be improved if more data points were available.

The analysis was also applied to the distorted cylinder described in Chapter 4 for the principal modes (2,2) and (2,3). Table 5-1 shows the amplitudes of the coefficients determined by the Generalized Least Squares theory to be nearly identical to those determined by the normal least squares procedure of Chapter 3. More interesting is the value determined for Δ which, theoretically, should be zero or a multiple of π. As explained in section 2.1.4 (special case 4) however the determination of Δ for these cases is bound to be somewhat uncertain.

Tables 5-2(a), (b) and (c) show the effect of initial

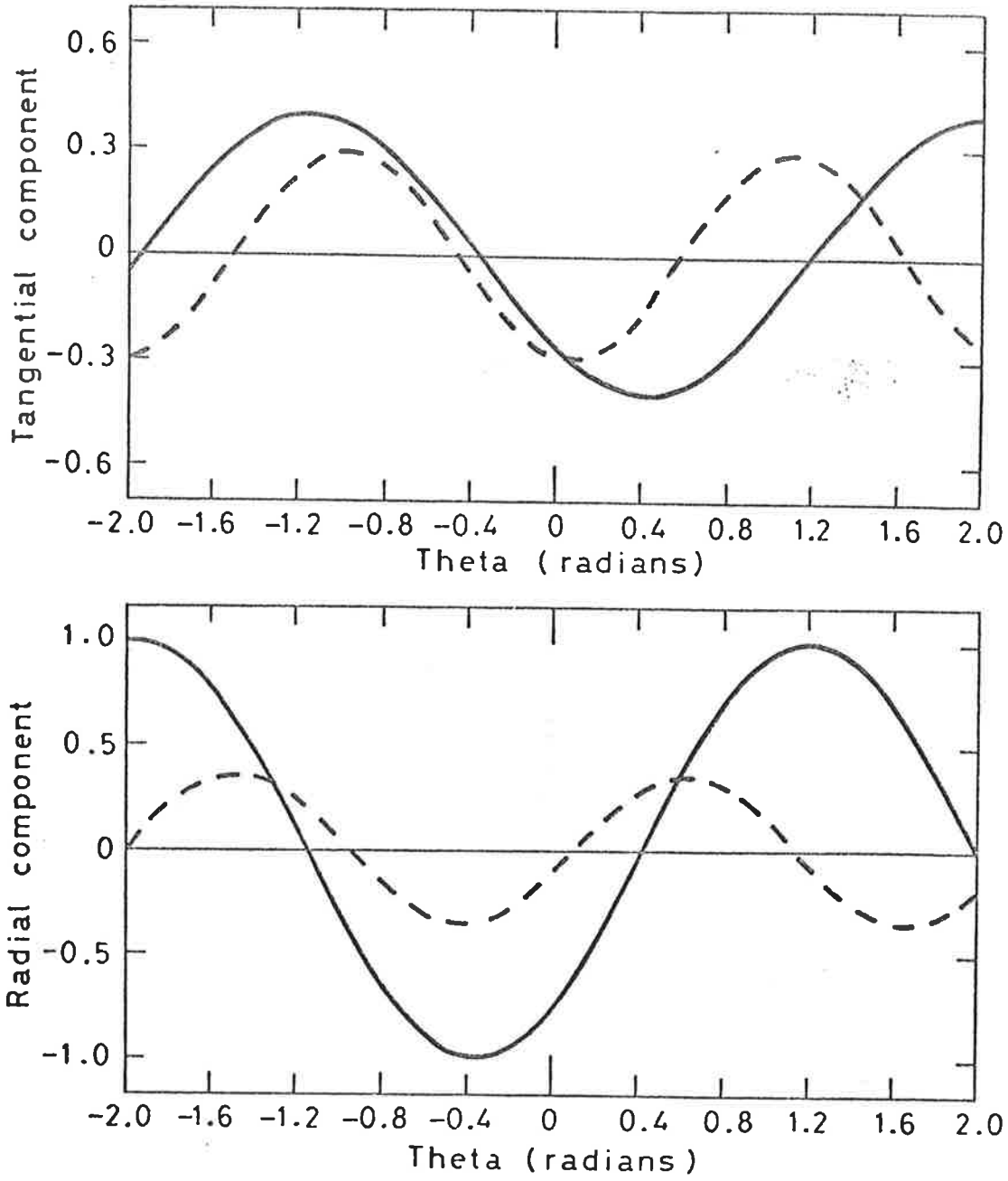

FIG. 5-4 COMPONENTS OF TWO COUPLED MODES - PERFECT CYLINDER

——— Mode (3,2)

---- Mode (3,3)

conditions on the final solution for three cases. The starting magnitudes of the amplitude parameters are equal but are varied with respect to the phase parameter. Hence the notation [1,.1] in Tables 5-2 is taken to mean [1,1,1,1,1,1,1,1,.1] which is the starting vector. All other starting conditions tried but not shown in Tables 5-2 resulted in exactly similar solutions. In the case of Table 5-2 (a) the optimum solution oscillated between that of the second and third columns. For Tables 5-2(b) and (c) it is clear that the higher order solution (represented by the larger residual $\sum (f_q)^2$) is incorrect in the phase Δ. Hence the optimum solution is that with the least residual.

TABLE 5-1

COMPARISON OF GENERALIZED AND NORMAL LEAST SQUARES PROCEDURES IN THE DETERMINATION OF COMPONENTS OF PRINCIPAL MODES (2,2) AND (2,3) FOR A DISTORTED CYLINDER

PARAMETER	PRINCIPAL MODE (2,2) $N^1 = 2$ $N^2 = 3$		PRINCIPAL MODE (2,3) $N^1 = 3$ $N^2 = 4$	
	GENERALIZED	NORMAL	GENERALIZED	NORMAL
x_N^1	-.074	-.062	.633	.683
x_N^2	.236	.150	-.032	-.083
y_N^1	.771	.784	-.131	-.167
y_N^2	.023	.002	-.202	-.258
w_N^1	.183	.272	-.028	-.002
w_N^2	-.022	-.031	-.081	-.070
z_N^1	.008	.008	-.177	-.152
z_N^2	.052	-.015	.002	-.010
Δ	2.411	π	2.702	π
$\sum(fq)^2$	.082	.467	.101	.064

TABLE 5-2 (a)

EFFECT OF INITIAL CONDITIONS ON SOLUTION PRINCIPAL MODE (2,2) OF UNDISTORTED CYLINDER $N^1 = 2$, $N^2 = 3$

PARAMETER	INITIAL CONDITIONS $[R_1 - R_8, R_9]$		
	[1,1]	[.1,1][1,10^{-5}]	
x_N^1	-.163	-.163	-.165
x_N^2	.025	-.084	-.026
y_N^1	1.037	1.037	1.038
y_N^2	.004	.034	.022
w_N^1	.460	.463	.454
w_N^2	.003	-.002	.016
z_N^1	.075	.070	.075
z_N^2	-.086	.170	.126
Δ	1.261	4.693	4.566
$\sum(fq)^2$	.300	.283	.294
		↑ Solution Oscillated ↑	

TABLE 5-2(b)

EFFECT OF INITIAL CONDITIONS ON SOLUTION PRINCIPAL MODE (2,2) OF DISTORTED CYLINDER $N^1 = 2$, $N^2 = 3$

PARAMETER	INITIAL CONDITIONS $[R_1 - R_8, R_9]$	
	$[1,1][1,10^{-5}][.5,1]$ $[.1,1][1,.1]$	$[.5,10^{-5}]$ $[.1,.1]$
x_N^1	-.029	-.074
x_N^2	-.027	.236
y_N^1	.622	.771
y_N^2	.236	.023
w_N^1	.218	.183
w_N^2	.125	-.022
z_N^1	.038	.008
z_N^2	-.113	.052
Δ	1.434	2.411
$\sum(fq)^2$	.254	.082

TABLE 5-2(c)

EFFECT OF INITIAL CONDITIONS ON SOLUTION PRINCIPAL MODE (2,3) OF DISTORTED CYLINDER $N^1 = 3$, $N^2 = 4$

PARAMETER	INITIAL CONDITIONS $[R_1 - R_8, R_9]$	
	$[.5,10^{-5}][.5,1][.5,.5]$ $[5,10^{-5}][1,1]$	$[1,2][1,3]$ $[1,10^{-5}]$
x_N^1	.466	.633
x_N^2	.167	-.032
y_N^1	-.097	-.131
y_N^2	.038	-.202
w_N^1	-.038	-.028
w_N^2	.032	-.081
z_N^1	-.203	-.177
z_N^2	-.178	.002
Δ	4.861 or 1.424	2.702 or 3.581
$\sum(fq)^2$	.593	.101

APPENDIX I

FLOW DIAGRAM OF MICROPROGRAM FOR DATA SYSTEM

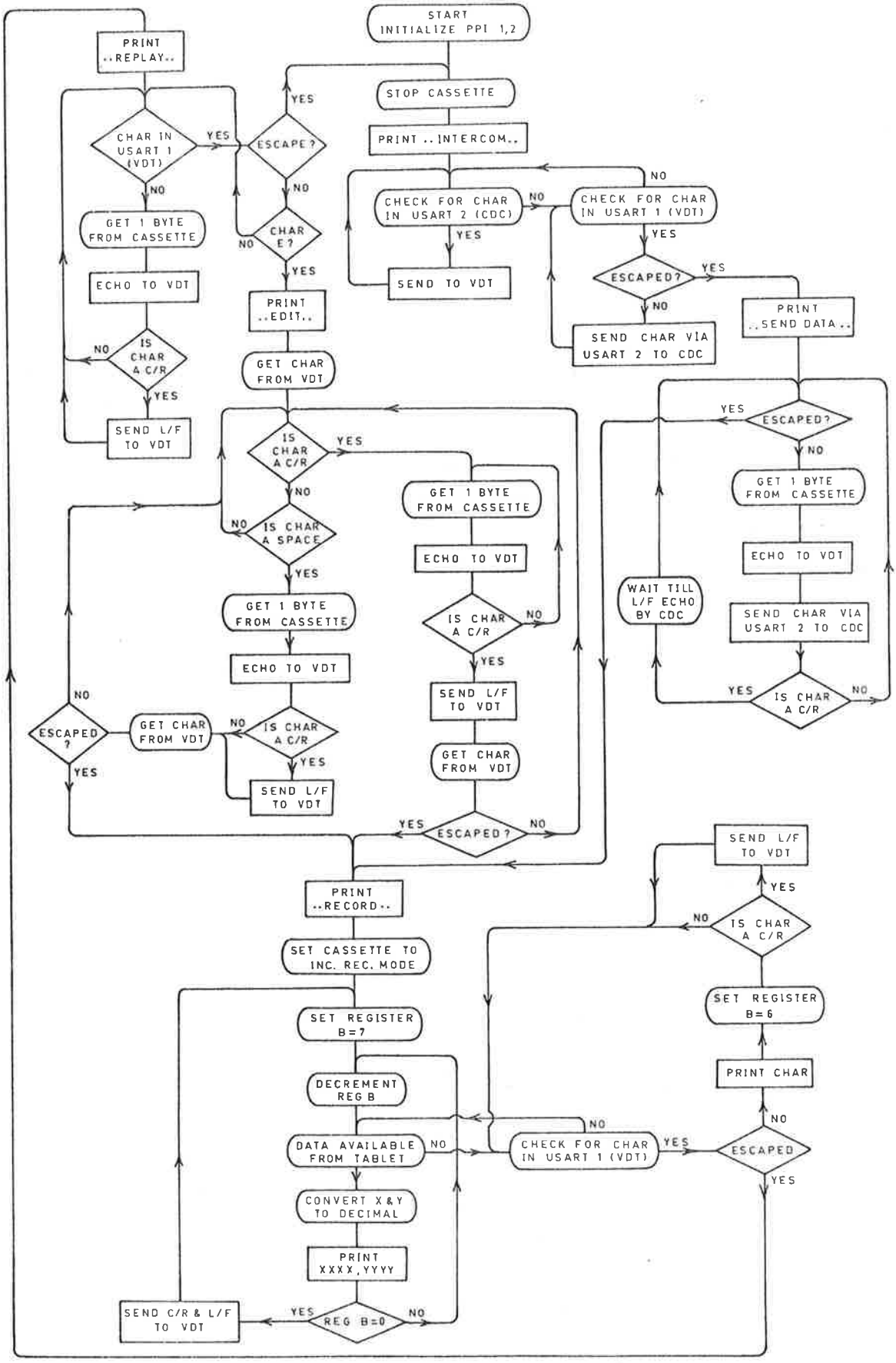

APPENDIX II

MATRIX FOR THE NORMAL EQUATIONS

$$A = \begin{bmatrix} K_1\sin(N^1\xi_1),\ K_1\cos(N^1\xi_1),\ S_1\sin(N^1\xi_1),\ S_1\cos(N^1\xi_1),\ - - - -,\ K_1\sin(N^2\xi_1),\ K_1\cos(N^2\xi_1),\ S_1\sin(N^2\xi_1),\ S_1\cos(N^2\xi_1) \\ K_2\sin(N^1\xi_2),\ K_2\cos(N^1\xi_2),\ S_2\sin(N^1\xi_2),\ S_2\cos(N^1\xi_2),\ - - - -,\ K_2\sin(N^2\xi_2),\ K_2\cos(N^2\xi_2),\ S_2\sin(N^2\xi_2),\ S_2\cos(N^2\xi_2) \\ \vdots \qquad\qquad\qquad\qquad\qquad\qquad\qquad\qquad\qquad\qquad\qquad\qquad\qquad\qquad\qquad\qquad\qquad\qquad \vdots \\ K_2\sin(N^1\xi_\tau),\ K_\tau\cos(N^1\xi_\tau),\ S_\tau\sin(N^1\xi_\tau),\ S_\tau\cos(N^1\xi_\tau),\ - - - -,\ K_\tau\sin(N^2\xi_\tau),\ K_\tau\cos(N^2\xi_\tau),\ S_\tau\sin(N^2\xi_\tau),\ S_\tau\cos(N^2\xi_\tau) \end{bmatrix}$$

APPENDIX III

THE STRAIN ENERGY INTEGRAL

Evaluation of the strain energy integral, equation (4.24) in the main text. There are 31 terms in the symmetric solutions (denote these St_1^s, St_2^s, ... etc) and 31 terms in the asymmetric solutions (denoted St_1^a, St_2^a, ... etc). The notation is defined in the main text.

$$St_1^s = \tfrac{1}{4} \sum_{ij\ell p} \lambda_i^2 U_{ij} U_{i\ell} (h_p^+ - h_p^-) \Pi^{j\ell p}$$

for St_1^a, replace $\Pi^{j\ell p}$ by $\Pi^p_{j\ell}$

$$St_2^s = -\tfrac{1}{4} \sum_{ij\ell pq} \lambda_i^3 U_{ij} W_{i\ell} (h_p^+ h_q^+ - h_p^- h_q^-) \Pi^{j\ell pq}$$

for St_2^a, replace $\Pi^{j\ell pq}$ by $\Pi^{pq}_{j\ell}$

$$St_3^s = \tfrac{1}{12} \sum_{ij\ell pqr} W_{ij} W_{i\ell} \lambda_i^4 (h_p^+ h_q^+ h_r^+ - h_p^- h_q^- h_r^-) \Pi^{j\ell pqr}$$

for St_3^a, replace $\Pi^{j\ell pqr}$ by $\Pi^{pqr}_{j\ell}$

$$St_4^s = \tfrac{1}{4} \sum_{ij\ell p} V_{ij} V_{i\ell} n_j n_\ell (h_p^+ - h_p^-) \Pi^{j\ell p}$$

for St_4^a, replace $\Pi^{j\ell p}$ by $\Pi^p_{j\ell}$

$$St_5^s = -\tfrac{1}{2} \sum_{ij\ell p} W_{ij} V_{i\ell} n_\ell (h_p^+ - h_p^-) \Pi^{j\ell p}$$

for St_5^a, replace $\Pi^{j\ell p}$ by $-\Pi^p_{j\ell}$

$$St_6^s = \tfrac{1}{4} \sum_{ij\ell p} W_{ij} W_{i\ell} (h_p^+ - h_p^-) \Pi^{j\ell p}$$

for St_6^a, replace $\Pi^{j\ell p}$ by $\Pi^p_{j\ell}$

$$St_7^s = \tfrac{1}{4} \sum_{ij\ell pq} V_{ij} W_{i\ell} n_j n_\ell^2 (h_p^+ h_q^+ - h_p^- h_p^-) \Pi^{j\ell pq}$$

for St_7^a, replace $\Pi^{j\ell pq}$ by $-\Pi_{j\ell}^{pq}$

$$St_8^s = -\tfrac{1}{4} \sum_{ij\ell pq} V_{ij} V_{i\ell} n_j n_\ell (h_p^+ h_q^+ - h_p^- h_q^-) \Pi^{j\ell pq}$$

for St_8^a, replace $\Pi^{j\ell pq}$ by $\Pi_{j\ell}^{pq}$

$$St_9^s = -\tfrac{1}{4} \sum_{ij\ell pq} W_{ij} W_{i\ell} n_\ell^2 (h_p^+ h_q^+ - h_p^- h_p^-) \Pi^{j\ell pq}$$

for St_9^a, replace $\Pi^{j\ell pq}$ by $\Pi_{j\ell}^{pq}$

$$St_{10}^s = \tfrac{1}{4} \sum_{ij\ell pq} W_{ij} V_{i\ell} n_\ell (h_p^+ h_q^+ - h_p^- h_q^-) \Pi^{j\ell pq}$$

for St_{10}^a, replace $\Pi^{j\ell pq}$ by $-\Pi_{j\ell}^{pq}$

$$St_{11}^s = \frac{1}{12} \sum_{ij\ell pqr} W_{ij} W_{i\ell} n_j^2 n_\ell^2 (h_p^+ h_q^+ h_r^+ - h_p^- h_q^- h_r^-) \Pi^{j\ell pqr}$$

for St_{11}^a, replace $\Pi^{j\ell pqr}$ by $\Pi_{j\ell}^{pqr}$

$$St_{12}^s = -\frac{1}{6} \sum_{ij\ell pqr} W_{ij} V_{i\ell} n_j^2 n_\ell (h_p^+ h_q^+ h_r^+ - h_p^- h_q^- h_r^-) \Pi^{j\ell pqr}$$

for St_{12}^a, replace $\Pi^{j\ell pqr}$ by $-\Pi_{j\ell}^{pqr}$

$$St_{13}^s = \frac{1}{12} \sum_{ij\ell pqr} V_{ij} V_{i\ell} n_j n_\ell (h_p^+ h_q^+ h_r^+ - h_p^- h_q^- h_r^-) \Pi^{j\ell pqr}$$

for St_{13}^a, replace $\Pi^{j\ell pqr}$ by $\Pi_{j\ell}^{pqr}$

$$St_{14}^s = -\frac{\nu}{2} \sum_{ij\ell p} U_{ij} V_{i\ell} \lambda_i n_\ell (h_p^+ - h_p^-) \Pi^{j\ell p}$$

for St_{14}^a, replace $\Pi^{j\ell p}$ by $-\Pi_{j\ell}^{p}$

$$St^s_{15} = \frac{\nu}{2} \sum_{ij\ell p} U_{ij} W_{i\ell} \lambda_i (h^+_p - h^-_p)\, \Pi^{j\ell p}$$

for St^a_{15}, replace $\Pi^{j\ell p}$ by $\Pi^p_{j\ell}$

$$St^s_{16} = \frac{\nu}{4} \sum_{ij\ell pq} U_{ij} W_{i\ell} \lambda_i n^2_\ell (h^+_p h^+_q - h^-_p h^-_q)\, \Pi^{j\ell pq}$$

for St^a_{16}, replace $\Pi^{j\ell pq}$ by $\Pi^{pq}_{j\ell}$

$$St^s_{17} = \frac{\nu}{4} \sum_{ij\ell pq} U_{ij} V_{i\ell} \lambda_i n_\ell (h^+_p h^+_q - h^-_p h^-_q) \Pi^{j\ell pq}$$

for St^a_{17}, replace $\Pi^{j\ell pq}$ by $-\Pi^{pq}_{j\ell}$

$$St^s_{18} = \frac{\nu}{4} \sum_{ij\ell pq} W_{ij} V_{i\ell} \lambda^2_i n_\ell (h^+_p h^+_q - h^-_p h^-_q)\, \Pi^{j\ell pq}$$

for St^a_{18}, replace $\Pi^{j\ell pq}$ by $-\Pi^{pq}_{j\ell}$

$$St^s_{19} = \frac{-\nu}{4} \sum_{ij\ell pq} W_{ij} W_{i\ell} \lambda^2_i (h^+_p h^+_q - h^-_p h^-_q)\, \Pi^{j\ell pq}$$

for St^a_{19}, replace $\Pi^{j\ell pq}$ by $\Pi^{pq}_{j\ell}$

$$St^s_{20} = \frac{\nu}{6} \sum_{ij\ell pqr} W_{ij} W_{i\ell} \lambda^2_i n^2_\ell (h^+_p h^+_q h^+_r - h^-_p h^-_q h^-_r)\, \Pi^{j\ell pqr}$$

for St^a_{20}, replace $\Pi^{j\ell pqr}$ by $\Pi^{pqr}_{j\ell}$

$$St^s_{21} = -\frac{\nu}{6} \sum_{ij\ell pqr} W_{ij} V_{i\ell} \lambda^2_i n_\ell (h^+_p h^+_q h^+_r - h^-_p h^-_q h^-_r)\, \Pi^{j\ell pqr}$$

for St^a_{21}, replace $\Pi^{j\ell pqr}$ by $-\Pi^{pqr}_{j\ell}$

$$St^s_{22} = \frac{(1-\nu)}{8} \sum_{ij\ell p} V_{ij} V_{i\ell} \lambda^2_i (h^+_p - h^-_p)\, \Pi^p_{j\ell}$$

for St^a_{22}, replace $\Pi^p_{j\ell}$ by $\Pi^{j\ell p}$

$$St^s_{23} = -\frac{(1-\nu)}{4} \sum_{ij\ell p} V_{ij} U_{i\ell} \lambda_i n_\ell (h^+_p - h^-_p)\, \Pi^p_{j\ell}$$

for St^a_{23}, replace $\Pi^p_{j\ell}$ by $-\Pi^{j\ell p}$

$$St^s_{24} = \frac{(1-\nu)}{8} \sum_{ij\ell p} U_{ij} U_{i\ell} n_j n_\ell (h^+_p - h^-_p)\, \Pi^p_{j\ell}$$

for St^a_{24}, replace $\Pi^p_{j\ell}$ by $\Pi^{j\ell p}$

$$St^s_{25} = \frac{(1-\nu)}{4} \sum_{ij\ell pq} V_{ij} W_{i\ell} \lambda^2_i n_\ell (h^+_p h^+_q - h^-_p h^-_q)\, \Pi^{pq}_{j\ell}$$

for St^a_{25}, replace $\Pi^{pq}_{j\ell}$ by $-\Pi^{j\ell pq}$

$$St^s_{26} = -\frac{(1-\nu)}{4} \sum_{ij\ell pq} V_{ij} V_{i\ell} \lambda^2_i (h^+_p h^+_q - h^-_p h^-_q)\, \Pi^{pq}_{j\ell}$$

for St^a_{26}, replace $\Pi^{pq}_{j\ell}$ by $\Pi^{j\ell pq}$

$$St^s_{27} = -\frac{(1-\nu)}{4} \sum_{ij\ell pq} U_{ij} W_{i\ell} n_j \lambda_i n_\ell (h^+_p h^+_q - h^-_p h^-_q)\, \Pi^{pq}_{j\ell}$$

for St^a_{27}, replace $\Pi^{pq}_{j\ell}$ by $\Pi^{j\ell pq}$

$$St^s_{28} = \frac{(1-\nu)}{4} \sum_{ij\ell pq} U_{ij} V_{i\ell} n_j \lambda_i (h^+_p h^+_q - h^-_p h^-_q)\, \Pi^{pq}_{j\ell}$$

for St^a_{28}, replace $\Pi^{pq}_{j\ell}$ by $-\Pi^{j\ell pq}$

$$St^s_{29} = \frac{(1-\nu)}{6} \sum_{ij\ell pqr} W_{ij} W_{i\ell} \lambda^2_i n_j n_\ell (h^+_p h^+_q h^+_r - h^-_p h^-_q h^-_r)\, \Pi^{pqr}_{j\ell}$$

for St^a_{29}, replace $\Pi^{pqr}_{j\ell}$ by $\Pi^{j\ell pqr}$

$$St^s_{30} = -\frac{(1-\nu)}{3} \sum_{ij\ell pqr} W_{ij} V_{i\ell} \lambda^2_i n_j (h^+_p h^+_q h^+_r - h^-_p h^-_q h^-_r)\, \Pi^{pqr}_{j\ell}$$

for St^a_{30}, replace $\Pi^{pqr}_{j\ell}$ by $-\Pi^{j\ell pqr}$

$$St^{s}_{31} = \frac{(1-\nu)}{6} \sum_{ij\ell pqr} V_{ij} V_{i\ell} \lambda_i^2 (h^+_p h^+_q h^+_r - h^-_p h^-_q h^-_r) \; \Pi^{pqr}_{j\ell}$$

for St^{a}_{31}, replace $\Pi^{pqr}_{j\ell}$ by $-\Pi^{j\ell pqr}$.

APPENDIX IV

COEFFICIENTS OF THE GENERALIZED STIFFNESS AND MASS MATRICES

Coefficients of matrix D. Denote D^s for symmetric solutions and D^a for asymmetric solutions.

$k = 1,M \qquad i = 0,N \qquad j = 0,N \qquad p = 0,P$

The matrix is a $3M(N+1)$ square matrix. Put $g = 3(k-1)(n+1)$.

The non-zero coefficients of matrix D are:

$D^s[g+i+1,\ g+j+1]$

$$= \sum_p (\lambda_k^2 \Pi^{ijp} + \frac{(1-\nu)}{2} ij\, \Pi^p_{ij})(h_p^+ - h_p^-)$$

$D^s[g+i+1,\ g+j+N+2]$

$$= \sum_p \left[(-\nu \lambda_k j \Pi^{ijp} - \frac{(1-\nu)}{2} \lambda_k i \Pi^p_{ij})(h_p^+ - h_p^-) \right.$$

$$\left. + \tfrac{1}{2} \sum_q (\nu \lambda_k j \Pi^{ijpq} + (1-\nu)\lambda_k i \Pi^{pq}_{ij})(h_p^+ h_q^+ - h_p^- h_q^-) \right]$$

$D^s[g+i+1,\ g+j+2N+3]$

$$= \sum_p \left\{ \nu \lambda_k \Pi^{ijp} (h_p^+ - h_p^-) \right.$$

$$\left. - \tfrac{1}{2} \sum_q \left[(\lambda_k^3 + \nu \lambda_k j^2) \Pi^{ijpq} - (1-\nu)\lambda_k ij \Pi^{pq}_{ij} \right] (h_p^+ h_q^+ - h_p^- h_q^-) \right\}$$

$$D^S[g+i+N+2,\ g+j+1]$$

$$= \sum_p \left\{ (-\nu\lambda_k i\Pi^{ijp} - \frac{(1-\nu)}{2}\lambda_k j\Pi^p_{ij})(h^+_p - h^-_p) \right.$$

$$\left. + \tfrac{1}{2}\sum_q (\nu\lambda_k i\Pi^{ijpq} + (1-\nu)\lambda_k j\Pi^{pq}_{ij})(h^+_p h^+_q - h^-_p h^-_q) \right\}$$

$$D^S[g+i+N+2,\ g+j+N+2]$$

$$= \sum_p \left\{ (j\,i\Pi^{ijp} + \frac{(1-\nu)}{2}\lambda^2_k \Pi^p_{ij})(h^+_p - h^-_p) \right.$$

$$+ \sum_q \left[-\tfrac{1}{2}(ij\Pi^{ijpq} + (1-\nu)\lambda^2_k \Pi^{pq}_{ij})(h^+_p h^+_q - h^-_p h^-_q) \right.$$

$$\left.\left. + \sum_r \tfrac{1}{3}(ij\Pi^{ijpqr} + 2(1-\nu)\lambda^2_k \Pi^{pqr}_{ij})(h^+_p h^+_q h^+_r - h^-_p h^-_q h^-_r) \right] \right\}$$

$$D^S[g+i+N+2, g+j+2N+3]$$

$$= \sum_p \left[-i\Pi^{ijp}(h^+_p - h^-_p) \right.$$

$$+ \sum_q \left\{ \tfrac{1}{2}[(ij^2 + i + \nu\lambda^2_k i)\Pi^{ijpq} + (1-\nu)\lambda^2_k j\Pi^{pq}_{ij}](h^+_p h^+_q - h^-_p h^-_q) \right.$$

$$\left.\left. - \sum_r \tfrac{1}{3}[(ij^2 + \nu\lambda^2_k i)\Pi^{ijpqr} + 2(1-\nu)\lambda^2_k j\Pi^{pqr}_{ij}](h^+_p h^+_q h^+_r - h^-_p h^-_q h^-_r) \right\} \right]$$

$$D^s[g+i+2N+3,\ g+j+1]$$

$$= \sum_p \Bigg\{ \nu\lambda_k \Pi^{ijp}(h_p^+ - h_p^-)$$

$$+ \tfrac{1}{2} \sum_q \Big\{ (-\lambda_k^3 + \nu\lambda_k i^2)\Pi^{ijpq} - (1-\nu)\lambda_k ij \Pi_{ij}^{pq} \Big\} (h_p^+ h_q^+ - h_p^- h_q^-) \Bigg\}$$

$$D^s[g+i+2N+3,\ g+j+N+2]$$

$$= \sum_p \Bigg\{ -j\Pi^{ijp}(h_p^+ - h_p^-)$$

$$+ \sum_p \Big\{ \tfrac{1}{2}[(ji^2 + j + \nu\lambda_k^2 j)\Pi^{ijpq} + (1-\nu)\lambda_k^2 i \Pi_{ij}^{pq}](h_p^+ h_q^+ - h_p^- h_q^-)$$

$$- \sum_r \tfrac{1}{3}[(i^2 j + \nu\lambda_k^2 j)\Pi^{ijpqr} + 2(1-\nu)\lambda_k^2 i \Pi_{ij}^{pqr}](h_p^+ h_q^+ h_r^+ - h_p^- h_q^- h_r^-) \Big\} \Bigg\}$$

$$D^s[g+i+2N+3,\ g+j+2N+3]$$

$$= \sum_p \Bigg\{ \Pi^{ijp}(h_p^+ - h_p^-)$$

$$+ \sum_q \Big\{ \tfrac{1}{2}(-j^2 - i^2 - \nu\lambda_k^2)\Pi^{ijpq}(h_p^+ h_q^+ - h_p^- h_q^-)$$

$$+ \sum_r \tfrac{1}{3} \Big[(\lambda_k^4 + i^2 j^2 + \nu\lambda_k^2 [i^2 + j^2])\Pi^{ijpqr}$$

$$+ 2(1-\nu)\lambda_k^2 ij \Pi_{ij}^{pqr} \Big] (h_p^+ h_q^+ h_r^+ - h_p^- h_q^- h_r^-) \Big\} \Bigg\}$$

The asymmetric solutions D^a are obtained by firstly changing the i,j notation in the Π functions from subscript to superscript and vice versa and changing the signs of the following groups of coefficients

$$D^s[g+i+1,\ g+j+N+2]$$

$$D^s[g+i+N+2,\ g+j+1]$$

$$D^s[g+i+N+2,\ g+j+2N+3]$$

$$D^s[g+i+2N+3,\ g+j+N+2]$$

Similarly, the coefficients of matrices Q^s and Q^a which are also $3M(N+1)$ square matrices are as follows

$$Q^s[g+i+1,\ g+j+1] = \sum_p (h_p^+ - h_p^-)\,\Pi^{ijp}$$

$$Q^s[g+i+N+2,\ g+j+N+2] = \sum_p (h_p^+ - h_p^-)\,\Pi_{ij}^{p}$$

$$Q^s[g+i+2N+3,\ g+j+2N+3] = \sum_p (h_p^+ - h_p^-)\,\Pi^{ijp}$$

For the asymmetric coefficients, simply change the i,j notation in the Π functions from subscript to superscript and vice-versa.

APPENDIX V

Solution of the Π functions of the form shown in equation (4.6) of the text.

$$\Pi^{ijp} = \int_0^{2\pi} \cos iX \cos jX \cos pX \, dX$$

$$= I_1 + I_2 + I_3 + I_4 \qquad \text{(A5.1)}$$

which are all zero unless

$$i + j + p = 0 \quad , \quad I_1 = \pi/2$$

$$i - j - p = 0 \quad , \quad I_2 = \pi/2$$

$$i + j - p = 0 \quad , \quad I_3 = \pi/2$$

$$i - j + p = 0 \quad , \quad I_4 = \pi/2$$

$$\Pi_{ij}^{p} = \int_0^{2\pi} \cos pX \sin iX \sin jX \, dX$$

$$= I_1 + I_2 + I_3 + I_4 \qquad \text{(A5.2)}$$

which are all zero unless

$$i + j + p = 0 \quad , \quad I_1 = -\pi/2$$

$$i - j - p = 0 \quad , \quad I_2 = +\pi/2$$

$$i + j - p = 0 \quad , \quad I_3 = -\pi/2$$

$$i - j + p = 0 \quad , \quad I_4 = +\pi/2$$

$$\Pi^{ijpq} = \int_0^{2\pi} \cos iX \cos jX \cos pX \cos qX \, dX$$

$$= I_1 + I_2 + \ldots + I_8 \qquad \text{(A5.3)}$$

which are all zero unless

$$i + j + p + q = 0 \quad , \quad I_1 = \pi/2$$
$$i + j - p - q = 0 \quad , \quad I_2 = \pi/2$$
$$i + j + p - q = 0 \quad , \quad I_3 = \pi/2$$
$$i + j - p + q = 0 \quad , \quad I_4 = \pi/2$$
$$i - j + p + q = 0 \quad , \quad I_5 = \pi/2$$
$$i - j - p - q = 0 \quad , \quad I_6 = \pi/2$$
$$i - j + p - q = 0 \quad , \quad I_7 = \pi/2$$
$$i - j - p + q = 0 \quad , \quad I_8 = \pi/2$$

$$\Pi_{ij}^{pq} = \int_0^{2\pi} \sin iX \sin jX \cos pX \cos qX \, dX$$

$$= I_1 + I_2 + \ldots + I_8 \qquad \text{(A5.4)}$$

which are all zero unless

$$i + j + p + q = 0 \quad , \quad I_1 = -\pi/2$$
$$i + j - p - q = 0 \quad , \quad I_2 = -\pi/2$$
$$i + j + p - q = 0 \quad , \quad I_3 = -\pi/2$$
$$i + j - p + q = 0 \quad , \quad I_4 = -\pi/2$$
$$i - j + p + q = 0 \quad , \quad I_5 = +\pi/2$$
$$i - j - p - q = 0 \quad , \quad I_6 = +\pi/2$$
$$i - j + p - q = 0 \quad , \quad I_7 = +\pi/2$$
$$i - j - p + q = 0 \quad , \quad I_8 = +\pi/2$$

$$\Pi^{ijpqr} = \int_0^{2\pi} \cos iX \cos jX \cos pX \cos qX \cos rX \, dX$$

$$= I_1 + I_2 + \ldots + I_{16} \qquad \text{(A5.5)}$$

which are all zero unless

$$i + j + p + q + r = 0 \quad , \quad I_1 = \pi/2$$
$$i - j - p - q - r = 0 \quad , \quad I_2 = \pi/2$$
$$i + j + p - q - r = 0 \quad , \quad I_3 = \pi/2$$
$$i - j - p + q + r = 0 \quad , \quad I_4 = \pi/2$$
$$i + j + p + q - r = 0 \quad , \quad I_5 = \pi/2$$
$$i - j - p - q + r = 0 \quad , \quad I_6 = \pi/2$$
$$i + j + p - q + r = 0 \quad , \quad I_7 = \pi/2$$
$$i - j - p + q - r = 0 \quad , \quad I_8 = \pi/2$$
$$i + j - p + q + r = 0 \quad , \quad I_9 = \pi/2$$
$$i - j + p - q - r = 0 \quad , \quad I_{10} = \pi/2$$
$$i + j - p - q - r = 0 \quad , \quad I_{11} = \pi/2$$
$$i - j + p + q + r = 0 \quad , \quad I_{12} = \pi/2$$
$$i + j - p + q - r = 0 \quad , \quad I_{13} = \pi/2$$
$$i - j + p - q + r = 0 \quad , \quad I_{14} = \pi/2$$
$$i + j - p - q + r = 0 \quad , \quad I_{15} = \pi/2$$
$$i - j + p + q - r = 0 \quad , \quad I_{16} = \pi/2$$

$$\Pi_{ij}^{pqr} = \int_0^{2\pi} \sin iX \sin jX \cos pX \cos qX \cos rX \, dX$$

$$= I_1 + I_2 + \ldots + I_{16} \qquad \text{(A5.6)}$$

which are all zero unless

$$i + j + p + q + r = 0 \quad , \quad I_1 = -\pi/2$$

$$i - j - p - q - r = 0 \quad , \quad I_2 = +\pi/2$$

$$i + j + p - q - r = 0 \quad , \quad I_3 = -\pi/2$$

$$i - j - p + q + r = 0 \quad , \quad I_4 = +\pi/2$$

$$i + j + p + q - r = 0 \quad , \quad I_5 = -\pi/2$$

$$i - j - p - q + r = 0 \quad , \quad I_6 = +\pi/2$$

$$i + j + p - q + r = 0 \quad , \quad I_7 = -\pi/2$$

$$i - j - p + q - r = 0 \quad , \quad I_8 = +\pi/2$$

$$i + j - p + q + r = 0 \quad , \quad I_9 = -\pi/2$$

$$i - j + p - q - r = 0 \quad , \quad I_{10} = +\pi/2$$

$$i + j - p - q - r = 0 \quad , \quad I_{11} = -\pi/2$$

$$i - j + p + q + r = 0 \quad , \quad I_{12} = +\pi/2$$

$$i + j - p + q - r = 0 \quad , \quad I_{13} = -\pi/2$$

$$i - j + p - q + r = 0 \quad , \quad I_{14} = +\pi/2$$

$$i + j - p - q + r = 0 \quad , \quad I_{15} = -\pi/2$$

$$i - j + p + q - r = 0 \quad , \quad I_{16} = +\pi/2$$

APPENDIX VI

SOUND RADIATION FROM CYLINDERS

The theory of time-averaged holography has been developed in this thesis to such a stage that the vibration components of an excited arbitrary surface at a single frequency may be determined without difficulty. In particular the component normal to the surface is of interest to the study of sound radiation from vibrating surfaces. In this Appendix the radiation efficiency of three steel cylinders is measured and compared with the theoretical predictions of Junger and Feit [148] assuming normal mode shapes.

A6.1 THEORY OF SOUND RADIATION FROM VIBRATING CIRCULAR CYLINDERS

The theory of sound radiation from circular cylinders presented here is taken from Junger and Feit [148]. Consider a cylinder of length L and mean radius a_o with shear-diaphragm ends. The acceleration of the vibration component normal to the surface may be expressed as a combination of the normal modes

$$\ddot{w}(X,\theta) = \sum_{m,n} \ddot{W}_{mn} \cos k_m X \cos n\theta \qquad (A6.1)$$

where $k_m = \frac{m\pi}{L}$, θ is the circumferential co-ordinate and X the co-ordinate along the generator measured from the body centre of the cylinder as shown in Fig. A6-1.

The pressure field may be expressed in the same form as the series

$$p_r(r,X,\theta) = \sum_{m,n} P_{mn} R_{mn}(r) \cos k_m X \cos n\theta \qquad (A6.2)$$

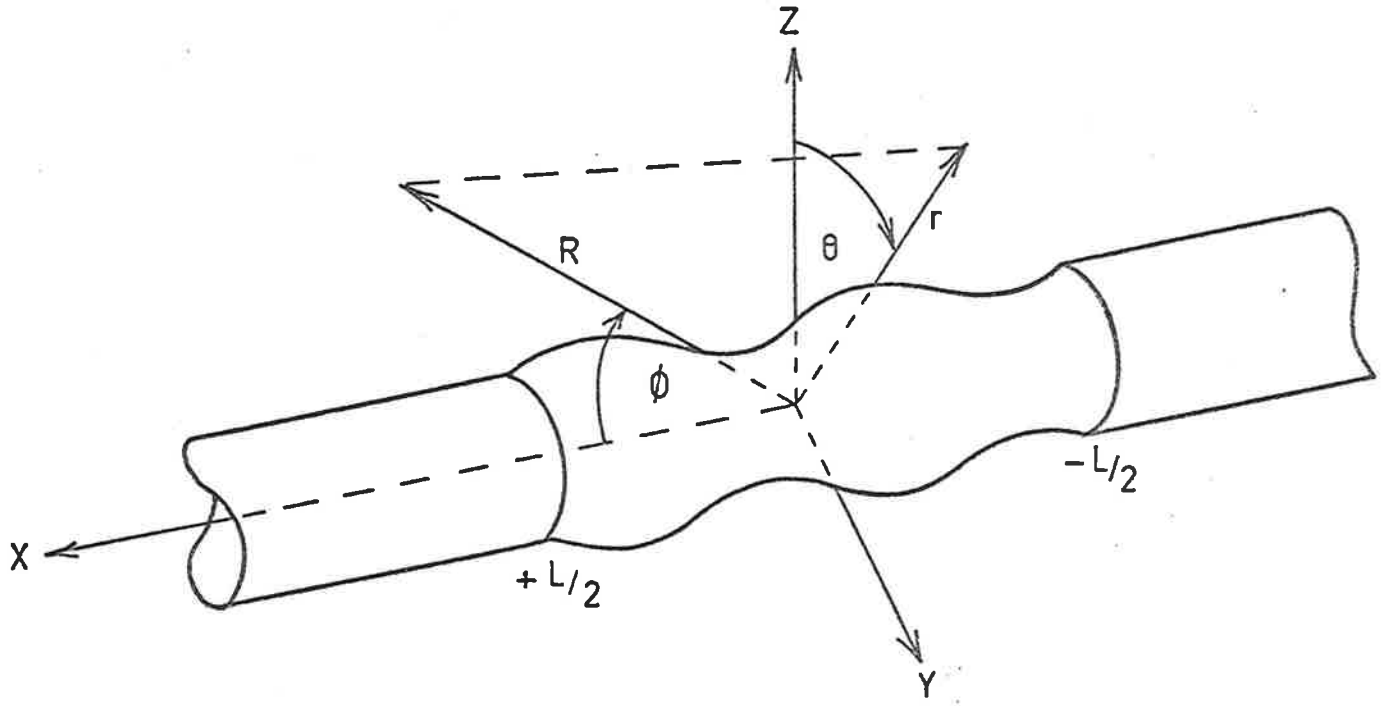

FIG. A6-1 CO-ORDINATE SYSTEM FOR A VIBRATING CYLINDER OF FINITE LENGTH WITH CYLINDRICAL BAFFLE.

where P_{mn} are coefficients to be determined from the boundary condition

$$\frac{\partial p_r}{\partial r}(r,X,\theta) = -\rho \ddot{w}(X,\theta) \Big|_{r=a_o} \tag{A6.3}$$

The radial harmonic $R_{mn}(r)$ is found first by noting that for steady state conditions it satisfies the three-dimensional Helmholtz equation which reduces to

$$[\frac{\partial^2}{\partial r^2} + \frac{1}{r}\frac{\partial}{\partial r} - \frac{n^2}{r^2} + (k^2 - k_m^2)]\, R_{mn}(r) = 0 \tag{A6.4}$$

This is Bessel's differential equation whose solutions are linear combinations of Bessel functions of the first and second kind and for outgoing waves

$$R_{mn}(r) = J_n[(k^2 - k_m^2)^{\frac{1}{2}} r] + i Y_n[(k^2 - k_m^2)^{\frac{1}{2}} r]$$

$$= H_n[(k^2 - k_m^2)^{\frac{1}{2}} r] \tag{A6.5}$$

where H_n is the Hankel function of the first kind.

Hence combining equations (A6.5) and (A6.2) and substituting the general solution into the boundary condition, equation (A6.3), and solving for P_{mn} gives

$$P_{mn} = \frac{\rho \ddot{W}_{mn}}{(k^2 - k_m^2)^{\frac{1}{2}} H_n'[(k^2 - k_m^2)^{\frac{1}{2}} a_o]} \tag{A6.6}$$

Hence the pressure field is

$$p_r(r,X,\theta) = -\rho \sum_{m,n} \frac{\ddot{W}_{mn} H_n[(k^2 - k_m^2)^{\frac{1}{2}} r]}{(k^2 - k_m^2)^{\frac{1}{2}} H_n'[(k^2 - k_m^2)^{\frac{1}{2}} a_o]} \cos k_m X \cos n\theta \tag{A6.7}$$

Considering now a finite number of standing waves $\cos k_m X$ confined to the region $|X| \leq L/2$ and applying the stationary-phase approximation to the far field gives

$$p_r(R,\theta,\phi) = \frac{2\rho e^{ikR} k_m (-1)^{m-1} \{ \begin{matrix} \cos \\ \sin \end{matrix} (kL\cos\phi/2)\}}{\pi k R \sin\phi (k_m^2 - k^2\cos^2\phi)}$$

$$\times \sum_n \frac{\ddot{W}_n (-1)^{n-1} \cos n\theta}{H_n'(k a_o \sin\phi)} \qquad \text{(A6.8)}$$

where cosine is used if m is odd and sine is used if m is even.

The total sound power Π is obtained by integrating the radial component of the sound intensity vector over a large sphere of radius R and hence

$$\Pi = \frac{R^2}{2\rho c_o} \int_o^{2\pi} \int_o^{\pi} |p(R,\theta,\phi)|^2 \sin\phi \, d\phi \, d\theta \qquad \text{(A6.9)}$$

and on substituting equation (A6.8) into equation (A6.9) gives

$$\Pi = \frac{2\rho L^2 \ddot{W}_n^2}{c_o \pi^3 k^2 m^2} \int_o^{\pi} \frac{\{ \begin{matrix} \cos^2 \\ \sin^2 \end{matrix} (kL\cos\phi/2)\}}{\sin\phi |H_n'(ka_o\sin\phi)|^2 [1 - \frac{k^2\cos^2\phi}{k_m^2}]} \, d\phi \qquad \text{(A6.10)}$$

for a single mode. Using the definition for radiation efficiency [146],

$$\sigma = \frac{\Pi}{\rho c_o S_A \langle \dot{W}^2 \rangle_{st}} \qquad \text{(A6.11)}$$

where $\langle \dot{W}^2 \rangle_{st}$ is the mean square velocity normal to the surface averaged over space and time and S_A is the radiation area very nearly equal to

$2\pi a_o L$, and noting that

$$\frac{(\ddot{W}_n)}{\omega^2} = 8 < \dot{W}_n^2 >_{st} \qquad (A6.12)$$

which results from averaging over two angular co-ordinates and time, then substituting equation (A6.10) into equation (A6.11) gives the final result also derived by Rennison [164]

$$\sigma_{mn} = \frac{16L}{\pi^4 m^2 a_o} \int_o^{\pi/2} \frac{\{ \begin{matrix} \cos^2 \\ \sin^2 \end{matrix} (K_a L \cos\phi / 2a_o) \}}{\sin\phi \left| H_n'(K_a \sin\phi) \right|^2 [1 - \{ \frac{K_a L \cos\phi}{a_o m\pi} \}^2]} \, d\phi \qquad (A6.13)$$

where K_a is the non-dimensional frequency parameter given by $K_a = \frac{\omega a_o}{c_o}$.

A6.2 EXPERIMENTAL ANALYSIS AND RESULTS

Three steel cylinders of length L = 398.8mm, mean radius a_o = 39.29mm and wall thicknesses 2.050mm, 2.845mm and 4.597mm were machined as in Fig. A6-2. Two stock cylinders of length 600mm and thickness 6mm acted as baffles and were machined at one end to form a thin ridge which fits perfectly into the lip at the edge of each cylinder thereby ensuring shear-diaphragm end conditions. Four 6mm diameter supporting rods held the structure in place with a little tension from springs mounted on one end as shown in Fig. A6-2. Pieces of mineral fibre were stuffed into the ends of the baffles to ensure an anechoic termination and eliminate the possibility of standing waves in the medium inside the structure. Although the theory outlined in the last section requires infinitely long baffles (see Fig. A6-2) the structure is at least five wavelengths in dimension at the lowest frequency considered and hence the error is assumed negligible. A

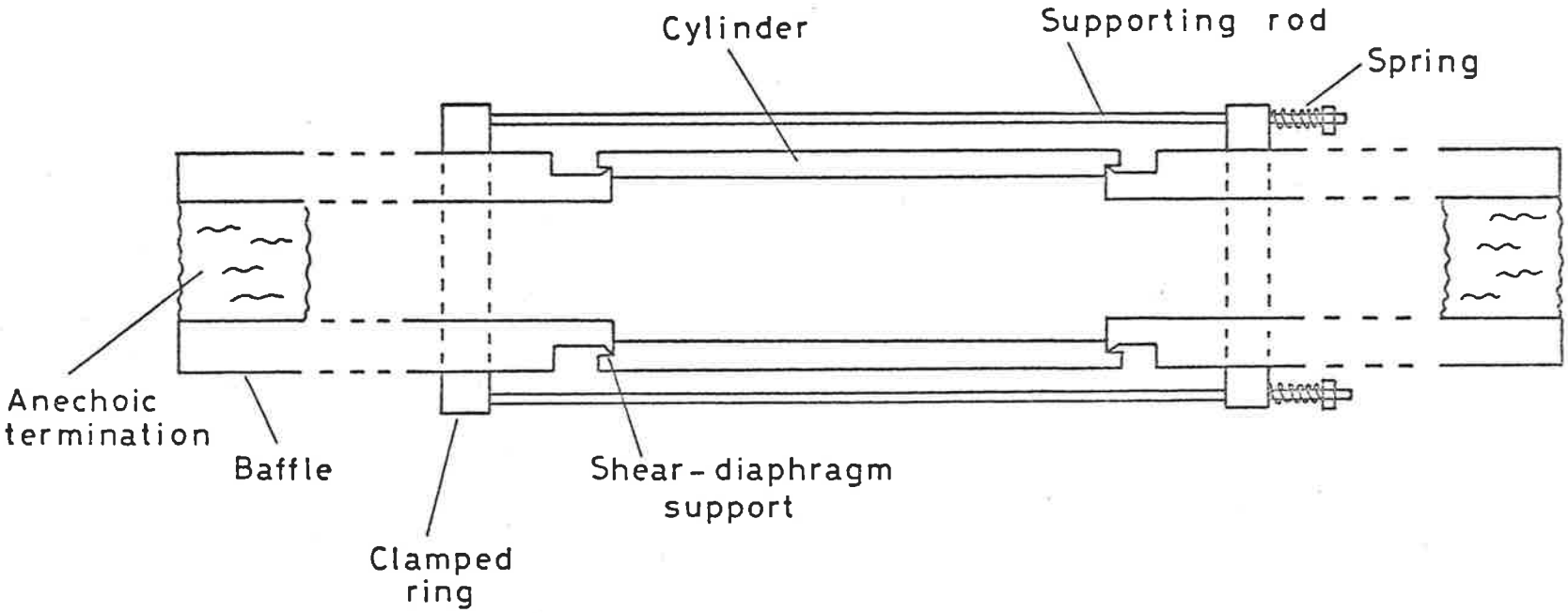

FIG. A6-2 SCHEMATIC CROSS-SECTION OF CYLINDER AND BAFFLES.

photograph of the apparatus is shown in Fig. A6-3.

The cylinder and supporting structure were placed in a reverberation room of volume $V_R = 181.5\,m^3$ and surface area $A_R = 195\,m^2$. The cylinder was excited using the modal driving system described in Section 2.2.2 and the acceleration monitored using a second B & K spectrometer and accelerometer.

The sound level in the reverberation room was measured using a B & K ½" microphone type 4133 and 2107 spectrometer connected to a data acquisition system [165]. The microphone scans the reverberation room using a traverse system and the sound field is further diffused by a rotating vane assembly (see Fig. A6-4). The data acquisition system samples and stores the output of the 2107 spectrometer at intervals of 1 second and at the end of one traverse of the room calculates the mean and standard deviation.

The reverberation time T_{60} of the room was measured in the normal way in third-octave bands and hence the Power Level calculated from [166]

$$L_w = L_p + 10 \log V_R - 10 \log T_{60} + 10 \log \left(1 + \frac{A_R c_o}{8 f V_R}\right) - 13.5 \qquad \text{(A6.14)}$$

where L_p in the sound level averaged over space and time determined using the data acquisition system. Hence, using equation (A6.11) the experimental radiation efficiency is

$$\sigma = 7.545 \frac{f^2\, 10^{(L_w - 120)/10}}{\ddot{W}^2} \qquad \text{(A6.15)}$$

where $\ddot{W}$ is the peak acceleration of the cylinder surface at a radial antinode.

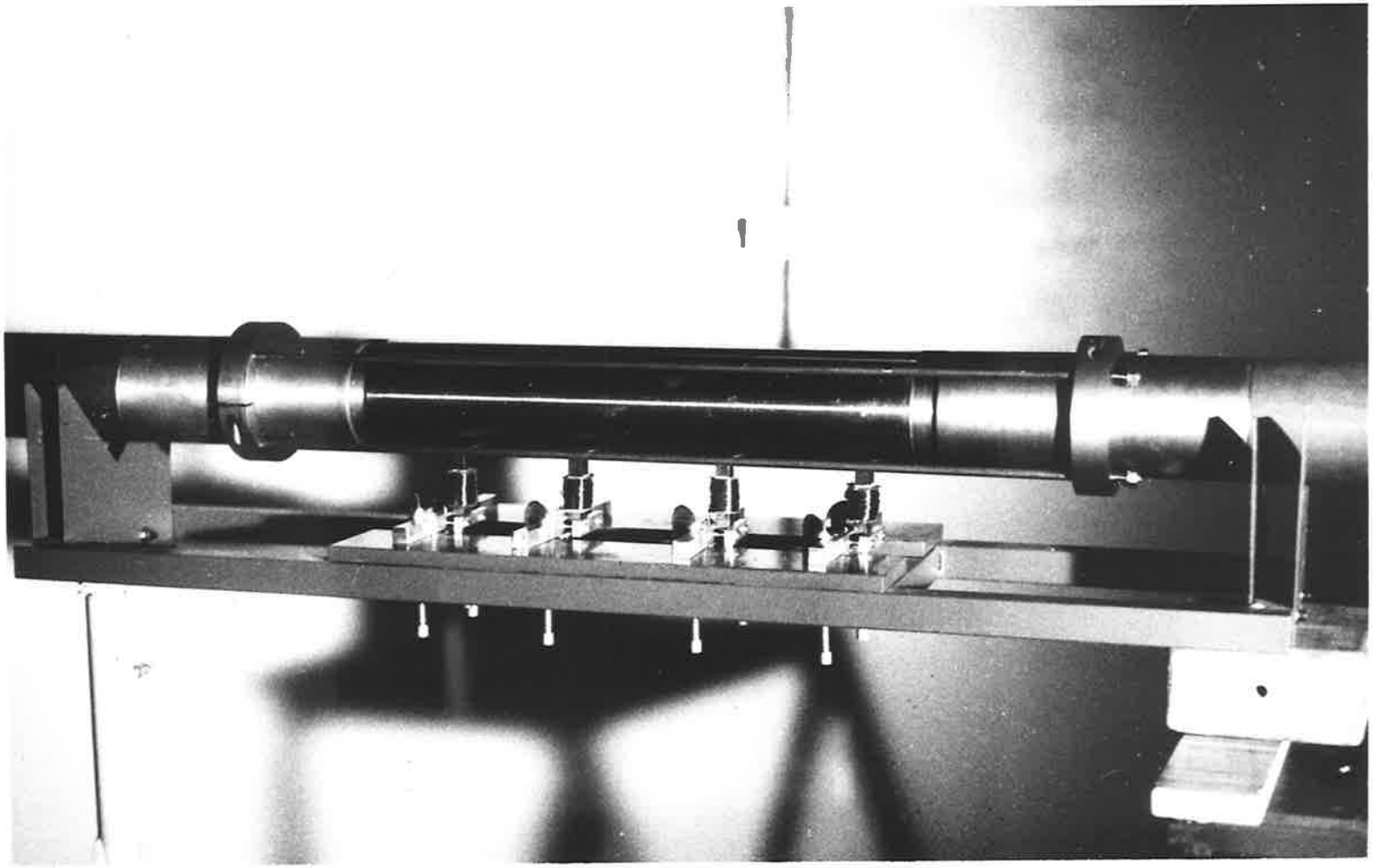

FIG. A6-3

Cylinder and supporting structure.

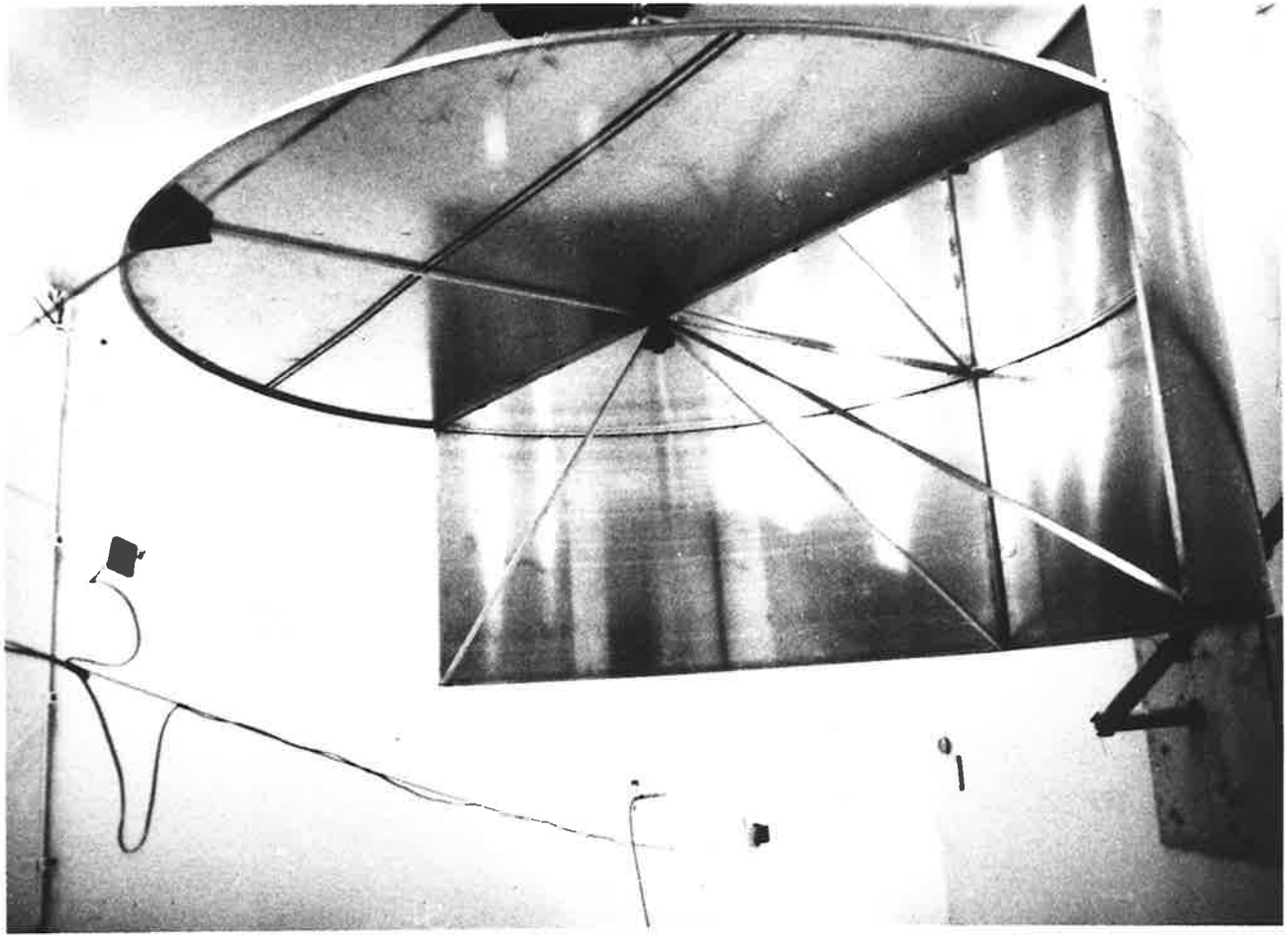

FIG. A6-4

The reverberation room, rotating vane

and microphone traverse.

Figs. A6-5(a) - (e) show the experimental results together with the theoretical curves calculated from equation (A6.13) using numerical integration. In general the experimental data are 5-10dB down from the theoretical curves which cannot be explained. To eliminate the possibility that the baffles are too small they were completely removed and new data taken. As expected, sound radiation from the lower order modes was dramatically reduced but for the higher order modes the results were identical. The error is not in the frequency parameter K_a as measured frequencies are less than 5% in error from theoretically determined frequencies.

However, assuming that the problem is resolved then the radiation efficiency of the distorted pipe may be calculated using the solution presented in Chapter 4 and compared with measured values.

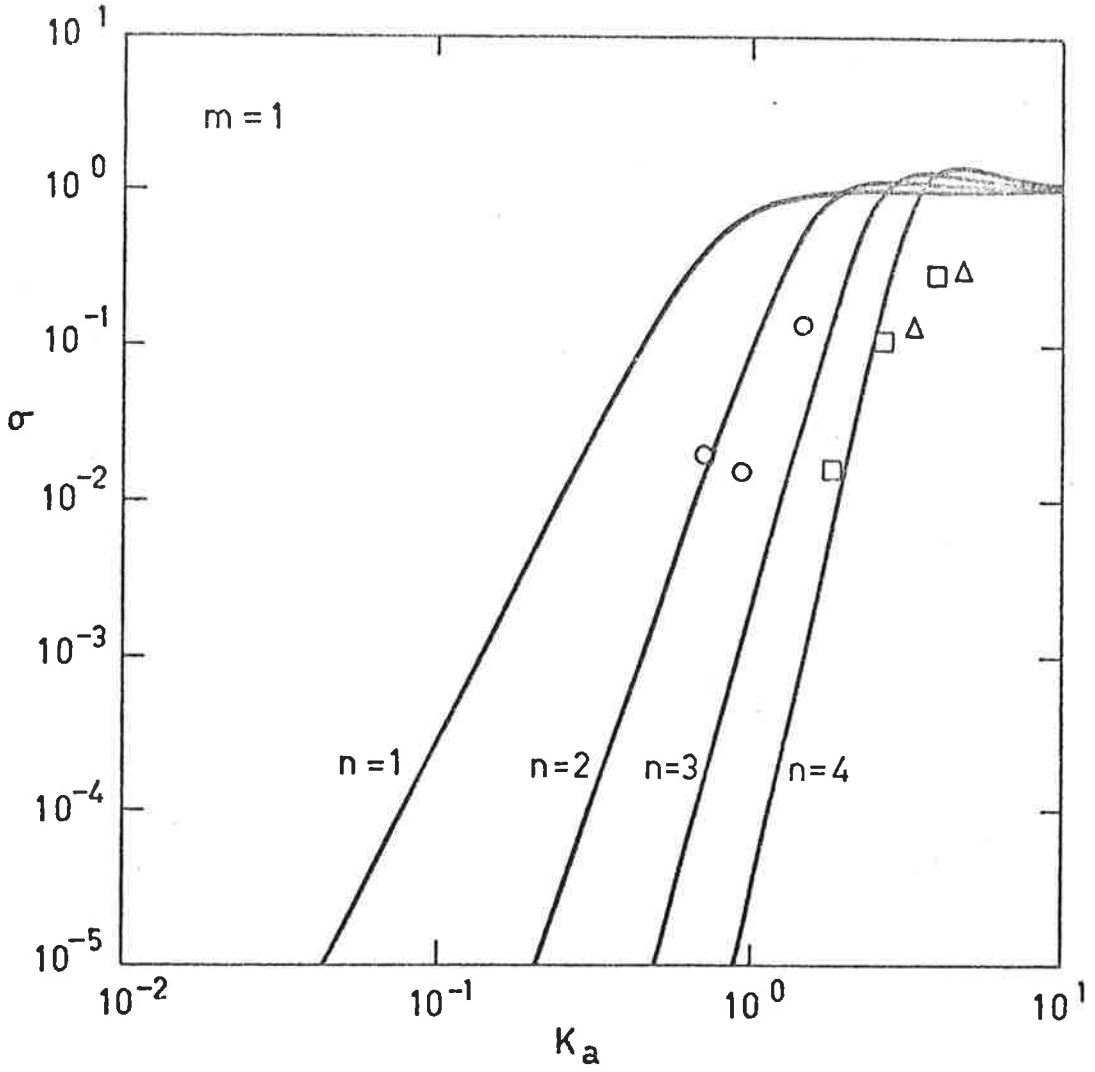

FIG. A6-5 (a) RADIATION EFFICIENCY OF STEEL CYLINDERS.

—— Theoretical curves. o, □, Δ Experimental points for n = 2, 3 and 4 respectively.

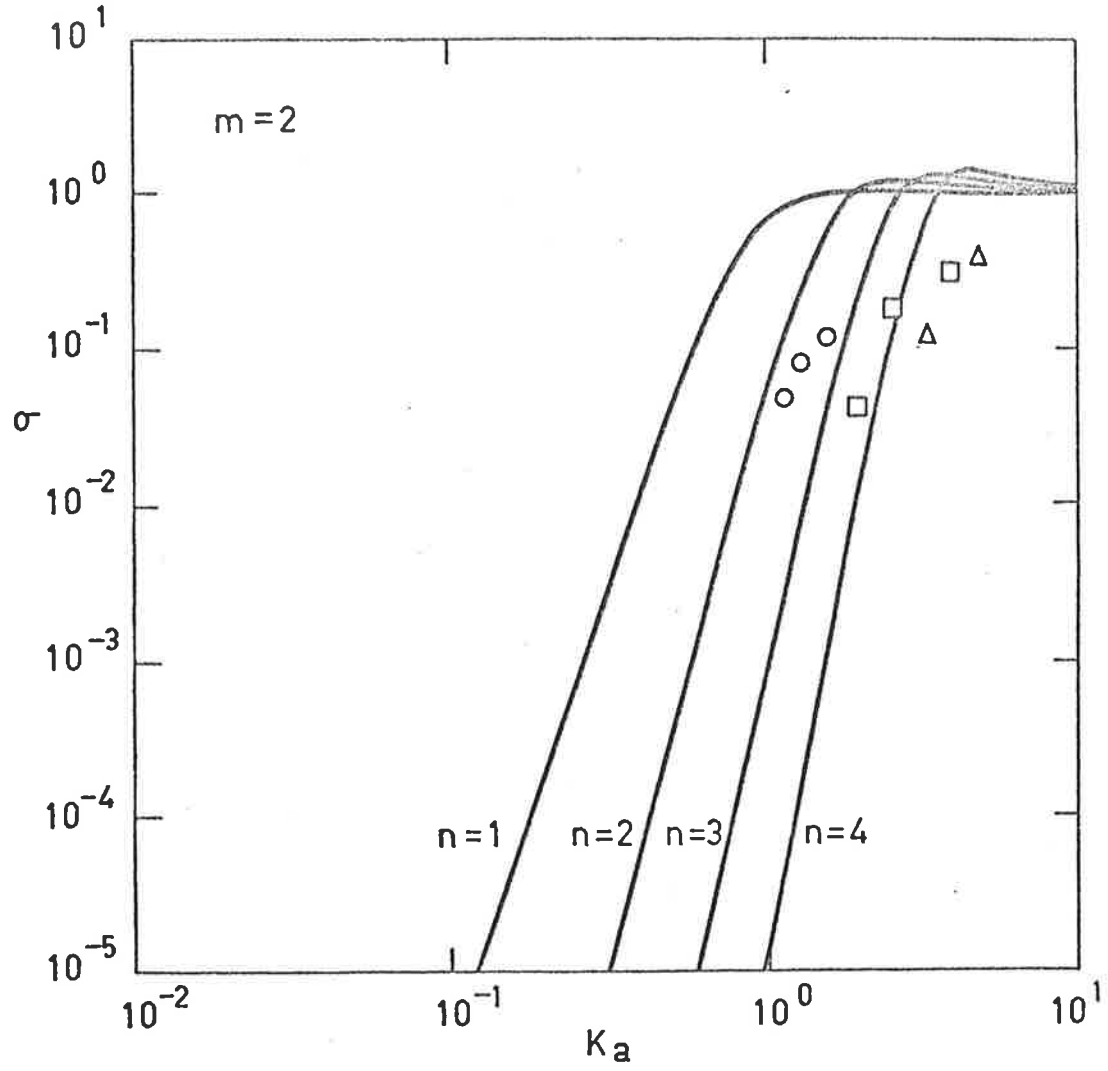

FIG. A6-5 (b) RADIATION EFFICIENCY OF STEEL CYLINDERS.

—— Theoretical curves. o, □, Δ Experimental points for n = 2, 3 and 4 respectively.

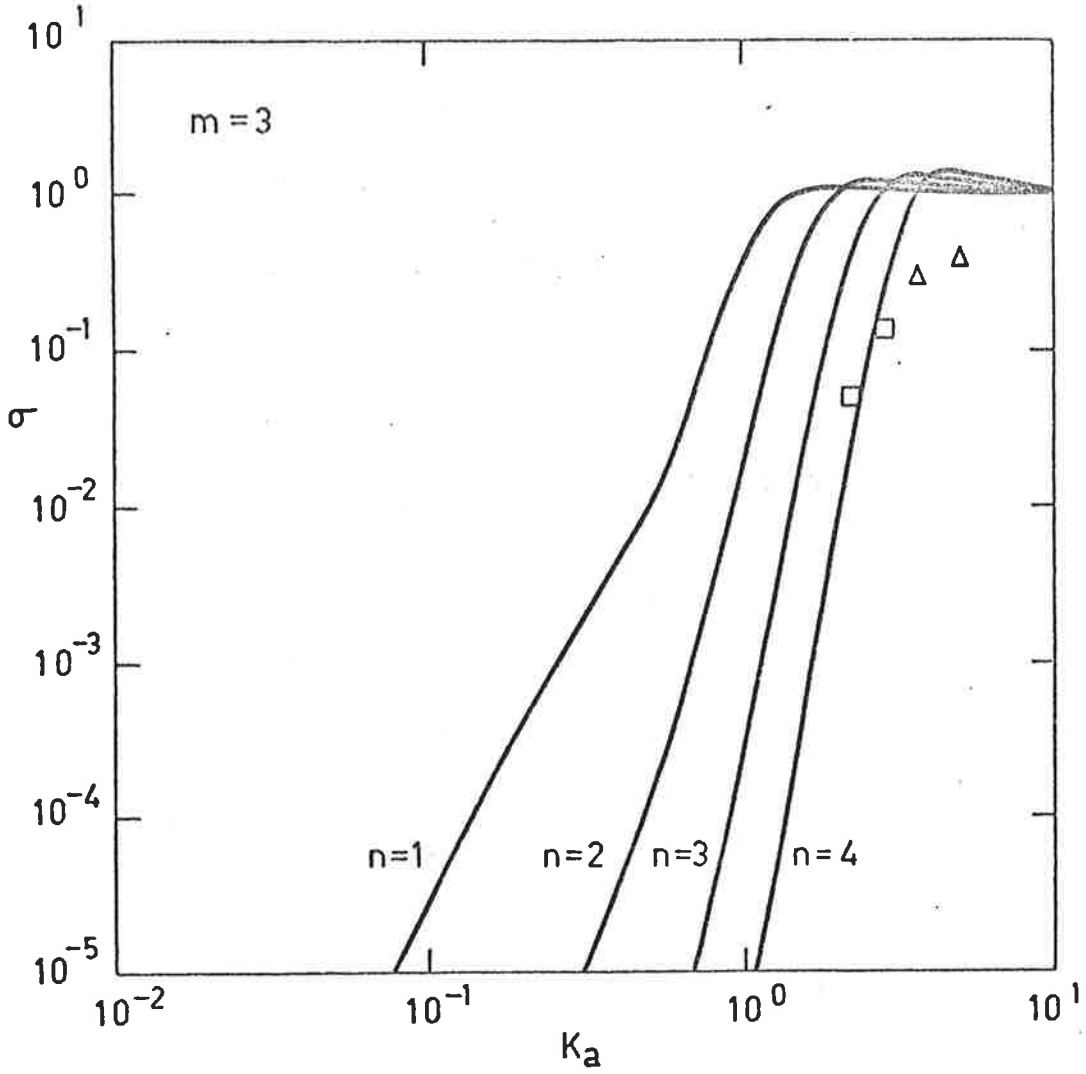

FIG. A6-5 (c) RADIATION EFFICIENCY OF STEEL CYLINDERS.

—— Theoretical curves. □, Δ Experimental points for n = 3 and 4 respectively.

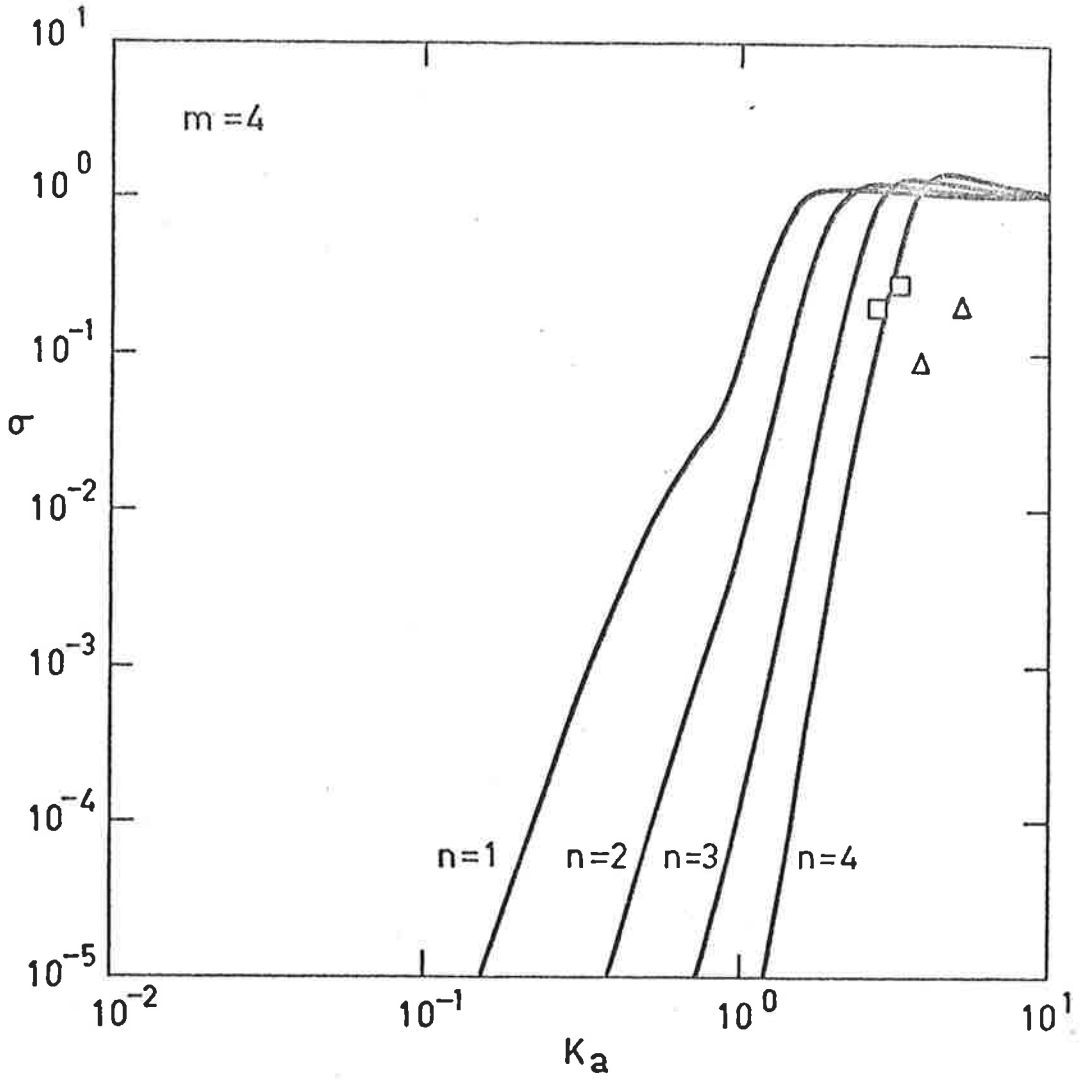

FIG. A6-5 (d) RADIATION EFFICIENCY OF STEEL CYLINDERS.

—— Theoretical curves. □,Δ Experimental points for n = 3 and 4 respectively.

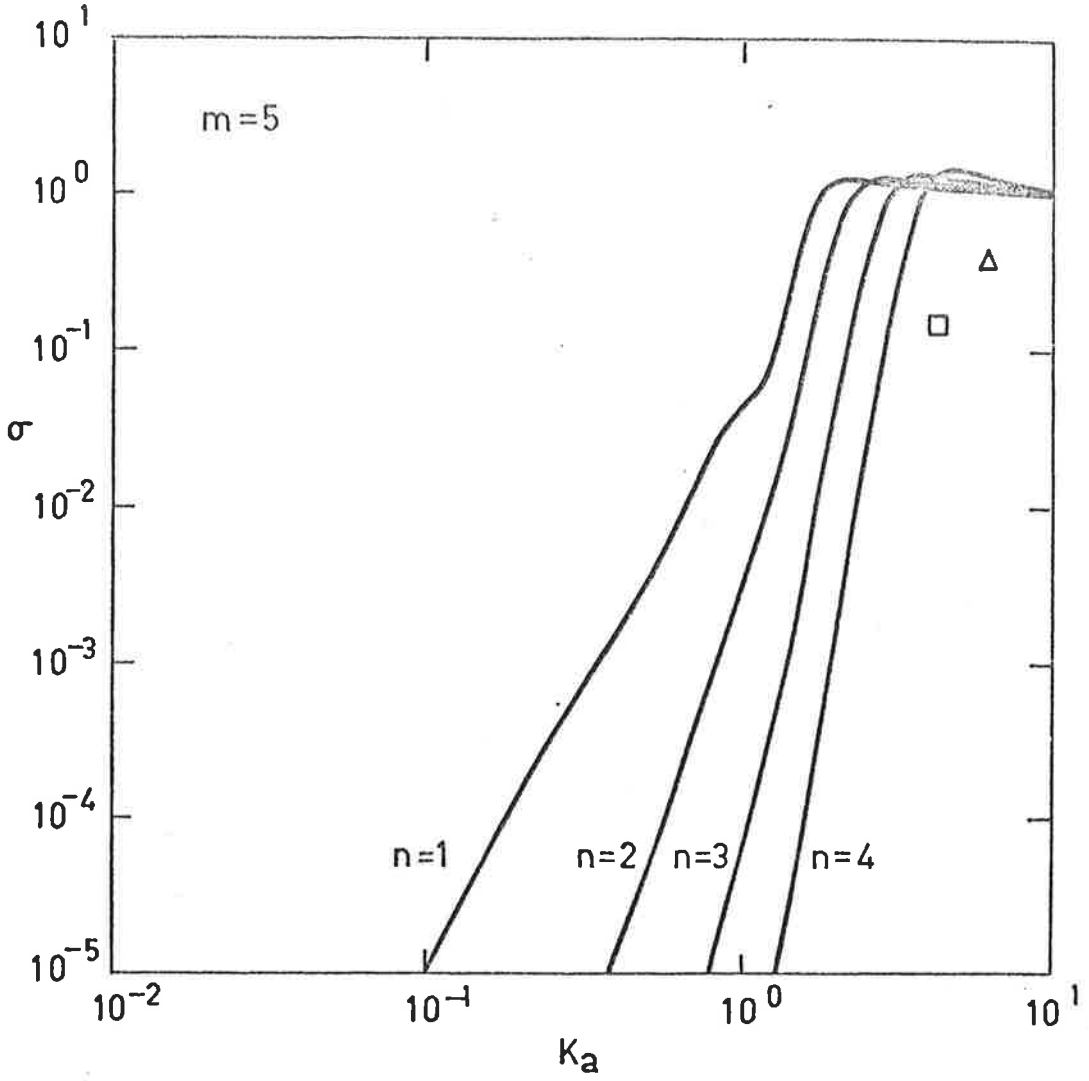

FIG. A6-5 (e) RADIATION EFFICIENCY OF STEEL CYLINDERS.

—— Theoretical curves. □, Δ Experimental points for n = 3 and 4 respectively.

Tonin, R., and Bies, D.A., (1977) Time-averaged holography for the study of three-dimensional vibrations.
Journal of Sound and Vibration, v. 52 (3), pp. 315-323.

REFERENCES

1. POWELL, R.L., & STETSON, K.A. (1965) — Interferometric Vibration Analysis by Wavefront Reconstruction. J. Optical Soc. Am. 55, 1593-1598.

2. STETSON, K.A., & POWELL, R.L. (1966) — Hologram Interferometry. J. Optical Soc. Am. 56, 1161-1166.

3. LALOR, E. (1968) — Conditions for the Validity of the Angular Spectrum of Plane Waves. J. Optical Soc. Am. 58, 1235-1237.

4. BROWN, G.M., GRANT, R.M. & STROKE, G.W. (1969) — Theory of Holographic Interferometry. J. Acoust. Soc. Am. 45, 1166-1179.

5. BUTUSOV, M.M. (1974) — Time-averaged Holographic Vibrometry; Features of Interference Pattern Recording. Opt. Spectrosc., 37, 301-303.

6. HILDEBRAND, B.P. (1970) — General Theory of Holography. J. Optical Soc. Am. 60, 1511-1517.

7. LURIE, M. (1966) — Effects of Partial Coherence on Holography with Diffuse Illumination. J. Optical Soc. Am. 56, 1369-1372.

8. NEUMANN, D.B. (1968) — Holography of Moving Scenes. J. Optical Soc. Am. 58, 447-454.

9. LEVI, L. (1975) — The Effect of Mechanical Vibrations on Holograms. Optics Communications, 13, 252-253.

10. LURIE, M. & ZAMBUTO, M. (1968) — A Verification of Holographic Measurement of Vibration. Applied Optics, 7, 2323-2325.

11. SOLODKIN, Y.N. (1973) (Novosibirsk) — A Holographic Interferometer as a Measuring Instrument. Automatic Monitoring & Measuring, Sept/Oct, 26-29.

12. BORZA, D.N. (1976) — Contributions to Vibration Measurement by Holographic Interferometry. Rev. Roum. Phys., 21, 657-659.

13. THEOCARIS, P.S. (1964) — Isopachic Patterns by the Moire Method. Experimental Mechanics, June, 153-159.

14. ROWE, S.H. (1971) — Projected Interference Fringes in Holographic Interferometry. J. Optical Soc. Am. 61, 1599-1603.

15. HUNG, Y.Y., LIANG, C.Y., HOVANESIAN, J.D., & DURELLI, A.J. (1977) — Time-averaged Shadow-moire Method for Studying Vibrations. Applied Optics, 16, 1717-1719.

16. JOYEUX, D. (1976) Real Time Measurement of Very Small Transverse Displacements of Diffuse Objects by Random Moire. 1: Theory Applied Optics, 15, 1241-1255.

17. OVECHKIN, A.P., VLADIMIROV, A.S., GOLUBEV, B.V., DUKHOPEL, I.I., LOVKOV, S.Y., POPOV, V.A., & FEDINA, L.G. (1975) A Holographic Interferometer with a Narrow Reference Beam for Studying Phase Objects. Sov.J.Opt.Technol., 42, 727-729.

18. ZEILIKOVICH, I.S. & KOMISSARUK, V.A. (1975) Localization of Fringes in Holographic Interferometry of Phase Objects with Diffuse Scatterers. Opt. Spectrosc., 39, 563-564.

19. DANDLIKER, R., MAROM, E., MOTTIER, F.M. (1976) Two-reference-beam Holographic Interferometry. J. Optical Soc. Am., 66, 23-30.

20. TSURUTA, T., SHIOTAKE, N. & ITOH, Y. (1968) Hologram Interferometry Using Two Reference Beams. Japanese Journal of Applied Physics, 7, 1092-1100.

21. BIES, D.A. (1974) The Investigation of the Uses of Holography for the Study of Vibrating and Acoustically Radiating Surfaces. Noise, Shock & Vibration Conference, (Monash Univ. Press, Melb.) pp 406-415.

22. FRANKORT, F.J.M. (1976) Vibration Patterns and Radiation Behaviour of Loudspeaker Cones. Philips Technical Review, 36, 1-15.

23. VASIL'YEV, A.M., DE, S.T., LOGINOV, A.V. & SOLODKIN, Y.N. (1973) Holographic Interferometry and the Vibrations of Objects. Automatic Monitoring & Measuring, Sept/Oct 22-23.

24. ZAKHAROV, V.P., EVTIKHIEV, N.N., SNEZHKO, Y.A., & TYCHINSKII, V.P. (1976) Application of Laser Interferometry for the Investigation of Vibratory Processes. Sov. Phys. Acoust. 22, 17-19.

25. GREGUSS, P. (1976) Holographic Interferometry in Biomedical Sciences. Optics and Laser Technology, Aug. 153-159.

26. HOGMOEN, K. & GUNDERSEN, T. (1977) Holographic Investigation of Stapes Footplate Movements. Acustica, 37, 198-202.

27. CHERNOV, V.P. & GORBATENKO, B.B. (1975) Color Holographic Interferogram. Opt. Spectrosc., 39, 550-551.

28. FRYER, P.A. (1970) Vibration Analysis by Holography. Rep. Prog. Phys., 33, 489-531.

29. JACOBSON, C.F. & HUBBARD, P.A. (1970) Holographic Techniques for the Analysis of Steady-State and Transient Vibrations. Holographic Instrumentation Applications Conf., Ames Research Center, California, January 13-14. 41-55.

30. HAINES, K.A. & HILDEBRAND, B.P. (1966) Surface-Deformation Measurement Using the Wavefront Reconstruction Technique. Applied Optics, 5, 595-602.

31. SOLLID, J.E. (1969) Holographic Interferometry Applied to Measurements of Small Static Displacements of Diffusely Reflecting Surfaces. Applied Optics, 8, 1587-1595.

32. DUIR, S.K. & SIKORA, J.P. (1972) An Improved Method for Obtaining the General-displacement Field from a Holographic Interferogram. Experimental Mechanics, July, 323-327.

33. SCIAMMARELLA, C.A., & GILBERT, J.A. (1973) Strain Analysis of a Disk Subjected to Diametral Compression by Means of Holographic Interferometry. Applied Optics, 12, 1951-1956.

34. BELLANI, F., & SONA, A. (1974) Measurement of Three-Dimensional Displacements by Scanning a Double-Exposure Hologram. Applied Optics, 13, 1337-1341.

35. STETSON, K.A. (1975) Homogeneous Deformations: Determination by Fringe Vectors in Hologram Interferometry. Applied Optics, 14, 2256-2259.

36. PRYPUTNIEWICZ, R. & STETSON, K.A. (1976) Holographic Strain Analysis: Extension of Fringe-Vector Method to Include Perspective. Applied Optics, 15, 725-728.

37. HU, C.P., TURNER, J.L. & TAYLOR, C.E. (1976) Holographic Interferometry: Compensation for Rigid Body Motion. Applied Optics, 15, 1558-1564.

38. ENNOS, A.E. (1968) Measurement of In-Plane Surface Strain by Hologram Interferometry. J. of Scientific Instruments (Journal of Physics E), 1 , 731-734.

39. SCIAMMARELLA, C.A. & GILBERT, J.A. (1976) A Holographic-moire Technique to Obtain Separate Patterns for Components of Displacement. Experimental Mechanics, June, 215-220.

40. BARKER, D.B. & FOURNEY, M.E. (1976) — Displacement Measurements in the Interior of 3-D Bodies Using Scattered-Light Speckle Patterns. Experimental Mechanics, June, 209-214.

41. TSURUTA, T., SHIOTAKE, N. & ITOH, Y. (1969) — Formation and Localization of Holographically Produced Interference Fringes. Optica Acta, 16, 723-733.

42. STETSON, K.A. (1969) — A Rigorous Treatment of the Fringes of Hologram Interferometry. Optik 29, 386-400.

43. STETSON, K.A. & MOLIN, N.E. (1970) — Measurement of Fringe Loci and Localization in Hologram Interferometry for Pivot Motion, In-Plane Rotation and In-Plane Translation, Part 1. Optik, 31, 157-177.

44. MOLIN, N.E. & STETSON, K.A. (1970) — Measurement of Fringe Loci and Localization in Hologram Interferometry for Pivot Motion, In-Plane Rotation and In-Plane Translation, Part II. Optik, 31, 281-291.

45. STETSON, K.A. (1970) — The Argument of the Fringe Function in Hologram Interferometry of General Deformations. Optik, 31, 576-591.

46. MOLIN, N.E. & STETSON, K.A. (1971) — Fringe Localization in Hologram Interferometry of Mutually Independent and Dependent Rotations around Orthogonal, Non-Intersecting Axes. Optik, 33, 399-422.

47. STETSON, K.A. (1974) — Fringe Interpretation for Hologram Interferometry of Rigid-Body Motions and Homogeneous Deformations. J. Optical Soc. Am. 64, 1-10.

48. STETSON, K.A. (1975) — Fringe Vectors and Observed-Fringe Vectors in Hologram Interferometry. Applied Optics, 14, 272-273.

49. WALLES, S. (1970) — On the Concept of Homologous Rays in Holographic Interferometry of Diffusely Reflecting Surfaces. Optica Acta, 17, 899-913.

50. ABRAMSON, N. (1969) — The Holo-Diagram: a Practical Device for Making and Evaluating Holograms. Applied Optics, 8, 1235-1240.

51. ABRAMSON, N. (1970) — The Holo-Diagram. II: a Practical Device for Information Retrieval in Hologram Interferometry. Applied Optics, 9, 97-101.

52. ABRAMSON, N. (1970) — The Holo-Diagram. III: A Practical Device for Predicting Fringe Patterns in Hologram Interferometry. Applied Optics, 9 , 2311-2320.

53. ABRAMSON, N. (1971) — The Holo-Diagram. IV: A Practical Device for Simulating Fringe Patterns in Hologram Interferometry. Applied Optics, 10, 2155-2161.

54. ABRAMSON, N. (1972) — The Holo-Diagram. V: A Device for Practical Interpreting of Hologram Interference Fringes. Applied Optics, 11, 1143-1147.

55. ABRAMSON, N. (1972) — The Holo-Diagram. VI: Practical Device in Coherent Optics. Applied Optics, 11, 2562-2571.

56. ABRAMSON, N. (1974) — Sandwich Hologram Interferometry: A New Dimension in Holographic Comparison. Applied Optics, 13, 2019-2025.

57. MATSUMOTO, T., IWATA, K. & NAGATA, R. (1973) — Measuring Accuracy of Three-Dimensional Displacements in Holographic Interferometry. Applied Optics, 12, 961-967.

58. REDMAN, J.D. (1967) — Holographic Velocity Measurement. J. Sci. Instrum., 44, 1032-1033.

59. VIKRAM, C.S. & SIROHI, R.S. (1971) — Use of Pre- and Post-Exposure in Holographic Measurement of High Velocities. Physics Letters, 36A, 279-280.

60. GUPTA, P.C. & SINGH, K. (1975) — Characteristic Fringe Function for Time-Average Holography of Periodic Nonsinusoidal Vibrations. Applied Optics, 14, 129-133.

61. GUPTA, P.C. & SINGH, K. (1976) — Holographic Weighted Subtraction in Time-Average Hologram Interferometry of Periodic, Non-Sinusoidal Vibrations. Indian J. Phys., 50, 32-40.

62. GUPTA, P.C. & SINGH, K. (1976) — Laser Speckle Interferometry of Constant Velocity and Quadratic Motion: A Theoretical Analysis. Indian J. Phys., 50, 334-339.

63. GUPTA, P.C. & SINGH, K. (1976) — Analysis of Cn^2 Vibrations by Time-Average Holography. Indian Journal of Pure & Applied Physics, 14, 367-371.

64. JANTA, J. & MILER, M. (1972) — Time-Average Holographic Interferometry of Damped Oscillations. Optik, 36, 185-195.

65. ZAMBUTO, M. & LURIE, M. (1970) — Holographic Measurement of General Forms of Motion. Applied Optics, 9, 2066-2072.

66. VIKRAM, C.S. (1975) — Holographic Interferometry of Superposition of Two Motions. Optik, 43, 65-70.

67. VIKRAM, C.S. (1976) — Holographic Interferometry of Superposition of Motions with Different Time Functions. Optik, 45, 55-64.

68. VIKRAM, C.S. (1973) — Time-Average Holography of Objects Vibrating Sinusoidally and Moving with Constant Acceleration. Optics Communications, 8, 355-357.

69. VIKRAM, C.S. (1973) — A Coherent Moire Technique for Time-Average Holography of Objects Vibrating Sinusoidally with Uniform Slow Drift. Physics Letters, 45A, 426.

70. VIKRAM, C.S. & SIROHI, R.S. (1971) — Holographic Images of Objects Moving with Constant Acceleration. Applied Optics, 10, 672-673.

71. VIKRAM, C.S. & SIROHI, R.S. (1971) — Time-Average Holography of Objects Vibrating Sinusoidally with Uniform Slow Drift. Physics Letters, 35A, 460-461.

72. VIKRAM, C.S. (1974) — Quadruple-Exposure Holographic Interferometry for Analysis of Superposition of Ramp Motion and Sinusoidal Vibration. Optics Communications, 10, 290-291.

73. WILSON, A.D. & STROPE, D.H. (1970) — Time-Average Holographic Interferometry of a Circular Plate Vibrating Simultaneously in Two Rationally Related Modes. Journal of the Optical Society of America, 60, 1162-1165.

74. WILSON, A.D. (1971) — Computed Time-Average Holographic Interferometric Fringes of a Circular Plate Vibrating Simultaneously in Two Rationally or Irrationally Related Modes. J. Optical Soc. Am., 61, 924-929.

75. REDDY, G.R. (1975) — Holographic Interferometry of Non-Harmonic Periodic Motions. Indian J. Phys., 50, 445-448.

76. STETSON, K.A. (1972) Method of Stationary Phase for Analysis of Fringe Functions in Hologram Interferometry. Applied Optics, 11, 1725-1731.

77. VIKRAM, C.S. (1974) Stroboscopic Holographic Interferometry of Vibration Simultaneously in Two Sinusoidal Modes. Optics Communications, 11, 360-364.

78. DALLAS, W.J. & LOHMANN, A.W. (1975) Deciphering Vibration Holograms. Optics Communications, 13, 134-137.

79. WILSON, A.D. (1970) Characteristic Functions for Time-Average Holography. J. Optical Soc. Am., 60, 1068-1071.

80. STETSON, K.A. (1971) Hologram Interferometry of Nonsinusoidal Vibrations Analyzed by Density Functions. J. Optical Soc. Am., 61, 1359-1362.

81. STETSON, K.A. (1972) Fringes of Hologram Interferometry for Simple Nonlinear Oscillations. J.Opt. Soc.Ar Letters to the Editor, 62, 297-298.

82. VIKRAM, C.S. & BOSE, G. (1975) Holographic Interferometry of Damped Oscillations with Two Frequencies. Optik, 43, 253-258.

83. STETSON, K.A. & TAYLOR, P.A. (1972) Analysis of Static Deflections by Holographically Recorded Vibration Modes. Journal of Physics E, 5, 923-926.

84. STETSON, K.A. & TAYLOR, P.A. (1971) The Use of Normal Mode theory in Holographic Vibration Analysis with Application to an Asymmetrical Circular Disk. Journal of Physics E, 4, 1009-1015.

85. EVENSEN, D.A. (1976) Application of Holography to Panel Flutter. AIAA Journal, 14, 1671-1674.

86. MOLIN, N.E. & STETSON, K.A. (1969) Measuring Combination Mode Vibration Patterns by Hologram Interferometry. Journal of Scientific Instruments, 2, 609-612.

87. SHAJENKO, P. & JOHNSON, C.D. (1968) Stroboscopic Holographic Interferometry. Applied Physics Letters, 13, 44-46.

88. MILER, M. (1975) Stroboscopic Holography in Ramp Approximation. Optics Communications, 14, 406-408.

89. TAKAI, N., YAMADA, M. & IDOGAWA, T. (1976) — Holographic Interferometry Using a Reference Wave with a Sinusoidally Modulated Amplitude. Optics and Laser Technology, Feb, 21-23.

90. ALEKSOFF, C.C. (1969) — Time Average Holography Extended. Applied Physics Letters, 14, 23-24.

91. NEUMANN, D.B., JACOBSON, C.F. & BROWN, G.M. (1970) — Holographic Technique for Determining the Phase of Vibrating Objects. Applied Optics, 9, 1357-1362.

92. ALEKSOFF, C.C. (1971) — Temporally Modulated Holography. Applied Optics, 10, 1329-1341.

93. MOTTIER, F.M. (1969) — Time-Averaged Holography with Triangular Phase Modulation of the Reference Wave. Applied Physics Letters, 15, 285-287.

94. GUPTA, P.C. & AGGARWAL, A.K. (1976) — Simultaneous Detection of Direction of Motion and Fringe Order Determination in Holographic Displacement Measurement. Applied Optics, 15, 2961-2963.

95. STETSON, K.A. (1970) — Effects of Beam Modulation on Fringe Loci and Localization in Time-Average Hologram Interferometry. J. Optical Soc. Am., 60, 1378-1388.

96. LOKBERG, O.J. & HOGMOEN, K. (1976) — Vibration Phase Mapping Using Electronic Speckle Pattern Interferometry. Applied Optics, 15, 2701-2704.

97. BELOGORODSKII, B.A., BUTUSOV, M.M. & TURKEVICH, Y.G. (1972) — Holographic Method of Vibration Analysis with a Phase-Modulated Reference Beam. Soviet Physics - Acoustics, 17, 378-379.

98. BUTUSOV, M.M. (1973) — A Holographic System for Underwater Examination of Vibrations. Automatic Monitoring & Measuring, Sept/Oct, 24-25.

99. YONEYAMA, M. (1975) FUJIMOTO, J. & OGAWA, H. — Holographic Recording Methods for Vibrating Mode of Loudspeaker under External Disturbance. Journal of the Acoustical Society of Japan, 31, 614-622.

100. LEVITT, J.A. & STETSON, K.A. (1976) — Mechanical Vibrations: Mapping Their Phase with Hologram Interferometry. Applied Optics, 15, 195-199.

101. LIEM, S.D. & HAZELL, C.R. (1973) — Vibration Analysis of Circular Cylinders by Holographic Interferometry. Journal of Sound and Vibration, 29,475-481.

102. TONIN, R. & BIES, D.A. (1977) — Time-Averaged Holography for the Study of Three-Dimensional Vibrations. Journal of Sound and Vibration, 52, 315-323.

103. ALEKSANDROV, E.B. & BONCH-BRUEVICH, A.M. (1967) — Investigation of Surface Strains by the Hologram Technique. Sov. Phys. Tech. Physics, 12, 258-265.

104. TUSCHAK, P.A. & ALLAIRE, R.A. (1975) — Axisymmetric Vibrations of a Cylindrical Resonator Measured by Holographic Interferometry. Experimental Mechanics, March, 81-88.

105. TONIN, R. & BIES, D.A. (1978) — Analysis of Three-Dimensional Vibrations from Time-Averaged Holograms. Submitted to Applied Optics for publication.

106. TONIN, R. & BIES, D.A. (1978) — General Theory of Time-Averaged Holography for the Study of Three-Dimensional Vibrations at a Single Frequency. Submitted to Journal of the Optical Society of America for publication.

107. VLASOV, N.G. & SHTAN'KO, A.E. (1976) — Determination of Order Number and Sign of Interference Fringes. Sov. Phys. Tech. Phys., 21, 111-112.

108. ARCHBOLD, E. & ENNOS, A.E. (1975) — Two-Dimensional Vibrations Analysed by Speckle Photography. Optics and Laser Technology, Feb, 17-21.

109. ZELENKA, J.S. & VARNER, J.R. (1968) — A New Method for Generating Depth Contours Holographically. Applied Optics, 7, 2107-2110.

110. MEADOWS, D.M., JOHNSON, W.O. & ALLEN, J.B. (1970) — Generation of Surface Contours by Moire Patterns. Applied Optics, 9, 942-947.

111. TAKASAKI, H. (1970) — Moire Topography. Applied Optics, 9, 1457-1472.

112. TAKASAKI, H. (1973) — Moire Topography. Applied Optics, 12, 845-850.

113. TSURUTA, T., ITOH, Y. & ANZAI, S. (1970) — Moire Topography for the Measurement of Film Flatness. Applied Optics, 9, 2802-2804.

114. ALLEN, J.B. & MEADOWS, D.M. (1971) — Removal of Unwanted Patterns from Moire Contour Maps by Grid Translation Techniques. Applied Optics, 10, 210-212.

115. DESSUS, B., GERARDIN, J.P. & MOUSSELET, P. (1975) — Une 'Methode des Franges' en Temps reel et ses Applications Industrielles: Deformations, Vibrations, Courbes de Niveau. Optical and Quantum Electronics, 7, 15-45.

116. TABOADA, J. & ALTSCHULER, B.R. (1976) — Rectangular Grid Fringe Pattern for Topographic Applications. Applied Optics, 15, 597-599.

117. ABRAMSON, N. (1976) — Holographic Contouring by Translation. Applied Optics, 15, 1018-1022.

118. ABRAMSON, N. (1975) — Sandwich Hologram Interferometry. 2: Some Practical Calculations. Applied Optics, 14, 981-984.

119. ABRAMSON, N. (1976) — Sandwich Hologram Interferometry. 3: Contouring. Applied Optics, 15, 200-205.

120. YOSHINO, Y., TSUKIJI, M. & TAKASAKI, H. (1976) — Moire Topography by Means of a Grating Hologram. Applied Optics, 15, 2414-2417.

121. HILDEBRAND, B.P. & HAINES, K.A. (1967) — Multiple-Wavelength and Multiple-Source Holography Applied to Contour Generation. J. Optical Soc. Am., 57, 155-162.

122. VARNER, J.R. (1971) — Simplified Multiple-Frequency Holographic Contouring. App. Opt. 10, 212.

123. FRIESEM, A.A. & LEVY, U. (1976) — Fringe Formation in Two-Wavelength Contour Holography. Applied Optics, 15, 3009-3020.

124. MILES, C.A. & SPEIGHT, B.S. (1975) — Recording the Shape of Animals by a Moire Method. J. Phys. E., 8, 773-776.

125. LEISSA, A.W. (1973) — Vibration of Shells. (NASA SP-288), Chapter 2, pp 31-61.

126. ARNOLD, R.N. & WARBURTON, G.B. (1949) — Flexural Vibrations of the Walls of Thin Cylindrical Shells Having Freely Supported Ends. Proc. Roy. Soc.A, 197, 238-256.

127. ARNOLD, R.N. & WARBURTON, G.B. (1953) — The Flexural Vibrations of Thin Cylinders. Proc.(A) Institution of Mech. Eng. (London), 167, 62-74.

128. WARBURTON, G.B. (1961) — Vibration of a Cylindrical Shell in an Acoustic Medium. Journal Mechanical Engineering Science, 3, 69-79.

129. WARBURTON, G.B. (1965) Vibration of Thin Cylindrical Shells. Journal Mechanical Engineering Science, 7, 399-407.

130. WARBURTON, G.B. (1977) Free Vibrations of Circular Cylindrical Shells. (Letters to the Editor). Journal of Sound and Vibration, 50, 599-601.

131. LEE, W.F.Z., & SAIBEL, E. (1952) Free Vibrations of Constrained Beams. J. Applied Mechanics, (ASME Trans Series E), 19, 471-477.

132. JONES, R.P.N. (1960) The Effect of Small Changes in Mass and Stiffness on the Natural Frequencies and Modes of Vibrating Systems. Int. J. Mech. Sci., 1, 350-355.

133. JONES, R.P.N. & MAHALINGAM, S. (1960) The Natural Frequencies of Free and Constrained Non-Uniform Beams. Journal of the Royal Aeronautical Society, 64, 697-699.

134. STETSON, K.A. (1975) Perturbation Method of Structural Design Relevant to Holographic Vibration Analysis. AIAA Journal, 13, 457-459.

135. LAURA, P.A.A., SUSEMIHL, E.A., POMBO, J.L.,LUISONI, L.E. & GELOS, R. (1977) On the Dynamic Behaviour of Structural Elements Carrying Elastically Mounted, Concentrated Masses. Applied Acoustics,10, 121-145.

136. HURTY, W.C., & RUBINSTEIN, M.F. (1964) Dynamics of Structures. (Prentice-Hall Inc.)

137. FIRTH, D. (1975) The Vibration of a Distorted Circular Cylinder Containing Liquid. Transactions of the 3rd International Conference on Structural Mechanics in Reactor Technology, paper F2/10, Sept., 1-7.

138. ROSEN, A. & SINGER, J. (1974) Effect of Axisymmetric Imperfections on the Vibrations of Cylindrical Shells under Axial Compression. AIAA Journal, 12, 995-997.

139. ROSEN, A., et al. (1975) Influence of Asymmetric Imperfections on the Vibrations of Axially Compressed Cylindrical Shells. Israel Institute of Technology, Technical Report AD-A017 682.

140. YOUSRI, S.N. & FAHY, F.J. (1976) Distorted Cylindrical Shell Response to Internal Acoustic Excitation Below the Cut-Off Frequency. ISVR Technical Report No. 82, Univ. of Southampton.

141. TODA, S. & KOMATSU, K. (1977) Vibrations of Circular Cylindrical Shells with Cutouts. Journal of Sound and Vibration, 52, 497-510.

142. BROGAN, F., FORSBERG, K. & SMITH, S. (1968) Experimental and Analytical Investigation of the Dynamic Behavior of a Cylinder with a Cutout. AIAA/ASME 9th Structures, Structural Dynamics and Materials Conference, Palm Springs, California, No. 68-318.

143. TONIN, R. & BIES, D.A. (1978) The Vibration of Circular Cylinders of Variable Thickness. Submitted to Journal of Sound and Vibration for publication.

144. HANSEN, C.H. & BIES, D.A. (1975) Optical Holography for the Study of Sound Radiation from Vibrating Surfaces. University of Adelaide, South Australia, Technical Report No. TN 3/1975.

145. KUHN, G.F. & MORFEY, C.L. (1976) Transmission of Low-Frequency Internal Sound Through Pipe Walls. Journal of Sound and Vibration, 47, 147-161.

146. CREMER, L. & HECKL, M. (1973) Structure-Borne Sound - Structural Vibrations and Sound Radiation at Audio Frequencies. (Springer-Verlag Berlin Heidelberg New York), Chapter VI, pp 455-491.

147. YOUSRI, S.N. & FAHY, F.J. (1975) Acoustic Radiation by Unbaffled Cylindrical Beams in Multi-Modal Transverse Vibration. Journal of Sound and Vibration, 40, 299-306.

148. JUNGER, M.C. & FEIT, D. (1972) Sound, Structures, and Their Interaction. MIT Press, Cambridge.

149. MANNING, J.E. & MAIDANIK, G. (1964) Radiation Properties of Cylindrical Shells. J. Acoust. Soc. Am., 36 1691-1698.

150. IVANOV, V.S. & ROMANOV, V.N. (1975) Determination of the Sound Radiation from a Point-Driven Infinitely Long Thin Cylinder. Sov. Phys. Acoust., 21, 129-135.

151. BERNBLIT, M.V. (1976) Sound Radiation from a Ribbed Cylindrical Shell. Sov. Phys. Acoust., 21, 518-521.

152. BERNBLIT, M.V. (1976) Sound Radiation from a Point-Driven Thin Cylindrical Shell with Rigid Massive Septa. Sov. Phys. Acoust. 22, 3-7.

153. SPENDLEY, W. (1969) Optimization, Symposium of the Institute of Mathematics and Its Applications. (Academic Press, London and New York), Chapter 16, pp 259-269.

154. POWELL, M.J.D. (1965) A Method for Minimizing a Sum of Squares on Non-Linear Functions Without Calculating Derivatives. Computer Journal, 7, 303-307.

155. ERF, R.K. (Ed.) (1974) Holographic Non-destructive Testing, (Academic Press, New York), pp 202.

156. SHIRAKAWA, K. & MIZOGUCHI, K. (1977) Dynamic Response of a Cylindrical Shell to a Concentrated Periodical Force. Bulletin of the JSME, 20, 9-16.

157. A method suggested to D.A. Bies by Prof. Isador Rudnick of the University of California, L.A.

158. KREYSZIG, E. (1967) Advanced Engineering Mathematics. 2nd Edition, Wiley.

159. BUCKINGHAM, R.A. (1962) Numerical Methods. (Pitman Press).

160. BARTLETT, D.P. (1915) The Method of Least Squares. (Rumford Press, Concord, N.H.)

161. FAIRES, V.M. (1965) Design of Machine Elements. 4th Edition. (The MacMillan Company, New York/Collier-MacMillan Limited, London). pp 567-577.

162. Eigensystem Subroutine Package (EISPACK) which is available from Argonne National Laboratory. Applied Mathematics Division, 9700 S. Cass Avenue, Argonne, Illinois 60439 U.S.A.

163. Matrix Inverse Package (MATINV) contributed by Los Alamos Scientific Laboratory (1969).

164. RENNISON, D.C. (1976) The Vibrational Response of and the Acoustic Radiation from Thin-Walled Pipes, Excited by Random Fluctuating Pressure Fields. Ph.D. Thesis, Department of Mechanical Engineering, University of Adelaide.

165. The data acquisition system was conceived by D.A. Bies and designed by P. Walker of the University of Adelaide.

166. BERANEK, L. (1971) Noise and Vibration Control. (McGraw Hill, New York).